

Summer 2023

First Principles Doping Analysis of Perovskite- And Ruddlesden-Popper-Based Solid Oxide Fuel Cells

Nicholas Alexander Szaro

Follow this and additional works at: <https://scholarcommons.sc.edu/etd>



Part of the [Chemical Engineering Commons](#)

Recommended Citation

Szaro, N. A. (2023). *First Principles Doping Analysis of Perovskite- And Ruddlesden-Popper-Based Solid Oxide Fuel Cells*. (Doctoral dissertation). Retrieved from <https://scholarcommons.sc.edu/etd/7400>

This Open Access Dissertation is brought to you by Scholar Commons. It has been accepted for inclusion in Theses and Dissertations by an authorized administrator of Scholar Commons. For more information, please contact digres@mailbox.sc.edu.

FIRST PRINCIPLES DOPING ANALYSIS OF PEROVSKITE- AND
RUDDLESDEN-POPPEL-BASED SOLID OXIDE FUEL CELLS

by

Nicholas Alexander Szaro

Bachelor of Science
University of Georgia, 2017

Submitted in Partial Fulfillment of the Requirements

For the Degree of Doctor of Philosophy in

Chemical Engineering

College of Engineering and Computing

University of South Carolina

2023

Accepted by:

Andreas Heyden, Major Professor

Salai C. Ammal, Committee Member

William E. Mustain, Committee Member

Fanglin Chen, Committee Member

Melissa A. Moss, Committee Member

Ann Vail, Dean of the Graduate School

© Copyright by Nicholas Alexander Szaro, 2023
All Rights Reserved.

DEDICATION

To Madeline, my heart.

ACKNOWLEDGEMENTS

I thank my advisor and mentor, Dr. Andreas Heyden for his wisdom and ingenuity. I thank Dr. Salai Ammal for her expertise and patience. I thank the current and past members of the Heyden research group: Charles, Dia, Kyun-Eun, Wenqiang, Mehdi, Saleheen, Olajide, Bhawana, Paratee, Panuwat, Mubarak, and Subrata for their help and friendship. Lastly, I gratefully acknowledge the financial support from the U.S. National Science Foundation.

ABSTRACT

Solid oxide fuel cells (SOFCs) have shown significant promise as a high efficiency energy conversion technology. SOFCs are solid-state, high temperature (600 – 1000 °C), and electrochemical conversion devices that can operate with a wide variety of fuels such as hydrogen, syngas, and hydrocarbon feedstocks. The state-of-the-art SOFC is manufactured with a lanthanum strontium manganite (LSM) cathode, an yttria-stabilized-zirconia electrolyte (YSZ), and a nickel on yttria-stabilized-zirconia (Ni/YSZ) cermet anode. LSM || YSZ || Ni/YSZ SOFCs operate at or above 800 °C to achieve sufficient oxide mobility. The high temperatures introduce problems such as long device start-up, particle sintering, and material degradation due to thermal stresses. To remedy these problems, ongoing SOFC research focuses on the intermediate temperature (IT) range between 600 and 800 °C. Intermediate range research primarily focuses on the discovery and design of novel materials for the anode, cathode, and electrolyte layers of the SOFC. This dissertation focuses on the material design of two promising classes of IT materials: the Ruddlesden-Popper (RP) phase and the cubic perovskite.

For the first aim, the bulk structural, electronic, and ionic conduction properties for the RP perovskite $(\text{Sr,Pr})_2\text{FeO}_4$ (SPF) family are investigated as a function of Pr^{3+} concentration. For a given dopant-configuration, generalized gradient approximation-based density functional theory is used to model the relationship between Pr^{3+} concentration, iron oxidation state, and charge compensation with defect formation to explain doping trends for electronic and ionic conduction. For the second aim and to

better understand how A-site doped RP materials behave as oxidation catalysts, SrLaFeO₄ is modeled to elaborate the oxidation mechanisms of hydrogen and syngas fuels. Two (001) Fe-terminated surface models are proposed that differ by the elemental identity of the underlying rocksalt layer. The FeO₂-SrO (001) surface displays higher activity for both hydrogen and syngas oxidation relative to the FeO₂-LaO (001) for all cell voltages including short circuit conditions. Lastly, for the third aim, a high-throughput approach is utilized to model 4793 unique perovskites elemental configurations in order to discover novel proton-conducting electrolyte materials. A filtering scheme based on electrical conductivity and thermodynamic stability under water-containing conditions yields 116 suitable configurations. For all passing configurations, oxygen vacancy defect and hydration formation are modeled to elaborate on trends related to proton conductivity. Four distinct elemental regimes are identified: acceptor-dopant, Sn-containing, BaZrO₃-like, and BaCeO₃-like. Acceptor-dopant configurations are best at forming oxygen vacancy defects and hydration relative to all other elemental regimes – consistent with experiments. A final filter related to the thermodynamic stability of CO₂-containing conditions yields 43 promising configurations from the original 4793.

TABLE OF CONTENTS

Dedication	iii
Acknowledgements	iv
Abstract	v
List of Tables	viii
List of Figures	xi
Chapter 1: Introduction	1
Chapter 2: An Ab Initio Study of the Oxygen Defect Formation and Oxide Ion Migration in $(\text{Sr}_{1-x}\text{Pr}_x)_2\text{FeO}_{4\pm\delta}$	7
Chapter 3: Theoretical Investigation of the Electrochemical Oxidation of H_2 and CO Fuels on a Ruddlesden-Popper $\text{SrLaFeO}_{4-\delta}$ Anode	45
Chapter 4: First Principles Material Screening and Discovery of Perovskite Electrolytes for Proton-Conducting Solid Oxide Fuel Cells	94
Chapter 5: Conclusion	132
References	137
Appendix A: Supporting Information for An Ab Initio Study of the Oxygen Defect Formation and Oxide Ion Migration in $(\text{Sr}_{1-x}\text{Pr}_x)_2\text{FeO}_{4\pm\delta}$	153
Appendix B: Supporting Information for Theoretical Investigation of the Electrochemical Oxidation of H_2 and CO Fuels on a Ruddlesden-Popper $\text{SrLaFeO}_{4-\delta}$ Anode	166
Appendix C: Supporting Information for First Principles Material Screening and Discovery of Perovskite Electrolytes for Proton-Conducting Solid Oxide Fuel Cells	177
Appendix D: Copyright Permissions	203

LIST OF TABLES

<p>Table 2.1: Average Fe magnetic moment (μ_B) and Bader charges (e) for $(\text{Sr}_{1-x}\text{Pr}_x)_2\text{FeO}_{4\pm\delta}$ with and without oxygen vacancy ($\text{V}_{\text{O}}^{\cdot\cdot}$) and interstitial oxygen ($\text{O}_i^{\prime\prime}$) defects for $x = 0, 0.125, 0.25, 0.375,$ and 0.5.</p>	37
<p>Table 2.2: Formation energies (in eV) of oxygen vacancies ($\Delta E_{f,\text{vac}}$) and interstitial oxygen defects ($\Delta E_{f,\text{int}}$) calculated for $(\text{Sr}_{1-x}\text{Pr}_x)_2\text{FeO}_{4\pm\delta}$ with $x = 0, 0.125, 0.25, 0.375,$ and 0.5.</p>	38
<p>Table 2.3: Magnetic moment (μ_B) and Bader charges (e) of nearest neighbor(s) Fe to the oxide defect for $(\text{Sr}_{1-x}\text{Pr}_x)_2\text{FeO}_{4\pm\delta}$ with $x = 0, 0.125, 0.25, 0.375,$ and 0.5. P refers to defect free or the pristine state. D refers to the defect-containing state.</p>	39
<p>Table 2.4: Migration energies (top number) and relative vacancy formation energies (bottom number in parenthesis) in eV for all non-identical oxygen vacancy migration jump routes.</p>	42
<p>Table 3.1: Forward rate (k_{for}) and equilibrium constants (K_{eq}) for all short-circuit reaction steps for H_2 and CO oxidation on the $\text{FeO}_2\text{-LaO}$ and $\text{FeO}_2\text{-SrO}$ surface models at 1073 K ($P_{\text{H}_2,\text{CO}} = 1.00$ atm, $P_{\text{H}_2\text{O},\text{CO}_2} = 0.03$ atm, and $P_{\text{O}_2} = 0.21$ atm).</p>	89
<p>Table 3.2: Degree of rate control (DRC), apparent activation energies (calculated in the temperature range of 973-1273 K), and turnover frequencies calculated for H_2 and CO oxidation over $\text{FeO}_2\text{-LaO}$ and $\text{FeO}_2\text{-SrO}$ surfaces at short circuit conditions ($T = 1073$ K, $P_{\text{H}_2,\text{CO}} = 1.00$ atm, $P_{\text{H}_2\text{O},\text{CO}_2} = 0.03$ atm, and $P_{\text{O}_2} = 0.21$ atm).</p>	89
<p>Table 3.3: Transition state free energies of the dissociative adsorption of hydrogen ($\Delta G_{\text{H}_2}^\ddagger$ in eV) and surface water formation ($\Delta G_{\text{H}_2\text{O}}^\ddagger$ in eV) at 1073 K, $P_{\text{H}_2}(\text{gas}) = 1.0$ atm, $P_{\text{H}_2\text{O}}(\text{gas}) = 0.03$ atm, and $P_{\text{O}_2}(\text{gas}) = 0.21$ atm) calculated with reference to the energies of initial active site and H_2 gas, and turnover frequency (TOF in s^{-1}) of H_2 oxidation calculated at short circuit conditions for single surface metal atom doped $\text{Fe}_{1-x}\text{M}_x\text{O}_2\text{-LaO}$ and $\text{Fe}_{1-x}\text{M}_x\text{O}_2\text{-SrO}$ ($x = 0.11$; $\text{M} = \text{Fe}, \text{Co}, \text{Ni}, \text{Mn}$) surface models.</p>	91

Table 3.4: Reaction free energies for the dissociative adsorption of H ₂ S (ΔG^{ads} in eV, equation 3.19) and oxygen replacement reaction (ΔG^{repl} in eV, equation 3.21) for the Fe _{1-x} M _x O ₂ -LaO and Fe _{1-x} M _x O ₂ -SrO (x= 0.11; M = Fe, Co, Ni, Mn) surface models calculated at T = 1073 K, C _{H₂S} = 50 ppm, P _{H₂} = 1 atm, and P _{H₂O} = 0.03 atm.	92
Table 4.1: List of materials that passed the four filters described in Figure 4.2. Included in this table are the elemental configuration, the computed bandgap (in eV), vacancy formation energy (ΔE_{vac} in eV), and hydration energy (ΔE_{hydr} in eV).	126
Table A.1: Calculated harmonic phonon energy (E) and Helmholtz free energy (F) of vacancy formation energy due to vibrational contributions for Sr ₂ FeO ₄	156
Table A.2: Relative energies of all possible conformers generated by the site-occupancy disorder (SOD) package for (Sr _{1-x} Pr _x) ₂ FeO ₄ (x = 0.125) starting with the magnetic configuration A shown in Figure 2.1(b).	156
Table A.3: Relative energies of all possible conformers generated by the site-occupancy disorder (SOD) package for (Sr _{1-x} Pr _x) ₂ FeO ₄ (x = 0.25) starting with the magnetic configuration A shown in Figure 2.1(b).	157
Table A.4: Relative energies of all possible conformers generated by the site-occupancy disorder (SOD) package for (Sr _{1-x} Pr _x) ₂ FeO ₄ (x = 0.375) starting with the magnetic configuration A shown in Figure 2.1(b).	158
Table A.5: Relative energies of all possible conformers generated by the site-occupancy disorder (SOD) package for (Sr _{1-x} Pr _x) ₂ FeO ₄ (x = 0.5) starting with the magnetic configuration A shown in Figure 2.1(b).	159
Table A.6: Relative Energies (in eV) and average Fe Magnetic Moment (in μB) for the magnetic moment configurations presented in Figure 2.1(b) for (Sr _{1-x} Pr _x) ₂ FeO ₄	161
Table A.7: Relative Energies (in eV) for the magnetic moment configurations presented in Figure 2.1(b) for all minimum energy defect calculations.	162
Table A.8: Oxygen Bader charges and the bond length between the interstitial defect and the next nearest oxygen (NNO) for each dopant-configuration.	162

Table A.9: Composite vacancy-mediated migration energy ($\Delta H_{f,vac} + \Delta H_{mig}$ in eV) for each dopant-configuration for all migration pathways.	163
Table B.1: Reaction rates (in s^{-1}) calculated for the elementary steps of H_2 electro-oxidation on the FeO_2-LaO and FeO_2-SrO surface models at a representative temperature of 1073 K and a cell voltage of 0.7 V with different symmetry factor (β) values.	173
Table B.2: Reaction rates (in s^{-1}) calculated for the elementary steps of CO electro-oxidation on the FeO_2-LaO and FeO_2-SrO surface models at a representative temperature of 1073 K and a cell voltage of 0.7 V with different symmetry factor (β) values.	174
Table B.3: Computed reaction rates (s^{-1}) for H_2 electro-oxidation, CO electro-oxidation, and WGS in the presence of syngas fuel with different $H_2:CO$ ratios at an operating voltage of 0.7 V and $\beta = 0.5$	175
Table B.4: Degree of rate control (DRC) and turnover frequencies calculated for H_2 and CO oxidation over FeO_2-LaO and FeO_2-SrO surfaces at an operating $V_{cell} = 0.7$ and $\beta = 0.5$ conditions ($T = 1073$ K, $P_{H_2,CO} = 1.00$ atm, $P_{H_2O,CO_2} = 0.03$ atm, and $P_{O_2} = 0.21$ atm).	175
Table C.1: Transition metals that have U-J values and require energy shifts for mixed GGA/GGA+U energetics in this study.	190
Table C.2: Table of configurations that pass Filter 3 (e.g., insulating, stable under anodic and cathodic operating conditions) with computed vacancy and protonic defect formation, and hydration energies.	191
Table C.3: List of materials that are stable under anodic and cathodic conditions but yield a bandgap between 1.0 and 2.0 eV.	198
Table C.4: Calculated Bader charges for $Ba_{0.125}Sr_{0.875}Sn_{0.125}Zr_{0.875}O_3$ and BCO based on the lowest energy vacancy site.	201
Table C.5: List of materials that passed Filter 3 (e.g., greater than > 2.0 eV bandgap; stable in anodic and cathodic) and display CO_2 metastability with E_{hull} values between 0.041 and 0.081 eV/atom.	201

LIST OF FIGURES

<p>Figure 2.1: Polyhedral representations of the lowest energy dopant-configurations for a) Sr_2FeO_4, b) $\text{Sr}_{1.75}\text{Pr}_{0.25}\text{FeO}_4$ (structure 7), c) $\text{Sr}_{1.5}\text{Pr}_{0.5}\text{FeO}_4$ (structure 23), d) $\text{Sr}_{1.25}\text{Pr}_{0.75}\text{FeO}_4$ (structure 56), and e) SrPrFeO_4 (structure 45).</p>	34
<p>Figure 2.2: Effect of Pr dopant concentration on the structural parameters of $(\text{Sr}_{1-x}\text{Pr}_x)_2\text{FeO}_4$ a) cell volume (\AA^3), b) average Fe-O bond lengths (\AA), and c) average Fe-O-Fe angle (deg.).</p>	35
<p>Figure 2.3: PDOS for Fe 3d (black) and O 2p (red) states for $(\text{Sr}_{1-x}\text{Pr}_x)_2\text{FeO}_4$: a) $x = 0$, b) $x = 0.125$, c) $x = 0.25$, d) $x = 0.375$, and e) $x = 0.5$. Energies are referred to the Fermi level (E_F). Positive PDOS values represent α-spins states and negative values represent β-spin states.</p>	36
<p>Figure 2.4: Lowest energy oxide defect conformers identified for $(\text{Sr}_{1-x}\text{Pr}_x)_2\text{FeO}_{4\pm\delta}$ a) $x = 0$, b) $x = 0.125$, c) $x = 0.25$, d) $x = 0.375$, and e) $x = 0.5$. δ is modeled as a value of ± 0.125.</p>	38
<p>Figure 2.5: The variation of $\Delta E_{f,\text{vac}}$ (in eV) with λ (dimensionless) for $\text{Sr}_2\text{FeO}_{4-\delta}$ (red), $\text{Sr}_{1.75}\text{Pr}_{0.25}\text{FeO}_{4-\delta}$ (yellow), $\text{Sr}_{1.5}\text{Pr}_{0.5}\text{FeO}_{4-\delta}$ (green), $\text{Sr}_{1.25}\text{Pr}_{0.75}\text{FeO}_{4-\delta}$ (black), and $\text{SrPrFeO}_{4-\delta}$ (blue). The lowest energy vacancy site and all non-equivalent sites are included in this figure. A positive λ value indicates an increase in the extent of charge that is absorbed into the oxygen sublattice.</p>	39
<p>Figure 2.6: Average distance of the minimum energy interstitial defect to neighboring A-site ions versus the energy of interstitial formation for $x = 0$ (red), $x = 0.125$ (yellow), 0.25 (green), 0.375 (black), and 0.5 (blue). The legend labels the elemental identity of the neighboring A-site ions.</p>	40
<p>Figure 2.7: Defect formation energy as a function of Fermi Energy at 800 $^\circ\text{C}$ for a) Sr_2FeO_4, b) $\text{Sr}_{1.25}\text{Pr}_{0.75}\text{FeO}_4$, and c) SrPrFeO_4. Configurations with $x = 0.125$ and $x = 0.25$ are not shown due to predicted metallic state. The blue and red lines represent the optimized vacancy and interstitial defect for each dopant-configuration, respectively. The dashed line represents the self-consistent Fermi-level, and the solid black lines represents the</p>	

computed CBM for a given dopant-configuration.	41
Figure 2.8: Schematic of the vacancy migration jump routes around the minimum energy vacancy site (filled black circle) for a) Sr_2FeO_4 , b) $\text{Sr}_{1.75}\text{Pr}_{0.25}\text{FeO}_4$, c) $\text{Sr}_{1.5}\text{Pr}_{0.5}\text{FeO}_4$, d) $\text{Sr}_{1.25}\text{Pr}_{0.75}\text{FeO}_4$, and e) SrPrFeO_4 . The numbers presented inside the structures correspond to the jump routes presented in Table 2.4 for each dopant configuration.	43
Figure 2.9: Graphical Abstract.	44
Figure 3.1: Proposed scheme or outline for the investigation fuel oxidation on the $\text{SrLaFeO}_{4-\delta}$ anode.	82
Figure 3.2: (a) The $2 \times 2 \times 1$ polyhedral representation of the I4mm supercell model of bulk SrLaFeO_4 (SLF) and (b-c) the $3 \times 3 \times 1$ unit cells of SLF (001) surface models where (b) FeO_2 -LaO and (c) FeO_2 -SrO represent the FeO_2 -terminated surfaces with LaO or SrO in the second layer, respectively.	83
Figure 3.3: Proposed mechanism for H_2 oxidation on $\text{SrLaFeO}_{4-\delta}$ surface. The TS structures are in reference to the specific elementary reaction step. The vacancy (black) refers to the oxygen vacancy generated during H_2 oxidation.	84
Figure 3.4: Relative free energy profiles (eV) for the H_2 oxidation network on the FeO_2 -LaO (blue) and FeO_2 -SrO (orange) surface models ($T = 1073 \text{ K}$; $P_{\text{H}_2}(\text{gas}) = 1.0 \text{ atm}$; $P_{\text{H}_2\text{O}}(\text{gas}) = 0.03 \text{ atm}$; $P_{\text{O}_2}(\text{gas}) = 0.21 \text{ atm}$). All energies are with reference to the sum of the energies of the initial state (IM_{H_21}) and the gas phase molecules.	85
Figure 3.5: Proposed mechanism for CO oxidation on $\text{SrLaFeO}_{4-\delta}$ surface. The TS structures are in reference to the specific elementary reaction step. The vacancy (black) refers to the vacancy generated during CO oxidation.	86
Figure 3.6: Relative free energy profiles (eV) for the CO oxidation network on the FeO_2 -LaO (blue) and FeO_2 -SrO (orange) surface models ($T = 1073 \text{ K}$; $P_{\text{CO}}(\text{gas}) = 1.0 \text{ atm}$; $P_{\text{CO}_2}(\text{gas}) = 0.03 \text{ atm}$; $P_{\text{O}_2}(\text{gas}) = 0.21 \text{ atm}$). All energies are with reference to the sum of the energies of the initial state ($\text{IM}_{\text{CO}1}$) and the gas phase molecules.	87
Figure 3.7: Proposed mechanism for syngas oxidation and water-gas shift (WGS) on $\text{SrLaFeO}_{4-\delta}$ surface. The vacancy (black) refers to the vacancy generated during syngas oxidation or water-gas shift.	88

Figure 3.8: Calculated polarization curves at 1073 K for a) H₂ oxidation and b) CO oxidation on FeO₂-LaO (blue) and FeO₂-SrO (orange) surface models (P_{H₂,CO} = 1.00 atm, P_{H₂O,CO₂} = 0.03 atm, and P_{O₂} = 0.21 atm). (c-d) Calculated polarization curves for syngas oxidation at 1073 K on FeO₂-LaO (c) and FeO₂-SrO (d) surface models (P_{H₂,CO} = 1.00 atm, P_{H₂O} = 0.03 atm, P_{CO₂} = 0.003 atm, and P_{O₂} = 0.21 atm). β = 0.5 is used for all charge transfer reactions.90

Figure 3.9: Degree of rate control (DRC) analysis for H₂ oxidation on a) FeO₂-LaO and b) FeO₂-SrO surfaces and degree of rate control for CO oxidation on c) FeO₂-LaO and d) FeO₂-SrO surfaces as a function of cell potential (T = 1073 K; P_{H₂,CO} = 1.00 atm, P_{H₂O,CO₂} = 0.03 atm, and P_{O₂} = 0.21 atm).91

Figure 3.10: Top views of optimized structures of a) sulfur adsorbed on the oxygen vacancy (H₂S + M-V_o^{••}-Fe₁ ↔ H₂ + M-S-Fe₁, M = Fe, Co, Ni, Mn) and b) sulfur replacing surface oxygen (H₂S + M-O_o^x-Fe₂ ↔ H₂O + M-S-Fe₂, M = Fe, Co, Ni, Mn), respectively.92

Figure 3.11: Graphical Abstract.93

Figure 4.1: a) General structure of the perovskite oxide (ABO₃) used for all computed compositions in this study, b) cubic unit cell of BaZrO₃, and c) orthorhombic unit cell of BaCeO₃.125

Figure 4.2: Computational workflow for the DFT-based high-throughput screening process used in this study. The number below each filter box refers to the number of materials that pass the corresponding filter criterion.125

Figure 4.3: Scatter plots of vacancy formation energy (ΔE_{vac} in eV) verses hydration energy (ΔE_{hydr} in eV) for the 116 perovskite oxides that passed the first three filters. a) Materials organized with respect to A-site doping where A_{1.0}, A_{0.875}, A_{0.75}, and A_{0.5} correspond to the materials with 0%, 12.5%, 25%, and 50% doping at the A-site, respectively, b) magnified scatter plot around BZO taken from a), c) materials organized with respect to B-site doping where B_{1.0}, B_{0.875}, B_{0.75}, and B_{0.5} correspond to the materials with 0%, 12.5%, 25%, and 50% doping at the B-site, respectively, and d) magnified scatter plot around BZO taken from c).128

Figure 4.4: Scatter plots of vacancy formation energy (ΔE_{vac} in eV) verses hydration energy (ΔE_{hydr} in eV) for the 116 perovskite oxides that passed the first three filters categorized into the following groups, (a) alkali metals, (b) group 3 elements, (c) group 4 elements, (d) group 5 elements, (e) d-block: period 4 elements, (f) d-block:

periods 5 and 6 elements, (g) p-block elements, and (h) lanthanides.	129
Figure 4.5: Scatter plots of vacancy formation energy (ΔE_{vac} in eV) verses hydration energy (ΔE_{hydr} in eV) for the 43 perovskite oxides that passed the first four filters. a) Materials organized with respect to A-site doping where $A_{1.0}$, $A_{0.875}$, $A_{0.75}$, and $A_{0.5}$ correspond to the materials with 0%, 12.5%, 25%, and 50% doping at the A-site, respectively, b) magnified scatter plot around BZO taken from a), c) materials organized with respect to B-site doping where $B_{1.0}$, $B_{0.875}$, $B_{0.75}$, and $B_{0.5}$ correspond to the materials with 0%, 12.5%, 25%, and 50% doping at the B-site, respectively, and d) magnified scatter plot around BZO taken from d). BCO did not pass the CO_2 stability test and is included in the figure only as a benchmark.	130
Figure 4.6: DFT-based high-throughput screening process used for identifying electrode materials. The number above each filter box refers to the number of materials that pass the corresponding filter criterion.	131
Figure 4.7: Graphical Abstract.	131
Figure A.1: a) The $2 \times 2 \times 1$ polyhedral representation of the $I4/mmm$ supercell model of Sr_2FeO_4 , and b) all unique Fe magnetic moment arrangements examined in this study. Structures visualized with VESTA.	163
Figure A.2: Representative interstitial sites (black spheres) considered for $(\text{Sr}_{1-x}\text{Pr}_x)_2\text{FeO}_4$. The lattice parameters of all dopant configurations are fixed at the values of the pristine cell.	164
Figure A.3: Variation of supercell volume during structure optimization of $(\text{Sr}_{1-x}\text{Pr}_x)_2\text{FeO}_4$. All conformations generated by the SOD package ⁹ are displayed for $x = 0.125$ (7 points, green), $x = 0.25$ (42 points, yellow), $x = 0.375$ (122 points, red) and $x = 0.5$ (181 points, blue). The black dashes represent the average volume for a given dopant-configuration.	164
Figure A.4: PDOS for Fe 3d (black) and O 2p (red) states for the FM configuration of Sr_2FeO_4 . Energies are referred to the Fermi level (EF). Positive PDOS values represent α -spins states and negative values represent β -spin states.	165
Figure B.1: Highlighted areas correspond to the atoms that are displaced for vibrational frequency calculations.	172

Figure B.2: Relative free energy profiles (eV) for the H ₂ oxidation network on the Fe _{1-x} M _x O ₂ -LaO (x = 0.11; M = Fe, Co, Mn, and Ni) surface models. All energies are with reference to the sum of the energies of the initial state (IM1) and the gas phase molecules (T = 1073 K; P _{H₂} (gas) = 1.0 atm; P _{H₂O} (gas) = 0.03 atm; P _{O₂} (gas) = 0.21 atm).	176
Figure B.3: Relative free energy profiles (eV) for the H ₂ oxidation network on the Fe _{1-x} M _x O ₂ -SrO (x = 0.11; M = Fe, Co, Mn, and Ni) surface models. All energies are with reference to the sum of the energies of the initial state (IM1) and the gas phase molecules (T = 1073 K; P _{H₂} (gas) = 1.0 atm; P _{H₂O} (gas) = 0.03 atm; P _{O₂} (gas) = 0.21 atm).	176
Figure C.1: Schematic structures of A _x A' _{1-x} BO ₃ : a) A _{0.875} A' _{0.125} BO ₃ , b), A _{0.75} A' _{0.25} BO ₃ , c) A _{0.625} A' _{0.375} BO ₃ , and d) A _{0.5} A' _{0.5} BO ₃	188
Figure C.2: Schematic structures of AB _y A' _{1-y} O ₃ : a) AB _{0.875} B' _{0.125} BO ₃ , b), AB _{0.75} B' _{0.25} O ₃ , c) AB _{0.625} B' _{0.375} O ₃ , and d) AB _{0.5} B' _{0.5} O ₃	189
Figure C.3: Schematic structures of A _{0.875} A' _{0.125} B _y A' _{1-y} O ₃ : a) A _{0.875} A' _{0.125} B _{0.875} B' _{0.125} BO ₃ , b), A _{0.875} A' _{0.125} B _{0.75} B' _{0.25} O ₃ , and c) A _{0.875} A' _{0.125} B _{0.5} B' _{0.5} O ₃	189
Figure C.4: Schematic structures of A _{0.75} A' _{0.25} B _y A' _{1-y} O ₃ : a) A _{0.75} A' _{0.25} B _{0.875} B' _{0.125} BO ₃ , b), A _{0.75} A' _{0.25} B _{0.75} B' _{0.25} O ₃ , and c) A _{0.75} A' _{0.25} B _{0.5} B' _{0.5} O ₃	189
Figure C.5: Schematic structures of A _{0.5} A' _{0.5} B _y A' _{1-y} O ₃ : a) A _{0.5} A' _{0.5} B _{0.875} B' _{0.125} BO ₃ , b), A _{0.5} A' _{0.5} B _{0.75} B' _{0.25} O ₃ , and c) A _{0.5} A' _{0.5} B _{0.5} B' _{0.5} O ₃	190
Figure C.6: a) Bar graph of the A-site elemental frequency of Filter 1 passing configurations (e.g., > 2.0 eV bandgap) and b) a bar graph of the B-site elemental frequency of Filter 1 passing configurations.	195
Figure C.7: a) Bar graph of the A-site elemental frequency of Filter 2 passing configurations (e.g., > 2.0 eV bandgap, E _{hull} < 0.041 eV/atom) and b) a bar graph of the B-site elemental frequency of Filter 1 passing.	196
Figure C.8: a) Bar graph of the A-site elemental frequency of Filter 3 passing configurations (e.g., > 2.0 eV bandgap and E _{hull} < 0.041 eV/atom for anodic conditions) and b) a bar graph of the B-site elemental frequency of Filter 2 passing configurations.	197

Figure C.9: a) Scatter plot of vacancy formation energy (ΔE_{vac} in eV) versus hydration energy (ΔE_{hydr} in eV) for the 116 materials that passed the first three filters organized with respect to their stability under CO_2 environment. The legends stable, metastable, and unstable refer to the materials exhibiting $E_{\text{hull}} < 0.041$ eV/atom, $E_{\text{hull}} = 0.041-0.081$ eV/atom, and $E_{\text{hull}} > 0.081$ eV/atom, respectively under CO_2 environment. Dashed lines outline the regime with favorable defect formation activity (low ΔE_{vac} and ΔE_{hydr} values). BZO and BCO are included as benchmarking materials as a black diamond and triangle, respectively.199

Figure C.10: a) Bar graph of the A-site elemental frequency of Filter 1a passing configurations and b) a bar graph of the B-site elemental frequency of Filter 1a passing configurations (e.g., < 0.5 eV bandgap).200

CHAPTER 1

INTRODUCTION

To conduct practical predictions of material properties, ab initio computational methods based on Kohn-Sham density functional theory are the preferred tools to model complex material structures such as perovskites. In addition to modeling material properties, ab initio computational methods are utilized to model catalytic particles and reaction pathways for both thermochemical and electrochemical systems. Therefore, ab initio computational methods are essential tools to help design better performing solid oxide fuel cell (SOFC) materials. The major goal of oxide-conducting solid oxide fuel cell research is to lower operating temperatures by designing materials with high oxygen mobility, catalytic activity, or both. The complimentary proton-conducting solid oxide fuel cells require the design of thermodynamically stable materials, especially in CO₂-containing conditions. In order to expedite material design and discovery, computational tools complement experimental design by outlining activity relationships as function of doping ratios and elemental identity. From these computationally derived relationships, experimentalists can better define the variable phase space for design of experiment studies.

This dissertation focuses on the ab initio computational design of perovskite and Ruddlesden-Popper phase oxide-based materials for solid oxide fuel cell applications. This dissertation is composed in manuscript style outlining the development of activity relationships for Ruddlesden-Popper phase cathode and anode materials (Chapter 2),

Ruddlesden-Popper phase-based anodes (Chapter 3), and proton-conducting perovskite electrolyte materials (Chapter 4). Chapter 1 outlines how Sr-based Ruddlesden-Popper materials doped with varying concentrations of Pr^{3+} (0%, 12.5%, 25%, 37.5%, and 50%) modulate the structural, electronic, and ionic properties of RP materials. Low concentrations of Pr^{3+} yield high electronic activity, high oxygen vacancy defect concentrations under anodic conditions, and low oxygen interstitial defect concentrations under cathodic conditions. The bulk electronic conductivity of doped RP materials increases with a small introduction of Pr^{3+} (e.g., 12.5% and 25%). The bulk electronic conductivity appears to be a function of the ratio of Fe^{4+} to Fe^{3+} present for a given Pr^{3+} concentration. The Fe^{4+} -only configuration (e.g., 0% Pr^{3+}) yields semi-conducting behavior while the Fe^{3+} -only configuration (e.g., 50% Pr^{3+}) yields insulating behavior. In contrast, an intermediate ratio yields high electronic conduction behavior relative to the extrema. Regarding ionic conductivity, the ability to form oxygen vacancy defects is significantly less for the 50% Pr^{3+} concentration relative to all smaller Pr^{3+} concentrations. This decrease is due to the overreduction of Fe upon oxygen vacancy formation yielding an upper bound for Pr^{3+} doping before significantly decreasing native oxygen vacancy concentration. The kinetic mechanism of oxygen vacancy-mediated diffusion primarily occurs along the FeO_2 -plane of the perovskite component of the Ruddlesden-Popper structure. Three different pathways were analyzed: same-site oxide migration, nearest-neighbor oxide hopping, and out-of-the- FeO_2 -plane oxide migration. Same-site migration yielded high kinetic barriers due to the lack of electronic support from the Fe-O sublattice in contrast to nearest-neighbor hopping and out-of-the- FeO_2 -plane migration. These pathways yield similar kinetic barriers due to not disrupting the

Fe-O sublattice. The barriers of nearest-neighbor hopping and out-of-the-FeO₂-plane migration slightly decrease with increasing Pr³⁺ concentration up to a concentration of 37.5%. For 50% Pr³⁺, barriers for oxide migration are increased relative to all other Pr³⁺ concentrations – consistent with the results of oxide vacancy formation.

Chapter 2 outlines the elaboration of oxidation mechanisms of H₂, CO, and syngas fuels on SrLaFeO₄. SrLaFeO₄ has been incrementally modulated in the experimental literature either by direct B-site doping, by acting as a scaffold for the exsolution of transition metal nanoparticles, or by utilizing both strategies at once. The experimental literature indicates that SrLaFeO₄ has sufficient oxidation catalytic activity, that SrLaFeO₄ is stable under both H₂O- and H₂S-containing conditions, and that both B-site doping and exsolution increase catalytic activity. To help direct future research with RP-based anodes, SrLaFeO₄ is selected as a model RP to understand its intrinsic catalytic activity and to relate how doping modulates oxidation activity. Therefore, two SrLaFeO₄-based surface models were analyzed – Fe-terminated FeO₂-LaO (001) and FeO₂-SrO (001). The two models differ by the A-site elemental identity of the underlying rocksalt layer. For all voltages, including thermochemical or short circuit conditions, indicate that FeO₂-SrO (001) is more active for H₂, CO, and syngas oxidation. The degree of rate control analysis at short circuit conditions indicates that the key catalytically limiting step is surface H₂O formation for H₂ oxidation and surface CO₂ formation for CO oxidation. At open circuit conditions, oxide migration is the key catalytically limiting step. At approximately a cell voltage of 0.9 V, a change in the rate-limiting step occurs and this change has a clear effect on the theoretical polarization curve of SrLaFeO₄. The current density changes from logarithmic at high potentials to non-exponential growth at low

potentials. This behavior change is due to when the rate-determining step occurs – either after the charge-transfer step (e.g., H₂O and CO₂ desorption) for high cell potentials or before the charge-transfer step for low cell potentials. Introduction of B-site dopants (e.g., Co, Mn, and Ni) improves the catalytic activity of the FeO₂-LaO-based (001) surface. Co yields a three orders of magnitude improvement over base FeO₂-LaO (001). For FeO₂-SrO-based (001) surfaces, the activity for the doped surfaces displayed lowered activity relative to base FeO₂-SrO (001). The activity decrease was due to the change in the rate-determining step shifting from surface H₂O formation to the dissociative adsorption of H₂. Lastly, base SrLaFeO₄ stability under 50 ppm H₂S was evaluated with two possible reactions – sulfur dissociative adsorption and oxide replacement. Base SrLaFeO₄ is stable against both H₂S poisoning mechanisms for both surface models while the oxide replacement mechanism became slightly favorable (e.g., 0.0 – -0.2 eV) for Co or FeCo_{0.11}Fe₈₉O₂-LaO, Mn or FeMn_{0.11}Fe₈₉O₂-SrO, and Ni or FeNi_{0.11}Fe₈₉O₂-LaO.

Chapter 4 outlines a high-throughput study to develop elemental trends and to discover novel materials related to proton-conducting solid oxide fuel cell electrolytes. 4793 perovskites with unique elemental configurations were calculated with varying A- and B-site elemental compositions and doping ratios (e.g., 0%, 12.5%, 25%, 50%). Elements from the alkali metals, alkaline earth, the d-block, the lanthanide f-block, and the p-block metalloids were included. To develop elemental trends and to discover novel materials, different filters based on electronic conductivity and thermodynamic stability were used to eliminate materials. Filter 1 – based on low electronic conductivity (e.g., bandgap < 2.0 eV), eliminated 3887 materials. Filter 2 – based on thermodynamic stability under anodic conditions (e.g., E_{hull} < 0.04 eV/atom under 1 atm H₂ and 0.03 atm

H₂O conditions), eliminated 781 materials. Filter 3 - based on thermodynamic stability under cathodic conditions (e.g., $E_{\text{hull}} < 0.04$ eV/atom under 0.21 atm O₂ and 30% relative humidity), eliminated 9 materials. Lastly, Filter 4 – based on thermodynamic stability under CO₂-containing conditions (e.g., $E_{\text{hull}} < 0.04$ eV/atom under 1 atm CO₂), eliminated 73 materials. 116 materials pass Filter 3 and 43 materials pass Filter 4. To evaluate the ionic conductivity of Filter 3 materials, the thermodynamic ability of hydration for each passing configuration is evaluated by calculation of two defect formation processes: oxygen vacancy and proton insertion. Four elemental regions of different defect formation activity are identified: Sn-containing, acceptor-dopant, BaCeO₃-like, and BaZrO₃-like. The Sn-containing region is primarily composed of either a pure or co-doped A-site of alkaline earth elements and a Zr-based B-site doped with group 14 elements, specifically Sn. Notably, this region is active with regards to oxygen vacancy formation but poor with regards to hydration formation. The acceptor-dopant region is highly active at both oxygen vacancy defect formation and hydration formation and is primarily composed of Zr-based materials doped with either group 3 or group 13 elements at the B-site or alkali metal elements at the A-site. The BaCeO₃-like region is similar in activity to native BaCeO₃, and all Filter 3 passing materials that contain Ce are in this region. Other notable elemental groups include the following when co-doped together: f-block lanthanides and group 5 elements, and alkali metals and group 5 elements. Lastly, the BaZrO₃-like region is similar in activity to native BaZrO₃. A-site doping with alkaline earth elements yields little effect on modulating defect formation for BaZrO₃-like materials. A secondary observation is that B-site doping with group 4 elements also yields little effect on modulating defect formation. Overall, the following

configurations were found to best for proton-conducting electrolyte applications by displaying low electrical conductivity, good H₂O and CO₂ (meta)stability, and high defect formation activity: BaFe_{0.125}Ta_{0.125}Zr_{0.75}O₃, BaFe_{0.125}Nb_{0.125}Zr_{0.75}O₃, Bi_{0.125}Ba_{0.875}Fe_{0.125}Zr_{0.75}O₃, SrMn_{0.125}Zr_{0.875}O₃, Rb_{0.125}Ba_{0.875}ZrO₃, Rb_{0.125}Ba_{0.875}V_{0.125}Zr_{0.875}O₃, Rb_{0.125}Sr_{0.875}V_{0.125}Zr_{0.875}O₃, and Cs_{0.125}Ba_{0.875}ZrO₃.

The following chapters are reproductions of the manuscripts as of the date of the submission of this dissertation. The reference numbers in a manuscript chapter refer to a reference listed in the reference section of that corresponding manuscript chapter. The dissertation reference section that follows the conclusion is a cumulative list of all unique references from all the manuscript chapters (e.g., redundant references are excluded after the first appearance of a reference).

CHAPTER 2

AN AB INITIO STUDY OF THE OXYGEN DEFECT FORMATION AND OXIDE ION MIGRATION IN $(\text{Sr}_{1-x}\text{Pr}_x)_2\text{FeO}_{4\pm\delta}$ ¹

¹ Szaro, N.; Ammal, S.; Chen., F.; Heyden, A. *J. Power Sources*, **2021**, 230602, 515, 10.1016/j.jpowsour.2021.230602. Reprinted here with permission of the publisher.

2.1 ABSTRACT

The $\text{Sr}_{n+1}\text{Fe}_n\text{O}_{3n+1}$ Ruddlesden-Popper (RP) perovskite family displays promising oxygen permeability and serves as a host stoichiometry for the design of solid oxide electrode materials. A strategy to tune electronic and ionic properties is the introduction of substitutional dopants like Pr^{3+} to the A-site. In this study, we investigate the bulk structural, electronic, and oxygen migration properties for the $n = 1$ RP perovskite $(\text{Sr}_{1-x}\text{Pr}_x)_2\text{FeO}_{4+\delta}$ ($x = 0, 0.125, 0.25, 0.375, \text{ and } 0.5$). The oxygen partial pressure is adjusted to elucidate how anodic and cathodic operating conditions influence the formation of oxygen defects. Under anodic conditions, the oxygen vacancy is the dominant oxide defect for all dopant-configurations. Under cathodic conditions, oxygen vacancy defects dominate for configurations from $x = 0$ to $x = 0.375$ while the oxygen peroxide interstitial defect becomes the primary defect for $x = 0.5$. Next, we examine the relationship between Pr^{3+} concentration, iron oxidation state, and charge compensation with defect formation to explain the trends in vacancy and peroxide interstitial formation energies. Results clarify the role of lanthanide A-site substitutional dopants on the electronic conductivity and oxide defect formation and migration in Sr-based RP perovskites. These atomic-scale insights suggest design directions for RP perovskites in SOCFs.

2.2 INTRODUCTION

Mixed ionic-electronic conducting (MIEC) materials have found use as oxygen permeation membranes and solid oxide fuel cell (SOFC) anodes and cathodes¹⁻³. For SOFC applications, MIEC design is primarily focused on reducing high oxygen reduction overpotentials at the cathode and increasing the stability of the anode against coking and

sulfur poisoning^{4,5}. Mitigation of these losses can shift the operating temperatures of SOFCs from greater than 800 °C to the intermediate-temperature (IT) regime between 600 and 800 °C^{6,7}. High temperatures facilitate fast reaction kinetics without the need for expensive metal catalysts (e.g., Pt), but cause premature aging of the SOFC stack^{6,8}. While transition metal-based cubic (e.g. BSCF, LSM, and LSCF)⁹⁻¹¹ and double perovskites (e.g. SFMO)¹²⁻¹⁵ have encountered widespread attention as MIEC materials in SOFCs, these materials are disadvantaged by poor ionic conductivity at low temperatures¹⁶ and suffer from degradation at SOFC operating conditions^{17,18}. In order to circumvent these difficulties, another class of perovskite materials called Ruddlesden-Popper (RP) phase oxides have been explored which display enhanced oxygen transport and promising catalytic activity for both hydrogen and hydrocarbon oxidation under high sulfur conditions¹⁹⁻²².

Recent studies investigated $\text{Sr}_3\text{Fe}_2\text{O}_{7-\delta}$, the $n = 2$ member in the $\text{Sr}_{n+1}\text{Fe}_n\text{O}_{3n+1}$ series, as a possible cathode material²³⁻²⁵ due to its excellent structural stability. A computational study by Ota et al.²⁶ elucidated the relationship of vacancy defect formation and migration in $\text{Sr}_3\text{Fe}_2\text{O}_{7-\delta}$ as a function of the non-stoichiometry factor (δ) and identified defect stability with $\delta = 0.25$. The vacancy defects were found to be predominantly located between the bilayers of the FeO_2 planes. To evaluate the catalytic activity of $\text{Sr}_3\text{Fe}_2\text{O}_{7-\delta}$, Tan et al. examined the oxygen reduction reaction (ORR) kinetics on both FeO_2 and SrO (001) surfaces and concluded that the O_2 dissociation barrier needs to be reduced to decrease kinetic losses²⁷. A common strategy used to improve the performance of such MIEC materials is to utilize substitutional dopants in order to tune the electronic, ionic, and catalytic properties. Kagomiya et al. reported that the

introduction of La^{3+} lowered the vacancy migration barrier between the $(\text{Sr},\text{La})\text{FeO}_3$ perovskite layers and a change in oxide ion migration mechanism was observed at temperatures above $830\text{ }^\circ\text{C}$ ²⁴. Here, we focus on the bulk properties of $\text{Sr}_2\text{FeO}_{4\pm\delta}$, the $n = 1$ member of $\text{Sr}_{n+1}\text{Fe}_n\text{O}_{3n+1}$ at the intermediate temperature regime (e.g., $800\text{ }^\circ\text{C}$). $\text{Sr}_2\text{FeO}_{4\pm\delta}$ decomposes to $\text{Sr}_3\text{Fe}_2\text{O}_{7-\delta}$ at $930\text{ }^\circ\text{C}$ under atmospheric oxygen ²⁸ and therefore, we find that it is constructive to elucidate the defect formation and migration of $\text{Sr}_2\text{FeO}_{4\pm\delta}$ as this phase is likely to coexist with $\text{Sr}_3\text{Fe}_2\text{O}_{7-\delta}$ in the intermediate temperature regime. In order to understand the effect of doping at the A-site, we further examined the bulk properties of the $(\text{Sr}_{1-x}\text{Pr}_x)_2\text{FeO}_{4\pm\delta}$ (SPF) material. We chose Pr^{3+} as A-site dopant because experimental studies reported that the anode material, $\text{Pr}_{0.8}\text{Sr}_{1.2}(\text{Co},\text{Fe})_{0.8}\text{Nb}_{0.2}\text{O}_{4\pm\delta}$ (PSCFN) displayed excellent oxidation kinetics, good stability under H_2S , and negligible coke formation ^{12,29}. Furthermore, a recent study by Tan et al. ³⁰ reported that the $\text{Pr}_{0.8}\text{Sr}_{1.2}(\text{Fe},\text{Ni})\text{O}_{4-\delta}$ (PSNF) material with exsolved NiFe nanoparticles is a promising anode material for direct hydrocarbon fuel SOFCs. We intend in this study to understand how the introduction of an A-site dopant affects the Sr_2FeO_4 series as a function of applied partial pressure of oxygen (e.g., anodic and cathodic conditions) at the interface of the IT operating regime (e.g., 1073 K).

This study utilizes density functional theory (DFT) to examine the bulk structural, electronic, and oxygen defect formation properties of SPF ($x = 0, 0.125, 0.25, 0.375,$ and 0.5) as a function of the concentration of Pr^{3+} and oxygen partial pressure. Here, we considered all possible arrangements of Sr/Pr for a given composition within a 56-atom supercell and outlined the effects of oxygen defect formation with δ values of ± 0.125 . We show that Pr^{3+} substitution strongly influences the structural and electronic properties,

oxide defect formation energies, and oxide migration barriers of the SPF family. The findings of this work, particularly the relationship of Pr^{3+} concentration and oxygen defect formation energy, provide a baseline understanding for future material design related to $(\text{Sr}_{1-x}\text{Pr}_x)_2\text{FeO}_4$ and supplement material design for other $(\text{Sr},\text{A})_2\text{FeO}_4$ RP perovskites.

2.3 METHODS

Electronic energies are obtained with spin-polarized Kohn-Sham DFT + U calculations with periodic boundary conditions via the Vienna Ab Initio Simulation Package (VASP)³¹. Electron exchange-correlation effects were evaluated by utilizing the generalized gradient approximation (GGA) with the Perdew, Burke, and Ernzerhof (PBE) functional^{32,33}. Dudarev's approach for DFT + U calculations is used to correct for the inadequate description of localized 3d electrons on transition metals and 4f electrons on lanthanides³⁴. A U-J parameter of 4.0 eV was chosen for the Fe 3d electrons where the selection of this value is based on a method validation study by Ota et al. for the $\text{Sr}_3\text{Fe}_2\text{O}_{7-\delta}$ system^{15,26}. A U-J parameter of 6.0 eV was chosen for Pr 4f electrons based on earlier studies of PrO_2 ^{35,36}. The nuclei and core electrons were represented by the frozen-core projector-augmented wave (PAW) approach using the following valence configurations: Sr (4s4p5s), Pr (5p6s4f), Fe (3p3d4s), and O (2s2p)³⁷. The plane-wave basis set was set to a kinetic cutoff of 750 eV. Integration over the Brillouin zone used the tetrahedron method with Blöchl corrections for all calculations³⁸. All unit cell and $2 \times 2 \times 1$ supercell calculations utilized a $9 \times 9 \times 3$ and $5 \times 5 \times 3$ Monkhorst-Pack (MP) k-point mesh, respectively³⁹. The convergence criteria for SCF energy calculations and ionic relaxations were set to 10^{-6} eV and $0.02 \text{ eV}/\text{\AA}$, respectively.

A 56 atom $2 \times 2 \times 1$ supercell of SPF shown in Figure A.1(a) was utilized for the oxygen defect calculations. The dopant-configuration models were developed using the site-occupancy disorder (SOD) package on the $2 \times 2 \times 1$ supercell of Sr_2FeO_4 , that allowed us to compute all possible non-symmetrical dopant-configurations⁴⁰. In order to minimize the computational complexity of this study, all structures generated by SOD were initially optimized with the same initial magnetic moment configuration, denoted as configuration A in Figure A.1(b). The lowest energy structure identified for each dopant-configuration was selected as the representative model structure for further calculations. In order to identify the most stable magnetic configuration for iron, the representative model structure for each dopant configuration was then tested with different possible magnetic moment configurations presented in Figure A.1(b). The formation of oxygen vacancy defects ($\text{V}_{\text{O}}^{\cdot\cdot}$ in Kröger-Vink notation⁴¹) was examined considering all non-identical oxygen atoms in the 56-atom supercell. The representative sites used for interstitial defect simulations ($\text{O}_i^{\prime\prime}$) are illustrated in Figure A.2.

Formation free energies of oxygen defects, in each charge state q , were calculated utilizing the following equation:

$$\Delta G_f(q) = E_{\text{defect}} - E_{\text{pristine}} \pm n_o(E_o + \mu_o) + q(E_{VBM} + E_F) + E_{\text{corr}} \quad (2.1)$$

where E_{defect} being the SCF energy of the relaxed supercell containing a defect in charge state q , E_{pristine} being the SCF energy of the pristine supercell in a neutral charge state, n_o being the number of oxygen atoms removed or added to the pristine supercell, E_o and μ_o correspond to the energy and chemical potential of an oxygen atom, respectively (referenced to half the energy and chemical potential of a gas phase O_2 molecule). Based on the vibrational analysis of the pristine and vacancy structures of Sr_2FeO_4 that indicate

these contributions cancel each other out (see Table A.1), further vibrational contributions are not calculated for all other dopant-configurations^{42,43}. The chemical potential of an oxygen molecule, $\mu_{O_2}(T, p^\circ)$, is calculated using the following expression with reference to a total pressure p° of 1 atm:

$$\mu_{O_2} = \mu_{O_2}(T, p^\circ) + k_b T \ln \left(\frac{p_{O_2}}{p^\circ} \right) \quad (2.2)$$

It is well known that GGA tends to overestimate the binding energy of the O_2 molecule and therefore, we utilize the following correction scheme based on the H_2O splitting reaction to calculate E_{O_2} ⁴⁴⁻⁴⁶:

$$E_{O_2}^{tot} = 2[(E_{H_2O}^{DFT} + E_{H_2O}^{ZPE}) - (E_{H_2}^{DFT} + E_{H_2}^{ZPE}) - E_{HOF}] - E_{O_2}^{ZPE} \quad (2.3)$$

Here, E_i^{ZPE} is the experimental zero-point energy of the corresponding gas molecules, E_{HOF} is the experimental heat of formation of a gas-phase H_2O molecule ($T = 0$ K), and E_i^{DFT} is the energy calculated with PBE functional. E_{VBM} in equation (2.1) is the energy of the valence band maximum (VBM) for the pristine supercell, and E_F is equal to the Fermi energy referenced with respect to the VBM. E_{corr} is calculated utilizing the python charged defect toolkit (pyCDT)⁴⁷. pyCDT calculates two correction terms: the image-charge correction via the Kumagai and Oba scheme⁴⁸⁻⁵⁰ and the potential alignment correction. The self-consistent Fermi energy is calculated using the SC-FERMI code^{42,51}. For all oxygen migration calculations, we utilized the nudged elastic band (NEB) algorithm to determine the minimum energy pathway⁵². All spring forces were converged to 0.025 eV/Å. For Bader charge analysis, we utilized the Henkelman algorithm^{52,53}. All structures are visualized with VESTA⁵⁴. Lastly, we computed the phase stability of all considered dopant configurations at $T = 0$ K, i.e., we are neglecting

entropy contributions. Details of these calculations are presented in section A.1 of Appendix A.

2.4 RESULTS AND DISCUSSION

2.4.1 STRUCTURAL AND ELECTRONIC PROPERTIES

Utilizing the site-occupancy disorder (SOD) package, the $2 \times 2 \times 1$ supercell of $(\text{Sr}_{1-x}\text{Pr}_x)_2\text{FeO}_4$ ($x = 0$) was converted into 7, 42, 122 and 181 possible non-symmetrical conformers for $x = 0.125, 0.25, 0.375$ and 0.5 , respectively. In order to elaborate on the phase stability of each dopant-configuration (see section A.1 of Appendix A), we compute that Sr_2FeO_4 and SrPrFeO_4 are stable dopant-configurations. For $\text{Sr}_{1.75}\text{Pr}_{0.25}\text{FeO}_4$, $\text{Sr}_{1.5}\text{Pr}_{0.5}\text{FeO}_4$, and $\text{Sr}_{1.25}\text{Pr}_{0.75}\text{FeO}_4$, we compute 0.001163, 0.000405, and 0.000938 eV/atom above the convex hull, respectively, i.e., these structures are practically on the convex hull and thus, at least a large fraction of these structures is thermodynamically stable. The thermodynamic stability of SrPrFeO_4 is observed experimentally as a sintering co-product under hydrogen conditions for the RP $\text{PrSrFe}_{0.8}\text{Ru}_{0.1}\text{Nb}_{0.1}\text{O}_{4+\delta}$, and perovskites $\text{Pr}_{0.4}\text{Sr}_{0.6}(\text{Co}_{0.2}\text{Fe}_{0.8})_{1-x}\text{Mo}_x\text{O}_{3-\sigma}$ and $\text{Pr}_{0.4}\text{Sr}_{0.6}\text{Co}_{0.2}\text{Fe}_{0.7}\text{Nb}_{0.1}\text{O}_{3-\sigma}$ ⁵⁵⁻⁵⁷. We present the calculated volumes of all supercell conformers and their relative energies in Figure A.3 and Tables A.2–5, respectively. The lowest energy configurations identified from this analysis are illustrated in Figure 2.1 and these conformers were selected for further study. The configurational entropy that accompanies dopant-configurations with a greater degree of disorder is expected to decrease the relative free energy at high temperatures, a parameter that is ignored in this study to limit the computational effort. A clear observation upon Pr^{3+} introduction to Sr_2FeO_4 is the preferential formation of a clean SrO layer and a mixed Sr/PrO rocksalt

layer segmented by the FeO₂ layers. For $x = 0.5$, the lowest energy structure has two distinct rocksalt layers composed of SrO and PrO as displayed in Figure 2.1(e). Table A.6 outlines the relative energy distribution of each model dopant-configuration as a function of the initial iron magnetic moment configurations presented in Figure A.1(b). For each dopant-configuration, we select the magnetic configuration with a relative minimum energy for further analysis. For undoped Sr₂FeO₄, our calculations predicted similar energies for FM and AFM configurations. However, electronic structure calculations revealed a metallic behavior for the FM configurations (Figure A.4) and a small bandgap was observed for AFM configurations as explained in the later section and Figure 2.3(a). Since experimental studies reported a bandgap of 0.8–1.0 eV^{58,59,62} for Sr₂FeO₄, we chose the AFM configuration for further analysis. Increasing the Pr³⁺ concentration increases the average magnetic moment of Fe as the number of high spin (HS) Fe⁴⁺ are reduced to HS Fe³⁺. This relationship is consistent for all starting magnetic configurations indicating that the predicted oxidation state of Fe is independent of the starting magnetic configuration.

Figure 2.2 outlines the supercell structural parameters of (Sr_{1-x}Pr_x)₂FeO₄ as a function of Pr³⁺ concentration. A gradual increase in the Pr³⁺ content results in an expansion of the SPF supercell volume, elongation of Fe–O bonds, and a gradual decrease in Fe–O–Fe angles. Octahedral tilt increases with increasing Pr³⁺ content due to the mixed presence of 2+ and 3+ A-site atoms in the rocksalt layers. The observed increase in unit cell volume while substituting Sr²⁺ with Pr³⁺, an ion with a smaller native ionic radius (1.18 Å vs 0.99 Å)⁶⁰, appears to be counterintuitive. A similar counterintuitive observation was made by Ritzmann et al. where the introduction of Sr²⁺

to the A-site of the orthorhombic perovskite $\text{LaFeO}_{3-\delta}$ decreased the supercell volume and Fe–O bond lengths, whereas the Fe–O–Fe angles increased toward 180° ⁶¹. This behavior was attributed to the formation of electron holes that shift the (Sr,Lu)FeO₃ series from an insulator to a p-type semiconductor⁶¹. In order to understand such electronic effects of Pr^{3+} substitution to the Sr_2FeO_4 perovskite in this study, we examined the partial density of states (PDOS) plots of each dopant-configuration as displayed in Figure 2.3. A small bandgap of 0.34 eV was observed for Sr_2FeO_4 (Figure 2.3(a)) which is smaller than the experimental value (0.8–1.0 eV^{58,59,62}) due to the well-known error of GGA which tends to underestimate semiconductor bandgaps and overestimate computed unit cell lattice constants⁶³. The electronic structure of the $(\text{Sr}_{1-x}\text{Pr}_x)_2\text{FeO}_4$ system exhibits a metallic character when $x = 0.125$ and 0.25 , semiconductor behavior when $x = 0.375$, and an insulator behavior for $x = 0.5$. Noticeably for $x = 0.375$ (Figure 2.3(d)), a small band of O 2p states appear in the bandgap suggesting a semiconductor behavior, whereas a clear large gap of 2.55 eV was observed for $x = 0.5$ (Figure 2.3(e)) suggesting that the system became an insulator. To understand the significant increase in the width of the bandgap from $x = 0.375$ and 0.5 , we examined the effect of Pr^{3+} concentration on the oxidation state and magnetic moment of iron. As the content of Pr^{3+} increases, charge compensation is required to maintain system electroneutrality which can be achieved by changing the oxidation state of iron. Introduction of Pr^{3+} is expected to reduce the oxidation state of iron from 4+ ($x = 0$) to a mixture of 3+/4+ ($x = 0.125$ to 0.375) and to 3+ ($x = 0.5$). To establish the effects of charge compensation as the system is reduced, we analyze the magnetic moment of iron and the computed Bader charges for each element as shown in Table 2.1. In the case of pristine $(\text{Sr}_{1-x}\text{Pr}_x)_2\text{FeO}_4$, increasing the Pr^{3+} content

increases the magnetic moment of iron. While the Bader charge of iron stays constant, the Bader charge of O becomes more negative. The increase in the magnetic moment of Fe is expected as the number of HS $d^4 Fe^{4+}$ decreases with increasing Pr^{3+} content and the number of Fe^{3+} HS d^5 states increases, according to crystal field theory⁶⁴. The invariance of the iron Bader charge is not unexpected and is explained in terms of the iron sublattice directly donating charge onto the oxygen sublattice upon reduction. Furthermore, the PDOS plots illustrated in Figure 2.3 revealed that the magnitude of O 2p states below the Fermi level increases with Pr^{3+} introduction indicating an increased charge delocalization across the oxygen sublattice as opposed to charge localization across the iron sublattice. Therefore, increasing Pr^{3+} reduces the system which shifts the Fermi level up relative to the vacuum⁶⁵.

2.4.2 OXYGEN DEFECT FORMATION

Here, we examine the stability of oxygen defects in SPF with respect to Pr^{3+} concentration. The formation energies of various oxygen vacancies ($V_{O^{\bullet\bullet}}$) and interstitial oxygen ($O_i^{\prime\prime}$) defects were calculated using equation (2.1). The configurations with lowest defect formation energy identified for each defect type with respect to Pr^{3+} concentration are illustrated in Figure 2.4 and the corresponding defect formation energies are presented in Table 2.2. Magnetic moment variation tests for each minimum defect are presented in Table A.7. These energies outline the following trends: the vacancy formation energy is essentially constant from $x = 0$ to 0.375 with a dramatic increase between $x = 0.375$ and 0.5, and interstitial formation energy decreases gradually with increasing Pr^{3+} concentration except for a slight negative deviation for $x = 0.125$. Free energies of these defect formations (ΔG) calculated at anodic ($T = 1073$ K; $P_{O_2} = 10^{-20}$

atm) and cathodic ($T = 1073 \text{ K}$; $P_{\text{O}_2} = 0.21 \text{ atm}$) conditions suggest that the formation of vacancy defects is favorable compared to the interstitial oxygen defects at both anodic and cathodic conditions for $x = 0$ to 0.375 . In the case of $x = 0.5$, formation of an interstitial oxygen defect is more favorable than the vacancy defect under cathodic conditions. The defect formation energies calculated for SPF seem to be lower than the vacancy formation energies reported for other $n = 1$ RP oxides. For example, the equatorial and apical vacancy formation energies for La-based cuprate (La_2CuO_4) were reported as 3.02 eV and 4.48 eV ⁶⁶, respectively and that of La-based nickelate (La_2NiO_4) were 3.73 and 4.01 eV , respectively ⁶⁷. Sr-based manganate doped with Ce ($\text{Ce}_x\text{Sr}_{2-x}\text{MnO}_4$) displayed a minimum vacancy formation energy of 1.76 eV ⁶⁸ which is closer to the values calculated for SPF. These studies suggest that the vacancy defect formation is favored in A^{2+} -based RP oxides due to the more positive oxidation state of the B-site TM.

In order to explain the trends observed in vacancy defect formation of SPF, we examine how the average Bader charges of iron (Table 2.1) as well as the Bader charges on the nearest irons to the vacancy defect (Table 2.3) change as a function of Pr^{3+} concentration. As a vacancy is formed, the average iron Bader charge is essentially constant from $x = 0$ to $x = 0.375$ but decreases by 0.16 e for $x = 0.5$. The Bader charges on the nearest irons to the vacancy defect are essentially unchanged for $x = 0$ and $x = 0.125$, decrease by $\sim 0.1 \text{ e}$ for $x = 0.25$ and 0.375 , and decrease by $\sim 0.5 \text{ e}$ for $x = 0.5$. Ideally, all the Fe atoms in SPF with $x = 0.5$ should be in a Fe^{3+} state, and therefore, further reduction of iron results in mixed Fe^{3+} and Fe^{2+} states. Table 2.3 displays that the magnetic moment of iron atoms nearest to the vacancy site in case of $x = 0.5$ is reduced by 0.5 compared to the pristine system confirming the reduction of iron to the HS $d^6 \text{ Fe}^{2+}$

state ⁶⁴. In addition, the calculated Bader charges for this system reveal that the electrons released upon vacancy formation are transferred to the next-nearest irons of the oxide defect resulting in the generation of Fe²⁺ as opposed to charge donation to the oxygen sublattice that was observed with Pr³⁺ introduction. To visualize such charge compensation during vacancy formation, we employ the degree of delocalization factor (λ) outlined by Muñoz-García et al. ^{69,70}:

$$\lambda = \frac{(N - 1)(\langle q_{O,nonstoichiometric} \rangle - \langle q_{O,stoichiometric} \rangle)}{\langle q_{O,stoichiometric} \rangle} \quad (2.4)$$

In equation (2.4), N refers to the number of oxygen ions in the pristine supercell and $\langle q_{O, nonstoichiometric} \rangle$ and $\langle q_{O, stoichiometric} \rangle$ refer to the average Bader charge on the oxygen sublattice in the defect and pristine supercells, respectively. Visualizing this metric in Figure 2.5, we identify that the vacancy formation energy is strongly dependent on how well charge is redistributed to the oxygen sublattice. The overreduction of iron in the case of $x = 0.5$ is unfavorable as excess charge upon vacancy formation is not redistributed to the oxygen sublattice, but directly localizes on the neighboring irons causing an increase in ionicity on the iron sublattice. Therefore, we conclude that the formation of less stable Fe²⁺ ions upon vacancy formation in the case of $x = 0.5$ is primarily responsible for the precipitous change in vacancy formation energy.

The interstitial formation energy is found to decrease gradually as the Pr³⁺ concentration increases with a negative deviation observed for $x = 0.125$ (Table 2.2). While the vacancy defects are found to be most stable along the FeO₂ layer, interstitial defects are most stable in the rocksalt layers (e.g., SrO and PrO layers) as displayed in Figure 2.4. The relationship among the average distance between the interstitial defect to its two neighboring A-site cations, A-site identity, and interstitial formation energy is

illustrated in Figure 2.6. The nearest neighbor elements to the interstitial oxygen were identified as (Sr, Sr) for $x = 0$ and $x = 0.25$, (Sr, Pr) for $x = 0.125$ and $x = 0.375$, and (Pr, Pr) for $x = 0.5$. For $x = 0$ and 0.25 , which do not include a Pr^{3+} neighbor, the observed decrease in interstitial formation energy by 0.13 eV and a 0.554 Å decrease in the average A-site neighboring distance originate from the increased concentration of Pr^{3+} in the lattice. For all other configurations, the interstitial formation energy is determined directly by the preferential neighboring A-site configuration that maximizes the number of neighboring Pr^{3+} cations. Figure 2.6 displays that the interstitial formation energy and average distance to its neighbors are very close for $x = 0.125$ and 0.375 with one Pr^{3+} neighbor. This also explains the negative deviation observed for $x = 0.125$ for which the interstitial oxygen formation is facilitated by the presence of neighboring Pr^{3+} cations compared to $x = 0.25$. A more favorable interstitial oxygen formation is observed for $x = 0.5$ which has two neighboring Pr^{3+} cations, although the average distance to its neighbors is very similar to those of $x = 0.125$ and 0.375 . Therefore, the average distance of the interstitial defect to its nearest neighbors is a weak function of interstitial formation whereas the observed trend in interstitial formation energy is directly controlled by the identity of its neighboring A-site elements.

Interstitial defects can be of two possible types: peroxide interstitial (O^{1-}) or oxide interstitial (O^{2-}). Table 2.3 outlines that the Bader charge of the interstitial defect for each dopant-configuration is ~ -0.75 e, a value that is $\sim 55\%$ of the average oxygen Bader charge. In all the minimum interstitial defect conformers displayed in Figure 2.6, the interstitial oxygen binds to an axial oxygen. The bond distances of these dimers (~ 1.5 Å, Table A.8) are indicative of the formation of a peroxide interstitial defect as opposed to

an oxide interstitial defect for which the O–O distance is expected to be $\sim 2.6 \text{ \AA}$ ^{65,71}.

Furthermore, the Bader charge on the next nearest oxygen atom to the defect is found to be very similar to that of the interstitial defect (Table A.8). This result is consistent with the observation made by Xie et al. that peroxide interstitials form via $\text{O}^{2-}(\text{lattice}) + \frac{1}{2}\text{O}_2 \rightarrow \text{O}_2^{2-}$, a reaction which does not involve redox chemistry in the system⁶⁵. In addition, we found that the magnetic moment of iron is unaffected by the formation of an interstitial oxygen defect (Table 2.1, Table 2.3), i.e., we conclude that formation of an interstitial oxygen defect is not a redox process. As opposed to the vacancy formation energy, which is a strong function of charge compensation of the iron atoms neighboring the vacancy defect, the peroxide interstitial defect energy is primarily a function of the proximity of the peroxide defect to the neighboring cationic A-site.

The formation energies of charged defects for materials with a non-zero bandgap depend directly on the Fermi energy, E_F , as displayed in equation (2.1). Therefore, we plot the formation energy of the relative lowest energy defect against the Fermi level for the following charge states: 2+, 1+, and 0 for the vacancy defect, and 1- and 0 for the peroxide interstitial defect. We also allow the external operating conditions to influence the defect formation energies by holding the temperature at 1073 K and partial pressure of oxygen at 10–20 atm and 0.21 atm corresponding to anodic and cathodic conditions, respectively^{15,61}. To better interpret the electronic conduction behavior at operating conditions, we compute the self-consistent Fermi level for each dopant-configuration^{42,51}. The self-consistently computed Fermi level is unphysical for $x = 0$ and 0.375 dopant-configurations under anodic conditions. The prominence of highly negative vacancy formation energies for all values in the computed bandgap is a violation of the

assumed non-interacting defect assumption at the dilute limit ⁵¹. Despite the breakdown of the assumed non-interacting defect assumption, SPF appears to be of n-conductivity under anodic conditions due to a high concentration of electron releasing vacancy defects and a reduction of Fe⁴⁺ to Fe³⁺ upon vacancy formation ⁴². Based on Figure 2.7, we observe that the oxide vacancy is the dominant defect for dopant-configurations $x = 0$, 0.375, and 0.5 under anodic conditions. Charged defects are dominant for $x = 0$, 0.375, and 0.5 until a Fermi level of -0.019 , 0.094 , and 1.561 eV, respectively. Under cathodic conditions, the self-consistent Fermi level is always located within the bandgap for each dopant-configuration and is located closer to the conduction band minimum (CBM) than the VBM for $x = 0$ and 0.375. Based on the self-consistent Fermi level, neutral oxygen vacancies are the dominant defects for $x = 0$ and 0.375. For $x = 0.5$, the neutral peroxide interstitial defect is the dominant oxide defect where the 2+ vacancy defect displays a 0.548 eV thermodynamic barrier at the computed self-consistent Fermi level, indicating that SPF under high Pr³⁺ concentration and atmospheric oxygen pressure is likely to exist in a slight hyperstoichiometric state, i.e., interstitials are more plentiful than vacancy defects.

2.4.3 OXYGEN MIGRATION

Bulk oxygen mobility is approximated by the self-diffusion coefficient, D_O (see equation (2.5)) ^{61,69}.

$$D_O = C_{V_O^{\cdot\cdot}} D_V \quad (2.5)$$

The local vacancy defect concentration or $C_{V_O^{\cdot\cdot}}$ is determined by the vacancy formation free energy (ΔG_{vac}), and the vacancy diffusion coefficient or D_V (equation (2.5)) is a function of the migration free energy (ΔG_{mig}). The migration free energy is the

energy required to migrate an oxide defect from one site to another ⁶¹. Under the assumption of non-interacting vacancy defects, can be expressed as following (equation (2.6)).

$$D_0 = Ae^{-(\Delta H_{f,vac} + \Delta H_{mig})/k_b T} \quad (2.6)$$

A or the preexponential factor incorporates the jump frequency of vacancy hopping and the entropy of vacancy formation and migration. The composite migration energy is the sum of the enthalpy of vacancy defect formation and the migration enthalpy. We approximate these enthalpies as the energy of vacancy formation and migration energy, respectively. We computed all non-equivalent jump routes of vacancy-mediated oxygen migration between the equilibrium defect site and next-nearest adjacent sites. Despite thermodynamic favorability under cathodic conditions, we did not compute the interstitial migration pathways for $x = 0.5$ and focused solely on the vacancy migration schemes for each dopant-configuration in order to determine trends in vacancy-mediated oxygen migration as a function of Pr^{3+} concentration. As depicted in Figure 2.8, there are 3, 9, 9, 9, and 4 jump routes for the dopant-configurations with $x = 0, 0.125, 0.25, 0.375,$ and $0.5,$ respectively. The relative energies of vacancy formation for all corresponding sites and the calculated barriers of migration are listed in Table 2.4.

Notably, path 1 for each dopant-configuration is highly unfavorable as migration barriers exceed 2.5 eV. Path 1 involves the longest oxide migration path that includes breaking the charge stabilization of the iron-oxygen sublattice in-the- FeO_2 plane. Introduction of Pr^{3+} slightly decreases the in-the- FeO_2 plane migration barriers relative to Sr_2FeO_4 with $x = 0.5$ as an outlier. Compared to Sr_2FeO_4 , the in-the- FeO_2 plane barriers remain unchanged for $x = 0.25$, decrease by $\sim 0.1\text{--}0.3$ eV for $x = 0.125$ and 0.375 , and

increase by ~ 0.2 eV for $x = 0.5$. Out-of-the-plane migration barriers directly depend on the local A-site ion composition above and below the FeO_2 plane. For migration into the pure SrO rocksalt layer, the migration barriers stay essentially constant for all configurations between $x = 0$ and 0.375 relative to Sr_2FeO_4 as the local A-site environment is similar. Energy barriers for migration into the mixed (Sr,Pr)O rocksalt layer decrease with increasing Pr^{3+} concentration with a maximum decrease of ~ 0.3 eV observed for $x = 0.375$ relative to Sr_2FeO_4 . In both cases of in-the-plane and out-of-the-plane migration, decrease in migration barrier is observed with increased oxide defect proximity to Pr^{3+} which can be attested to a combined effect of Pr^{3+} having a greater ionic charge and smaller ionic radius than Sr^{2+} . The out-of-the- FeO_2 plane migration trend does not hold for $x = 0.5$ as vacancy formation in the pure SrO and PrO rocksalt layers are highly unfavorable relative to the minimum energy vacancy site. Therefore, the observed large increase in migration barrier for the out-of-the- FeO_2 plane migration in the case of $x = 0.5$ is possibly derived from a combined result of forming vacancy defects in rocksalt layers and the harsh charge localization penalty due to overreduction of iron as discussed in section 2.4.2. To compare vacancy-mediated migration to other $n = 1$ RP oxides, Routbort et al. demonstrated experimentally for oxygen-deficient $\text{La}_{1.9}\text{Sr}_{0.1}\text{CuO}_{4-\delta}$ a barrier of 0.80 eV, a value lower than our SPF calculations⁷². As a comparison to SrPrFeO_4 , a molecular dynamics study by Tealdi et al.⁷³ displays for $\text{LaSrCoO}_{4-\delta}$ a barrier of 6.02 eV for in-the-plane migration path O1 – O2 (Table 2.4), a barrier range of 1.0–1.1 eV for in-the-plane migration path O1 – O3, and a barrier of 1.14 for out-of-the-plane migration path O1 – O5, values that are ~ 0.2 – 0.4 eV smaller than our calculation for SrPrFeO_4 .

Next, we determine the favorable defect diffusion pathway based on the calculated composite oxide migration barriers for each dopant configuration (Table A.9). The computed primary jump pathways are out-of-the-FeO₂ plane for $x = 0.25$ (path 5) and 0.375 (path 7); and in-the-FeO₂ plane for $x = 0$ (path 2), 0.125 (path 5), and 0.5 (path 2). As a first approximation to the self-diffusion coefficient under anodic and cathodic environmental conditions, we utilize ΔG_{vac} to determine the primary jump pathways under anodic and cathodic conditions. Under anodic conditions, the strongly negative free energy for $x = 0$ to 0.375 indicates that a high concentration of vacancy defects is thermodynamically strongly favorable (Table 2.2). For these negative energies, the primary jump pathways are determined solely by the migration energy for $x = 0$ to 0.375 with out-of-the-FeO₂ plane migration favored for $x = 0$ (path 3), 0.25 (path 6), and 0.375 (path 8); and in-the-FeO₂ plane migration for $x = 0.125$ (path 5) and 0.5 (path 2). Future work will investigate intermolecular defect corrections to the non-interacting defect assumption at the dilute limit. Under cathodic conditions, all free energies are above 0 eV; therefore, the primary jump pathways are out-of-the-FeO₂ plane for $x = 0.25$ (path 5) and 0.375 (path 7); and in-the-FeO₂ plane for $x = 0$ (path 2), 0.125 (path 5), and 0.5 (path 2). For $x = 0.25$, the thermodynamic barrier of 0.035 eV could require intermolecular defect corrections at the dilute limit.

2.5 CONCLUSIONS

We have presented a first principles DFT + U study displaying how Pr³⁺ substitution at the A-site influences oxygen defect formation and transport in (Sr_{1-x}Pr_x)₂FeO_{4±δ}. A clear relationship between the structural and electronic properties of SPF are explained in terms of the average Fe oxidation state. Electronic conductivity improves

with an introduction of small amounts ($x = 0.125$ and 0.25) of Pr^{3+} such that a mixture of Fe^{4+} and Fe^{3+} ions can coexist with an increased octahedral tilt to the lattice. The bandgap increases and the system becomes an insulator when the Sr to Pr ratio becomes 1:1. The vacancy formation energy remains nearly the same from $x = 0$ to $x = 0.375$ and a sharp increase is observed for $x = 0.5$ due to the overreduction of Fe. For dopant-configuration $x = 0.5$, all Fe atoms are already reduced to a 3+ oxidation state such that further reduction of Fe to a 2+ oxidation state upon vacancy formation becomes unfavorable. Interstitial defects exist in a peroxide state where the interstitial formation energy is directly related to the identity of the neighboring A-site element. The interstitial defect formation energy decreases with increasing proximity to Pr^{3+} as opposed to Sr^{2+} . Lastly, ionic conductivity is primarily controlled by a vacancy-mediated process due to the high concentration of vacancy defects under both anodic and cathodic conditions. Vacancy diffusion is especially costly for $x = 0.5$ due to the high energy of vacancy formation, especially in the rocksalt layer. Based on the interstitial favorability under cathodic conditions for $x = 0.5$, future work will investigate the role of interstitial-mediated diffusion for $x = 0.5$ and higher Pr^{3+} concentrations. Overall, introduction of small amounts of Pr^{3+} at the A-site improves the electronic conductivity of Sr_2FeO_4 , and either improves or maintains a constant oxide diffusivity relative to Sr_2FeO_4 . This study is intended to help the design and optimization of RP-based materials for direct use in SOFCs. Future studies will investigate the role of B-site variation with transition metals like Co, Ni, and Cu as related to their effects on defect formation, redox stability, and oxide migration.

2.6 ACKNOWLEDGMENTS

This work was sponsored by the National Science Foundation under Grant No. DMR-1832809. In addition, this work was partially supported by the South Carolina Smart State Center for Strategic Approaches to the Generation of Electricity (SAGE). Computing resources provided by Extreme Science and Engineering Discovery Environment (XSEDE) facilities located at Texas Advanced Computing Center (TACC) and San Diego Supercomputer Center (SDSC) (grand no. TG-CTS090100), U.S. Department of Energy facilities located at the National Energy Research Scientific Computing Center (NERSC) under Contract No. DE-AC02-05CH11231 and Pacific Northwest National Laboratory (Ringgold ID 130367, Grant Proposal 51711) and the High-Performance Computing clusters located at University of South Carolina are gratefully acknowledged.

2.7 BIBLIOGRAPHY

- (1) Sunarso, J.; Baumann, S.; Serra, J. M.; Meulenber, W. A.; Liu, S.; Lin, Y. S.; Diniz da Costa, J. C. Mixed Ionic-Electronic Conducting (MIEC) Ceramic-Based Membranes for Oxygen Separation. *J. Memb. Sci.*, **2008**, *320* (1–2), 13–41. 10.1016/j.memsci.2008.03.074.
- (2) Zhang, C.; Sunarso, J.; Liu, S. Designing CO₂-Resistant Oxygen-Selective Mixed Ionic–Electronic Conducting Membranes: Guidelines, Recent Advances, and Forward Directions. *Chem. Soc. Rev.*, **2017**, *46* (10), 2941–3005. 10.1039/c6cs00841k.
- (3) Riess, I. Mixed Ionic–Electronic Conductors—Material Properties and Applications. *Solid State Ion.*, **2003**, *157* (1–4), 1–17. 10.1016/S0167-2738(02)00182-0.
- (4) Adler, S. B. Factors Governing Oxygen Reduction in Solid Oxide Fuel Cell Cathodes. *Chem. Rev.*, **2004**, *104* (10), 4791–4843. 10.1021/cr020724o.
- (5) Yang, L.; Wang, S.; Blinn, K.; Liu, M.; Liu, Z.; Cheng, Z.; Liu, M. Enhanced Sulfur and Coking Tolerance of a Mixed Ion Conductor for SOFCs: BaZr_{0.1}Ce_{0.7}Y_{0.2-x}Yb_xO_{3-δ}. *Science*, **2009**, *326* (5949), 126–129.

10.1126/science.1174811.

- (6) Gao, Z.; Mogni, L. V.; Miller, E. C.; Railsback, J. G.; Barnett, S. A. A Perspective on Low-Temperature Solid Oxide Fuel Cells. *Energy Environ. Sci.*, **2016**, *9* (5), 1602–1644. 10.1039/c5ee03858h.
- (7) Brett, D. J. L.; Atkinson, A.; Brandon, N. P.; Skinner, S. J. Intermediate Temperature Solid Oxide Fuel Cells. *Chem. Soc. Rev.*, **2008**, *37* (8), 1568–1578. 10.1039/b612060c.
- (8) Steele, B. C. H.; Heinzel, A. Materials for Fuel-Cell Technologies. *Nature*, **2001**, *414*, 345–352. 10.1038/35104620.
- (9) Shao, Z.; Haile, S. M. A High-Performance Cathode for the next Generation of Solid-Oxide Fuel Cells. *Nature*, **2004**, *3* (1978), 170–173. 10.1038/nature02863.
- (10) Tietz, F.; Haanappel, V. A. C.; Mai, A.; Mertens, J.; Stöver, D. Performance of LSCF Cathodes in Cell Tests. *J. Power Sources*, **2006**, *156* (1), 20–22. 10.1016/j.jpowsour.2005.08.015.
- (11) Fu, C.; Sun, K.; Zhang, N.; Chen, X.; Zhou, D. Electrochemical Characteristics of LSCF–SDC Composite Cathode for Intermediate Temperature SOFC. *Electrochim. Acta*, **2007**, *52* (13), 4589–4594. 10.1016/j.electacta.2007.01.001.
- (12) Yang, C.; Yang, Z.; Jin, C.; Xiao, G.; Chen, F.; Han, M. Sulfur-Tolerant Redox-Reversible Anode Material for Direct Hydrocarbon Solid Oxide Fuel Cells. *Adv. Mater.*, **2012**, *24* (11), 1439–1443. 10.1002/adma.201104852.
- (13) Liu, Q.; Dong, X.; Xiao, G.; Zhao, F.; Chen, F. A Novel Electrode Material for Symmetrical SOFCs. *Adv. Mater.*, **2010**, *22* (48), 5478–5482. 10.1002/adma.201001044.
- (14) Xiao, G.; Liu, Q.; Zhao, F.; Zhang, L.; Xia, C.; Chen, F. Sr₂Fe_{1.5}Mo_{0.5}O₆ as Cathodes for Intermediate-Temperature Solid Oxide Fuel Cells with La_{0.8}Sr_{0.2}Ga_{0.87}Mg_{0.13}O₃ Electrolyte. *J. Electrochem. Soc.*, **2011**, *158* (5). 10.1149/1.3556085.
- (15) Suthirakun, S.; Ammal, S. C.; Muñoz-García, A. B.; Xiao, G.; Chen, F.; Zur Loye, H. C.; Carter, E. A.; Heyden, A. Theoretical Investigation of H₂ Oxidation on the Sr₂Fe_{1.5}Mo_{0.5}O₆ (001) Perovskite Surface under Anodic Solid Oxide Fuel Cell Conditions. *J. Am. Chem. Soc.*, **2014**, *136* (23), 8374–8386. 10.1021/ja502629j.
- (16) Jiang, Y.; Wang, S.; Zhang, Y.; Yan, J.; Li, W. Kinetic Study of the Formation of Oxygen Vacancy on Lanthanum Manganite Electrodes. *J. Electrochem. Soc.*, **1998**, *145* (2), 373–378. 10.1149/1.1838271.

- (17) Jiang, S. P. Development of Lanthanum Strontium Cobalt Ferrite Perovskite Electrodes of Solid Oxide Fuel Cells – A Review. *Int. J. Hydrog. Energy*, **2019**, *44* (14), 7448–7493. 10.1016/j.ijhydene.2019.01.212.
- (18) Švarcová, S.; Wiik, K.; Tolchard, J.; Bouwmeester, H. J. M.; Grande, T. Structural Instability of Cubic Perovskite $\text{Ba}_x\text{Sr}_{1-x}\text{Co}_{1-y}\text{Fe}_y\text{O}_{3-\delta}$. *Solid State Ion.*, **2008**, *178* (35–36), 1787–1791. 10.1016/j.ssi.2007.11.031.
- (19) Hernández, A. M.; Moggi, L.; Caneiro, A. $\text{La}_2\text{NiO}_{4+\delta}$ as Cathode for SOFC: Reactivity Study with YSZ and CGO Electrolytes. *Int. J. Hydrog. Energy*, **2010**, *35* (11), 6031–6036. 10.1016/j.ijhydene.2009.12.077.
- (20) Guan, B.; Li, W.; Zhang, H.; Liu, X. Oxygen Reduction Reaction Kinetics in Sr-Doped $\text{La}_2\text{NiO}_{4+\delta}$ Ruddlesden-Popper Phase as Cathode for Solid Oxide Fuel Cells. *J. Electrochem. Soc.*, **2015**, *162* (7), F707–F712. 10.1149/2.0541507jes.
- (21) Chung, Y. S.; Kim, T.; Shin, T. H.; Yoon, H.; Park, S.; Sammes, N. M.; Kim, W. B.; Chung, J. S. In Situ Preparation of a $\text{La}_{1.2}\text{Sr}_{0.8}\text{Mn}_{0.4}\text{Fe}_{0.6}\text{O}_4$ Ruddlesden–Popper Phase with Exsolved Fe Nanoparticles as an Anode for SOFCs. *J. Mater. Chem. A*, **2017**, *5* (14), 6437–6446. 10.1039/c6ta09692a.
- (22) Yang, C.; Li, J.; Lin, Y.; Liu, J.; Chen, F.; Liu, M. In Situ Fabrication of CoFe Alloy Nanoparticles Structured $(\text{Pr}_{0.4}\text{Sr}_{0.6})_3(\text{Fe}_{0.85}\text{Nb}_{0.15})_2\text{O}_7$ Ceramic Anode for Direct Hydrocarbon Solid Oxide Fuel Cells. *Nano Energy*, **2015**, *11*, 704–710. 10.1016/j.nanoen.2014.12.001.
- (23) Huan, D.; Wang, Z.; Wang, Z.; Peng, R.; Xia, C.; Lu, Y. High-Performanced Cathode with a Two-Layered R–P Structure for Intermediate Temperature Solid Oxide Fuel Cells. *ACS Appl. Mater. Interfaces*, **2016**, *8* (7), 4592–4599. 10.1021/acsami.5b10844.
- (24) Kagomiya, I.; Jimbo, K.; Kakimoto, K. I.; Nakayama, M.; Masson, O. Oxygen Vacancy Formation and the Ion Migration Mechanism in Layered Perovskite $(\text{Sr},\text{La})_3\text{Fe}_2\text{O}_{7-\delta}$. *Phys. Chem. Chem. Phys.*, **2014**, *16* (22), 10875–10882. 10.1039/c4cp00736k.
- (25) Ling, Y.; Guo, T.; Zhang, X.; Budiman, R. A.; Fujimaki, Y.; Nakamura, T.; Lin, B.; Kawada, T.; Amezawa, K. Evaluation of Electrical Conductivity and Oxygen Diffusivity of the Typical Ruddlesden-Popper Oxide $\text{Sr}_3\text{Fe}_2\text{O}_{7-\delta}$. *Ceram. Int.*, **2017**, *43* (18), 16264–16269. 10.1016/j.ceramint.2017.08.211.
- (26) Ota, T.; Kizaki, H.; Morikawa, Y. Mechanistic Analysis of Oxygen Vacancy Formation and Ionic Transport in $\text{Sr}_3\text{Fe}_2\text{O}_{7-\delta}$. *J. Phys. Chem. C*, **2018**, *122* (8), 4172–4181. 10.1021/acs.jpcc.7b11904.
- (27) Tan, W.; Huan, D.; Yang, W.; Shi, N.; Wang, W.; Peng, R.; Wu, X.; Lu, Y. A

First-Principles Study on Divergent Reactions of Using a $\text{Sr}_3\text{Fe}_2\text{O}_7$ Cathode in Both Oxygen Ion Conducting and Proton Conducting Solid Oxide Fuel Cells. *RSC Adv.*, **2018**, 8 (47), 26448–26460. 10.1039/c8ra04059a.

- (28) Fossdal, A.; Einarsrud, M. A.; Grande, T. Phase Equilibria in the Pseudo-Binary System $\text{SrO}-\text{Fe}_2\text{O}_3$. *J. Solid State Chem.*, **2004**, 177 (8), 2933–2942. 10.1016/j.jssc.2004.05.007.
- (29) Yang, C.; Yang, Z.; Jin, C.; Liu, M.; Chen, F. High Performance Solid Oxide Electrolysis Cells Using $\text{Pr}_{0.8}\text{Sr}_{1.2}(\text{Co},\text{Fe})_{0.8}\text{Nb}_{0.2}\text{O}_{4+\delta}-\text{Co}-\text{Fe}$ Alloy Hydrogen Electrodes. *Int. J. Hydrog. Energy*, **2013**, 38 (26), 11202–11208. 10.1016/j.ijhydene.2013.06.086.
- (30) Tan, T.; Qin, M.; Li, K.; Zhou, M.; Liu, T.; Yang, C.; Liu, M. In-Situ Exsolved NiFe Alloy Nanoparticles on $\text{Pr}_{0.8}\text{Sr}_{1.2}(\text{Ni},\text{Fe})\text{O}_{4-\delta}$ for Direct Hydrocarbon Fuel Solid Oxide Fuel Cells. *Int. J. Hydrog. Energy*, **2020**, 45 (53), 29407–29416. 10.1016/j.ijhydene.2020.07.250.
- (31) Kresse, G.; Furthmüller, J. Efficient Iterative Schemes for Ab Initio Total-Energy Calculations Using a Plane-Wave Basis Set *Phys. Rev. B*, **1996**, 54 (16), 11169–11186. 10.1103/PhysRevB.54.11169.
- (32) Perdew, J. P.; Wang, Y. Accurate and Simple Analytic Representation of the Electron-Gas Correlation Energy. *Phys. Rev. B*, **1992**, 45 (7), 13244–13249. 10.1103/PhysRevB.98.079904.
- (33) Perdew, J. P.; Yue, W. Accurate and Simple Density Functional for the Electronic Exchange Energy: Generalized Gradient Approximation. *Phys. Rev. B*, **1986**, 33 (12), 8800–8802. 10.1103/PhysRevB.33.8800.
- (34) Dudarev, S.; Botton, G. Electron-Energy-Loss Spectra and the Structural Stability of Nickel Oxide: An LSDA+U Study. *Phys. Rev. B*, **1998**, 57 (3), 1505–1509. 10.1103/PhysRevB.57.1505.
- (35) Zhou, F.; Ozoliņš, V. Obtaining Correct Orbital Ground States in F-Electron Systems Using a Nonspherical Self-Interaction-Corrected LDA+U Method. *Phys. Rev. B*, **2009**, 80 (12), 1–6. 10.1103/PhysRevB.80.125127.
- (36) Tran, F.; Schweifer, J.; Blaha, P.; Schwarz, K.; Novák, P. PBE+U Calculations of the Jahn-Teller Effect in PrO_2 . *Phys. Rev. B*, **2008**, 77 (8), 1–9. 10.1103/PhysRevB.77.085123.
- (37) Blöchl, P. E. Projector Augmented-Wave Method. *Phys. Rev. B*, **1994**, 50 (24), 17953–17979. 10.1103/PhysRevB.50.17953.
- (38) Blöchl, P. E.; Jepsen, O.; Andersen, O. K. Improved Tetrahedron Method for

- Brillouin-Zone Integrations. *Phys. Rev. B*, **1994**, *49* (23), 16223–16233. doi.org/10.1103/PhysRevB.49.16223.
- (39) Pack, J. D.; Monkhorst, H. J. Special Points for Brillouin-Zone Integrations. *Phys. Rev. B*, **1977**, *16* (4), 1748–1749. 10.1103/PhysRevB.16.1748.
- (40) Grau-Crespo, R.; Hamad, S.; Catlow, C. R. A.; De Leeuw, N. H. Symmetry-Adapted Configurational Modelling of Fractional Site Occupancy in Solids. *J. Phys. Condens. Matter*, **2007**, *19* (25). 10.1088/0953-8984/19/25/256201.
- (41) Kröger, F. A.; Vink, H. J. Relations between the Concentrations of Imperfections in Solids. *J. Phys. Chem. Solids*, **1958**, *5* (3), 208–223. 10.1016/0022-3697(58)90069-6.
- (42) Taylor, F. H.; Buckeridge, J.; Catlow, C. R. A. Defects and Oxide Ion Migration in the Solid Oxide Fuel Cell Cathode Material LaFeO₃. *Chem. Mater.*, **2016**, *28* (22), 8210–8220. 10.1021/acs.chemmater.6b03048.
- (43) Suthirakun, S.; Xiao, G.; Ammal, S. C.; Chen, F.; Zur Loye, H. C.; Heyden, A. Rational Design of Mixed Ionic and Electronic Conducting Perovskite Oxides for Solid Oxide Fuel Cell Anode Materials: A Case Study for Doped SrTiO₃. *J. Power Sources*, **2014**, *245*, 875–885. 10.1016/j.jpowsour.2013.07.040.
- (44) Ammal, S. C.; Heyden, A. Modeling the Noble Metal/TiO₂ (110) Interface with Hybrid DFT Functionals: A Periodic Electrostatic Embedded Cluster Model Study. *J. Chem. Phys.*, **2010**, *133* (16). 10.1063/1.3497037.
- (45) Nørskov, J. K.; Rossmeisl, J.; Logadottir, A.; Lindqvist, L.; Kitchin, J. R.; Bligaard, T.; Jónsson, H. Origin of the Overpotential for Oxygen Reduction at a Fuel-Cell Cathode. *J. Phys. Chem. B*, **2004**, *108* (46), 17886–17892. 10.1021/jp047349j.
- (46) Atkins, P.; Paula, J. De; Keeler, J. *Atkins' Physical Chemistry*, 11th ed.; Oxford University Press: Oxford, England, 2018.
- (47) Broberg, D.; Medasani, B.; Zimmermann, N. E. R.; Yu, G.; Canning, A.; Haranczyk, M.; Asta, M.; Hautier, G. PyCDT: A Python Toolkit for Modeling Point Defects in Semiconductors and Insulators. *Comput. Phys. Commun.*, **2018**, *226*, 165–179. 10.1016/j.cpc.2018.01.004.
- (48) Freysoldt, C.; Neugebauer, J.; Van De Walle, C. G. Fully Ab Initio Finite-Size Corrections for Charged-Defect Supercell Calculations. *Phys. Rev. Lett.*, **2009**, *102* (1), 1–4. 10.1103/PhysRevLett.102.016402.
- (49) Freysoldt, C.; Neugebauer, J.; Van de Walle, C. G. Electrostatic Interactions between Charged Defects in Supercells. *Phys. Status Solidi Basic Res.*, **2011**, *248* (5), 1067–1076. 10.1002/pssb.201046289.

- (50) Kumagai, Y.; Oba, F. Electrostatics-Based Finite-Size Corrections for First-Principles Point Defect Calculations. *Phys. Rev. B*, **2014**, *89* (19). 10.1103/PhysRevB.89.195205.
- (51) Buckeridge, J. Equilibrium Point Defect and Charge Carrier Concentrations in a Material Determined through Calculation of the Self-Consistent Fermi Energy. *Comput. Phys. Commun.*, **2019**, *244*, 329–342. 10.1016/j.cpc.2019.06.017.
- (52) Henkelman, G.; Arnaldsson, A.; Jónsson, H. A Fast and Robust Algorithm for Bader Decomposition of Charge Density. *Comput. Mater. Sci.*, **2006**, *36* (3), 354–360. 10.1016/j.commatsci.2005.04.010.
- (53) Tang, W.; Sanville, E.; Henkelman, G. A Grid-Based Bader Analysis Algorithm without Lattice Bias. *J. Phys. Condens. Matter*, **2009**, *21* (8). 10.1088/0953-8984/21/8/084204.
- (54) Momma, K.; Izumi, F. VESTA 3 for Three-Dimensional Visualization of Crystal, Volumetric and Morphology Data. *J. Appl. Crystallogr.*, **2011**, *44* (6), 1272–1276. 10.1107/S0021889811038970.
- (55) Qin, M.; Xiao, Y.; Yang, H.; Tan, T.; Wang, Z.; Fan, X.; Yang, C. Ru/Nb Co-Doped Perovskite Anode: Achieving Good Coking Resistance in Hydrocarbon Fuels via Core-Shell Nanocatalysts Exsolution. *Appl. Catal. B Environ.*, **2021**, *299*, 120613. 10.1016/j.apcatb.2021.120613.
- (56) Zhang, P.; Guan, G.; Khaerudini, D. S.; Hao, X.; Xue, C.; Han, M.; Kasai, Y.; Abudula, A. B-Site Mo-Doped Perovskite $\text{Pr}_{0.4}\text{Sr}_{0.6}(\text{Co}_{0.2}\text{Fe}_{0.8})_{1-x}\text{Mo}_x\text{O}_{3-\sigma}$ ($x = 0, 0.05, 0.1$ and 0.2) as Electrode for Symmetrical Solid Oxide Fuel Cell. *J. Power Sources*, **2015**, *276*, 347–356. 10.1016/j.jpowsour.2014.11.141.
- (57) Zhang, P.; Guan, G.; Khaerudini, D. S.; Hao, X.; Xue, C.; Han, M.; Kasai, Y.; Abudula, A. Mechanisms of Methane Decomposition and Carbon Species Oxidation on the $\text{Pr}_{0.4}\text{Sr}_{0.6}\text{Co}_{0.2}\text{Fe}_{0.7}\text{Nb}_{0.1}\text{O}_{3-\sigma}$ Electrode with High Catalytic Activity. *J. Mater. Chem. A*, **2015**, *3* (45), 22816–22823. 10.1039/c5ta07599h.
- (58) Chen, Y.; Jung, W.; Cai, Z.; Kim, J. J.; Tuller, H. L.; Yildiz, B. Impact of Sr Segregation on the Electronic Structure and Oxygen Reduction Activity of $\text{SrTi}_{1-x}\text{Fe}_x\text{O}_3$ Surfaces. *Energy Environ. Sci.*, **2012**, *5* (7), 7979–7988. 10.1039/c2ee21463f.
- (59) Matsuno, J.; Okimoto, Y.; Kawasaki, M.; Tokura, Y. Variation of the Electronic Structure in Systematically Synthesized Sr_2MO_4 ($M=\text{Ti}, \text{V}, \text{Cr}, \text{Mn},$ and Co). *Phys. Rev. Lett.*, **2005**, *95* (17), 1–4. 10.1103/PhysRevLett.95.176404.
- (60) Shannon, R. D. Revised Effective Ionic Radii and Systematic Studies of

- Interatomic Distances in Halides and Chalcogenides. *Acta Crystallogr.*, **1976**, *32* (5), 751–767. 10.1107/S0567739476001551.
- (61) Ritzmann, A. M.; Muñoz-García, A. B.; Pavone, M.; Keith, J. A.; Carter, E. A. Ab Initio DFT+U Analysis of Oxygen Vacancy Formation and Migration in $\text{La}_{1-x}\text{Sr}_x\text{FeO}_{3-\delta}$ ($x = 0, 0.25, 0.50$). *Chem. Mater.*, **2013**, *25* (15), 3011–3019. 10.1021/cm401052w.
- (62) Adler, P.; Goncharov, A. F.; Syassen, K.; Schönherr, E. Optical Reflectivity and Raman Spectra of Sr_2FeO_4 under Pressure. *Phys. Rev. B*, **1994**, *50* (16), 11396–11402. 10.1103/PhysRevB.50.11396.
- (63) He, L.; Liu, F.; Hautier, G.; Oliveira, M. J. T.; Marques, M. A. L.; Vila, F. D.; Rehr, J. J.; Rignanese, G. M.; Zhou, A. Accuracy of Generalized Gradient Approximation Functionals for Density-Functional Perturbation Theory Calculations. *Phys. Rev. B*, **2014**, *89* (6), 1–15. 10.1103/PhysRevB.89.064305.
- (64) Miessler, G. L.; Tarr, D. A. *Inorganic Chemistry*, 2nd ed.; Pearson Education, Inc. Pearson Prentice Hall: Upper Saddle River, New Jersey, 1998.
- (65) Xie, W.; Lee, Y. L.; Shao-Horn, Y.; Morgan, D. Oxygen Point Defect Chemistry in Ruddlesden–Popper Oxides $(\text{La}_{1-x}\text{Sr}_x)_2\text{MO}_{4+\delta}$ ($M = \text{Co}, \text{Ni}, \text{Cu}$). *J. Phys. Chem. Lett.*, **2016**, *7* (10), 1939–1944. 10.1021/acs.jpcclett.6b00739.
- (66) Hu, X.; Li, M.; Xie, Y.; Yang, Y.; Wu, X.; Xia, C. Oxygen-Deficient Ruddlesden–Popper-Type Lanthanum Strontium Cuprate Doped with Bismuth as a Cathode for Solid Oxide Fuel Cells. *ACS Appl. Mater. Interfaces*, **2019**. 10.1021/acsami.9b05445.
- (67) Zhou, J.; Chen, G.; Wu, K.; Cheng, Y. Interaction of La_2NiO_4 (100) Surface with Oxygen Molecule: A First-Principles Study. *J. Phys. Chem. C*, **2013**, *117* (25), 12991–12999. 10.1021/jp403094x.
- (68) Barcellos, D. R.; Coury, F. G.; Emery, A.; Sanders, M.; Tong, J.; McDaniel, A.; Wolverton, C.; Kaufman, M.; O’Hayre, R. Phase Identification of the Layered Perovskite $\text{Ce}_x\text{Sr}_{2-x}\text{MnO}_4$ and Application for Solar Thermochemical Water Splitting. *Inorg. Chem.*, **2019**, *58* (12), 7705–7714. 10.1021/acs.inorgchem.8b03487.
- (69) Muñoz-García, A. B.; Ritzmann, A. M.; Pavone, M.; Keith, J. A.; Carter, E. A. Oxygen Transport in Perovskite-Type Solid Oxide Fuel Cell Materials: Insights from Quantum Mechanics. *Acc. Chem. Res.*, **2014**, *47* (11), 3340–3348. 10.1021/ar4003174.
- (70) Ritzmann, A. M.; Dieterich, J. M.; Carter, E. A. Density Functional Theory + U Analysis of the Electronic Structure and Defect Chemistry of LSCF

($\text{La}_{0.5}\text{Sr}_{0.5}\text{Co}_{0.25}\text{Fe}_{0.75}\text{O}_{3-\delta}$). *Phys. Chem. Chem. Phys.*, **2016**, *18* (17), 12260–12269. 10.1039/c6cp01720g.

- (71) Xu, S.; Jacobs, R.; Morgan, D. Factors Controlling Oxygen Interstitial Diffusion in the Ruddlesden–Popper Oxide $\text{La}_{2-x}\text{Sr}_x\text{NiO}_{4+\delta}$. *Chem. Mater.*, **2018**, *30* (20), 7166–7177. 10.1021/acs.chemmater.8b03146.
- (72) Routbort, J. L.; Rothman, S. J.; Flandermeyer, B. K.; Nowicki, L. J.; Baker, J. E. Oxygen Diffusion in $\text{La}_{2-x}\text{Sr}_x\text{CuO}_{4-y}$. *J. Mater. Res.*, **1988**, *3* (1), 116–121. 10.1557/JMR.1988.0116.
- (73) Tealdi, C.; Ferrara, C.; Mustarelli, P.; Islam, M. S. Vacancy and Interstitial Oxide Ion Migration in Heavily Doped $\text{La}_{2-x}\text{Sr}_x\text{CoO}_{4\pm\delta}$. *J. Mater. Chem.*, **2012**, *22* (18), 8969–8975. 10.1039/c2jm30769c.

2.8 TABLES AND FIGURES

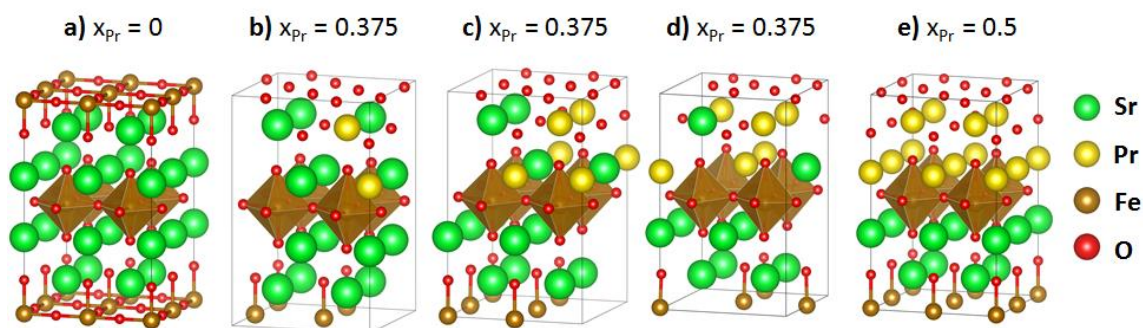


Figure 2.1: Polyhedral representations of the lowest energy dopant-configurations for a) Sr_2FeO_4 , b) $\text{Sr}_{1.75}\text{Pr}_{0.25}\text{FeO}_4$ (structure 7), c) $\text{Sr}_{1.5}\text{Pr}_{0.5}\text{FeO}_4$ (structure 23), d) $\text{Sr}_{1.25}\text{Pr}_{0.75}\text{FeO}_4$ (structure 56), and e) SrPrFeO_4 (structure 45).

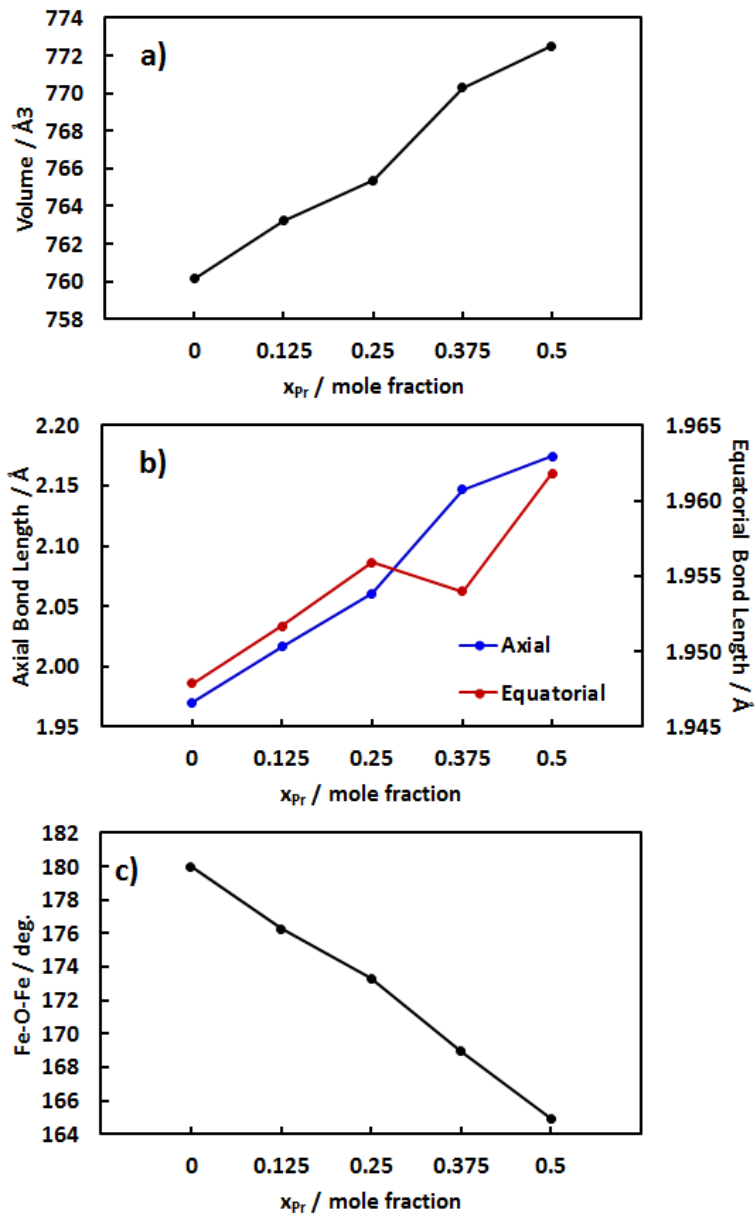


Figure 2.2: Effect of Pr dopant concentration on the structural parameters of $(Sr_{1-x}Pr_x)_2FeO_4$ a) cell volume (\AA^3), b) average Fe-O bond lengths (\AA), and c) average Fe-O-Fe angle (deg.).

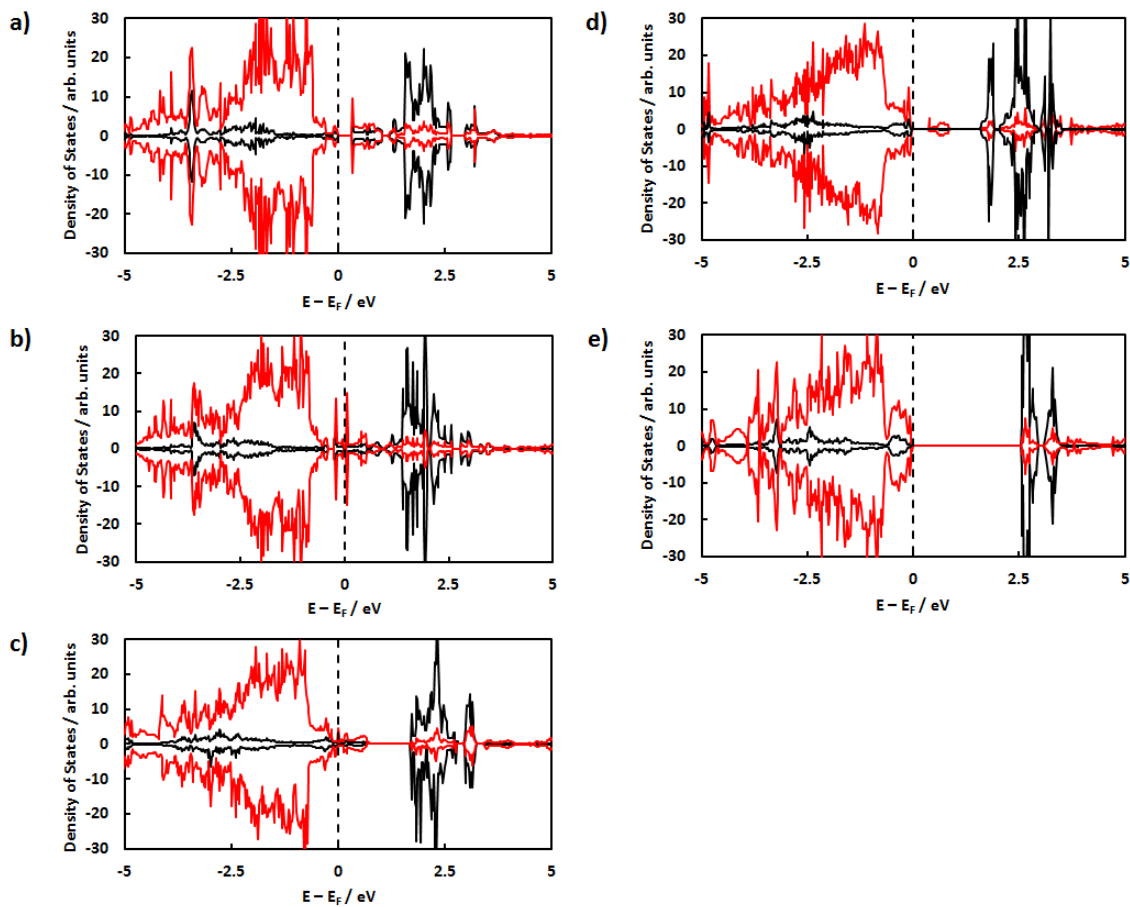


Figure 2.3: PDOS for Fe 3d (black) and O 2p (red) states for $(\text{Sr}_{1-x}\text{Pr}_x)_2\text{FeO}_4$: a) $x = 0$, b) $x = 0.125$, c) $x = 0.25$, d) $x = 0.375$, and e) $x = 0.5$. Energies are referred to the Fermi level (E_F). Positive PDOS values represent α -spins states and negative values represent β -spin states.

Table 2.1: Average Fe magnetic moment (μ_B) and Bader charges (e) for $(\text{Sr}_{1-x}\text{Pr}_x)_2\text{FeO}_{4+\delta}$ with and without oxygen vacancy ($\text{V}_{\text{O}^{\cdot\cdot}}$) and interstitial oxygen ($\text{O}_i^{\cdot\cdot}$) defects for $x = 0, 0.125, 0.25, 0.375,$ and 0.5 .

		x = 0	x = 0.125	x = 0.25	x = 0.375	x = 0.5
Pristine	μ_{Fe}	3.73	3.84	3.91	4.02	4.10
	q_{Fe}	1.73	1.74	1.73	1.74	1.75
	q_{O}	-1.21	-1.25	-1.27	-1.31	-1.35
	q_{Sr}	1.56	1.55	1.54	1.54	1.53
	q_{Pr}	---	2.11	2.10	2.10	2.12
With $\text{V}_{\text{O}^{\cdot\cdot}}$	μ_{Fe}	3.82	3.81	3.99	4.08	3.97
	q_{Fe}	1.72	1.72	1.70	1.70	1.59
	q_{O}	-1.24	-1.27	-1.31	-1.34	-1.34
	q_{Sr}	1.54	1.54	1.55	1.54	1.53
	q_{Pr}	---	2.08	2.09	2.09	2.08
With $\text{O}_i^{\cdot\cdot}$	μ_{Fe}	3.68	3.81	3.90	4.02	4.10
	q_{Fe}	1.79	1.81	1.76	1.70	1.72
	q_{O}	-1.19	-1.22	-1.24	-1.27	-1.30
	q_{Sr}	1.55	1.55	1.55	1.54	1.53
	q_{Pr}	---	2.11	2.10	2.11	2.11

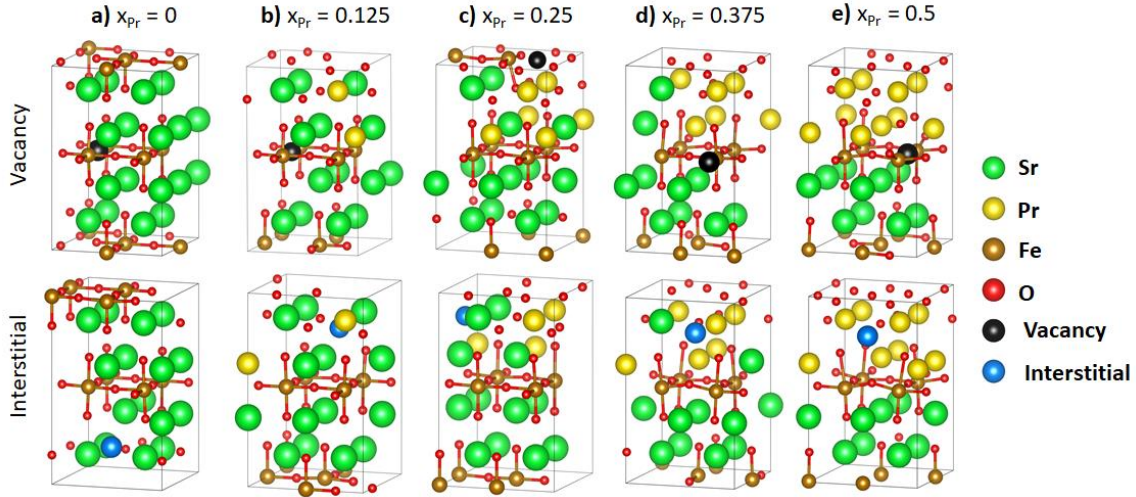


Figure 2.4: Lowest energy oxide defect conformers identified for $(\text{Sr}_{1-x}\text{Pr}_x)_2\text{FeO}_{4\pm\delta}$ a) $x = 0$, b) $x = 0.125$, c) $x = 0.25$, d) $x = 0.375$, and e) $x = 0.5$. δ is modeled as a value of ± 0.125 .

Table 2.2: Formation energies (in eV) of oxygen vacancies ($\Delta E_{f,\text{vac}}$) and interstitial oxygen defects ($\Delta E_{f,\text{int}}$) calculated for $(\text{Sr}_{1-x}\text{Pr}_x)_2\text{FeO}_{4\pm\delta}$ with $x = 0, 0.125, 0.25, 0.375$, and 0.5 .

X_{Pr}	$\Delta E_{f,\text{vac}} (0 \text{ K})$	$\Delta E_{f,\text{int}} (0 \text{ K})$	1073 K, $P_{\text{O}_2} = 10^{-20} \text{ atm}$		1073 K, $P_{\text{O}_2} = 0.21 \text{ atm}$	
			$\Delta G_{f,\text{vac}}$	$\Delta G_{f,\text{int}}$	$\Delta G_{f,\text{vac}}$	$\Delta G_{f,\text{int}}$
0	1.465	0.578	-1.910	3.953	0.198	1.845
0.125	1.497	0.294	-1.879	3.670	0.230	1.561
0.25	1.302	0.447	-2.074	3.822	0.035	1.714
0.375	1.617	0.283	-1.759	3.659	0.350	1.550
0.5	3.876	0.146	0.488	3.509	2.597	1.400

Table 2.3: Magnetic moment (μ_B) and Bader charges (e) of nearest neighbor(s) Fe to the oxide defect for $(\text{Sr}_{1-x}\text{Pr}_x)_2\text{FeO}_{4\pm\delta}$ with $x = 0, 0.125, 0.25, 0.375,$ and 0.5 . P refers to defect free or the pristine state. D refers to the defect-containing state.

	x = 0		x = 0.125		x = 0.25		x = 0.375		x = 0.5	
	P	D	P	D	P	D	P	D	P	D
Vacancy										
q_{Fe}	1.73, 1.73	1.75, 1.75	1.74, 1.74	1.72, 1.73	1.73, 1.71	1.66, 1.64	1.75, 1.73	1.64, 1.64	1.75, 1.75	1.21, 1.22
μ_{Fe}	3.73, 3.73	3.65, 3.65	3.85, 3.85	3.31, 3.31	3.81, 3.78	3.99, 4.03	4.07, 4.10	4.03, 4.02	4.10, 4.10	3.60, 3.60
Interstitial										
q_{O}^*	---	-0.69	---	-0.75	---	-0.75	---	-0.74	---	-0.76
q_{Fe}	1.73	1.84	1.74	1.80	1.73	1.75	1.74	1.62	1.75	1.72
μ_{Fe}	3.73	3.67	3.85	3.91	3.81	3.88	3.85	3.84	4.10	4.09

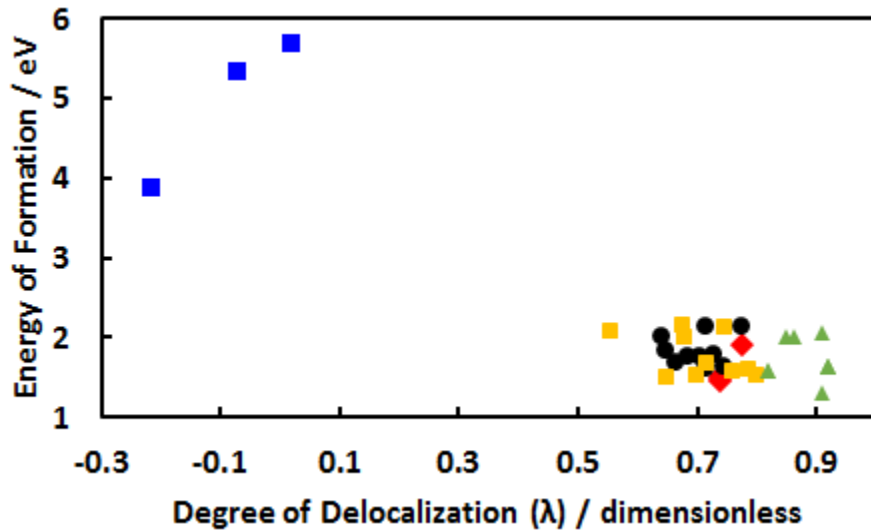


Figure 2.5: The variation of $\Delta E_{f,\text{vac}}$ (in eV) with λ (dimensionless) for $\text{Sr}_2\text{FeO}_{4-\delta}$ (red), $\text{Sr}_{1.75}\text{Pr}_{0.25}\text{FeO}_{4-\delta}$ (yellow), $\text{Sr}_{1.5}\text{Pr}_{0.5}\text{FeO}_{4-\delta}$ (green), $\text{Sr}_{1.25}\text{Pr}_{0.75}\text{FeO}_{4-\delta}$ (black), and $\text{SrPrFeO}_{4-\delta}$ (blue). The lowest energy vacancy site and all non-equivalent sites are included in this figure. A positive λ value indicates an increase in the extent of charge that is absorbed into the oxygen sublattice.

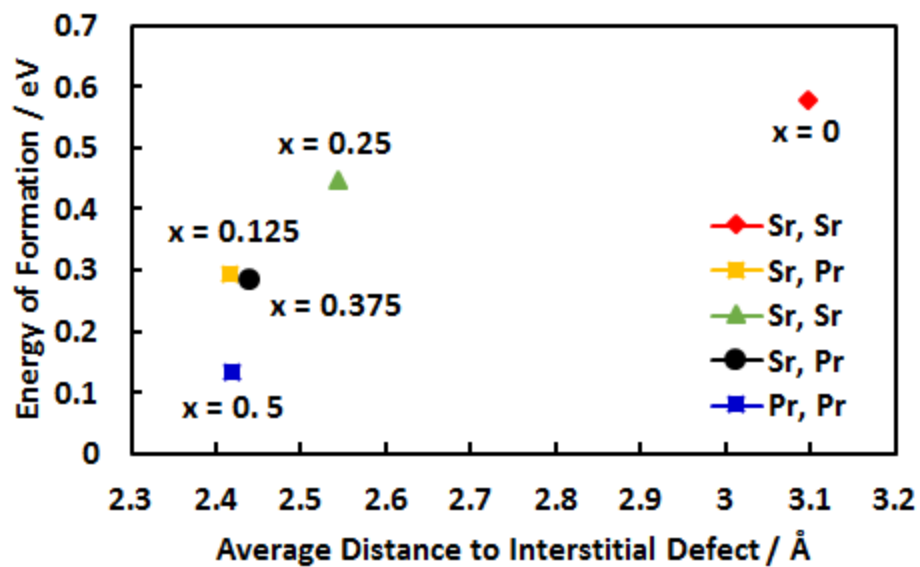


Figure 2.6: Average distance of the minimum energy interstitial defect to neighboring A-site ions versus the energy of interstitial formation for $x = 0$ (red), $x = 0.125$ (yellow), 0.25 (green), 0.375 (black), and 0.5 (blue). The legend labels the elemental identity of the neighboring A-site ions.

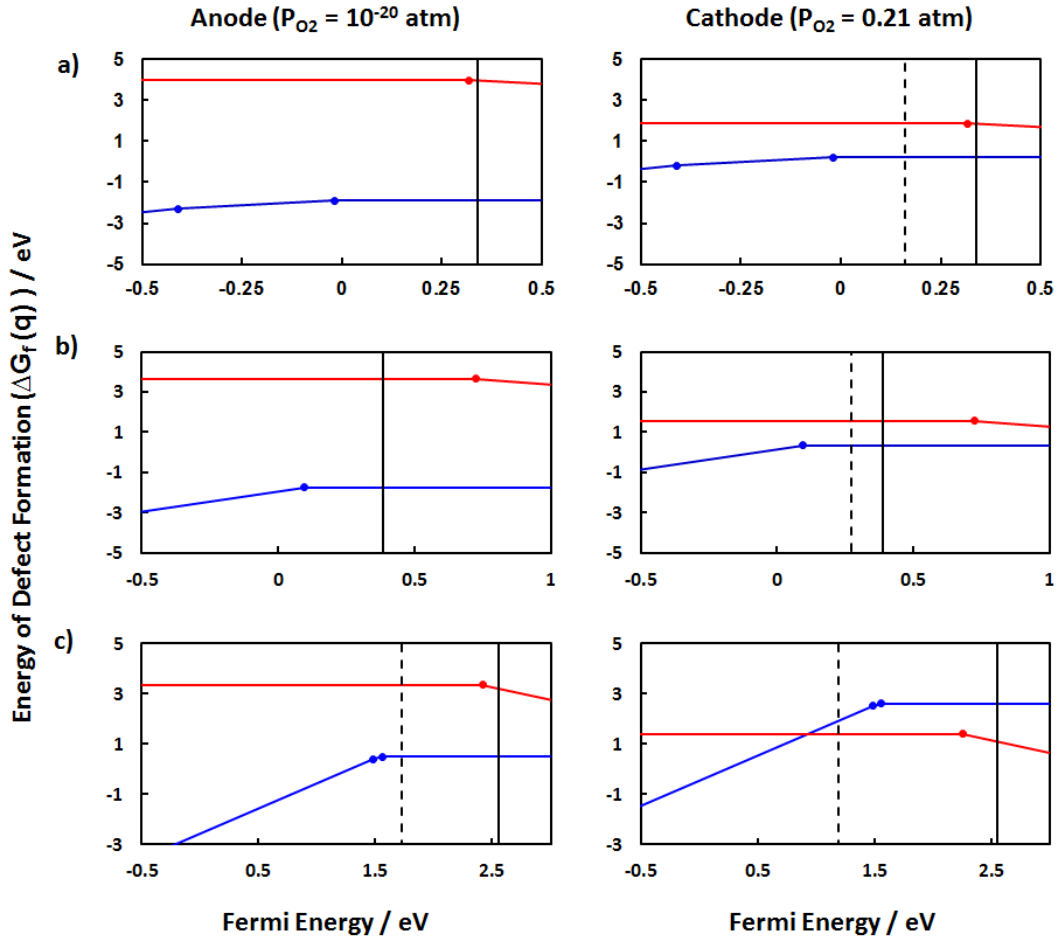


Figure 2.7: Defect formation energy as a function of Fermi Energy at 800 °C for a) Sr_2FeO_4 , b) $\text{Sr}_{1.25}\text{Pr}_{0.75}\text{FeO}_4$, and c) SrPrFeO_4 . Configurations with $x = 0.125$ and $x = 0.25$ are not shown due to predicted metallic state. The blue and red lines represent the optimized vacancy and interstitial defect for each dopant-configuration, respectively. The dashed line represents the self-consistent Fermi-level, and the solid black lines represents the computed CBM for a given dopant-configuration.

Table 2.4: Migration energies (top number) and relative vacancy formation energies (bottom number in parenthesis) in eV for all non-identical oxygen vacancy migration jump routes.

Jump Route	Dopant-Configuration				
	x = 0	x = 0.125	x = 0.25	x = 0.375	x = 0.5
1. (O1 – O2)	2.652 (0.000)	3.638 (0.079)	3.892 (0.270)	3.539 (0.127)	5.710 (0.000)
2. (O1 – O3)	1.135 (0.000)	1.045 (0.031)	1.105 (0.319)	0.889 (0.127)	1.305 (0.000)
3. (O1 – O4)	1.009 (0.425)	1.027 (0.101)	1.132 (0.320)	0.947 (0.063)	2.813 (1.818)
4. (O1 – O5)	---	1.087 (0.021)	1.177 (0.319)	1.087 (0.175)	1.533 (1.461)
5. (O1 – O6)	---	0.869 (0.177)	1.130 (0.319)	1.058 (0.001)	---
6. (O1 – O7)	---	0.996 (0.640)	0.919 (0.699)	0.840 (0.384)	---
7. (O1 – O8)	---	0.985 (0.507)	1.084 (0.270)	1.104 (0.513)	---
8. (O1 – O9)	---	1.043 (0.574)	0.937 (0.698)	0.703 (0.204)	---
9. (O1 – O10)	---	1.062 (0.654)	1.152 (0.748)	1.039 (0.522)	---

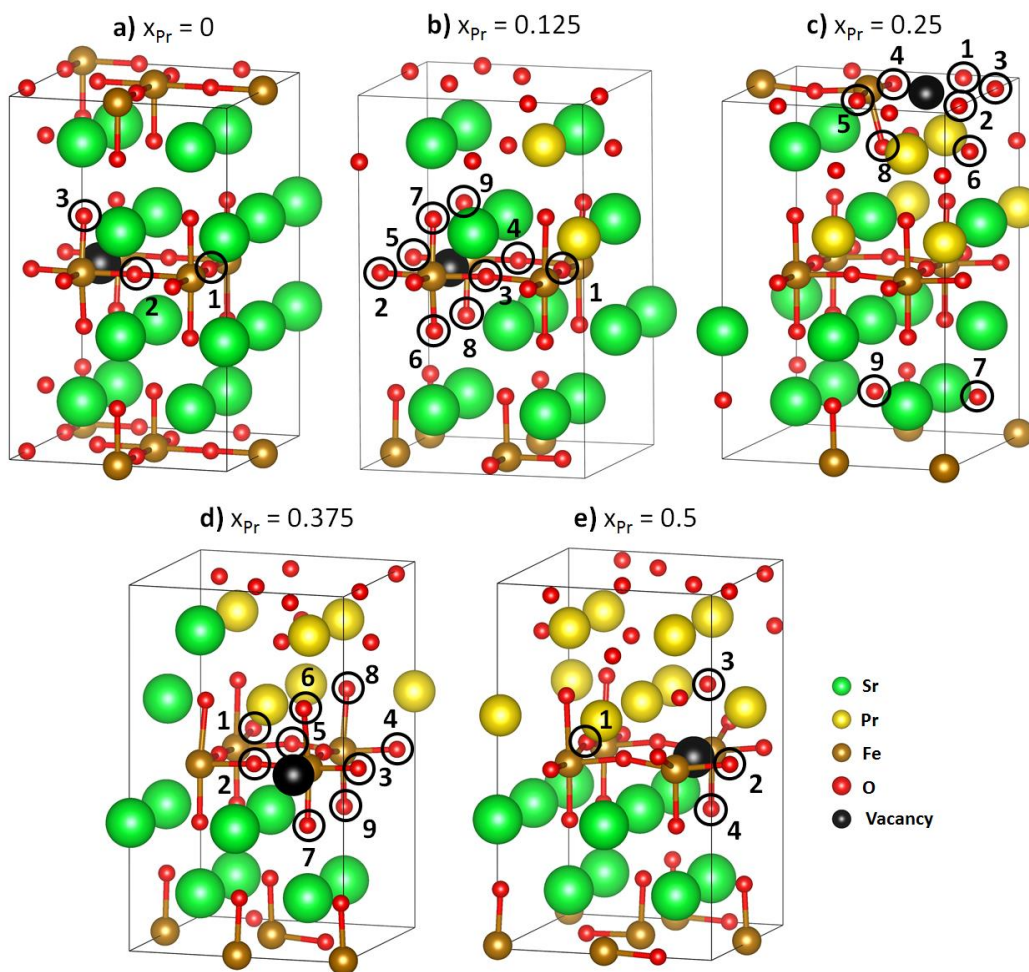


Figure 2.8: Schematic of the vacancy migration jump routes around the minimum energy vacancy site (filled black circle) for a) Sr₂FeO₄, b) Sr_{1.75}Pr_{0.25}FeO₄, c) Sr_{1.5}Pr_{0.5}FeO₄, d) Sr_{1.25}Pr_{0.75}FeO₄, and e) SrPrFeO₄. The numbers presented inside the structures correspond to the jump routes presented in Table 2.4 for each dopant configuration.

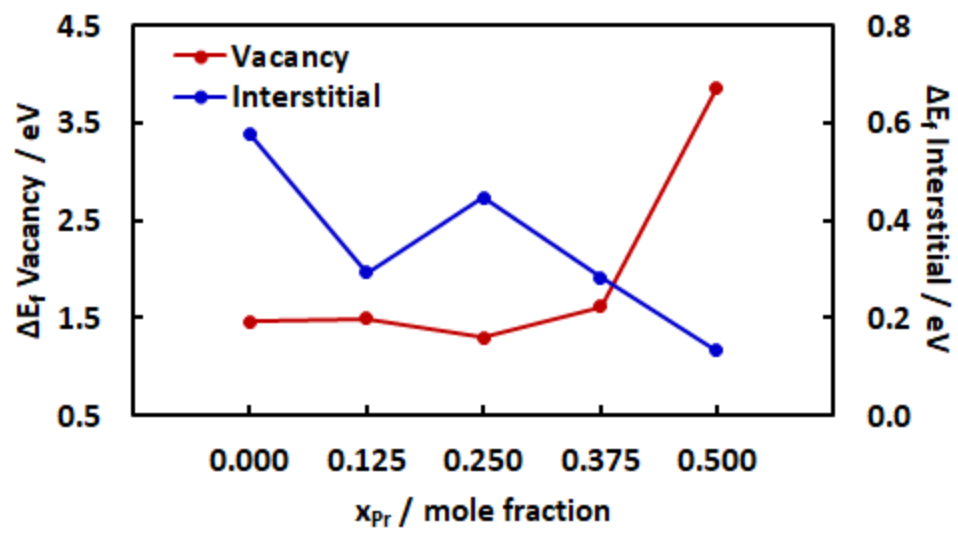


Figure 2.9: Graphical Abstract

CHAPTER 3

THEORETICAL INVESTIGATION OF THE ELECTROCHEMICAL OXIDATION OF H₂ AND CO FUELS ON A RUDDLESSEN-POPPER SrLaFeO_{4±δ} ANODE ²

² Szaro, N.; Ammal, S.; Chen., F.; Heyden, A. *ACS Appl. Mater. Interfaces*, **2023**, *15* (25), 30139-30151, 10.1021/acsami.3c03256. Reprinted (adapted) with permission of the publisher. Copyright 2023 American Chemical Society.

3.1 ABSTRACT

The electrochemical oxidation of H₂ and CO fuels have been investigated on the Ruddlesden-Popper layered perovskite, SrLaFeO_{4-δ} (SLF), under anodic solid oxide fuel cell conditions using periodic density functional theory and microkinetic modeling techniques. Two distinct FeO₂-plane terminated surface models differing in terms of the underlying rocksalt layer (SrO or LaO) are used to identify the active site and limiting factors for the electro-oxidation of H₂, CO, and syngas fuels. Microkinetic modeling predicted an order of magnitude higher turnover frequency for the electro-oxidation of H₂ compared to CO for SLF at short circuit conditions. The surface model with an underlying SrO layer was found to be more active with respect to H₂ oxidation than the LaO-based surface model. At an operating voltage of less than 0.7 V, surface H₂O/CO₂ formation was found to be the key rate-limiting step and the surface H₂O/CO₂ desorption was the key charge transfer step. In contrast, the bulk oxygen migration process was found to affect the overall rate at high cell voltage conditions above 0.9 V. In the presence of syngas fuel, the overall electrochemical activity is derived mainly from H₂ electro-oxidation and CO₂ is chemically shifted to CO via the reverse water-gas shift reaction. Substitutional doping of a surface Fe atom with Co, Ni, and Mn revealed that the H₂ electro-oxidation activity of FeO₂-plane terminated anodes with an underlying LaO rocksalt layer can be improved with dopant introduction, with Co yielding a three orders of magnitude higher activity relative to the undoped LaO surface model. Constrained *ab initio* thermodynamic analysis furthermore suggested that the SLF anodes are resistant towards sulfur poisoning both in the presence and absence of dopants. Our findings reflect the role of various elements in controlling the fuel oxidation activity of

SLF anodes that could aid the development of new Ruddlesden-Popper phase materials for fuel cell applications.

3.2 INTRODUCTION

Solid oxide fuel cells (SOFCs) are solid-state electrochemical devices that display the promising ability to oxidize both hydrogen gas and hydrocarbon-based fuels directly into electricity with high efficiency ^{1,2}. SOFC adoption for practical use is limited due to high operating temperatures and material decomposition resulting from mechanical and chemical instabilities ³. Selection of stable and active anode materials is a crucial part of SOFC development since fuel oxidation occurs at the anode. Nickel-yttria stabilized zirconia (Ni/YSZ) is considered the state-of-the-art anode cermet material for SOFC applications; however, it suffers from redox instability, particle agglomeration, and sulfur poisoning ⁴. Extensive research has been performed to identify alternate anode materials that can circumvent these drawbacks of Ni/YSZ. A recent review summarizes the reports focusing on single-phase and composite electrode materials that are both sulfur resistant and ionically conductive at or below 800 °C ⁵. Perovskite-based mixed ionic and electronic conductors (MIECs) such as LSCM and SFMO have been proposed as promising alternative candidates for anodic applications ⁶⁻⁸. In addition to the traditional perovskite-based compounds, the Ruddlesden-Popper (RP) phase materials with K_2NiF_4 -type ($A_{n+1}B_nO_{3n+1}$, $n = 1$ to ∞) structure have also received attention as potential candidates for SOFC applications. Here, the A-site refers to an alkali, an alkaline earth, or a rare earth metal; and the B-site refers to a transition metal.

The layered RP oxides display high ionic conductivity and catalytic activity for the oxygen reduction reaction, and thus being developed for use in metal-air batteries,

supercapacitors, and cathodic applications⁹⁻¹³. Recent studies have also examined the performance of RP oxides as anodes for SOFCs. Xu et al. demonstrated that SrLaFeO_{4-δ} (SLFO_{4-δ} or SLF) has chemical compatibility with the commonly used Sm_{0.2}Ce_{0.8}O_{1.9} (SDC) and La_{0.8}Sr_{0.2}Ga_{0.85}Mg_{0.15}O₃ (LSGM) electrolytes and exhibits electro-catalytic activity towards wet H₂ (P_{max} of 0.63 W/cm² at 800 °C) with sulfur resistance for greater than 80 hours under H₂ + 50 ppm H₂S feed¹⁴. To further enhance the catalytic activity of SLF, Wang et al. synthesized a composite anode of exsolved Fe-Ni alloy nanoparticles on a SLF substrate that displayed increased catalytic activity relative to pure SLF, especially at temperatures lower than 700 °C¹⁵. In another study, Wu et al. reported that a composite anode of exsolved Fe-Ni alloy nanoparticles on a SrLaFe_{0.75}Ni_{0.25}O₄ substrate displayed a power output of 0.54 W/cm² at 800 °C under H₂ + 1000 ppm H₂S feed¹⁶. In addition to Ni, other transition metals, such as Co and Mn – have also been utilized to modulate SLF performance. For example, Chang et al. used SLF as a pure catalyst layer with exsolved Co-Fe alloy nanoparticles for a direct methane-based anode displaying coking resistance¹⁷. Furthermore, Park et al. utilized Co-Fe alloy nanoparticles on a related material, Sr_{0.8}La_{1.2}Co_{0.4}Fe_{0.6}O₄ for direct H₂ oxidation and observed max power density of 0.73 W/cm²¹⁸, Li et al. used a Fe₃Co₂ + Sr_{0.8}La_{1.2}Mn_{0.4}Fe_{0.6}O₄ anode to display excellent activity under 200 ppm H₂-H₂S conditions¹⁹, and Chung et al. displayed a max power density of 0.72 W/cm² with Fe + Sr_{0.8}La_{1.2}Mn_{0.4}Fe_{0.6}O₄ in the presence of H₂²⁰. Overall, these experimental studies demonstrate that SLF (with its B-site doped conformers) can be regarded as a promising anode material class due to its observed native electrochemical activity, stability under concentrated sulfur feeds, and ability to serve as an exsolved nanoparticle substrate. However, a deeper understanding of the fuel

oxidation mechanism on these substrates is lacking and the role of B-site dopant metals in the electrochemical activity and sulfur resistance is not well understood, which are crucial for the development of alternative RP oxide-based anode materials.

Computational studies performed over RP oxides have focused on understanding the oxygen reduction process over $\text{Sr}_3\text{Fe}_2\text{O}_7$ ²¹ and La_2NiO_4 ^{22,23} materials for cathodic applications. While the theoretical studies on anode reactions over RP oxides are rare, the fuel oxidation mechanism has been widely investigated over perovskite materials for anode applications. Suthirakun et al. and Han et al. investigated H_2 oxidation mechanism on the double perovskite $\text{Sr}_2\text{Fe}_{1.5}\text{Mo}_{0.5}\text{O}_6$ (SFMO)^{24,25} and Ren et al. studied CO_2 reduction on the $(\text{Sr},\text{La})(\text{Fe},\text{Mn},\text{Ni})\text{O}_3$ perovskite for electrolysis applications²⁶. Heyden and coworkers examined the oxidation mechanism of CO and syngas over SFMO²⁷ and further explored different poisoning mechanisms of sulfur via thermodynamic analysis on SFMO²⁸. These studies provided a fundamental understanding of reactions at the anode and the role of different elements in enhancing/inhibiting the electrochemical activity. Herein, we conducted a mechanistic investigation of H_2 , CO, and syngas fuel oxidation reactions on $\text{SrLaFeO}_{4-\delta}$ using a combination of density functional theory (DFT) and microkinetic modeling techniques as illustrated in Figure 3.1. We examined the electrochemical activity of different SLF surfaces with respect to cell voltage and explored the sulfur poisoning mechanism on these surfaces. Furthermore, we analyzed the effects of a single-atom surface B-site doping with Co, Mn, and Ni dopants on the kinetic activity of H_2 oxidation and sulfur stability. We used standard SOFC operating conditions to determine rate-controlling steps and polarization curves that could aid the design of future RP-based materials for SOFC applications.

3.3 METHODS

Electronic energies are obtained with spin-polarized Kohn-Sham DFT+U calculations with periodic boundary conditions using the Vienna Ab Initio Simulation Package (VASP) version 5.4.4^{29,30}. Electron exchange-correlation effects were evaluated by utilizing the generalized gradient approximation (GGA) with the Perdew, Burke, and Ernzerhof (PBE) functional^{31,32}. Dudarev's approach for DFT+U calculations is used to correct the inadequate description of localized 3d electrons on transition metals³³. The U-J parameter of 4.0 was used for Fe d-block electrons in accordance with earlier reports^{34,35}. In the case of dopants, the U-J parameters of 3.32 (Co), 3.9 (Mn), and 6.0 (Ni) eV were chosen based on the values utilized by the Materials Project^{36,37}. The nuclei and core electrons were represented by the frozen-core projector-augmented wave (PAW) approach using the following valence configurations: Sr (4s² 4p⁶ 5s²), La (5s² 5p⁶ 5d¹ 6s²), Fe (3p⁶ 3d⁶ 4s²), Co (3p⁶ 4s² 3d⁷), Mn (3p⁶ 4s² 3d⁵), Ni (3s² 3p⁶ 4s² 3d⁸), O (2s² 2p⁴), H (1s), and C (2s² 2p²)³⁸. The plane-wave basis set was set to a kinetic cutoff of 700 eV. Integration over the Brillouin zone used the Gaussian method with a smearing width of 0.05 eV for all calculations. The convergence criteria for electronic energy and ionic relaxations were set to 10⁻⁶ eV and 0.05 eV/Å, respectively. Ferromagnetic (FM) ordering is chosen as the initial magnetic moment configuration for all transition metals. While the single bulk unit cell calculations utilized a 9 × 9 × 5 Monkhorst-Pack (MP) k-point mesh³⁹, the bulk vacancy calculations were carried out with a 2 × 2 × 1 bulk structure supercell utilizing a 5 × 5 × 3 MP k-point mesh as adopted in our earlier work on (Sr_{1-x}Pr_x)₂FeO_{4±δ} RP oxide³⁵. Fuel oxidation mechanisms were examined on 3 × 3 × 1 surface slab models (1.5 × 1.5 × 1 supercell units) using a 3 × 3 × 1 MP k-point mesh.

Dipole and quadrupole corrections to the energy were incorporated using a modified version of the Markov and Payne method⁴⁰. For transition state (TS) structure calculations, we used the VTST implementation of the climbing image nudged elastic band (CI-NEB) and dimer methods⁴¹⁻⁴⁴. All spring forces are converged to 0.05 eV/Å. The VESTA 3 program is used to visualize the optimized structures⁴⁵.

The following expression was utilized to calculate the chemical potential (μ_i) of any gaseous species (H₂, O₂, CO, H₂O, CO₂, H₂S, and CH₄),

$$\mu_i = \mu_i(T, p^\circ) + k_B T \ln \left(\frac{p_i}{p^\circ} \right) \quad (3.1)$$

where $\mu_i(T, p^\circ)$ is calculated from the partition functions of the gaseous species referenced to a pressure (p°) of 1 atm, k_B is the Boltzmann constant, T is temperature, and p_i is the applied partial pressure of a gaseous species. Details regarding the calculation of these free energies are described in Section B.1 of Appendix B. Since GGA tends to overestimate the binding energy of O₂, the energy of O₂ molecule (E_{O_2}) is calculated using the following correction scheme based on the H₂O splitting reaction⁴⁶⁻⁴⁸.

$$E_{O_2} = 2[(E_{DFT,H_2O} + E_{ZPE,Exp. H_2O}) - (E_{DFT,H_2} + E_{ZPE,Exp. H_2}) - E_{Exp. HOF}] - E_{ZPE,Exp. O_2} \quad (3.2)$$

Here, $E_{DFT,i}$ is the energy of the corresponding gas molecule calculated with the PBE functional, $E_{ZPE,Exp,i}$ is the experimental zero-point energy, and $E_{Exp. HOF}$ is the experimental heat of formation of a gas-phase H₂O molecule. In addition, PBE is known to underestimate the gas phase energy of the CO molecule⁴⁹; and therefore, we utilized a correction of -0.42 eV as determined by Ammal and Heyden²⁷. Adsorption free energies of all intermediates, $G_{ads,i}$, were calculated based on the following equations⁵⁰:

$$G_{ads,i} = G_{slab+intermediate,i} - G_{slab} - N_H\mu_H - N_O\mu_O - N_C\mu_C \quad (3.3)$$

$$\mu_H = \frac{1}{2}\mu_{H_2} \quad (3.4)$$

$$\mu_O = \mu_{H_2O} - \mu_{H_2} \quad (3.5)$$

$$\mu_C = \mu_{CH_4} - 2\mu_{H_2} \quad (3.6)$$

$G_{slab+intermediate,i}$ is the free energy of the surface with adsorbed intermediate, G_{slab} is the free energy of the bare surface model, and the chemical potentials of the molecules, μ_{H_2} , μ_{O_2} , and μ_{CH_4} are calculated using equation (3.1). N_H , N_O , and N_C are the number of H, O, and C atoms in the adsorbed surface intermediates. The reaction (ΔG_i^{rxn}) and activation (ΔG_i^\ddagger) free energies of an elementary step were calculated using the following equations:

$$\Delta G_i^{rxn} = \sum_j v_{ij} G_{ads,j}^i \quad (3.7)$$

$$\Delta G_i^\ddagger = G_{ads,i}^\ddagger - \sum_j G_{ads,i}^R \quad (3.8)$$

v_{ij} and $G_{ads,j}^i$ are the stoichiometric coefficient and adsorption energy of an intermediate j in reaction step i , respectively. We note here that all reaction and activation free energies are independent of the reference state.

For an adsorption elementary reaction, $A + * \rightarrow A^*$, where $*$ and A^* represent an empty site and adsorbed species on the slab model, respectively, collision theory was used to calculate the forward or adsorption rate constant ($k_{for,i}$).

$$k_{for,i} = \frac{10^5 S_{unit}}{(2\pi m_i k_B T)^{\frac{1}{2}}} (s^{-1} atm^{-1}) \quad (3.9)$$

Here, m_i is the molecular weight of the adsorbing species and S_{unit} is the surface area of our slab models ($1.39 \times 10^{-18} m^2$). A sticking coefficient of unity is used in all

simulations^{24,25}. Transition state theory was used to calculate the forward rate constant (k_{for}) for a surface reaction $A^* \rightarrow B^*$.

$$k_{for} = \frac{k_B T}{h} e^{\frac{-\Delta G_i^\ddagger}{k_B T}} \quad (3.10)$$

The equilibrium constant (K_{eq}) for an elementary reaction is computed with the following equation:

$$K_{eq} = e^{\frac{-\Delta G_i^{rxn}}{k_B T}} \quad (3.11)$$

Based on the calculated forward and equilibrium constants for each elementary step, we constructed a microkinetic model as a set of ordinary differential equations. The microkinetic model is solved via MATLAB with ODE15s⁵¹. The steady-state solution provides a probability density for the system to occupy each discrete state and we refer to these probabilities as surface coverages or θ_i . The turnover frequency (TOF) of each pathway was calculated using the calculated surface coverages. For syngas fuel, we combined all elementary reactions from the H₂ and CO oxidation pathways into one microkinetic model. We used Campbell's degree of rate control ($X_{RC,i}$) to identify rate-controlling steps using the following expression^{52,53}:

$$X_{RC,i} = \left(\frac{\partial \ln(TOF)}{\partial \ln(k_i)} \right)_{k_i, k_j \neq i} \quad (3.12)$$

The apparent activation energy (E_{app}) was calculated over a temperature range of 973 to 1373 K using the expression:

$$E_{app} = RT^2 \left(\frac{\partial \ln(TOF)}{\partial T} \right)_{P, Y_i} \quad (3.13)$$

3.4 RESULTS AND DISCUSSION

3.4.1 DEVELOPMENT OF SLF BULK SURFACE MODELS

The bulk structure of SLF was optimized using the computational setup described above starting from the structure obtained from materials project entry mp-1218154^{36,54,55} with a unit cell of 14 atoms and a space group of I4mm. The calculated lattice parameters ($a = b = 3.929$ (Å) and $c = 12.626$ (Å)) of this RP oxide are close to the experimental lattice parameters ($a = b = 3.8750$ (Å) and $c = 12.727$ (Å)) reported in the literature^{14,56}. We utilized a $2 \times 2 \times 1$ supercell (56 atoms) to compute the free energy of oxygen vacancy formation and the bulk vacancy-mediated migration energy as displayed in Figure 3.2(a). Details regarding the mechanics of the bulk vacancy-mediated migration are outlined in Appendix B Section B.2. We calculated the free energy barrier of vacancy-mediated diffusion as 1.30 eV at $T = 1073$ K and $P_{O_2} = 10^{-20}$ atm⁵⁷. This value is consistent with other $n = 1$ RP oxides with a 50% A-site doping ratio such as SrPrFeO₄ (1.3 eV)³⁵ and LaSrCoO₄ (~ 1.1 eV)⁵⁸, respectively.

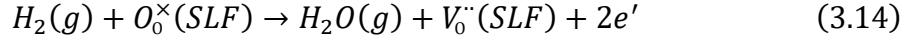
Computational studies performed over Sr_{n+1}Fe_nO_{3n+1} RP oxides suggested that the (001) facet of these oxides is thermodynamically stable⁵⁹ and kinetically active for O₂ reduction²¹ and NO oxidation⁶⁰. Therefore, the (001) surface models of SLF were constructed for the present study. Four possible (001) terminations are possible for SLF with two FeO₂-plane terminations and two rocksalt layer (LaO and SrO) terminations. Only the FeO₂-plane terminations are considered here because they are expected to be more catalytically active due to the ability of Fe to readily adopt different oxidation states relative to alkaline earth Sr or lanthanide La. The two FeO₂-terminated surfaces differ in terms of the nearest underlying rocksalt layer (LaO or SrO) as shown in Figure 3.2(b-c)

and are designated as FeO₂-LaO and FeO₂-SrO surfaces. The SLF surface models were developed following the approach outlined by Akbay et al. for the La₂NiO₄ RP oxide using a 2 × 2 × 4/3 unit cell model²³. Here, we used a 3 × 3 × 1 unit cell slab model (1.5 × 1.5 × 1 supercell units) that was found to be large enough to avoid the interaction between an adsorbent with its periodic replica and be computationally affordable. These slab models are composed of seven atomic layers and have a computed surface area of 1.39 × 10⁻¹⁸ m². A vacuum gap of 15 Å was used to minimize the interaction between images along the z-axis. The bottom-most FeO₂-plane and a rocksalt layer (e.g., 2 bottom layers) were fixed in all calculations to mimic a semi-infinite bulk crystal.

Oxygen nonstoichiometry via oxygen vacancies is expected for these RP oxides under low oxygen partial pressures (reducing conditions) found in SOFC anodic operating conditions. To capture a representative example of the SLF surface structure under SOFC operating conditions, we computed the Gibb's free energy of oxygen vacancy formation on each surface model that can determine the thermodynamic drive to form surface vacancies. We compute the free energy of surface vacancy formation as -0.83 and -2.56 eV for FeO₂-LaO and FeO₂-SrO, respectively, at anodic operating conditions (1073 K, P_{O₂} = 10⁻²⁰ atm). As both surfaces indicate favorability to form oxygen vacancies on the FeO₂-plane, we utilized a representative model of a single surface oxygen vacancy for both surfaces, a model similar to the ones adopted by Akbay et al., Zhou et al., and Gu and Nikolla^{22,23,61} for examining reactions on RP oxides. An expanded analysis of the oxygen vacancy density as a function of oxygen chemical potential is provided in Section B.3 of Appendix B.

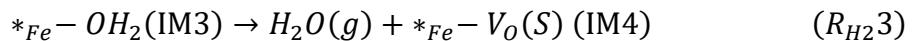
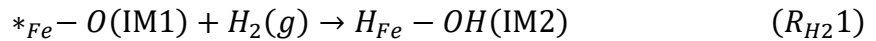
3.4.2 H₂ OXIDATION MECHANISM ON SLF (001) SURFACES

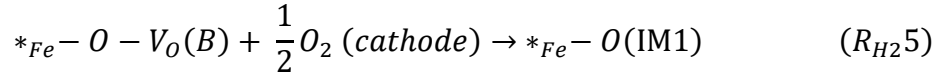
The overall electrochemical oxidation of H₂ on the SLF anodes can be expressed (in Kröger-Vink notation ⁶²) as:



Here, O_0^\times and V_0'' refer to an oxygen atom and a doubly positive charged oxygen vacancy on the SLF surface, respectively. Based on the gas phase reaction free energy of $H_2 + \frac{1}{2} O_2 \rightarrow H_2O$ ($\Delta G = -2.2$ eV; $T = 1073$ K, $P_{H_2}^{anode} = 1$ atm, $P_{O_2}^{cathode} = 0.21$ atm) the $2e'$ oxidation process should yield a cell voltage of 1.1 V. Figure 3.3 illustrates our proposed catalytic cycle for the oxidation of H₂ on the SLF (001) surface models with elementary reactions R_{H2}1 to R_{H2}5 occurring at an active site $*_{Fe}-O$, where $*_{Fe}$ represents an adsorbate free Fe atom on the surface.

All DFT+U calculations were performed on charge-neutral surface models; and therefore, the net charge on the elementary reactions R_{H2}1 to R_{H2}5 is zero. However, the electrochemical charge transfer process is considered in the microkinetic model. The first elementary step in the H₂ oxidation process ($R_{H_2}1$) outlines the dissociative adsorption of the feed gas on a metal (Fe) site and a neighboring oxygen atom, forming a surface hydroxyl complex. The second ($R_{H_2}2$) and third ($R_{H_2}3$) elementary reactions describe the formation of H₂O on the surface and desorption of H₂O leading to the formation of surface oxygen vacancy ($V_O(S)$), respectively.





The fourth elementary step (R_{H24}) outlines the migration of a bulk oxygen atom to the surface vacancy creating a bulk oxygen vacancy ($V_O(B)$) which is filled by an oxygen ion from the cathode in the final elementary step (R_{H25}). The replenishment of bulk oxygen vacancy at the anode by an oxygen ion from cathode (R_{H25}) involves multiple elementary processes such as, oxygen reduction reaction at the cathode ($V_{O,cathode}^{\cdot\cdot} + \frac{1}{2}O_2(g) + 2e' \rightarrow O_{O,cathode}^{\times}$), exchange of oxygen ion from the cathode to the electrolyte ($V_{O,electrolyte}^{\cdot\cdot} + O_{O,cathode}^{\times} \rightarrow V_{O,cathode}^{\cdot\cdot} + O_{O,electrolyte}^{\times}$), and final exchange of an oxygen ion from the electrolyte to the anode ($V_{O,anode}^{\cdot\cdot} + O_{O,electrolyte}^{\times} \rightarrow V_{O,electrolyte}^{\cdot\cdot} + O_{O,anode}^{\times}$). We hold that the anode is primarily controlling SOFC performance since experimental studies observed that the introduction of Fe-Ni alloy particles to SLF anode improved the overall cell performance^{14,15}. Therefore, we assumed that the oxygen reduction at the cathode and ion migration through the electrolyte are fast and considered the bulk vacancy-mediated migration of SLF oxygen to be the limiting factor for R_{H25} . The SLF bulk oxygen diffusion barrier of 1.30 eV obtained from the bulk SLF DFT calculations is used to calculate the rate of R_{H25} .

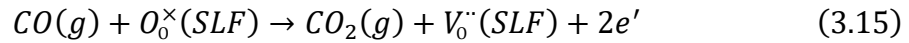
Figure 3.4 displays the free energy profiles for H_2 oxidation on the two FeO_2 -terminated surfaces calculated at SOFC operating conditions. The transition state (TS) structures are numbered with reference to the corresponding elementary reaction steps. We note here that the initial active site ($IM_{H2}1$) of both FeO_2 -LaO and FeO_2 -SrO surface models already possess a surface oxygen vacancy. Thus, dissociative adsorption of H_2

($R_{H2}1$) preferably occurs on the Fe-O site neighboring the surface vacancy forming $H_{Fe}-OH$ ($IM_{H2}2$) where the H bonded to the Fe atom sits at the vacancy site (Figure 3.3). This process is endergonic by 1.00 eV on the FeO_2-LaO surface and 1.57 eV on the FeO_2-SrO surface. However, the process is kinetically favored over FeO_2-SrO ($\Delta G^{TS1} = 1.89$ eV) by 0.71 eV compared to FeO_2-LaO ($\Delta G^{TS1} = 2.60$ eV). The H_2O formation process which involves the transfer of an H atom from Fe to the hydroxyl group ($R_{H2}2$) is both kinetically and thermodynamically favored on the FeO_2-SrO ($\Delta G^{TS2} = 2.21$ eV; $\Delta G^{IM3} = 0.05$ eV) relative to the FeO_2-LaO surface ($\Delta G^{TS2} = 2.73$ eV; $\Delta G^{IM3} = 1.18$ eV). The H_2O molecule in $*_{Fe}-OH_2$ ($IM_{H2}3$) is weakly bound to the Fe atom with Fe-O distances of 2.11 Å and 2.30 Å on the FeO_2-LaO and FeO_2-SrO surfaces, respectively. While desorption of H_2O ($R_{H2}3$) leading to the formation of surface oxygen vacancy ($IM_{H2}4$) was found to be exergonic on both surfaces, the vacancy structure on the FeO_2-SrO surface is more stable by 1.39 eV compared to FeO_2-LaO surface. Furthermore, these results suggest that the formation of a second oxygen vacancy is favorable on the FeO_2-SrO surface under SOFC operating conditions, whereas it is slightly endergonic by 0.12 eV on the FeO_2-LaO surface. Migration of an oxygen from the subsurface layer to the surface oxygen vacancy ($R_{H2}4$) generating a bulk oxygen vacancy ($IM_{H2}5$) is an exergonic process by -0.34 eV for the FeO_2-LaO surface with a kinetic barrier of only 0.35 eV, whereas it is an endergonic process by 0.32 eV for the FeO_2-SrO surface and requires a kinetic barrier as high as 1.61 eV. A similar trend was observed by Gu and Nikolla⁶¹ and in our earlier work on $(Sr,A^{3+})_{n+1}Fe_nO_{3n+1}$ -based RP oxides which revealed that the ease of formation and migration of bulk oxygen vacancy in the rocksalt layer of RP oxides depends on the oxidation state of the neighboring ion³⁵. We complete the catalytic cycle by filling this

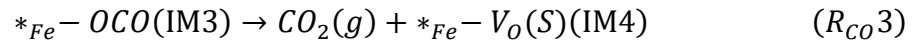
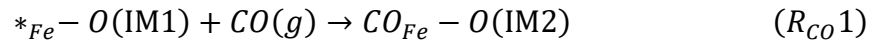
bulk oxygen vacancy using an oxide ion from the cathode ($R_{H2}5$). Overall, the free energy profiles suggest that the H_2 oxidation process could be favorable on the FeO_2 -SrO surface compared to the FeO_2 -LaO surface. The TS corresponding to the water formation process ($TS_{H2}2$) was found to be the highest energy state on the free energy profiles and could be rate-limiting for both the surfaces.

3.4.3 CO OXIDATION MECHANISM ON SLF (001) SURFACES

The overall electrochemical oxidation of CO on the SLF anodes can be expressed as:



Here again, the gas phase reaction free energy of $CO + \frac{1}{2} O_2 \rightarrow CO_2$ is calculated to be - 2.2 eV at SOFC operating conditions and thus the maximum open-circuit voltage at these conditions for the $2e'$ oxidation process is 1.1 V. Figure 3.5 illustrates our proposed catalytic cycle for the oxidation of CO at an active site $*_{Fe}-O$ on the SLF (001) surface models which includes five elementary reactions defined as $R_{CO}1$ to $R_{CO}5$. The oxidation of CO on the SLF surface forming CO_2 and a surface oxygen vacancy can be described in the first 3 elementary reactions which involve adsorption of CO on the Fe metal site ($R_{CO}1$), migration of CO to the neighboring oxygen forming CO_2 ($R_{CO}2$), and desorption of CO_2 leaving a surface vacancy ($R_{CO}3$).



The surface vacancy structure $*_{Fe}-V_O(S)(IM4)$ formed after CO_2 desorption is the same vacancy structure obtained in the H_2 oxidation process and thus the last two steps $R_{CO4} - R_{CO5}$ are equivalent to the elementary reactions $R_{H24} - R_{H25}$.

Figure 3.6 displays the free energy profiles calculated for the CO oxidation process on the two FeO_2 -terminated surfaces at SOFC operating conditions. CO interacts weakly with the two Fe atoms next to the native surface oxygen vacancy site (R_{CO1}) with average Fe-C bond distances of 2.32 and 2.27 Å on the FeO_2 -LaO and FeO_2 -SrO surfaces, respectively. The adsorption process is endergonic on both surfaces with ΔG ranging from 1.73 eV (FeO_2 -LaO) to 1.97 eV (FeO_2 -SrO). As observed in the case of H_2 oxidation process (Figure 3.4), the CO_2 formation (R_{CO2}) and desorption (R_{CO3}) processes are also thermodynamically more favorable on FeO_2 -SrO surface compared to the FeO_2 -LaO surface. The activation free energy of CO_2 formation (TS_{CO2}) is 0.10 eV lower for the FeO_2 -SrO surface relative to the FeO_2 -LaO surface. Considering that TS_{CO2} is the highest energy state on the free energy profile for both surfaces, these results suggest that the FeO_2 -SrO surface could be more active for CO oxidation compared to the FeO_2 -LaO surface.

3.4.4 INSIGHTS FROM MICROKINETIC MODELING AND ANODE BIASING

The forward rate and equilibrium constants of each elementary step of H_2 and CO oxidation reactions calculated from the DFT+U reaction energies and activation barriers for the FeO_2 -LaO and FeO_2 -SrO surfaces are summarized in Table 3.1. These data are used to build a microkinetic model to obtain further information on the relative rates, apparent activation barriers, and rate controlling factors for these surfaces. Since the fuel oxidation occurring in SOFCs also involves charge transfer processes, we adapted two

types of microkinetic models that correspond to short circuit conditions and anode biasing. While the short circuit condition is equivalent to a thermochemical process, the anode biasing incorporates charge transfer effects. The results obtained from microkinetic analysis at short circuit conditions are summarized in Table 3.2. In accordance with the free energy profiles, the microkinetic analysis also revealed a three orders of magnitude higher turnover-frequency (TOF) and a 0.61 eV lower apparent activation energy for H₂ oxidation over FeO₂-SrO relative to the FeO₂-LaO surface. Campbell's degree of rate control analysis furthermore suggested that the H₂O formation process (R_{H_2O} , DRC = 0.92) is mainly rate-controlling for the FeO₂-SrO surface, whereas H₂ dissociation (R_{H_2} , DRC = 0.22) also controls the overall rate to a small extent in the case of FeO₂-LaO surface. Nonetheless, surface water formation (R_{H_2O}) appears to be the key step to improve the performance of SLF-based anodes under thermochemical conditions. The higher TOFs and lower apparent activation energy predicted for the FeO₂-SrO surface indicates that this surface controls H₂ oxidation activity at all temperatures considered here under short circuit conditions.

In the case of CO oxidation, FeO₂-SrO surface displays a higher TOF than the FeO₂-LaO surface by a factor of three. For both surfaces, the DRC analysis (Table 3.2) indicates that the TOFs are entirely controlled by the formation of surface carbon dioxide (R_{CO_2}) and the free energy diagram (Figure 3.6) revealed that TS_{CO_2} for FeO₂-LaO has a 0.10 eV higher free energy compared to that of FeO₂-SrO. Thus, the FeO₂-SrO surface exhibits a slightly higher TOF and lower apparent activation energy than the FeO₂-LaO surface. The apparent activation energies calculated for the CO oxidation process are lower by 0.76 and 0.33 eV than the ones calculated for H₂ oxidation process over FeO₂-

LaO and FeO₂-SrO surfaces, respectively. However, the calculated short circuit TOF for the H₂ oxidation process on the FeO₂-SrO surface at a temperature of 1073 K is an order of magnitude higher than the TOFs predicted for CO oxidation process over both surfaces.

Next, the effect of anode potential bias on the fuel oxidation process is examined for H₂, CO, and syngas fuels since a potential bias can alter the reaction free energies and activation barriers of elementary reactions that involve a charge transfer process. Here, we followed a similar methodology used in our earlier work on the SFMO double perovskite²⁴. As described earlier, the open-circuit potential (OCP) for H₂ and CO oxidation reactions are calculated as 1.1 V and we specify this value as our reference potential for the cathode. The possibilities of 0, 1, or 2 e⁻ charge transfer for a given elementary step are included in the microkinetic model. The free energies of elementary steps that involve charge transfer are shifted by the amount of charge multiplied by the cell voltage (ΔV) and these corrections to the free energy of reaction (ΔG_i^{rxn}) and activation barrier (ΔG_i^\ddagger) are incorporated using the following expressions:

$$\Delta G_i^{rxn}(\Delta V) = \Delta G_i^{rxn}(\Delta V = 0) + n_j F V \quad (3.16)$$

$$\Delta G_i^\ddagger(\Delta V) = \Delta G_i^\ddagger(\Delta V = 0) + n_j F \beta V \quad (3.17)$$

where n_j refers to the number of electrons transferred in the elementary charge transfer step, F is the Faraday's constant, β refers to the symmetry factor of the elementary step, and ΔV is the cell potential in volts *i.e.*, cathode reference potential subtracted by anode potential such that $\Delta V = 0$ refers to the short circuit condition. Two possible values for the symmetry factor, $\beta = 0$ and $\beta = 0.5$ were used in the present study to describe fast charge transfer and charge transfer that occurs during a reaction step experiencing a solid

phase interfacial potential, respectively⁶³. Greater details on our anode biasing methodology for H₂, CO, and syngas oxidation reactions are outlined in Section B.4 of the Appendix B. The elementary steps involved in this extended microkinetic model and the calculated rates for H₂ and CO electro-oxidation reactions at a representative cell voltage of 0.7 V are presented in Tables B.1 and B.2 of Appendix B. In the presence of syngas fuel, both H₂ and CO electro-oxidation reactions can occur together with the thermochemical water-gas shift (WGS) reaction as shown in Figure 3.7. In the case of H₂ oxidation, the elementary reaction rates calculated with $\beta = 0$ suggest that the possibilities of two-electron charge transfer during $R_{H_2 2}$ or $R_{H_2 3}$, and two one-electron charge transfers during $R_{H_2 2}$ and $R_{H_2 3}$ are all equally favorable on both surface models. However, the two-electron charge transfer during H₂O desorption process ($R_{H_2 3}$) is found to be more favorable compared to other possible charge transfer possibilities when β value is increased to 0.5. Similarly, the possibility of two-electron charge transfer during CO₂ desorption process ($R_{CO 3}$) is found to be more favorable with $\beta = 0.5$, whereas multiple possibilities of charge transfer became equally favorable when $\beta = 0$ is used in the microkinetic model. While the overall TOFs calculated for the H₂ oxidation process at a cell voltage of 0.7 V ($\beta = 0.5$) are decreased relative to short circuit conditions, the trends observed between the two SLF surfaces are similar to short circuit conditions. For example, the calculated TOFs for H₂ and CO oxidation processes over the FeO₂-LaO surface at $\Delta V = 0.7$ V are lower than the FeO₂-SrO surface for both β values. To visualize any changes in activity trends observed in the presence of anode bias potentials, we calculated the current densities at different cell voltages.

The current density (i in Acm^{-2}) for a specific oxidation process is calculated using the relation, $i = zer\Gamma$, where z is the number of electron(s) involved in the reaction, r represents the calculated overall reaction rate or TOF (s^{-1}), and Γ is the number of active sites per surface area (cm^{-2}). The number of active sites per surface is set as the inverse of the surface area of our SLF models ($1.39 \times 10^{-18} \text{ m}^2$) for all fuels (e.g., one active site per surface model). The simulated polarization curves that reflect the kinetic relationship between the cell voltage and current density ($\beta = 0.5$) for H_2 , CO, and syngas oxidation processes are displayed in Figure 3.8. It is to be noted here that this simulation does not incorporate mesoscale and macroscale effects such as molecular and pore diffusion effects and does not incorporate explicit cathodic kinetics. While the omission of ohmic loss and mass transfer limitations in our model could be somewhat justified because of high temperatures used in SOFC cells, these factors could affect the cell performance at relevant operating conditions and a quantitative prediction of experimental cell behavior cannot be obtained from this analysis. Nonetheless, this analysis is aimed at understanding the relative activity of different surfaces for different fuel oxidation processes and how the potential bias affects the activity and rate-limiting process of these surfaces. The polarization curves calculated for H_2 oxidation (Figure 3.8(a)) predicted higher current densities for the $\text{FeO}_2\text{-SrO}$ surface than the $\text{FeO}_2\text{-LaO}$ surface at all cell voltages which is consistent with the TOFs and apparent activation barriers predicted at short circuit conditions (Table 3.2). At a cell voltage of 0.7 V, the current densities for H_2 oxidation on the $\text{FeO}_2\text{-SrO}$ surface are calculated as 0.27 ($\beta = 0$) and 0.11 ($\beta = 0.5$) A/cm^2 which are in the same order of magnitude reported by experimental studies ($\sim 0.72 \text{ A/cm}^2$)¹⁴. Since the TOFs and apparent activation barriers calculated for CO oxidation at

short circuit conditions are close for both surfaces, the current densities calculated for the FeO₂-LaO surface are also in the same order of magnitude with the FeO₂-SrO surface at cell voltages below 0.5 V (Figure 3.8(b)). However, 2-4 orders of magnitude higher current densities were observed for the FeO₂-SrO surface compared to the FeO₂-LaO surface at higher cell voltage conditions suggesting that there could be a change in rate-limiting process for CO oxidation between low and high voltage conditions. Figures 3.8(c-d) depict the syngas oxidation polarization curves for different ratios of syngas on the two FeO₂-terminated surfaces. The syngas oxidation mechanism incorporates all elementary steps from both H₂ and CO oxidation reactions which implies the existence of a water-gas shift (WGS) thermochemical mechanism in addition to the electro-oxidation processes, as illustrated in Figure 3.7. The rates calculated for individual reactions, such as H₂ electro-oxidation, CO electro-oxidation, and WGS for different ratios of H₂:CO at a cell voltage of 0.7 V are summarized in Table B.3 of Appendix B. On the FeO₂-LaO surface, the rates calculated for the CO electro-oxidation and WGS (producing H₂ and CO₂) are very similar and reverse H₂ electro-oxidation was observed for all ratios of H₂:CO. Since this surface is more active for CO electro-oxidation, the overall activity increases with increasing concentration of CO. H₂ electro-oxidation was found to be an order of magnitude higher than CO oxidation on the FeO₂-SrO surface at different H₂:CO ratios which further promotes reverse WGS (producing H₂O and CO). Here, the overall activity increases with increasing concentration of H₂. The reverse WGS rates on FeO₂-SrO are higher than WGS rates of FeO₂-LaO for all H₂:CO ratios. The simulated polarization curves for the FeO₂-LaO surface (Figure 3.8(c)) display that the current density increases with increasing concentration of CO at low cell voltages since this

surface exhibits higher activity towards CO oxidation at short circuit conditions. At cell voltages above 0.6 V, slightly higher current densities were observed for the syngas mixtures compared to pure H₂ or CO fuels for the FeO₂-LaO surface. On the FeO₂-SrO surface (Figure 3.8(d)), the current density increases with increasing concentration of H₂ at all cell voltages since H₂ electro-oxidation was found to be more favorable on this surface than CO electro-oxidation (Figures 3.7(a-b)). The calculated current densities for syngas (50% H₂ + 50% CO) oxidation on the FeO₂-SrO surface at a cell voltage of 0.7 V (0.09 ($\beta = 0$) and 0.04 ($\beta = 0.5$) A/cm²) are an order of magnitude lower than the experimental value (~ 0.27 A/cm²)¹⁴. Overall, the electrochemical activity of SLF anodes in the presence of syngas fuel seems to originate mainly from the H₂ electro-oxidation over the FeO₂-SrO surface and CO₂ is chemically reduced to CO via WGS which also produces H₂O.

To understand the polarization behavior of SLF anodes for the H₂ and CO electro-oxidation processes, we calculated the degree of rate control with respect to cell potential as displayed in Figure 3.9. The overall rates and degrees of rate control are summarized at a representative cell voltage of 0.7 V in Table B.4 of Appendix B. In accordance with the short-circuit analysis, the H₂O formation process ($R_{H_2 2}$) is mainly rate-limiting for H₂ oxidation at cell voltages < 0.8 V for both surfaces, whereas the bulk oxygen migration process ($R_{H_2 5}$) becomes dominantly rate-controlling at higher cell voltage conditions (Figures 3.9(a-b)). This change in rate-limiting step is reflected in the logarithmic polarization curves presented in Figure 3.8(a) for the H₂ electro-oxidation. Since our analysis with $\beta = 0.5$ suggested that the charge transfer occurs only in $R_{H_2 3}$ which involves H₂O desorption and surface vacancy formation, the current density did

not change much with the cell potential where R_{H_2} is rate-limiting in the regime of $\Delta V < 0.8$ V. Logarithmic changes in current density with high cell potentials are observed in the regime of $\Delta V > 0.8$ V where the rate-limiting oxide migration process occurs after the charge transfer process. Similarly, the rate-controlling process changes from CO_2 formation (R_{CO_2}) at low cell voltages (< 0.6 V) to bulk oxygen migration (R_{CO_5}) at $\Delta V > 0.6$ V for CO electro-oxidation on the FeO_2 -LaO surface (Figure 3.9(c)), whereas such change in the rate-limiting process is observed only above 0.9 V for the FeO_2 -SrO surface (Figure 3.9(d)). This trend is reflected in the polarization curves in Figure 3.8(b) where logarithmic current density is observed above 0.6 V for the FeO_2 -LaO surface and the current density remains nearly constant until 0.9 V for the FeO_2 -SrO surface. This is again consistent with the rate-limiting processes occurring before and after the charge transfer process (R_{CO_3}) in these different regimes. These results suggest that the overall performance of SLF anodes can be improved by identifying ways to reduce the surface H_2O/CO_2 formation and bulk oxygen diffusion barriers. For example, bulk SLF doping could decrease vacancy-mediated transport barriers and exsolvation strategies could decrease reactions barriers for key oxidation elementary steps and increase the anode electronic conductivity.

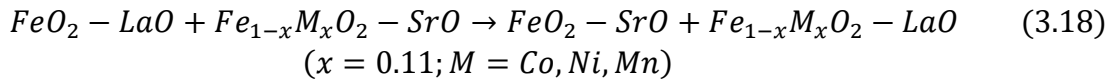
3.4.5 EFFECT OF B-SITE DOPING ON THE SLF OXIDATION ACTIVITY

Substitutional dopants are commonly used to improve the performance of MIEC materials since dopants can alter the electronic, ionic, and catalytic properties of the parent material. Here, we conducted a preliminary analysis of the effects of substitutional doping of the SLF surface models on the H_2 oxidation activity by replacing a surface Fe atom (active site Fe atom, $*_{Fe}-O$) by various dopants such as Co, Ni, and Mn. Our

microkinetic analysis for the non-doped SLF surface models predicted that the H₂O formation process is mainly rate-controlling at short circuit and low voltage conditions for H₂ oxidation, whereas the bulk oxide migration becomes rate-controlling at high voltage conditions. While substitutional doping of bulk SLF can improve the bulk oxygen diffusion barrier by increasing the concentration of vacancy defects^{35,64}, a careful analysis is necessary to identify appropriate dopant elements and effective doping ratios as well as elucidation of the diffusion mechanism which are all beyond the scope of this study. Here, we focused on strategies to modulate surface H₂O formation activity that could improve the H₂ oxidation activity of SLF materials at low cell voltage conditions.

The free energies of the TSs corresponding to H₂ dissociation ($TS_{H_2 1}$) and H₂O formation process ($TS_{H_2 2}$) together with the TOFs calculated at short circuit conditions for the two doped surface models, Fe_{1-x}M_xO₂-LaO and Fe_{1-x}M_xO₂-SrO ($x=0.11$; M = Fe, Co, Ni, Mn) are presented in Table 3.3 and the corresponding free energy diagrams are illustrated in Figures B.2 and B.3 of Appendix B. In the case of the Fe_{1-x}M_xO₂-LaO surface, our calculations indicate that the rate-controlling $TS_{H_2 2}$ is stabilized in the presence of dopants and consequently, the TOFs increase relative to the non-doped FeO₂-LaO surface. This indicates that Fe-site doping is a prudent strategy to improve the overall activity of SLF by making the FeO₂-LaO surface more viable for H₂ oxidation. Among the dopants considered here, Co displays the lowest free energy pathway for H₂ oxidation (Figure B.2 in Appendix B) and the TOFs calculated for these dopants are 3 orders of magnitude higher than the non-doped FeO₂-LaO surface and are in the same order of magnitude calculated for the non-doped FeO₂-SrO surface. For the Fe_{1-x}M_xO₂-SrO surface (Figure B.3 in Appendix B), dopants exhibited lower TOFs compared to the

non-doped FeO₂-SrO surface (Table 3.3). This trend indicates a change in rate-controlling step for the FeO₂-SrO surface in the presence of dopants. The free energy profiles presented in Figure B.3 reveal that the TSs corresponding to H₂ dissociation ($TS_{H_2}1$) are higher in energy compared to $TS_{H_2}2$ for all the dopants and the surface vacancy structures ($*_M - V_O(S)$, $IM_{H_2}4$) are significantly stabilized compared to FeO₂-SrO. Thus, our microkinetic model predicted a high surface coverage of $IM_{H_2}4$ for all the dopants (> 99% for Co). Consequently, rate-control analysis indicated that greater than 90% of the rate is controlled by bulk oxide migration ($R_{H_2}5$) process for all the dopants considered here. The highly stable surface vacancy structures observed for the doped Fe_{1-x}M_xO₂-SrO surface models further suggest that the catalytic cycle for fuel oxidation over these surfaces could involve multiple oxygen vacancies which is not considered in our preliminary analysis. Despite this limitation, we examined the thermodynamic favorability of doping for both surface models with the following equation.

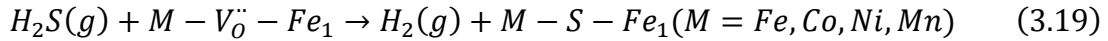


Co, Ni, and Mn display a reaction free energy (ΔG^{rxn}) of -0.77, -0.23, and -0.49, respectively suggesting that a combined presence of doped FeO₂-LaO surface with non-doped FeO₂-SrO surface is thermodynamically more favorable. Hence, the activity of SLF anodes is increased in the presence of all dopants as the more active doped FeO₂-LaO surfaces coexist with the highly active FeO₂-SrO surface. This combined effect increases the net number of active sites for doped SLF anodes, especially for the Co dopant. Overall, this analysis suggests that the H₂ oxidation activity of the FeO₂-LaO surfaces could be improved by doping with Co, Mn, and Ni. The activity of the FeO₂-SrO surface is decreased with dopant introduction due to a change in the rate-determining step

and a high driving force for the formation of surface vacancies. Among the three dopants, Co could yield the best performance.

3.4.6 EFFECT OF SULFUR POISONING ON THE ACTIVITY OF SLF

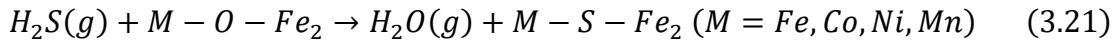
The experimental literature indicated that the SLF-based anodes exhibit high tolerance to sulfur and the fuel oxidation activity does not diminish in the presence of H₂S^{14,15}. In this work, we used constrained *ab initio* thermodynamics analysis to investigate the sulfur poisoning mechanism of doped and non-doped SLF surface models under SOFC operating conditions with the aim of understanding the limits of sulfur stability on these materials. As proposed earlier by Walker et al. for the SFMO material²⁸, two different mechanisms were considered for the interaction of sulfur with the SLF surfaces, namely, dissociative adsorption of H₂S on the SLF surface, and replacement of surface oxygen by sulfur (Figure 3.10). The H₂S dissociative adsorption reaction can be described as



The corresponding dissociative adsorption reaction free energy (ΔG^{ads}) is calculated by the following expression,

$$\Delta G^{ads} = (E_{H_2}^{DFT} + \mu_{H_2}) + G_{M-S-Fe_1}^{DFT+U} - (E_{H_2S}^{DFT} + \mu_{H_2S}) - G_{M-V_O^{\bullet\bullet}-Fe_1}^{DFT+U} \quad (3.20)$$

The oxide replacement reaction is described as



and the corresponding replacement reaction free energy (ΔG^{repl}) is calculated by the following expression,

$$\Delta G^{repl} = (E_{H_2O}^{DFT} + \mu_{H_2O}) + G_{M-S-Fe_2}^{DFT+U} - (E_{H_2S}^{DFT} + \mu_{H_2S}) - G_{M-O-Fe_2}^{DFT+U} \quad (3.22)$$

Fe_1 refers to the surface Fe atom that is directly connected to the oxygen vacancy where sulfur is adsorbed and Fe_2 is bonded to the surface oxygen that is replaced by sulfur (Figure 3.10). While both mechanisms produce surface sulfur, these sulfur atoms can have different effects on the proposed catalytic cycles of H_2 and CO oxidation. The dissociative adsorption process fills the native surface $V_O^{\bullet\bullet}$ with sulfur blocking the adsorption site for H_2 and CO, whereas the oxygen replacement mechanism replaces one of the neighboring surface oxygens that is involved in the formation of surface H_2O and CO_2 ; thus, this mechanism could affect the kinetic barriers for these reactions.

The free energies of sulfur adsorption and oxide replacement reactions (Table 3.4) calculated with a H_2S concentration of 50 ppm¹⁴ suggest that the sulfur adsorption process is in general less favorable than the oxide replacement process for all the dopants on the two surface models. While the oxide replacement reaction is still highly unfavorable on the non-doped FeO_2 -LaO surface ($\Delta G^{rep1} = 1.09$ eV), this reaction is endergonic only by 0.16 eV on FeO_2 -SrO surface. Further calculations indicate that the accumulation of sulfur on the FeO_2 -SrO surface via oxide replacement reaction is possible when the H_2S concentration increases above 290 ppm at a temperature of 1073 K. However, this amount is much larger than the H_2S concentration that normally poisons Ni/YSZ (< 15 ppm)⁴ suggesting that the SLF anodes are less susceptible for sulfur poisoning at concentrations of H_2S practical to SOFC conditions.

The free energies of the oxide replacement reaction on the FeO_2 -LaO surface decrease in the presence of dopants and the least stable dopants were Co and Ni which are nearly in equilibrium with a ΔG^{rep1} of 0.01 and -0.08 eV, respectively. On the other hand, the introduction of dopants on the FeO_2 -SrO surface increase the free energies of

oxide replacement reaction except for Mn for which an exergonic ΔG^{repl} of -0.15 eV was predicted by our calculations. As discussed earlier in Section 3.5, substitutional doping of Co and Ni on the FeO₂-LaO surface increases the TOFs for H₂ oxidation on this surface (Table 3.3); however, one of the active oxygen atoms involved in surface water formation could be replaced by sulfur when the H₂S concentration in the fuel becomes higher than 56 and 20 ppm, respectively. This could have a negative impact on the oxidation activity. Mn increases the TOF for H₂ oxidation on the FeO₂-LaO surface and displays resistance to oxide replacement with sulfur for H₂S concentrations below 1.7×10^5 ppm. In the case of FeO₂-SrO surface, the oxide replacement reaction on the Mn-doped surface becomes feasible when the H₂S concentration is > 10 ppm at 1073 K suggesting that Mn doping has negative effect on sulfur resistance on the more active surface. An overall comparison of H₂ oxidation TOFs (Table 3.3) and free energies of sulfur poisoning mechanisms (Table 3.4) reveals that doping with Co could improve activity on FeO₂-LaO surface, maintain adequate performance on the FeO₂-SrO surface, and displays sulfur resistance above the Ni/YSZ instability H₂S concentrations.

3.5 CONCLUSIONS

The activity of SLF based anode materials in the presence of H₂, CO, and syngas fuels was investigated using DFT + *U* theory and microkinetic modeling techniques. We constructed two representative FeO₂-terminated SLF (001) surface models with different underlying rocksalt (LaO and SrO) layers to examine the catalytic activity under anodic SOFC conditions. Microkinetic analysis performed under short circuit conditions indicated that the FeO₂-SrO surface is more active for both H₂ and CO oxidation. In the presence of anode bias potential, a similar trend was observed at all cell voltage

conditions. However, the CO oxidation activity of the FeO₂-SrO surface shifts from logarithmic scaling below cell voltages of 0.8 V such that the FeO₂-LaO surface activity only differs from the FeO₂-SrO activity by a factor of three at short circuit conditions. Kinetic rate control analysis revealed that the key rate-limiting step changes from surface H₂O/CO₂ formation at low cell voltage conditions to bulk oxygen migration at high voltage conditions for these oxidation processes on both surface models. The CO electro-oxidation activity of SLF surfaces is found to be 1-2 orders of magnitude lower than the H₂ electro-oxidation activity. Syngas oxidation incorporates elementary steps from both H₂ and CO electro-oxidation reactions implying the existence of the thermochemical WGS reaction. For the active FeO₂-SrO surface, syngas oxidation derives its current density from H₂ oxidation and CO₂ is thermochemically reduced to CO via reverse WGS.

Next, we conducted a preliminary analysis of the introduction of surface B-site dopants on the SLF surface models to understand the effect of dopants on the H₂ oxidation activity at short circuit conditions. The free energy of rate-limiting H₂O formation TS on the FeO₂-LaO surface decreased and consequently, an increase in TOF was observed for all dopants. For the Co dopant, it exhibited 3 orders of magnitude higher TOF than the non-doped surface. While a similar trend in the free energy of H₂O formation TS was observed on the FeO₂-SrO surface with the introduction of dopants, the calculated TOFs for the doped surfaces were found to be lower than the non-doped surface. Since doping significantly stabilizes the surface vacancy structure on the FeO₂-SrO surface, the oxidation reaction was found to be rate-controlled by bulk oxygen diffusion rather than the surface H₂O formation process. A thermodynamic analysis of surface dopant formation indicates the favorability of more active doped FeO₂-LaO

surfaces coexisting with the highly active non-doped FeO₂-SrO surface such that the number of active sites is increased in the presence of dopants. Lastly, we analyzed the sulfur poisoning mechanism of SLF surface models by examining the dissociative adsorption of H₂S and the replacement of surface oxygen by sulfur. The dissociative adsorption of H₂S reaction was found to be endergonic under SOFC operating conditions in the presence of 50 ppm of H₂S for all the doped and non-doped SLF surfaces which is consistent with the sulfur tolerance observed by experimental studies. In the cases of Fe_{1-x}M_xO₂-LaO (x = 0.11; M = Co and Ni) and Fe_{1-x}Mn_xO₂-SrO (x = 0.11) surfaces, lower free energies (-0.2 to 0.1 eV) calculated for the oxide replacement reactions suggest that the oxidation activity of these surfaces could be affected in the presence of slightly higher H₂S concentrations. Overall, SLF anodes exhibit reasonably good activity and sulfur resistance in the presence of H₂, CO, and syngas fuels and Co doping on the SLF surfaces seems to improve and/or maintain the catalytic activity of SLF while maintaining sulfur tolerance. Future work will focus on the effect of B-site doping on the bulk oxygen diffusion barrier to help the design of SLF based materials for direct use in SOFCs. Lastly, SLF-based anodes could have an impact on future hydrogen storage applications as an electrolysis material for H₂ generation or for energy generation in direct hydrocarbon fuel cells under sulfur-containing conditions with the help of prudent doping strategies as determined by experimental and ab initio studies.

3.6 ACKNOWLEDGMENTS

This work was supported by the National Science Foundation under Grant No. DMR- 1832809 and partially supported by the South Carolina Smart State Center for Strategic Approaches to the Generation of Electricity (SAGE). Computing resources are

provided by the U.S. Department of Energy facility located at National Energy Research Scientific Computing Center (NERSC) under Contract No. DE-AC02-05CH11231 and ACCESS facilities located at Texas Advanced Computing Center (TACC), San Diego Supercomputer Center (SDSC), and Purdue University (grant no. TG-CTS090100). Finally, computing resources provided by the University of South Carolina's High Performance Computing (HPC) group are gratefully acknowledged.

3.7 BIBLIOGRAPHY

- (1) Steele, B. C. H.; Heinzl, A. Materials for Fuel-Cell Technologies. *Nature*, **2001**, *414*, 345–352. 10.1038/35104620.
- (2) McIntosh, S.; Gorte, R. J. Direct Hydrocarbon Solid Oxide Fuel Cells. *Chem Rev.*, **2004**, *104* (10), 4845–4865. 10.1021/cr020725g.
- (3) Wachsman, E. D.; Lee, K. T. Lowering the Temperature of Solid Oxide Fuel Cells. *Science*, **2011**, *334* (6058), 935–939. 10.1126/science.1204090.
- (4) Shri Prakash, B.; Senthil Kumar, S.; Aruna, S. T. Properties and Development of Ni/YSZ as an Anode Material in Solid Oxide Fuel Cell: A Review. *Renew. and Sustain. Energy Rev.*, **2014**, *36*, 149–179. 10.1016/j.rser.2014.04.043.
- (5) Fallah Vostakola, M.; Amini Horri, B. Progress in Material Development for Low-Temperature Solid Oxide Fuel Cells: A Review. *Energies*, **2021**, *14* (5), 1280. 10.3390/en14051280.
- (6) Tao, S.; Irvine, J. T. S. A Redox-Stable Efficient Anode for Solid-Oxide Fuel Cells. *Nat. Mater.*, **2003**, *2* (5), 320–323. 10.1038/nmat871.
- (7) Liu, Q.; Yang, C.; Dong, X.; Chen, F. Perovskite $\text{Sr}_2\text{Fe}_{1.5}\text{Mo}_{0.5}\text{O}_{6-\delta}$ as Electrode Materials for Symmetrical Solid Oxide Electrolysis Cells. *Int. J. Hydrog. Energy*, **2010**, *35* (19), 10039–10044. 10.1016/j.ijhydene.2010.08.016.
- (8) Liu, Q.; Dong, X.; Xiao, G.; Zhao, F.; Chen, F. A Novel Electrode Material for Symmetrical SOFCs. *Adv. Mater.*, **2010**, *22* (48), 5478–5482. 10.1002/adma.201001044.

- (9) Ruddlesden, S. N.; Popper, P. New Compounds of the K_2NiF_4 Type. *Acta Crystallogr.*, **1957**, *10*, 538–539. 10.1107/s0365110x57001929.
- (10) Takeguchi, T.; Yamanaka, T.; Takahashi, H.; Watanabe, H.; Kuroki, T.; Nakanishi, H.; Oriyasa, Y.; Uchimoto, Y.; Takano, H.; Ohguri, N.; Matsuda, M.; Murota, T.; Uosaki, K.; Ueda, W. Layered Perovskite Oxide: A Reversible Air Electrode for Oxygen Evolution/Reduction in Rechargeable Metal-Air Batteries. *J. Am. Chem. Soc.*, **2013**, *135* (30), 11125–11130. 10.1021/ja403476v.
- (11) Zhao, H.; Mauvy, F.; Lalanne, C.; Bassat, J.; Fourcade, S.; Grenier, J. New Cathode Materials for ITSOFC: Phase Stability, Oxygen Exchange and Cathode Properties of $La_{2-x}NiO_{4+\delta}$. *Solid State Ion.*, **2008**, *179* (35–36), 2000–2005. 10.1016/j.ssi.2008.06.019.
- (12) Cao, Y.; Liang, J.; Li, X.; Yue, L.; Liu, Q.; Lu, S.; Asiri, A. M.; Hu, J.; Luo, Y.; Sun, X. Recent Advances in Perovskite Oxides as Electrode Materials for Supercapacitors. *Chem. Commun.*, **2021**, *57*, 2343–2355. 10.1039/d0cc07970g.
- (13) Li, X.; Zhao, H.; Liang, J.; Luo, Y.; Chen, G.; Shi, X.; Lu, S.; Gao, S.; Hu, J.; Liu, Q.; Sun, X. A-Site Perovskite Oxides: An Emerging Functional Material for Electrocatalysis and Photocatalysis. *J. Mater. Chem. A*, **2021**, *9*, 6650–6670. 10.1039/d0ta09756j.
- (14) Xu, L.; Yin, Y.-M.; Zhou, N.; Wang, Z.; Ma, Z.-F. Sulfur Tolerant Redox Stable Layered Perovskite $SrLaFeO_{4-\delta}$ as Anode for Solid Oxide Fuel Cells. *Electrochem. Commun.*, **2017**, *76*, 51–54. 10.1016/j.elecom.2017.01.017.
- (15) Wang, Z.; Yin, Y.-M.; Yu, Y.; Song, Y.; Ma, Z.-F.; Yin, J. Roles of Fe Ni Nanoparticles and $SrLaFeO_4$ Substrate in the Performance and Reliability of a Composite Anode Prepared through In-Situ Exsolution for Intermediate Temperature Solid Oxide Fuel Cells (I). *Int. J. Hydrog. Energy*, **2018**, *43* (22), 10440–10447. 10.1016/j.ijhydene.2018.04.090.
- (16) Wu, N.; Wang, W.; Zhong, Y.; Yang, G.; Qu, J.; Shao, Z. Nickel-Iron Alloy Nanoparticle-Decorated K_2NiF_4 -Type Oxide as an Efficient and Sulfur-Tolerant Anode for Solid Oxide Fuel Cells. *ChemElectroChem*, **2017**, *4* (9), 2378–2384. 10.1002/celec.201700211.
- (17) Chang, H.; Chen, H.; Shao, Z.; Shi, J.; Bai, J.; Li, S.-D. In Situ Fabrication of $(Sr,La)FeO_4$ with CoFe Alloy Nanoparticles as an Independent Catalyst Layer for

- Direct Methane-Based Solid Oxide Fuel Cells with a Nickel Cermet Anode. *J. Mater. Chem. A*, **2016**, *4* (36), 13997–14007. 10.1039/C6TA04639H.
- (18) Park, S.; Han, H.; Choi, J.; Lee, S.; Park, M.; Kim, W. B. Ruddlesden–Popper Oxide $(\text{La}_{0.6}\text{Sr}_{0.4})_2(\text{Co,Fe})\text{O}_4$ with Exsolved CoFe Nanoparticles for a Solid Oxide Fuel Cell Anode Catalyst. *Energy Technol.*, **2021**, *9* (7), 2100116. 10.1002/ente.202100116.
- (19) Li, H.; Song, Y.; Xu, M.; Wang, W.; Ran, R.; Zhou, W.; Shao, Z. Exsolved Alloy Nanoparticles Decorated Ruddlesden–Popper Perovskite as Sulfur-Tolerant Anodes for Solid Oxide Fuel Cells. *Energy Fuels*, **2020**, *34* (9), 11449–11457. 10.1021/acs.energyfuels.0c02228.
- (20) Chung, Y. S.; Kim, T.; Shin, T. H.; Yoon, H.; Park, S.; Sammes, N. M.; Kim, W. B.; Chung, J. S. In Situ Preparation of a $\text{La}_{1.2}\text{Sr}_{0.8}\text{Mn}_{0.4}\text{Fe}_{0.6}\text{O}_4$ Ruddlesden–Popper Phase with Exsolved Fe Nanoparticles as an Anode for SOFCs. *J. Mater. Chem. A*, **2017**, *5* (14), 6437–6446. 10.1039/c6ta09692a.
- (21) Tan, W.; Huan, D.; Yang, W.; Shi, N.; Wang, W.; Peng, R.; Wu, X.; Lu, Y. A First-Principles Study on Divergent Reactions of Using a $\text{Sr}_3\text{Fe}_2\text{O}_7$ Cathode in Both Oxygen Ion Conducting and Proton Conducting Solid Oxide Fuel Cells. *RSC Adv.* **2018**, *8* (47), 26448–26460. 10.1039/C8RA04059A.
- (22) Zhou, J.; Chen, G.; Wu, K.; Cheng, Y. Interaction of La_2NiO_4 (100) Surface with Oxygen Molecule: A First-Principles Study. *J. Phys. Chem. C*, **2013**, *117* (25), 12991–12999. 10.1021/jp403094x.
- (23) Akbay, T.; Staykov, A.; Druce, J.; Téllez, H.; Ishihara, T.; Kilner, J. A. The Interaction of Molecular Oxygen on LaO Terminated Surfaces of La_2NiO_4 . *J. Mater. Chem. A*, **2016**, *4* (34), 13113–13124. 10.1039/C6TA02715F.
- (24) Suthirakun, S.; Ammal, S. C.; Muñoz-García, A. B.; Xiao, G.; Chen, F.; zur Loye, H.-C.; Carter, E. A.; Heyden, A. Theoretical Investigation of H_2 Oxidation on the $\text{Sr}_2\text{Fe}_{1.5}\text{Mo}_{0.5}\text{O}_6$ (001) Perovskite Surface under Anodic Solid Oxide Fuel Cell Conditions. *J. Am. Chem. Soc.*, **2014**, *136* (23), 8374–8386. 10.1021/ja502629j.
- (25) Han, Z.; Dong, H.; Wu, Y.; Yang, Y. Locating the Rate-Limiting Step of Hydrogen Conversion on $\text{Sr}_2\text{Fe}_{1.5}\text{Mo}_{0.5}\text{O}_6$ (001) Surface: Implications for Efficient SOFC Anode Design. *Appl. Surf. Sci.*, **2022**, *595*, 153513. 10.1016/j.apsusc.2022.153513.

- (26) Ren, B.; Croiset, E.; Ricardez-Sandoval, L. A Theoretical Study on CO₂ Electrolysis through Synergistic Manipulation of Ni/Mn Doping and Oxygen Vacancies in La(Sr)FeO₃. *J. Catal.*, **2020**, *383*, 273–282. 10.1016/j.jcat.2020.01.033.
- (27) Ammal, S. C.; Heyden, A. Reaction Kinetics of the Electrochemical Oxidation of CO and Syngas Fuels on a Sr₂Fe_{1.5}Mo_{0.5}O_{6-δ} Perovskite Anode. *J. Mater. Chem. A.*, **2015**, *3* (43), 21618–21629. 10.1039/C5TA05056A.
- (28) Walker, E.; Ammal, S. C.; Suthirakun, S.; Chen, F.; Terejanu, G. A.; Heyden, A. Mechanism of Sulfur Poisoning of Sr₂Fe_{1.5}Mo_{0.5}O_{6-δ} Perovskite Anode under Solid Oxide Fuel Cell Conditions. *J. Phys. Chem. C*, **2014**, *118* (41), 23545–23552. 10.1021/jp507593k.
- (29) Kresse, G.; Furthmüller, J. Efficient Iterative Schemes for Ab Initio Total-Energy Calculations Using a Plane-Wave Basis Set *Phys. Rev. B*, **1996**, *54* (16), 11169–11186. 10.1103/PhysRevB.54.11169.
- (30) Joubert, D. From Ultrasoft Pseudopotentials to the Projector Augmented-Wave Method. *Phys. Rev. B*, **1999**, *59* (3), 1758–1775. 10.1103/PhysRevB.59.1758.
- (31) Perdew, J. P.; Yue, W. Accurate and Simple Density Functional for the Electronic Exchange Energy: Generalized Gradient Approximation. *Phys. Rev. B*, **1986**, *33* (12), 8800–8802. 10.1103/PhysRevB.33.8800.
- (32) Perdew, J. P.; Wang, Y. Accurate and Simple Analytic Representation of the Electron-Gas Correlation Energy. *Phys. Rev. B*, **1992**, *45* (23), 13244–13249. 10.1103/PhysRevB.45.13244.
- (33) Dudarev, S. L.; Botton, G. A.; Savrasov, S. Y.; Humphreys, C. J.; Sutton, A. P. Electron-Energy-Loss Spectra and the Structural Stability of Nickel Oxide: An LSDA+U Study. *Phys. Rev. B*, **1998**, *57* (3), 1505–1509. 10.1103/PhysRevB.57.1505.
- (34) Ota, T.; Kizaki, H.; Morikawa, Y. Mechanistic Analysis of Oxygen Vacancy Formation and Ionic Transport in Sr₃Fe₂O_{7-δ}. *J. Phys. Chem. C*, **2018**, *122* (8), 4172–4181. 10.1021/acs.jpcc.7b11904.

- (35) Szaro, N. A.; Ammal, S. C.; Chen, F.; Heyden, A. An Ab Initio Study of the Oxygen Defect Formation and Oxide Ion Migration in $(\text{Sr}_{1-x}\text{Pr}_x)_2\text{FeO}_{4+\delta}$. *J. Power Sources*, **2021**, *515*, 230602. 10.1016/j.jpowsour.2021.230602.
- (36) Jain, A.; Ong, S. P.; Hautier, G.; Chen, W.; Richards, W. D.; Dacek, S.; Cholia, S.; Gunter, D.; Skinner, D.; Ceder, G.; Persson, K. A. Commentary: The Materials Project: A Materials Genome Approach to Accelerating Materials Innovation. *APL Mater.*, **2013**, *1* (1), 011002. 10.1063/1.4812323.
- (37) Wang, L.; Maxisch, T.; Ceder, G. Oxidation Energies of Transition Metal Oxides within the GGA+U Framework. *Phys. Rev. B*, **2006**, *73* (19), 195107. 10.1103/PhysRevB.73.195107.
- (38) Blöchl, P. E. Projector Augmented-Wave Method. *Phys. Rev. B.*, **1994**, *50* (24), 17953–17979. 10.1103/PhysRevB.50.17953.
- (39) Monkhorst, H. J.; Pack, J. D. Special Points for Brillouin-Zone Integrations. *Phys. Rev. B*, **1976**, *13* (12), 5188–5192. 10.1103/PhysRevB.13.5188.
- (40) Makov, G.; Payne, M. C. Periodic Boundary Conditions in Ab Initio Calculations. *Phys. Rev. B*, **1995**, *51* (7), 4014–4022. 10.1103/PhysRevB.51.4014.
- (41) Henkelman, G.; Uberuaga, B. P.; Jónsson, H. A Climbing Image Nudged Elastic Band Method for Finding Saddle Points and Minimum Energy Paths. *J. Chem. Phys.*, **2000**, *113* (22), 9901–9904. 10.1063/1.1329672.
- (42) Heyden, A.; Bell, A. T.; Keil, F. J. Efficient Methods for Finding Transition States in Chemical Reactions: Comparison of Improved Dimer Method and Partitioned Rational Function Optimization Method. *J. Chem. Phys.*, **2005**, *123* (22), 224101. 10.1063/1.2104507.
- (43) Henkelman, G.; Jónsson, H. A Dimer Method for Finding Saddle Points on High Dimensional Potential Surfaces Using Only First Derivatives. *J. Chem. Phys.*, **1999**, *111* (15), 7010–7022. 10.1063/1.480097.
- (44) Olsen, R. A.; Kroes, G. J.; Henkelman, G.; Arnaldsson, A.; Jónsson, H. Comparison of Methods for Finding Saddle Points without Knowledge of the Final States. *J. Chem. Phys.*, **2004**, *121* (20), 9776–9792. 10.1063/1.1809574.

- (45) Momma, K.; Izumi, F. VESTA 3 for Three-Dimensional Visualization of Crystal, Volumetric and Morphology Data. *J. Appl. Cryst.*, **2011**, *44* (6), 1272–1276. 10.1107/S0021889811038970.
- (46) Ammal, S. C.; Heyden, A. Modeling the Noble Metal/TiO₂ (110) Interface with Hybrid DFT Functionals: A Periodic Electrostatic Embedded Cluster Model Study. *J. Chem. Phys.*, **2010**, *133* (16), 164703. 10.1063/1.3497037.
- (47) Nørskov, J. K.; Rossmeisl, J.; Logadottir, A.; Lindqvist, L.; Kitchin, J. R.; Bligaard, T.; Jónsson, H. Origin of the Overpotential for Oxygen Reduction at a Fuel-Cell Cathode. *J. Phys. Chem. B*, **2004**, *108* (46), 17886–17892. 10.1021/jp047349j.
- (48) Atkins, P. W.; Julio De Paula; Keeler, J. *Atkins' Physical Chemistry*; Oxford University Press: Oxford, 2018. pp 886
- (49) Peterson, A. A.; Abild-Pedersen, F.; Studt, F.; Rossmeisl, J.; Nørskov, J. K. How Copper Catalyzes the Electroreduction of Carbon Dioxide into Hydrocarbon Fuels. *Energy Environ. Sci.*, **2010**, *3* (9), 1311. 10.1039/c0ee00071j.
- (50) Yang, W.; Solomon, R. V.; Mamun, O.; Bond, J. Q.; Heyden, A. Investigation of the Reaction Mechanism of the Hydrodeoxygenation of Propionic Acid over a Rh(111) Surface: A First Principles Study. *J. Catal.*, **2020**, *391*, 98–110. 10.1016/j.jcat.2020.08.015.
- (51) Shampine, L. F.; Reichelt, M. W. The MATLAB Ode Suite. *SIAM J. Sci. Comput.*, **1997**, *18* (1), 1–22. 10.1137/S1064827594276424.
- (52) Stegelmann, C.; Andreasen, A.; Campbell, C. T. Degree of Rate Control: How Much the Energies of Intermediates and Transition States Control Rates. *J. Am. Chem. Soc.*, **2009**, *131* (23), 8077–8082. 10.1021/ja9000097.
- (53) Campbell, C. T. The Degree of Rate Control: A Powerful Tool for Catalysis Research. *ACS Catal.*, **2017**, *7* (4), 2770–2779. 10.1021/acscatal.7b00115.
- (54) Cheng, L.; Assary, R. S.; Qu, X.; Jain, A.; Ong, S. P.; Rajput, N. N.; Persson, K.; Curtiss, L. A. Accelerating Electrolyte Discovery for Energy Storage with High-Throughput Screening. *J. Phys. Chem. Lett.*, **2015**, *6* (2), 283–291. 10.1021/jz502319n.

- (55) Qu, X.; Jain, A.; Rajput, N. N.; Cheng, L.; Zhang, Y.; Ong, S. P.; Brafman, M.; Maginn, E.; Curtiss, L. A.; Persson, K. A. The Electrolyte Genome Project: A Big Data Approach in Battery Materials Discovery. *Comput. Mater. Sci.*, **2015**, *103*, 56–67. 10.1016/j.commatsci.2015.02.050.
- (56) Jung, M. H.; Alsmadi, A. M.; Chang, S.; Fitzsimmons, M. R.; Zhao, Y.; Lacerda, A. H.; Kawanaka, H.; El-Khatib, S.; Nakotte, H. Magnetic Ordering in Single-Crystalline SrLaFeO₄ and Sr_{1.1}La_{0.9}FeO₄. *J. Appl. Phys.*, **2005**, *97* (10), 10A926 10.1063/1.1861416.
- (57) Sun, C.; Stimming, U. Recent Anode Advances in Solid Oxide Fuel Cells. *J. Power Sources*, **2007**, *171* (2), 247–260. 10.1016/j.jpowsour.2007.06.086.
- (58) Tealdi, C.; Ferrara, C.; Mustarelli, P.; Islam, M. S. Vacancy and Interstitial Oxide Ion Migration in Heavily Doped La_{2-x}Sr_xCoO_{4±δ}. *J. Mater. Chem.*, **2012**, *22* (18), 8969–8975. 10.1039/c2jm30769c.
- (59) Huan, D.; Wang, Z.; Wang, Z.; Peng, R.; Xia, C.; Lu, Y. High-Performanced Cathode with a Two-Layered R–P Structure for Intermediate Temperature Solid Oxide Fuel Cells. *ACS Appl. Mater. Interfaces*, **2016**, *8* (7), 4592–4599. 10.1021/acsami.5b10844.
- (60) Takamatsu, A.; Tamai, K.; Hosokawa, S.; Tanaka, T.; Ehara, M.; Fukuda, R. Oxidation and Storage Mechanisms for Nitrogen Oxides on Various Terminated (001) Surfaces of SrFeO_{3-δ} and Sr₃Fe₂O_{7-δ} Perovskites. *ACS Appl Mater Interfaces* **2021**, *13* (6), 7216–7226. 10.1021/acsami.0c20724.
- (61) Gu, X. K.; Nikolla, E. Design of Ruddlesden-Popper Oxides with Optimal Surface Oxygen Exchange Properties for Oxygen Reduction and Evolution. *ACS Catal.*, **2017**, *7* (9), 5912–5920. 10.1021/acscatal.7b01483.
- (62) Kröger, F. A.; Vink, H. J. Relations between the Concentrations of Imperfections in Solids. *J. Phys. Chem. Solids*, **1958**, *5* (3), 208–223. 10.1016/0022-3697(58)90069-6.
- (63) Bockris, J. O.; Nagy, Z. Symmetry Factor and Transfer Coefficient. A Source of Confusion in Electrode Kinetics. *J. Chem. Educ.*, **1973**, *50* (12), 839. 10.1021/ed050p839.

- (64) Xie, W.; Lee, Y. L.; Shao-Horn, Y.; Morgan, D. Oxygen Point Defect Chemistry in Ruddlesden–Popper Oxides $(\text{La}_{1-x}\text{Sr}_x)_2\text{MO}_{4\pm\delta}$ ($M = \text{Co}, \text{Ni}, \text{Cu}$). *J. Phys. Chem. Lett.*, **2016**, 7 (10), 1939–1944. 10.1021/acs.jpcclett.6b00739.

3.8 FIGURES AND TABLES

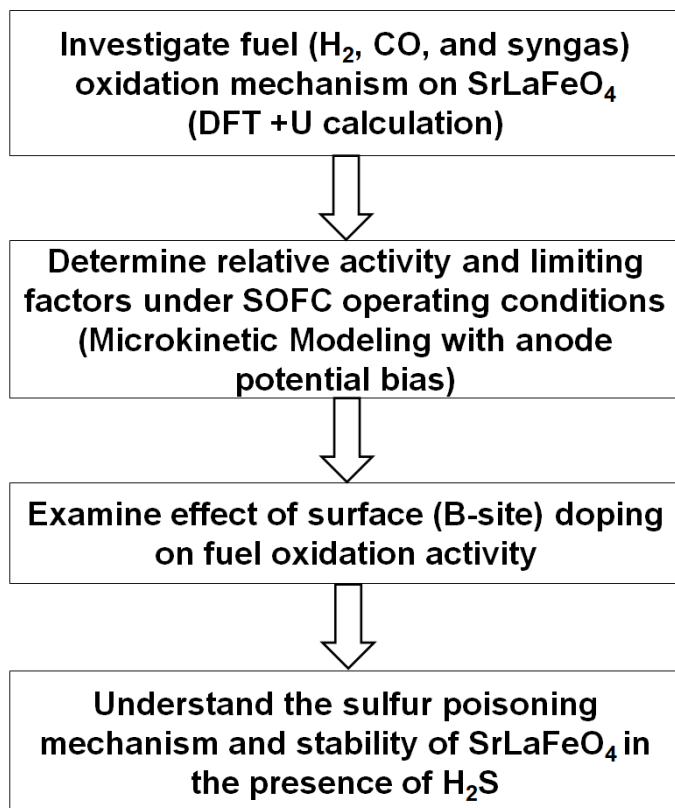


Figure 3.1: Proposed scheme or outline for the investigation fuel oxidation on the SrLaFeO_{4-δ} anode.

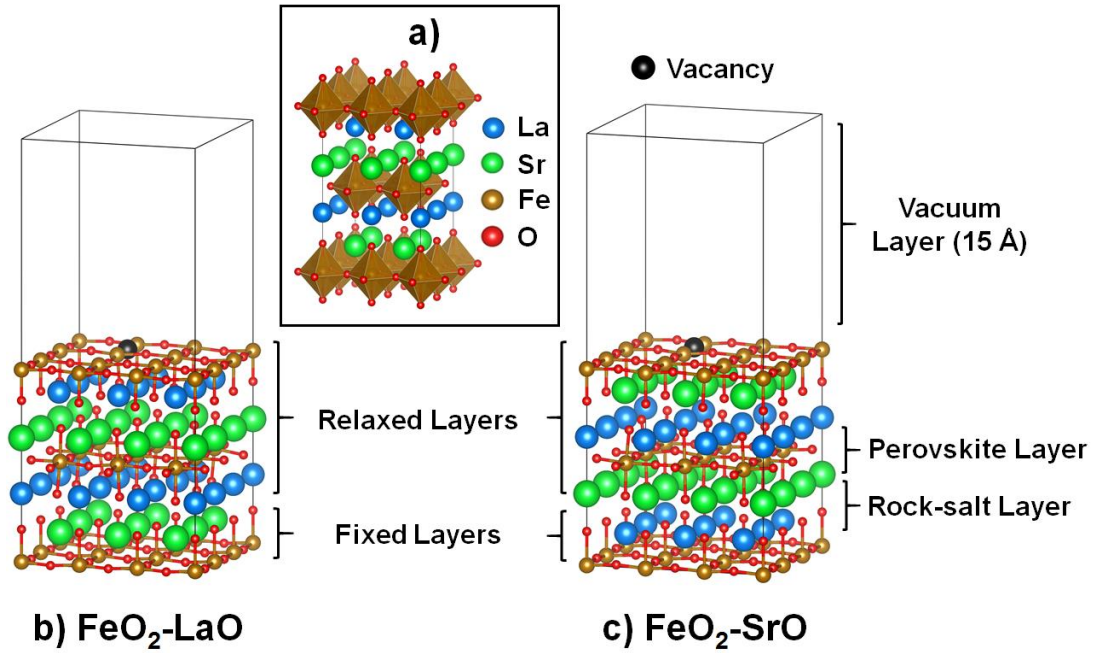


Figure 3.2: (a) The $2 \times 2 \times 1$ polyhedral representation of the $I4mm$ supercell model of bulk SrLaFeO_4 (SLF) and (b-c) the $3 \times 3 \times 1$ unit cells of SLF (001) surface models where (b) FeO_2 -LaO and (c) FeO_2 -SrO represent the FeO_2 -terminated surfaces with LaO or SrO in the second layer, respectively.

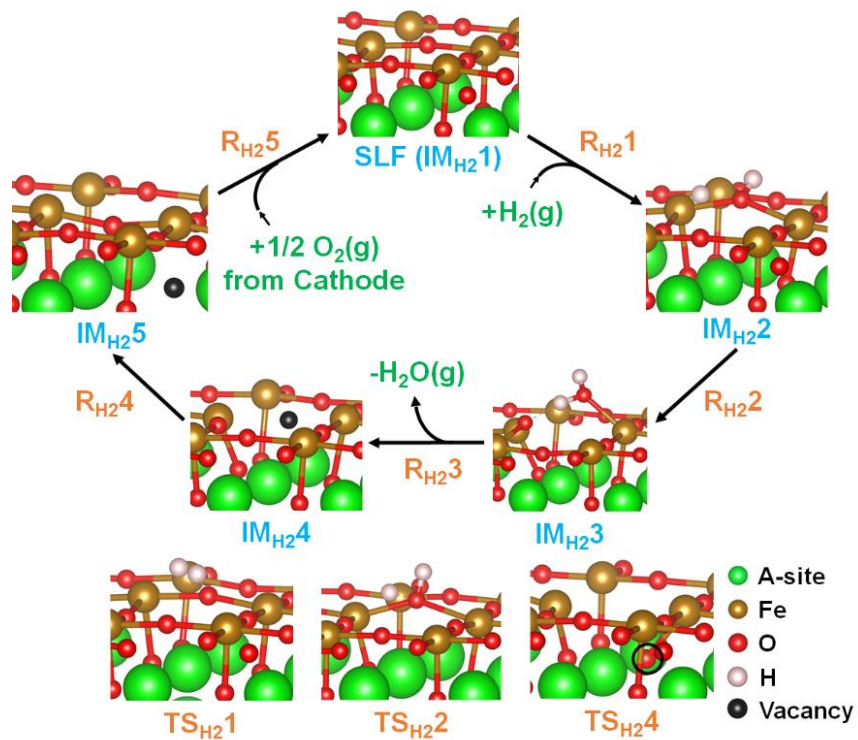


Figure 3.3: Proposed mechanism for H₂ oxidation on SrLaFeO_{4-δ} surface. The TS structures are in reference to the specific elementary reaction step. The vacancy (black) refers to the oxygen vacancy generated during H₂ oxidation.

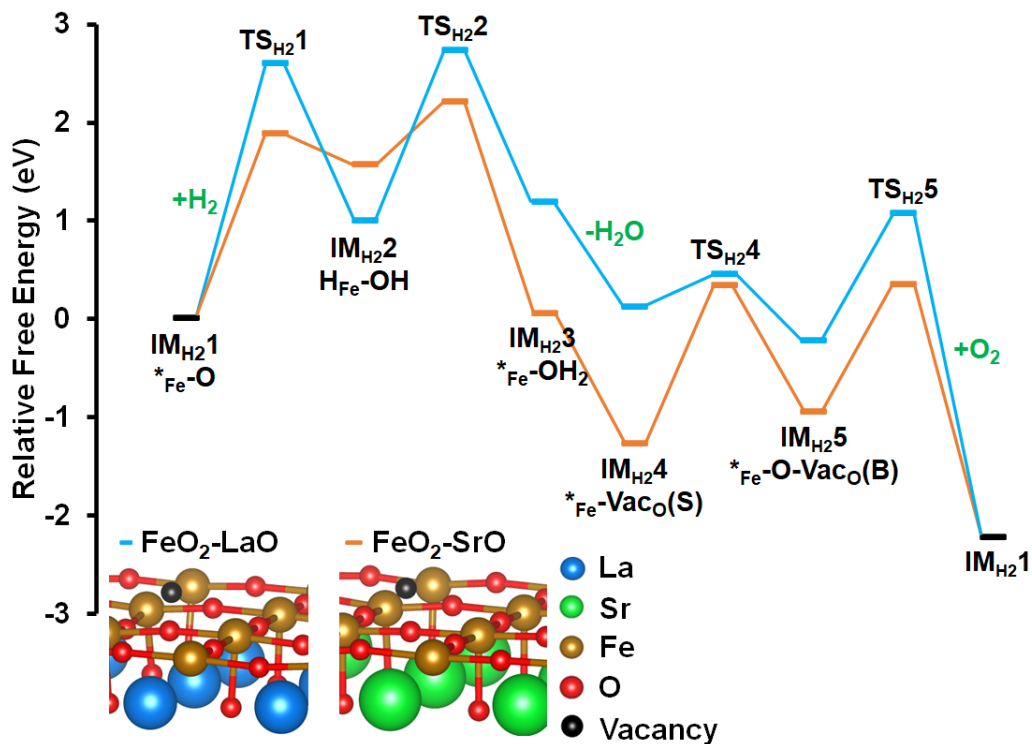


Figure 3.4: Relative free energy profiles (eV) for the H₂ oxidation network on the FeO₂-LaO (blue) and FeO₂-SrO (orange) surface models (T = 1073 K; P_{H2} (gas) = 1.0 atm; P_{H2O} (gas) = 0.03 atm; P_{O2} (gas) = 0.21 atm). All energies are with reference to the sum of the energies of the initial state (IM_{H2}1) and the gas phase molecules.

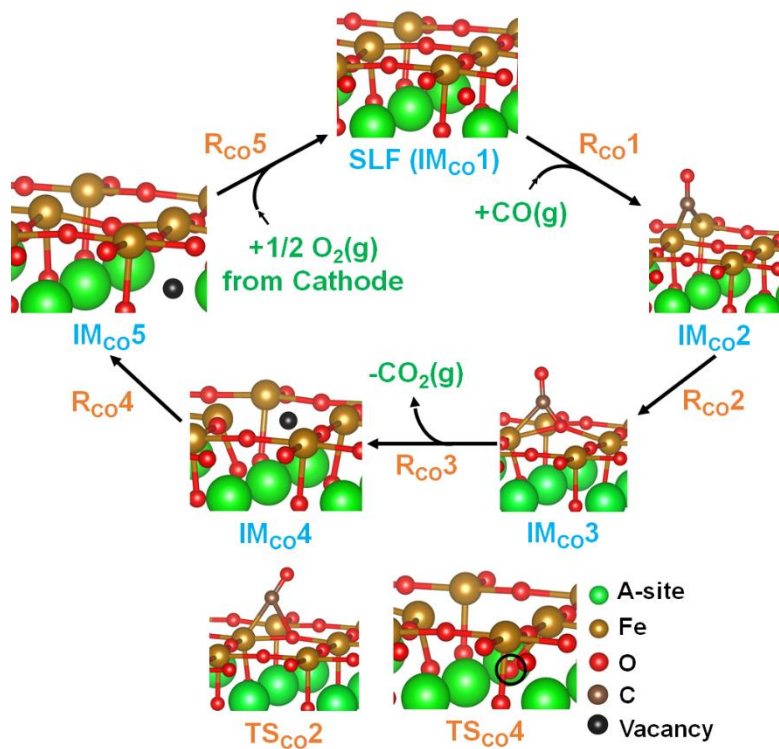


Figure 3.5: Proposed mechanism for CO oxidation on SrLaFeO_{4-δ} surface. The TS structures are in reference to the specific elementary reaction step. The vacancy (black) refers to the vacancy generated during CO oxidation.

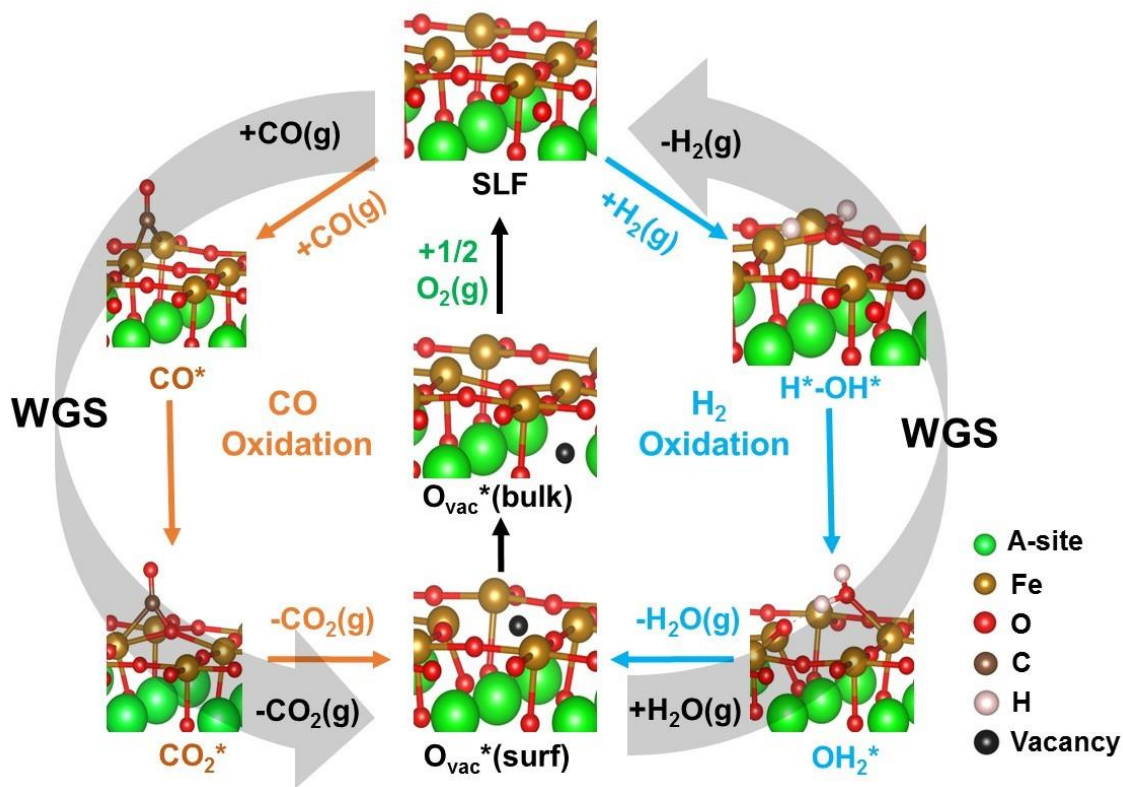


Figure 3.7: Proposed mechanism for syngas oxidation and water-gas shift (WGS) on SrLaFeO_{4-δ} surface. CO oxidation is displayed in orange, H₂ oxidation is displayed in blue, and water-gas shift (WGS) is displayed in black. The vacancy (black) refers to the vacancy generated during syngas oxidation or water-gas shift.

Table 3.1: Forward rate (k_{for}) and equilibrium constants (K_{eq}) for all short-circuit reaction steps for H_2 and CO oxidation on the $\text{FeO}_2\text{-LaO}$ and $\text{FeO}_2\text{-SrO}$ surface models at 1073 K ($P_{\text{H}_2,\text{CO}} = 1.00$ atm, $P_{\text{H}_2\text{O},\text{CO}_2} = 0.03$ atm, and $P_{\text{O}_2} = 0.21$ atm).

H_2 Reaction	$\text{FeO}_2\text{-LaO}$ Surface		$\text{FeO}_2\text{-SrO}$ Surface	
	k_{for} (s^{-1})	K_{eq}	k_{for} (s^{-1})	K_{eq}
R_{H_21}	1.40×10^1	2.09×10^{-5}	1.84×10^5	2.64×10^{-7}
R_{H_22}	1.55×10^5	1.33×10^{-1}	2.13×10^{10}	1.30×10^7
R_{H_23}	8.28×10^{12}	3.14×10^3	1.28×10^{14}	4.84×10^4
R_{H_24}	5.79×10^{11}	3.99×10^1	6.43×10^5	3.14×10^{-2}
R_{H_25}	1.76×10^7	5.39×10^9	1.76×10^7	3.59×10^5
CO Reaction	k_{for} (s^{-1})	K_{eq}	k_{for} (s^{-1})	K_{eq}
$\text{R}_{\text{CO}1}$	2.11×10^9	7.74×10^{-9}	2.11×10^9	5.73×10^{-10}
$\text{R}_{\text{CO}2}$	3.25×10^{10}	3.63×10^{-3}	1.32×10^{12}	5.49×10^3
$\text{R}_{\text{CO}3}$	5.45×10^{17}	3.24×10^8	1.56×10^{19}	9.28×10^9
$\text{R}_{\text{CO}4}$	5.79×10^{11}	3.99×10^1	6.43×10^5	3.14×10^{-2}
$\text{R}_{\text{CO}5}$	1.76×10^7	5.39×10^9	1.76×10^7	2.13×10^6

Table 3.2: Degree of rate control (DRC), apparent activation energies (calculated in the temperature range of 973-1273 K), and turnover frequencies calculated for H_2 and CO oxidation over $\text{FeO}_2\text{-LaO}$ and $\text{FeO}_2\text{-SrO}$ surfaces at short circuit conditions ($T = 1073$ K, $P_{\text{H}_2,\text{CO}} = 1.00$ atm, $P_{\text{H}_2\text{O},\text{CO}_2} = 0.03$ atm, and $P_{\text{O}_2} = 0.21$ atm).

Degree of Rate Control	H_2 Oxidation		CO Oxidation		
	$\text{FeO}_2\text{-LaO}$	$\text{FeO}_2\text{-SrO}$	$\text{FeO}_2\text{-LaO}$	$\text{FeO}_2\text{-SrO}$	
R_{H_21}	0.22	0.04	$\text{R}_{\text{CO}1}$	0.00	0.00
R_{H_22}	0.78	0.92	$\text{R}_{\text{CO}2}$	1.00	1.00
R_{H_23}	0.00	0.00	$\text{R}_{\text{CO}3}$	0.00	0.00
R_{H_24}	0.00	0.01	$\text{R}_{\text{CO}4}$	0.00	0.00
R_{H_25}	0.00	0.03	$\text{R}_{\text{CO}5}$	0.00	0.00
Apparent Activation Energy (eV)	1.47	0.86		0.71	0.53
Short Circuit Turnover Frequency (1/s)	2.64×10^0	5.29×10^3		2.52×10^2	7.53×10^2

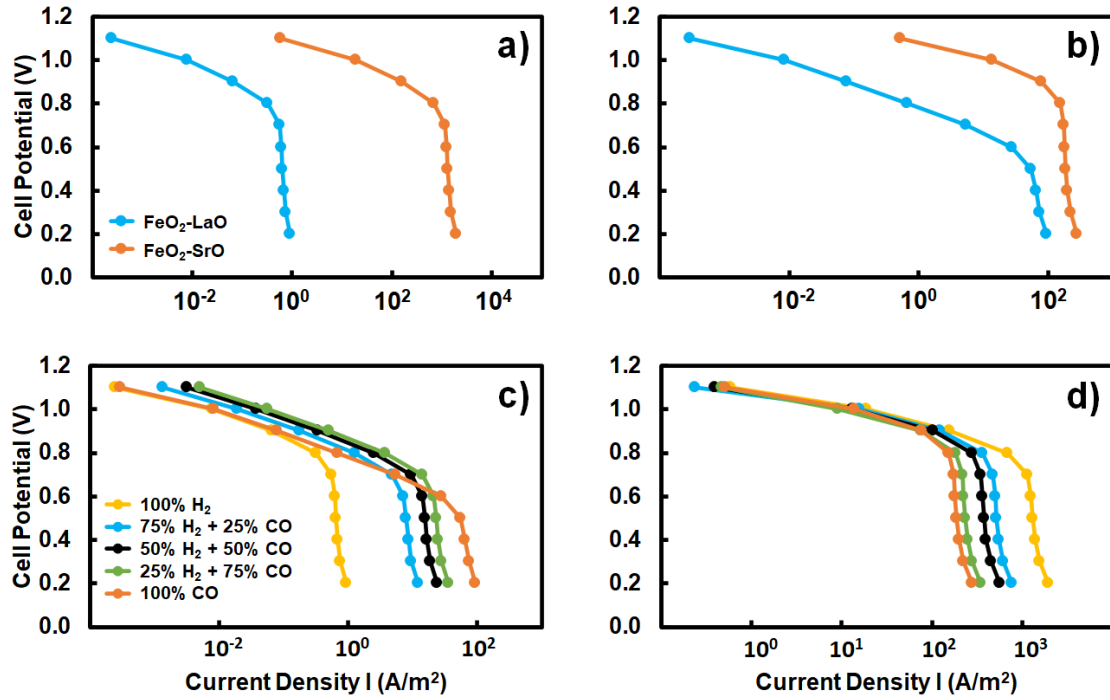


Figure 3.8: Calculated polarization curves at 1073 K for a) H₂ oxidation and b) CO oxidation on FeO₂-LaO (blue) and FeO₂-SrO (orange) surface models ($P_{\text{H}_2, \text{CO}} = 1.00$ atm, $P_{\text{H}_2\text{O}, \text{CO}_2} = 0.03$ atm, and $P_{\text{O}_2} = 0.21$ atm). (c-d) Calculated polarization curves for syngas oxidation at 1073 K on FeO₂-LaO (c) and FeO₂-SrO (d) surface models ($P_{\text{H}_2, \text{CO}} = 1.00$ atm, $P_{\text{H}_2\text{O}} = 0.03$ atm, $P_{\text{CO}_2} = 0.003$ atm, and $P_{\text{O}_2} = 0.21$ atm). $\beta = 0.5$ is used for all charge transfer reactions.

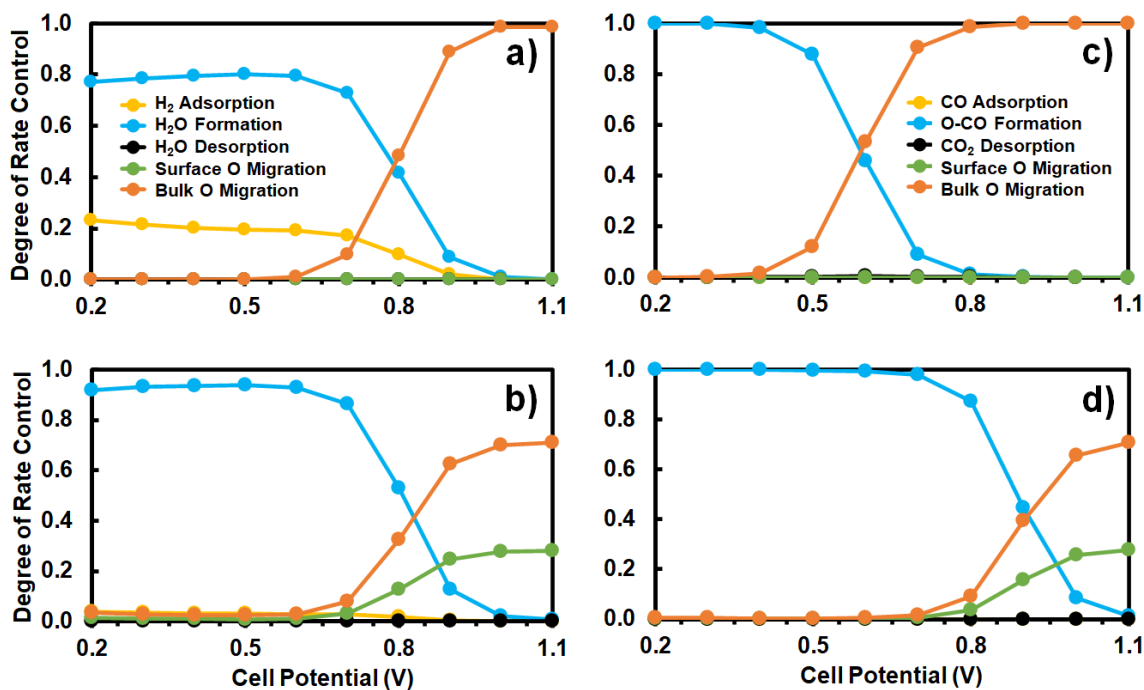


Figure 3.9: Degree of rate control (DRC) analysis for H₂ oxidation on a) FeO₂-LaO and b) FeO₂-SrO surfaces and degree of rate control for CO oxidation on c) FeO₂-LaO and d) FeO₂-SrO surfaces as a function of cell potential (T = 1073 K; P_{H₂,CO} = 1.00 atm, P_{H₂O,CO₂} = 0.03 atm, and P_{O₂} = 0.21 atm).

Table 3.3: Transition state free energies of the dissociative adsorption of hydrogen ($\Delta G^{\ddagger}_{H_2}$ in eV) and surface water formation ($\Delta G^{\ddagger}_{H_2O}$ in eV) at 1073 K, P_{H₂} (gas) = 1.0 atm, P_{H₂O} (gas) = 0.03 atm, and P_{O₂} (gas) = 0.21 atm) calculated with reference to the energies of initial active site and H₂ gas, and turnover frequency (TOF in s⁻¹) of H₂ oxidation calculated at short circuit conditions for single surface metal atom doped Fe_{1-x}M_xO₂-LaO and Fe_{1-x}M_xO₂-SrO (x = 0.11; M = Fe, Co, Ni, Mn) surface models.

Dopant (M)	$\Delta G^{\ddagger}_{H_2}$ (eV)		$\Delta G^{\ddagger}_{H_2O}$ (eV)		Short Circuit TOF (s ⁻¹)	
	Fe _{1-x} M _x O ₂ -LaO	Fe _{1-x} M _x O ₂ -SrO	Fe _{1-x} M _x O ₂ -LaO	Fe _{1-x} M _x O ₂ -SrO	Fe _{1-x} M _x O ₂ -LaO	Fe _{1-x} M _x O ₂ -SrO
Fe	2.60	1.89	2.73	2.21	2.64 × 10 ⁰	5.29 × 10 ³
Co	1.39	1.09	1.71	-0.07	9.41 × 10 ³	8.29 × 10 ²
Ni	1.58	2.39	2.43	1.75	8.65 × 10 ¹	2.10 × 10 ¹
Mn	1.85	2.23	2.28	1.87	3.79 × 10 ²	6.81 × 10 ²

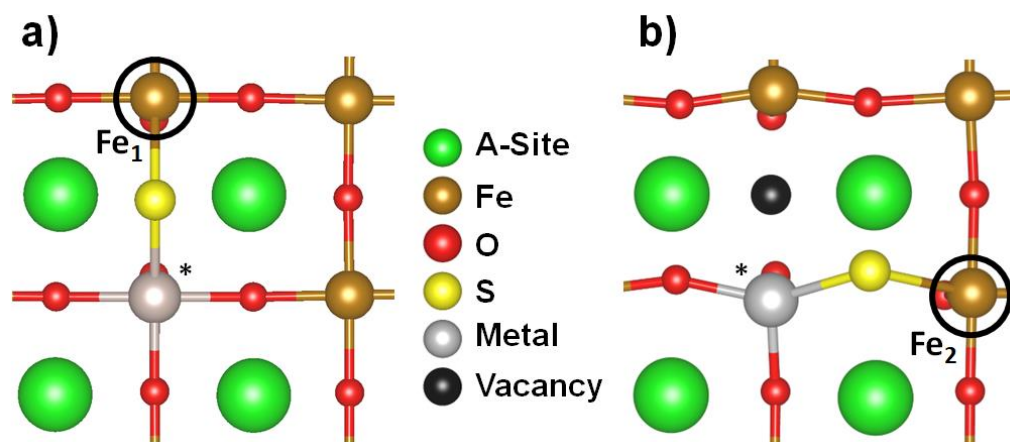


Figure 3.10: Top views of optimized structures of a) sulfur adsorbed on the oxygen vacancy ($\text{H}_2\text{S} + \text{M}-\text{V}_\text{O}^{\bullet\bullet}-\text{Fe}_1 \leftrightarrow \text{H}_2 + \text{M}-\text{S}-\text{Fe}_1$, $\text{M} = \text{Fe, Co, Ni, Mn}$) and b) sulfur replacing surface oxygen ($\text{H}_2\text{S} + \text{M}-\text{O}_\text{O}^\times-\text{Fe}_2 \leftrightarrow \text{H}_2\text{O} + \text{M}-\text{S}-\text{Fe}_2$, $\text{M} = \text{Fe, Co, Ni, Mn}$), respectively.

Table 3.4: Reaction free energies for the dissociative adsorption of H_2S (ΔG^{ads} in eV, equation 3.19) and oxygen replacement reaction (ΔG^{repl} in eV, equation 3.21) for the $\text{Fe}_{1-x}\text{M}_x\text{O}_2$ -LaO and $\text{Fe}_{1-x}\text{M}_x\text{O}_2$ -SrO ($x = 0.11$; $\text{M} = \text{Fe, Co, Ni, Mn}$) surface models calculated at $T = 1073$ K, $C_{\text{H}_2\text{S}} = 50$ ppm, $P_{\text{H}_2} = 1$ atm, and $P_{\text{H}_2\text{O}} = 0.03$ atm.

Dopant (M)	$\text{Fe}_{1-x}\text{M}_x\text{O}_2$ -LaO		$\text{Fe}_{1-x}\text{M}_x\text{O}_2$ -SrO	
	ΔG^{ads} (eV)	ΔG^{repl} (eV)	ΔG^{ads} (eV)	ΔG^{repl} (eV)
Fe	1.73	1.09	2.94	0.16
Co	2.25	0.01	1.74	0.61
Ni	4.04	-0.08	3.05	1.46
Mn	1.82	0.75	2.10	-0.15

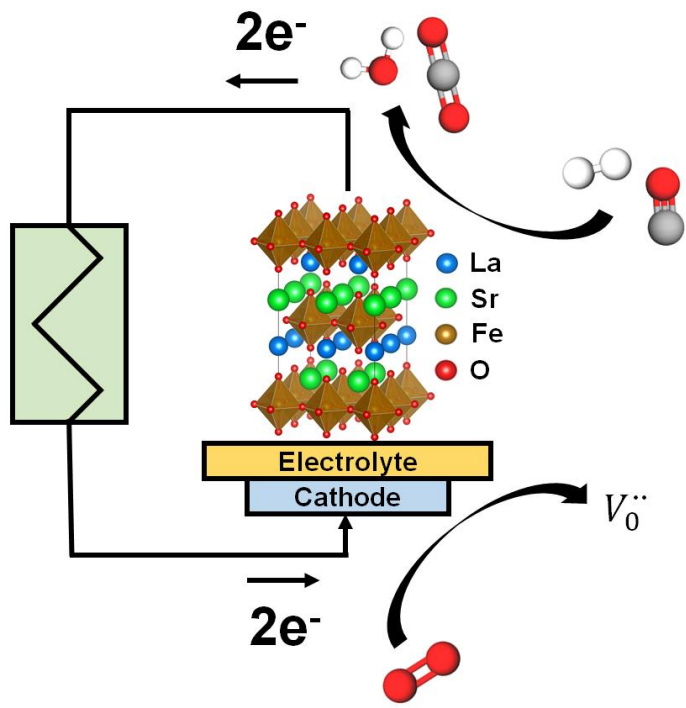


Figure 3.11: Graphical Abstract

CHAPTER 4

FIRST PRINCIPLES MATERIAL SCREENING AND DISCOVERY OF PEROVSKITE ELECTROLYTES FOR PROTON CONDUCTING SOLID OXIDE FUEL CELLS ³

⁴ Szaro, N.; Ammal, S.; Chen., F.; Heyden, A. *To Be Submitted*.

4.1 ABSTRACT

The perovskite oxide family is renowned for its ability to be modulated with elemental doping to tune desirable macroscopic properties. Perovskite oxides are commonly used as proton-conducting ceramic (PCC) electrolytes for solid-oxide fuel cells. PCC electrolytes must have thermodynamic stability in both oxidizing and reducing environments, low electronic conductivity, and the ability to readily form protonic defects. To help discover new PCC electrolyte materials and to understand the role of different elements and compositions on material properties, high-throughput materials screening together with first principles materials science can be utilized to scan a large elemental phase space. In this study, we conduct a high-throughput scan of 4793 materials to determine how different cation species modulate thermodynamic stability, electronic conductivity, and defect formation. Our filtering analysis identifies 116 materials (including BaZrO_3 and BaCeO_3) that are electronically inactive and thermodynamically stable under reducing and oxidizing conditions. Furthermore, we identify 43 materials (including BaZrO_3) that are also thermodynamically stable under pure CO_2 environment. For all the 116 materials, we conduct a thermodynamic analysis of oxygen vacancy and protonic defect formation to identify trends in ionic conductivity. This study provides a supplemental understanding of the role of elemental identity and doping ratios on material stability and activity that can aid the design of new perovskite oxides for proton-conducting applications.

4.2 INTRODUCTION

Solid oxide fuel cells (SOFCs) are electrochemical devices that directly oxidize hydrogen and hydrocarbon-based fuels with a higher theoretical efficiency relative to the

thermochemical combustion of hydrogen and hydrocarbon-based fuels ¹. For oxide-conducting SOFCs (O-SOFCs), the anode oxidizes incoming fuel and consumes negative oxide ions (O^{2-}), the cathode reduces incoming oxygen and produces O^{2-} , and the electrolyte layer conducts O^{2-} ions from one electrode to the other without the conduction of electrons. To overcome high activation energies associated with electrode kinetics and ionic conduction, high operating temperatures (e.g., $> 800\text{ }^{\circ}\text{C}$) are required which limits the practical applications and commercialization of SOFCs ^{2,3}. The electrolyte plays a vital role in determining the operating temperature of SOFCs based on the electrolyte's ability to conduct ions between the electrodes. Common O-SOFC electrolytes include YSZ, LSGM, and GDC ⁴⁻⁶ and require a typical functioning temperature of $700\text{-}1000\text{ }^{\circ}\text{C}$ to exhibit high ionic conductivity. Therefore, O-SOFCs suffer from high operational costs and premature aging due to mechanical stresses ^{4,7}. A possible solution to lower the electrolyte operating temperature is the utilization of proton-conducting solid oxide fuel cells (P-SOFCs) ^{8,9}. Proton-conducting ceramics (PCCs) have displayed promising ionic conductivity at temperatures as low as $400\text{ }^{\circ}\text{C}$ ¹⁰. Therefore, PCCs have attracted significant interest in the development of intermediate temperature (e.g., $\sim 650 - 800\text{ }^{\circ}\text{C}$) SOFCs.

The perovskite oxide material family with a general formula of ABO_3 (Figure 4.1(a)), where the A-site being an alkali metal, an alkaline earth, or a rare earth metal, and the B-site being a transition metal, has received significant research interest for proton-conducting applications ¹¹. The current state-of-the-art P-SOFC electrolytes are the acceptor-doped PCCs based on BaZrO_3 (BZO, Figure 4.1(b)) and BaCeO_3 (BCO, Figure 4.1(c)). BZO suffers from ionic conductivity problems due to high grain boundary

resistance, and BCO suffers from material instability in the presence of H₂O and CO₂ ^{12–14}. To better improve the performance of BZO and BCO, researchers have used elemental doping at the B-site to modulate ionic conductivity and thermodynamic stability. Zuo et al. co-doped BCO with Zr and Y to produce the material Ba(Zr_{0.1}Ce_{0.7}Y_{0.2})O_{3-δ} (BZCY7) which was found to display good conductivity ($\sim 9 \times 10^{-1}$ S cm⁻¹ at 700 °C) and thermodynamic stability under CO₂ environments ^{15,16}. Despite these promising properties, commercial adoption of BZCY7 (and other BZCY conformers) suffers from high manufacturing costs due to high sintering temperatures (> 1550 °C) and from a limited concentration of incorporated protons due to the acceptor-dopant proton trapping effect ^{17–20}. Beyond the BZO and BCO families, Zhou et al. reported that the perovskite SmNiO₃ could be a promising PCC for low temperature SOFCs ²¹. Brownmillerite, niobate, tantalite, and Ruddlesden-Popper material classes have also received attention as potential PCC materials for intermediate temperature P-SOFC applications ^{22–24}. However, only a limited number of these materials can satisfy most properties required for optimal PCCs at lower temperatures, such as high proton conductivity, low activation energy, chemical stability with neighboring electrode layers, and thermodynamic stability under H₂O and CO₂ environments. Understanding the role of cations and the structures of these complex oxides, such as perovskite-based materials, is critical to guide the development of novel PCC materials with high efficiency.

High-throughput first-principles material discovery and design strategy has been effectively used to identify new materials for O-SOFC applications ^{25,26}, thermionic emission devices ²⁷, solar cell applications ²⁸, and PCCs. For PCCs, Islam et al. ²⁹ sampled over 5000 ternary oxide materials with six formula classes, A_xBO₆, A_xBO₄,

$A_xB_2O_7$, A_xBO_3 , $A_xB_2O_5$, and A_xBO_2 , without considering any doping at the A- or B-sites. Thermodynamic stability of these materials in the presence of H_2O at 0 K, proton migration barriers, and proton incorporation capabilities were tested in this study and found that the materials with connected BO_6 octahedra, such as, perovskites $YbFeO_3$, $AcFeO_3$, $YbCoO_3$, and $CaFeO_3$ ($Pm\bar{3}m$); $Tb_2Mo_2O_7$ ($Fd\bar{3}m$); Eu_3MoO_7 ($P2_12_12_1$); brownmillerite $Sr_2Co_2O_5$ ($Pnma$); Mn_2TeO_6 ($P4_2/mnm$); and $NbMoO_4$ and $CrMoO_4$ ($Cmmm$), are in general good proton conductors. In terms of water stability, oxides containing A-site cations with high oxidation states and B-site cations including Zr, V, and Mo exhibit good stability, whereas oxides with Co, Ti, and Ce cations tend to degrade in the presence of H_2O . Furthermore, fast proton diffusion is favored along the BO_6 octahedra compared to other types of BO_x polyhedral. Furthermore, no perovskite material yielded a migration barrier greater than 0.97 eV and f-block-containing perovskites displayed a proton migration barrier range between 0.13 to 0.59 eV. While this study provided a general understanding and guidelines for identifying novel PCC materials from a large set of non-doped ternary oxide materials, introduction of A- and B-site dopants to these materials needs to be explored to further improve the stability and ionic conductivity.

Here, we conducted a density functional theory (DFT) high-throughput screening of a wide array of perovskite oxides to understand the influence of A- and B-site cations and dopants on proton conductivity and to discover novel PCC materials with good conductivity and phase stability under H_2 , H_2O and CO_2 environments. Starting from the database of materials analyzed by Jacobs et al.²⁵ and Ma et al.²⁷, the materials set is further expanded to 4793 distinct perovskites with a general $A_{1-x}A'_x B_{1-y}B'_y O_3$

stoichiometry and include binary, tertiary, quaternary, and quinary A- and B-site compositions. Our initial screening based on electronic conductivity (bandgap energy > 2.0 eV) and phase stability under cathode/anode environments resulted in 116 materials. For these compounds, we computed oxygen vacancy formation and hydration energies to determine the thermodynamic baseline of proton conductivity. Additional screening based on thermodynamic stability under CO₂ environment resulted in 43 materials that could satisfy key environmental stability requirements for proton conductors. This computational search serves to help enhance the understanding of the materials chemistry that governs proton conduction, electronic conductivity, and thermodynamic stability for a wide spectrum of perovskite oxides.

4.3 METHODS

Electronic structure and total energy calculations of the perovskite materials were performed using spin polarized DFT as implemented in the Vienna Ab Initio Simulation Package (VASP) version 5.4.4³⁰. The generalized gradient approximation (GGA) with the Perdew, Burke, and Ernzerhof (PBE) functional^{31,32} was used to evaluate electron exchange-correlation effects. The nuclei and core electrons were represented by the frozen-core projector-augmented wave (PAW) approach^{33,34}. All pseudopotentials used in the present study are equivalent to those used by Pymatgen (Python Materials Genomics) v2022.10.22³⁵ and the Materials Project³⁶ to maintain computational setup uniformity for phase stability analysis. For materials containing specific transition metals (e.g., V, Cr, Mn, Fe, Co, Ni), Dudarev's approach for DFT+U calculations is used to correct the inadequate description of localized 3d electrons^{37,38}. Effective U-J parameters used for these transition metals are taken from the Materials Project database and these

values are tabulated in Table C.1 of Appendix C. Integration over the Brillouin zone used the Gaussian smearing method ($\sigma = 0.05$ eV) for all calculations. The electronic energy and ionic relaxations were converged to 10^{-6} eV and 0.02 eV/Å, respectively. All $2 \times 2 \times 2$ supercell calculations (40 atoms per cell) utilized a $4 \times 4 \times 4$ Monkhorst-Pack (MP) k-point mesh consistent with earlier studies^{39,25,27}. The planewave cutoff energy of 520 eV was used for all the calculations to be consistent with the computational setup used in the Materials Project database.

All the perovskite materials chosen here for electronic and thermodynamic stability screenings have a chemical formula of ABO_3 and they do not possess any oxide or proton defects. It is noted that many of these materials may exhibit a degree of oxygen off-stoichiometry or hydrogen defect formation under SOFC operating conditions²⁵. Therefore, the ABO_3 materials used in this study represent a set of idealized compounds that can be used to efficiently screen materials and the off-stoichiometry analysis is considered out-of-scope for our first-pass screening study. The tertiary, quaternary, and quinary perovskites were modeled by introducing A- and/or B-site dopants in 12.5% increments with the dopant ratio ranging from 12.5% to 50%, excluding 37.5% in accordance with the earlier studies by Jacobs et al.²⁵ and Ma et al.²⁷. Also, in accordance with the aforementioned studies, a single ordering for doped compounds was considered by introducing dopant atoms as far away from each other as possible on the perovskite sublattice such that the number of permutations is tractable. Ma et al. have shown that different cation orderings, as displayed in Figures C.1-5, have little or no effect on the general electronic properties and convex hull stability²⁷. Further details regarding the computed configurations are outlined in Section C.1 of Appendix C.

The filtering methodology used for the high-throughput screening of PCC materials is presented in Figure 4.2. Our initial data set has 4793 perovskite materials with a general formula of $A_{1-x}A'_xB_{1-y}B'_yO_3$ and includes a majority of the 2913 materials analyzed by Jacobs et al.²⁵ and Ma et al.²⁷ as well as binary materials (ABO_3) taken from the Materials Project database. Here, we used four successive filters to eliminate materials that do not satisfy the requirements for effective PCCs. In the first stage (Filter 1), bandgap is used as elimination criterion and the materials exhibiting a bandgap less than 2.0 eV were eliminated from the dataset. A bandgap greater than 2.0 eV was selected to isolate compounds that are strongly insulating and suitable for electrolyte applications. The next three filters focused on identifying the materials that are stable under anodic oxidizing conditions (Filter 2), cathodic reducing conditions (Filter 3), and in the presence of CO_2 (Filter 4). The stability was determined from the energy above the convex hull of the phase diagram made from the constituent elements. A cutoff value of 40 meV/atom for E_{hull} was chosen to account for the uncertainty range of a typical DFT calculation and any material exhibiting an $E_{\text{hull}} > 40$ meV/atom for each filter were eliminated successively^{40,41}. We used the phase stability analysis tools in Pymatgen to compute multicomponent grand potential phase diagrams^{42,43}. All stability calculations were carried out under SOFC operating conditions at a typical intermediate temperature of 1073 K where the anode and cathode are open to H_2 and O_2 gas, respectively. For stability under CO_2 environment (Filter 4), the calculations were carried out in a system open to both O_2 and CO_2 . The chemical potentials of the gas molecules were calculated at typical SOFC conditions of $p(H_2) = 1$ atm and $p(H_2O) = 0.03$ atm for anode stability^{11,44}, $p(O_2) = 0.21$ atm and relative humidity of 30% for cathode stability^{25,45}, and 1 ppb CO

and $p(\text{CO}_2) = 1.00$ atm for CO_2 stability⁴⁶. Full details of these stability calculations can be found in Section C.2 of Appendix C.

Next, we evaluated the ability to form oxygen vacancy and protonic defects for the materials that passed the first three elimination criteria. The stability of a charge-neutral vacancy defect (V_{O}^{\times} in Kröger-Vink notation⁴⁷) was examined by creating an oxygen vacancy with a stoichiometry of $\text{ABO}_{3-\delta}$ ($\delta = 0.125$). All non-identical positions in the 40-atom supercell with 24 oxygen atoms were tested. For creating a charge-neutral protonic defect (OH^{\times}), a single proton is added to the oxygen that was identified as the minimum energy vacancy formation site. The defect structures were optimized using the same lattice vectors as the defect free cell. The defect formation energy (ΔE_f) for charge neutral defects is calculated utilizing the following equation⁴⁸:

$$\Delta E_f = E_{\text{defect}} - E_{\text{pristine}} + \sum_i n_i \mu_i \quad (4.1)$$

where E_{defect} and E_{pristine} correspond to the SCF energies of the relaxed supercells in the presence and absence of a defect, respectively, n_i being the number of defect atoms removed or added to the pristine supercell, and μ_i being the chemical potential of the defect atom. We conduct defect formation analysis at 0 K, and therefore, the chemical potentials of O and H are equivalent to E_{O} and E_{H} , respectively. E_{O} and E_{H} are defined with the following equations:

$$E_{\text{O}} = \frac{E_{\text{O}_2}}{2} \quad (4.2)$$

$$E_{\text{H}} = \frac{E_{\text{H}_2\text{O}} - E_{\text{O}}}{2} \quad (4.3)$$

E_{O_2} and $E_{\text{H}_2\text{O}}$ are equal to the 0 K energies for oxygen and water, respectively. We calculated the hydration energy utilizing the following equation^{29,49}:

$$\Delta E_{hydr} = 2\Delta E_{f,OH_0^\times} - \Delta E_{f,V_0^\times} \quad (4.4)$$

$\Delta E_{f,V_0^\times}$ is the charge-neutral formation of an oxygen vacancy and $\Delta E_{f,OH_0^\times}$ is the charge-neutral proton insertion energy. A detailed discussion regarding the calculations of defect formation energies and the derivation of ΔE_{hydr} is provided in Section C.1 of Appendix C.

4.4 RESULTS AND DISCUSSION

4.4.1 FILTER 1 – ELECTRONIC CONDUCTIVITY

One of the key requirements for an electrolyte material is that it should exhibit high ionic conductivity and at the same time high resistance towards electronic conductivity. Hence, we chose electronic conductivity as our first elimination criterion (Filter 1) and set a bandgap limit of 2.0 eV to isolate compounds that are strongly insulating. As displayed under Filter 1 in Figure 4.2, this filter eliminates 3,887 materials that exhibit a bandgap lower than 2.0 eV and the remaining 906 perovskites are considered for further screening. It is to be noted that the electrical conductivity analysis is done at 0 K and without considering any off-stoichiometry effects. Temperature effects such as magnetic transitions or structural changes are considered out-of-scope for this first-pass screening. A-site elemental analysis of the 906 passing compositions as displayed in Figure C.6(a) of Appendix C indicates that the alkaline earth metals Ba and Sr are the dominant A-site elements that are included in compounds that exhibit bandgap > 2.0 eV. Secondary dominant A-site elements include alkaline earth Ca, group 3 element Y, and the lanthanides La and Pr. The B-site elemental analysis is illustrated in Figure C.6(b) which suggests that the majority of the passing materials have Zr as a B-site element and Ce being the second dominant B-site element. Transition metals such as Co, Cr, Fe, and Ni

and p-block elements such as Ga, P, and Sb are the next prominent B-site elements of the identified insulating configurations.

4.4.2 FILTER 2 – THERMODYNAMIC STABILITY UNDER ANODE CONDITIONS

The second elimination criterion (Filter 2) focuses on excluding materials that are not stable under typical anode operating conditions ($T = 1073$ K, $p(\text{H}_2) = 1$ atm, and $p(\text{H}_2\text{O}) = 0.03$ atm). The energy above the convex hull (E_{hull}) at anode operating conditions was calculated for all the perovskite materials and we eliminated the materials with E_{hull} values above 0.041 eV/atom. E_{hull} acts as a measure of decomposition energy for a material and a value of $E_{\text{hull}} = 0$ means the configuration is formally stable and on the convex hull. As explained earlier in Section 2, the cutoff value of 0.041 eV/atom was chosen to account for the uncertainty range (40 meV/atom) of a typical DFT calculation^{40,41,50} and in addition, a similar value has been used in the literature for material metastability analysis in SOFC applications²⁵. This analysis eliminated 781 materials and we identified 125 perovskites that are both insulators and stable under anode operating conditions.

Further elemental analysis revealed that the materials with the following elements at the A-site, Be, Dy, Gd, Ho, Nd, Sm, and Y, were found to be unstable under anode conditions. Most of these elements are lanthanides except for the alkaline earth Be and group 3 element Y. Additionally, materials with the following B-site elements, Al, Cu, Mg, Mo, Ni, P, Pr, Re, Rh, Sb, and Zn, exhibited instability under anode operating conditions. The elemental analysis of the passing configurations is plotted in Figure C.7 of Appendix C. The primary A-site elements (Figure C.7(a)) of the passing configurations remain Ba and Sr as identified in the case of electronic conductivity

analysis (Figure C.6(a)) and Ca, Cs, La, and Rb being the prominent minority elements. Similarly, the dominant B-site element of the passing configurations remains Zr (Figure C.7(b)) with Ce, Hf, Sc, Sn, and Ti as the prominent minority elements. Transition metals Cr and Fe and group 5 metals Nb, V, and Ta, all appear in at least four of the passing configurations.

4.4.3 FILTER 3 – THERMODYNAMIC STABILITY UNDER CATHODE CONDITIONS

The next filter (Filter 3) focuses on identifying materials that are stable under typical cathode operating conditions of $T = 1073$ K, $p(\text{O}_2) = 0.21$ atm, and a relative humidity of 30%. We computed the energy above the convex hull for all materials under cathode operating conditions. Among the 125 perovskites identified from Filter 2, 9 materials were found to be unstable ($E_{\text{hull}} > 40$ meV/atom) under cathode operating conditions and thus eliminated from the data set. The materials that were found to be unstable under cathode operating conditions are, $\text{Ba}_{0.875}\text{Sn}_{0.125}\text{ZrO}_3$, $\text{Ba}_{0.75}\text{Sn}_{0.25}\text{ZrO}_3$, $\text{Sr}_{0.75}\text{Ca}_{0.25}\text{Zr}_{0.75}\text{V}_{0.25}\text{O}_3$, $\text{La}_{0.5}\text{Ca}_{0.5}\text{Zr}_{0.75}\text{Fe}_{0.25}\text{O}_3$, $\text{Pr}_{0.5}\text{Sr}_{0.5}\text{Zr}_{0.75}\text{Fe}_{0.25}\text{O}_3$, $\text{Y}_{0.5}\text{Ca}_{0.5}\text{Zr}_{0.75}\text{Fe}_{0.25}\text{O}_3$, $\text{Y}_{0.5}\text{Ca}_{0.5}\text{Zr}_{0.75}\text{Mn}_{0.25}\text{O}_3$, $\text{BaNb}_{0.5}\text{Cr}_{0.5}\text{O}_3$, and $\text{SrZr}_{0.75}\text{Re}_{0.25}\text{O}_3$. Further analysis indicated that the A-site elements, Pr and Sn, and B-site element Re are completely eliminated from the passing configurations. The 116 perovskite materials that passed these first 3 filters are listed in Table C.2 and the elemental analysis of these passing configurations are plotted in Figure C.8 of Appendix C. As observed earlier, Ba and Sr remain the dominant A-site elements and Zr is the dominant B-site element in these passing configurations. Next, we identified 15 configurations (Table C.3) that are stable under anodic and cathodic conditions but yield a bandgap between 1.0 and 2.0 eV.

These materials could be potential candidates for electrolyte applications, but we did not conduct oxygen vacancy and hydration analysis on these materials. The elemental composition of these configurations includes mixed A-sites composed of Ba, Ca, Sr, and Rb; and mainly a Zr majority B-site doped with Mn, Cr, V, Os, Rh, and Ru. Two unique configurations that do not include Zr are $\text{Ba}_{0.5}\text{Rb}_{0.5}\text{Ce}_{0.5}\text{Nb}_{0.5}\text{O}_3$ and $\text{Ba}_{0.5}\text{Rb}_{0.5}\text{Ce}_{0.5}\text{Ta}_{0.5}\text{O}_3$.

In agreement with the earlier report by Islam et al.²⁹, we find that Zr and V (and group 5 elements Nb and Ta) configurations generally are water stable. Our calculations also predicted good stability for Ti-containing configurations under humid conditions which contradicts the observation by these authors. Most Co- and Ni-containing materials were eliminated based on their instability under anode operating conditions. Cr, Fe, Tc, and Zn are the primary high group number d-block elements that are present in the materials passing Filter 3. We note here that the benchmarking PCCs, BCO and BZO are also included in the list of materials passing the first 3 filters which further suggests that our calculations are consistent with the experimentally observed stability of these materials¹² as discussed in Section C.3.2 of Appendix C.

4.4.5 FILTER 4 –THERMODYNAMIC STABILITY UNDER CO₂ CONDITIONS

One of the main drawbacks of BCO-based electrolytes is known to be the material instability in the presence of CO₂. Hence, we examined the thermodynamic stability of the perovskite materials in our data set under a CO₂ environment (T = 1073 K, 1 ppb CO, and p(CO₂) = 1.00 atm) by calculating the energy above the convex hull. This screening step (Filter 4) eliminates another 73 materials from the data set of 116 materials identified from Filter 3 leaving only 43 materials (Table 4.1) that are stable under a wide range of

environmental conditions and also exhibit high electronic resistivity. We note that BZO passes all the four filters in agreement with experimental observation^{51,52}. Other passing binary perovskite oxides include SrZrO₃ and YCrO₃. Overall, Ba (A-site) and Zr (B-site) are the predominant elements in the 43 configurations that passed all the four filters and Ce was eliminated completely from the list after CO₂ stability test. Other prominent alkaline earth A-site elements include Sr and Ca that are present in 24 and 7 configurations, respectively. Non-alkaline earth A-site elements including Cd, Rb, and Zn are also present in these configurations but only at low concentrations (e.g., 12.5%). Other prominent B-site elements include Hf, Sn, and Ti which are present in 6, 5, and 6 configurations, respectively. The presence of Zr, Hf and Ti in the passing configurations suggests that the presence of group 4 elements at the B-site could improve stability in the presence of CO₂ and water-containing conditions. Lastly, the transition metal Fe is present in 3 configurations and these configurations include more unique elements such as Bi and the group 5 metals, Nb and Ta.

4.4.6 VACANCY AND HYDRATION FORMATION ENERGY ANALYSIS

The ability to incorporate a high concentration of protons in the lattice is another key requirement for PCC electrolytes to achieve high proton conductivity. In perovskite oxides, this process occurs by the creation of an oxygen vacancy, which in general is promoted in the presence of an acceptor-dopant, and the hydration process at the vacancy site enables the proton incorporation. Hence, we calculated the oxygen vacancy formation and hydration energies for the 116 perovskite oxides that passed the first three filters. The calculated vacancy formation energies and hydration energies of these materials with respect to doping concentrations at A- and B-sites are displayed in Figures

4.3(a-d) with BCO and BZO as the benchmark materials. In Figure 4.3(a), the materials are organized by the extent of A-site doping such that $A_{1.0}$ refers to the non-doped configuration and $A_{0.875}$, $A_{0.75}$, and $A_{0.5}$ correspond to the materials with 12.5%, 25%, and 50% doping at the A-site, respectively. Among the 116 materials, 55 materials have non-doped A-site configuration ($A_{1.0}$), 26 materials have the $A_{0.75}$ configuration, and the $A_{0.875}$ and $A_{0.5}$ configurations were found in 25 and 10 materials, respectively. Figure 4.3(b) provides a magnified view around the benchmark BZO based on Figure 4.3(a). In Figure 4.3(c), the vacancy formation and hydration energies of the 116 materials are organized with respect to B-site doping, where $B_{1.0}$ refers to a non-doped B-site material and $B_{0.875}$, $B_{0.75}$, and $B_{0.5}$ correspond to the materials with 12.5%, 25%, and 50% doping at the B-site, respectively. Figure 4.3(d) provides a magnified view around the benchmark BZO based on Figure 4.3(c).

Four different regions are identified in Figure 4.3(a) and (c) that can be classified as, the Sn-containing region ($\Delta E_{\text{vac}} = 4.3 - 5.0$ eV, $\Delta E_{\text{hydr}} = 1.0 - 3.0$ eV), the acceptor-dopant region ($\Delta E_{\text{vac}} = 2.7 - 3.5$ eV, $\Delta E_{\text{hydr}} = -5.0 - -3.0$ eV), the BCO-like region ($\Delta E_{\text{vac}} = 4.5 - 5.5$ eV, $\Delta E_{\text{hydr}} = -2.0 - -1.0$ eV), and the BZO-like region ($\Delta E_{\text{vac}} = 6.0 - 7.0$ eV, $\Delta E_{\text{hydr}} = -1.0 - 1.0$ eV). A linear-like relationship spans across the three regions including the acceptor-dopant, BCO-like, and BZO-like regions. 70.7 % of A-site doped (e.g., $A_{0.875}$, $A_{0.75}$, and $A_{0.5}$) materials and 69.0 % of B-site doped (e.g., $B_{0.875}$, $B_{0.75}$, and $B_{0.5}$) materials exhibit oxygen vacancy formation energy values below 5.5 eV). Figure 4.3(b) displays all configurations located near the BZO-like region displaying a mixture of $A_{1.0}$, $A_{0.875}$, $A_{0.75}$, and $A_{0.5}$ materials with an $A_{1.0}$ cluster at higher oxygen vacancy defect and hydration energies relative to BZO. $A_{0.75}$ configurations primarily exhibit

better vacancy formation (0.7 – 1.0 eV lower) and hydration activity (0.3 – 0.6 eV lower) relative to BZO. Significant clustering of $B_{1.0}$ materials occurs in the BZO-like region with a small cluster in the acceptor-dopant region as displayed in Figures 4.3(c-d). In addition, a prominent cluster was found around the acceptor-dopant region for the $B_{0.875}$ configurations. $B_{0.75}$ and $B_{0.5}$ configurations cluster around the Sn-containing region and the intermediate zone between the BCO-like and BZO-like regions, especially for vacancy formation energies between 5.8 and 6.4 eV. We note that the outlier $A_{1.0}$ configuration, $BaPt_{0.125}Zr_{0.875}O_3$, located at the top left corner of Figures 4.3(a) and 4.3(c) displays excellent vacancy formation activity (~ 3 eV) but has Sn-like hydration activity (~ 2 eV).

Next, we analyzed the role of various elements in determining the oxygen vacancy formation and hydration activity for the 116 perovskites by categorizing them into different groups as displayed in Figure 4.4. As discussed earlier, materials with acceptor-dopant elements exhibit good activity for both vacancy formation and hydration process and most of these materials have $A_{1.0}$ and $B_{0.875}$ configurations (e.g., Figures 4.3(a) & 4.3(c)). Other materials that fall into this category are $Cs_{0.125}Ba_{0.875}ZrO_3$, $Rb_{0.125}Ba_{0.875}ZrO_3$, $Cs_{0.125}Sr_{0.875}ZrO_3$, $Rb_{0.125}Sr_{0.875}ZrO_3$, $Sr_{0.25}Ba_{0.75}In_{0.125}Zr_{0.875}O_3$, $Sr_{0.25}Ba_{0.75}Sc_{0.125}Zr_{0.875}O_3$, $Sr_{0.25}Ba_{0.75}Y_{0.125}Zr_{0.875}O_3$, and $La_{0.25}Sr_{0.75}Sc_{0.25}Zr_{0.75}O_3$. The categorized scattered plots in Figure 4.4 suggest that the materials fall into this acceptor-doped region have either alkali metals doping the A-site (Figure 4.4(a)), or group 3 (Figure 4.4(b)) and group 13 (Figure 4.4(g)) elements doping the B-site. Figure 4.4(a) further suggests that in addition to the high activity regime the alkali metals also exhibit another regime with stagnant hydration activity across a range of vacancy formation

energy. High defect formation activity occurs with an A-site doping ratio of 12.5% and a non-doped Zr B-site backbone. The introduction of a small percentage of the 1^+ -ion at the A-site oxidizes Zr such that hydration becomes favorable upon Zr reduction. For BCO-like alkali metal-containing configurations, B-site doping with group 5 elements (mostly V, Figure 4.4(d)) can also alter the oxidation state of Zr during vacancy formation and hydration processes. B-site doping with group 3 elements (Sc and Y, Figure 4.4(b)) also displays two regions of activity, the acceptor-dopant region and BZO-like region. The materials at the acceptor-dopant region are composed of an alkaline earth metal at the A-site and Zr at the B-site doped with 12.5% of a group 3 metal. Here, the acceptor-dopants, Sc^{3+} or Y^{3+} enable creation of oxygen vacancies which promotes the hydration process. Our results are consistent with experimental observations that acceptor-doped perovskites such as Y-doped BaZrO_3 (BZY) conformers are stable and display ionic conductivity^{9,53}. This acceptor-dopant activity was also observed for group 13 elements (Ga and In) as displayed in Figure 4.4(g). These elements are more active for vacancy formation but exhibit approximately 0.3 – 0.5 eV higher hydration energies relative to group 3 elements. Among the d-block elements, only Cr falls into this acceptor-dopant region when it is present in small concentrations (e.g., 12.5%) on the B-site as displayed in the bottom-left of Figure 4.4(e). This analysis suggests that doping the A-site with alkali metals or doping the B-site with both groups 3 and 13 elements can improve both the vacancy formation and hydration activities of the PCC materials. We note that BZY conformers are in general affected by the acceptor-dopant trapping effect where large proton rotation barriers isolate proton transportation to other oxygen sites in the material⁵⁴. Previous DFT studies outlined that Rb- and Cs-containing BZO conformers display a

localized or weaker proton trapping and similar proton migration barriers to BZY conformers^{19,55}. Examination of this effect on proton migration barriers (e.g., migration and transportation) is considered out-of-scope for this study (see Section C.3.3 of Appendix C).

Materials that have B-site doping with the p-block elements (Sn, Ge, and Bi; Figure 4.4(g)) fall into the Sn-containing region which exhibit slightly lower oxygen vacancy formation energies but higher hydration energies relative to BCO. Whereas, doping with lanthanides (mostly Ce, Figure 4.4(h)) results in similar vacancy formation activity but better hydration activity compared to BCO. Bader charge analysis provided in Table C.4 of Appendix C suggests that Ce⁴⁺ is reduced to Ce³⁺ and re-oxidized to Ce⁴⁺ during vacancy formation and hydration processes, respectively, and thus, the hydration activity is promoted on Ce-containing materials. On the other hand, Sn is reduced from 4⁺ to 2⁺ state during vacancy formation process and partially oxidizes back to the unfavorable 3⁺ state during hydration process. Therefore, materials with these group 14 elements exhibit reasonable vacancy formation activity but lower hydration activity. Previous experimental⁵⁶ and DFT⁵⁷ studies have shown Sn is an effective dopant when co-doped with acceptor-dopant Y in BZO to form BSYZ. BSYZ displays good stability and ionic conductivity but is affected by the proton trapping effect at high Y concentrations²⁰.

The perovskite oxides in the BCO-like region display intermediate vacancy formation and hydration energies and most of these materials are composed of A_{1.0} configuration with mixed B-site doping ratios of 12.5%, 25%, and 50% (Figures 4.3(a) & 3(c)). In addition to the Ce-containing lanthanide configurations (Figure 4.4(h)) discussed

above, the materials in the BCO-like region are composed of an alkali metal Rb (Figure 4.4(a)), group 5 elements V, Nb, and Ta (Figure 4.4(d)), and d-block elements Fe, Cr, Cd, and Zn (Figures 4.4(e) & 4.4(f)). The alkali metal-containing configuration in the BCO-like region, $\text{Rb}_{0.25}\text{Ba}_{0.75}\text{Ta}_{0.25}\text{Ce}_{0.75}\text{O}_3$ is free of Zr and is composed of Ce and the group 5 element Ta at the B-site, and therefore, this is a promising configuration for CO_2 -free conditions as lower sintering temperatures are expected. All other configurations with group 5 and d-block elements do not contain Ce. Regarding configurations containing d-block elements that can readily adopt multiple oxidation states, three Fe-containing oxides, $\text{BaFe}_{0.125}\text{Ta}_{0.125}\text{Zr}_{0.875}\text{O}_3$, $\text{BaFe}_{0.125}\text{Nb}_{0.125}\text{Zr}_{0.875}\text{O}_3$, and $\text{Bi}_{0.125}\text{Ba}_{0.875}\text{Fe}_{0.125}\text{Zr}_{0.875}\text{O}_3$, the Co-containing oxide $\text{La}_{0.25}\text{Ba}_{0.75}\text{Co}_{0.125}\text{Zr}_{0.875}\text{O}_3$ and the Cr-containing configuration, $\text{La}_{0.25}\text{Sr}_{0.75}\text{Cr}_{0.25}\text{Zr}_{0.75}\text{O}_3$ exhibit hydration energies similar to BCO. The Ce-containing configurations (Figure 4.4(h)) have a general stoichiometry of $\text{A}^{2+}\text{Zr}_x\text{Ce}_{1-x}\text{O}_3$. This is a classic strategy of mixing BZO and BCO without including the acceptor-dopant Y⁵². This analysis suggests that co-doping the B-site with Fe and a group 5 element could yield BCO-like defect formation activity.

The perovskite oxides in the BZO-like region display intermediate hydration energies but high vacancy formation energies (Figure 4.3(a)). Many of these configurations have co-doped alkaline earth elements such as Sr and Ba at the A-site and Zr-containing configurations that are co-doped with other group 4 elements such as Ti and Hf at the B-site. Among the group 4 elements, materials with Ti dopant exhibit better vacancy formation and hydration activity relative to BZO, whereas Hf-containing configurations exhibit similar or less activity than BZO (Figure 4.4(c)). A couple of other materials in the BZO-like region contain alkali metals at high concentrations (50%) at the

A-site together with group 5 metals at high concentrations (50%) at the B-site and exhibit slightly better hydration activity than BZO (Figures 4.4(a) & 4.4(d)). Most of the La-containing configurations in the BZO-like region also have the group 3 element Sc in the B-site at low doping ratios (12.5 – 25%) and exhibit slightly better vacancy formation activity than BZO (Figures 4.4(b) & 4.4(h)). Materials with d-block elements do not appear in the BZO-like region, whereas one configuration with the p-block element Si has similar activity as BZO (Figure 4.4(e)). Analysis of this region mainly suggests that doping with Ti can improve the activity relative to BZO.

Figure 4.5 displays the vacancy formation and hydration energies of the 43 configurations (Table 4.1) that passed all the four filters including the CO₂ stability test and are categorized with respect to A- and B-site doping ratios. We note here that the application of Filter 4 eliminates all materials in the acceptor-dopant region ($\Delta E_{\text{vac}} = 2.7 - 3.5$ eV, $\Delta E_{\text{hydr}} = -5.0 - -3.0$ eV; Figure 4.3), except for Ba_{0.875}Rb_{0.125}ZrO₃, suggesting that these materials are not stable under a 1 atm CO₂ environment. Only two configurations, BaPt_{0.125}Zr_{0.875}O₃ and SrMn_{0.125}Zr_{0.875}O₃, exhibit vacancy formation energies (2.9 – 3.2 eV) similar to that of acceptor-dopant materials, however, the hydration energies (-1.2 – 1.5 eV) are in the range of BCO-like or Sn-containing materials. While BCO itself did not pass the CO₂ stability test, other materials in the BCO-like region that exhibit similar or better vacancy formation and hydration activity are: BaFe_{0.125}Ta_{0.125}Zr_{0.875}O₃, BaFe_{0.125}Nb_{0.125}Zr_{0.875}O₃, Bi_{0.125}Ba_{0.875}Fe_{0.125}Zr_{0.875}O₃, BaRb_{0.125}Zr_{0.875}O₃, BaCd_{0.125}Zr_{0.875}O₃, and BaIr_{0.125}Zr_{0.875}O₃. In Appendix C, Figure C.9 displays the hydration energy versus vacancy formation energy for all the 116 materials that passed the first three filters and organized with respect to their stability under CO₂

environment. This figure clearly shows that most materials in the better defect formation activity region ($\Delta E_{\text{vac}} < 5$ eV and $\Delta E_{\text{hydr}} < -1.5$ eV) are either metastable ($E_{\text{hull}} = 0.041$ - 0.081 eV/atom) or unstable ($E_{\text{hull}} > 0.081$ eV/atom) in the presence of CO_2 . The metastable materials may be suitable for low pressure CO_2 (e.g., $p(\text{CO}_2) < 1.00$ atm) applications and are listed in Table C.5. Among these metastable materials, notable Ce-free materials that are BCO-like include the following: $\text{Rb}_{0.125}\text{Ba}_{0.875}\text{V}_{0.125}\text{Zr}_{0.875}\text{O}_3$, $\text{Rb}_{0.125}\text{Sr}_{0.875}\text{V}_{0.125}\text{Zr}_{0.875}\text{O}_3$, $\text{Zn}_{0.125}\text{Ba}_{0.875}\text{ZrO}_3$, and $\text{Cs}_{0.125}\text{Ba}_{0.875}\text{ZrO}_3$. For Zn- (and Cd-containing) configurations, Jeong et al. used DFT calculations to show that significant proton trapping affects Zn-doped BZO limiting its practical applicability⁵⁸. Overall, our analysis suggests that A-site doping with low concentration of an alkali metal complimented with low concentration group 5 metal doping at the B-site is an effective strategy to generate thermodynamically stable perovskite-based PCCs that are strongly insulating and adequate ionic conductors.

4.4.7 SECONDARY FILTERING FOR ELECTRODE MATERIALS

A secondary screening process used to propose materials that could have potential use for electrode applications is described in Figure 4.6. Since electrode materials should exhibit good electronic conductivity, our first elimination criterion (Filter 1a) focuses on identifying materials that exhibit smaller bandgap (< 0.5 eV) and we found 2636 materials out of the initial 4793 data set satisfy this criterion. These materials are further tested for stability under anode (Filter 2a) and cathode (Filter 2b) operating conditions as explained earlier for PCC materials screening. We found 341 materials that passed the anode stability test and only 50 materials passed the cathode stability test and could have potential use as an anode and cathode, respectively. We did not perform any secondary

analysis such as vacancy formation or ionic conductivity on these set of materials as this is considered out-of-scope for this study.

We examined the elemental composition of configurations that are electrically active (e.g., Filter 1a passing) in Figure C.10. For the A-site, the alkaline earth elements Ba and Sr are the most common elements with frequencies both above one thousand and Ca being the third most common element. Like the electrically inactive results (e.g., Filter 1), lanthanides La and Pr are the second most common elements. Group 3 element Y and other lanthanide elements such as Ce, Dy, Er, Gd, Nd, and Sm also occur at the A-site. A-site elements that pass Filter 1a but do not pass Filter 1 include lanthanides Ce and Er and alkali metals Li and Na. For the B-site, Fe and Zr are the most common elements followed by transition metals Co, Mn, and Ni, group 5 element Nb, and lanthanide Ce. Prominent B-site minority elements include group 5 elements Ta and V, group 15 elements P and Sb, and common 2⁺ elements such as Cu and Zn. B-site elements that pass Filter 1a but do not pass Filter 1 include Be, La, Os, Pd, Ru, and Sr. Lastly, in contrast to the electrically inactive results, configurations typically include low concentrations of Zr at the B-site.

4.5 CONCLUSION

In this study, we coupled first-principles materials science and a high-throughput screening methodology to analyze a wide variety of perovskite oxides for their potential use as proton conducting electrolyte materials. Starting from a data set of 4793 distinct perovskites with binary, tertiary, quaternary, and quinary compositions, our successive screening methodology focused on identifying materials that are strongly insulating, thermodynamically stable under various reaction environments, and have a better ability

to incorporate protons. At each filtering stage we have analyzed the elemental identity and the role of A- and B-site doping in the passing materials such that the desirable macroscopic properties can be tuned for the specific applications. Elemental analysis of the 116 materials that passed the electronic conductivity and thermodynamic stability tests revealed that most of these materials possess Ba and Sr at the A-site with Zr being the dominant element at the B-site. Less dominant elements that appear in at least eight configurations are Ca, La, and Rb at the A-site and Ce, Hf, Sc, Sn, and Ti at the B-site. In terms of doping content, many of the promising materials possess a non-doped A-site with Zr-containing B-site doped configurations. The second dominant configurations passing the stability tests include 12.5% and 25% doping at the A-site or 12.5% doping at the B-site suggesting that minimal doping is favorable for water stability. Our results are consistent with the experimental observation that the activity and stability of the state-of-the-art PCC material family based on Y-doped BZO is improved when the doping ratio is kept under 20%^{59,60}.

Oxygen vacancy formation and hydration energies of the 116 materials were calculated as a measure of their ability to incorporate protons and the materials were categorized into four regions based on their activity. Materials that fall into the acceptor-dopant region exhibit high activity for both vacancy formation and hydration processes and many of these materials have either alkali metal doped A-sites or B-sites doped with both groups 3 and 13 elements. A second set of materials identified in the Sn-containing region exhibit reasonable vacancy formation activity, but lower hydration activity and these materials mainly have B-sites doped with the p-block elements such as Sn, Ge, and Bi. The third region around the benchmark material BCO consists of materials exhibiting

intermediate vacancy formation and hydration energies and most of these materials have non-doped A-site configuration with mixed B-site doping ratios of 12.5%, 25%, and 50%. A fourth region includes configurations with an A-site co-doped with alkaline earth metals and a non-doped Zr B-site that behave similarly to the BZO benchmark material and exhibit poor activity for both vacancy formation and hydration processes. Although the materials in the acceptor-dopant region exhibit better defect formation activity, many of these materials are eliminated while applying the fourth filter that tests the stability under a CO₂ environment. The promising configurations identified from our high-throughput screening of PCC electrolytes that are strongly insulating, thermodynamically stable in the presence of H₂O and CO₂ (including borderline metastability under CO₂ with $E_{\text{hull}} < 0.08$ eV/atom) are: BaFe_{0.125}Ta_{0.125}Zr_{0.875}O₃, BaFe_{0.125}Nb_{0.125}Zr_{0.875}O₃, Bi_{0.125}Ba_{0.875}Fe_{0.125}Zr_{0.875}O₃, SrMn_{0.125}Zr_{0.875}O₃, BaRb_{0.125}Zr_{0.875}O₃, Rb_{0.125}Ba_{0.875}V_{0.125}Zr_{0.875}O₃, Rb_{0.125}Sr_{0.875}V_{0.125}Zr_{0.875}O₃, and Cs_{0.125}Ba_{0.875}ZrO₃. The acceptor-dopant configuration BaZr_{0.875}(Sc,Y)_{0.125}O₃ is also stable and active. Finally, a secondary screening analysis was also provided to identify stable electrode materials with good electronic conductivity.

In summary, this study serves to aid the fundamental understanding and principles for the design of perovskite-based proton conducting electrolytes. We elaborate on the role of elemental identity and doping ratios on thermodynamic stability and defect formation activity. Insights and guidelines obtained from this study could enable the selection of materials for various specific applications that require high electronic resistivity or good electronic conductivity, chemical stability against high oxidizing and reducing atmospheres and good proton incorporation ability. Future work will focus on

testing a greater number of quaternary and quinary configurations and compute proton migration barriers to better understand the elemental role on the proton trapping effect.

4.6 ACKNOWLEDGEMENTS

This work was supported by the National Science Foundation under Grant No. DMR- 1832809 and partially supported by the South Carolina Smart State Center for Strategic Approaches to the Generation of Electricity (SAGE). Computing resources are provided by the U.S. Department of Energy facility located at National Energy Research Scientific Computing Center (NERSC) under Contract No. DE-AC02-05CH11231 and ACCESS facilities located at Texas Advanced Computing Center (TACC), San Diego Supercomputer Center (SDSC), and Purdue University (grant no. TG-CTS090100). Finally, computing resources provided by the University of South Carolina's High Performance Computing (HPC) group are gratefully acknowledged.

4.7 BIBLIOGRAPHY

- (1) McIntosh, S.; Gorte, R. J. Direct Hydrocarbon Solid Oxide Fuel Cells. *Chem. Rev.*, **2004**, *104* (10), 4845–4866. 10.1021/cr020725g.
- (2) Wachsman, E. D.; Lee, K. T. Lowering the Temperature of Solid Oxide Fuel Cells. *Science*, **2011**, *334* (6058), 935–939. 10.1126/science.1204090.
- (3) Ormerod, R. M. Solid Oxide Fuel Cells. *Chem. Soc. Rev.*, **2003**, *32* (1), 17–28. 10.1039/b105764m.
- (4) Steele, B. C. H.; Heinzel, A. Materials for Fuel-Cell Technologies. *Nature*, **2001**, *414* (6861), 345–352. 10.1038/35104620.
- (5) Fergus, J. W. Electrolytes for Solid Oxide Fuel Cells. *J. Power Sources*, **2006**, *162* (1), 30–40. 10.1016/j.jpowsour.2006.06.062.
- (6) Jaiswal, N.; Tanwar, K.; Suman, R.; Kumar, D.; Upadhyay, S.; Parkash, O. A Brief Review on Ceria Based Solid Electrolytes for Solid Oxide Fuel Cells. *J. Alloys Compd.*, **2019**, *781*, 984–1005. 10.1016/j.jallcom.2018.12.015.

- (7) Gao, Z.; Mogni, L. v.; Miller, E. C.; Railsback, J. G.; Barnett, S. A. A Perspective on Low-Temperature Solid Oxide Fuel Cells. *Energy Environ. Sci.*, **2016**, *9* (5), 1602–1644. 10.1039/C5EE03858H.
- (8) Hossain, S.; Abdalla, A. M.; Jamain, S. N. B.; Zaini, J. H.; Azad, A. K. A Review on Proton Conducting Electrolytes for Clean Energy and Intermediate Temperature-Solid Oxide Fuel Cells. *Renew. Sustain. Energy Rev.*, **2017**, *79*, 750–764. 10.1016/j.rser.2017.05.147.
- (9) Fabbri, E.; Pergolesi, D.; Traversa, E. Materials Challenges toward Proton-Conducting Oxide Fuel Cells: A Critical Review. *Chem. Soc. Rev.* **2010**, *39* (11), 4355. 10.1039/b902343g.
- (10) Fallah Vostakola, M.; Amini Horri, B. Progress in Material Development for Low-Temperature Solid Oxide Fuel Cells: A Review. *Energies*, **2021**, *14* (5), 1280. 10.3390/en14051280.
- (11) Singh, K.; Kannan, R.; Thangadurai, V. Perspective of Perovskite-Type Oxides for Proton Conducting Solid Oxide Fuel Cells. *Solid State Ion.*, **2019**, *339*, 114951. 10.1016/j.ssi.2019.04.014.
- (12) Tanner, C. W.; Virkar, A. v. Instability of BaCeO₃ in H₂O-Containing Atmospheres. *J. Electrochem. Soc.*, **1996**, *143* (4), 1386–1389. 10.1149/1.1836647.
- (13) Gregori, G.; Merkle, R.; Maier, J. Ion Conduction and Redistribution at Grain Boundaries in Oxide Systems. *Prog. Mater. Sci.*, **2017**, *89*, 252–305. 10.1016/j.pmatsci.2017.04.009.
- (14) Gopalan, S.; Virkar, A. v. Thermodynamic Stabilities of SrCeO₃ and BaCeO₃ Using a Molten Salt Method and Galvanic Cells. *J. Electrochem. Soc.*, **1993**, *140* (4), 1060–1065. 10.1149/1.2056197.
- (15) Zuo, C.; Zha, S.; Liu, M.; Hatano, M.; Uchiyama, M. Ba(Zr_{0.1}Ce_{0.7}Y_{0.2})O_{3-δ} as an Electrolyte for Low-Temperature Solid-Oxide Fuel Cells. *Adv. Mat.*, **2006**, *18* (24), 3318–3320. 10.1002/adma.200601366.

- (16) Sawant, P.; Varma, S.; Wani, B. N.; Bharadwaj, S. R. Synthesis, Stability and Conductivity of $\text{BaCe}_{0.8-x}\text{Zr}_x\text{Y}_{0.2}\text{O}_{3-\delta}$ as Electrolyte for Proton Conducting SOFC. *Int. J. Hydrog. Energy*, **2012**, *37* (4), 3848–3856. 10.1016/j.ijhydene.2011.04.106.
- (17) Liu, Z.; Wang, X.; Liu, M.; Liu, J. Enhancing Sinterability and Electrochemical Properties of $\text{Ba}(\text{Zr}_{0.1}\text{Ce}_{0.7}\text{Y}_{0.2})\text{O}_{3-\delta}$ Proton Conducting Electrolyte for Solid Oxide Fuel Cells by Addition of NiO. *Int. J. Hydrog. Energy*, **2018**, *43* (29), 13501–13511. 10.1016/j.ijhydene.2018.05.089.
- (18) Lyagaeva, J.; Antonov, B.; Dunyushkina, L.; Kuimov, V.; Medvedev, D.; Demin, A.; Tsiakaras, P. Acceptor Doping Effects on Microstructure, Thermal and Electrical Properties of Proton-Conducting $\text{BaCe}_{0.5}\text{Zr}_{0.3}\text{Ln}_{0.2}\text{O}_{3-\delta}$ (Ln = Yb, Gd, Sm, Nd, La or Y) Ceramics for Solid Oxide Fuel Cell Applications. *Electrochim. Acta*, **2016**, *192*, 80–88. 10.1016/j.electacta.2016.01.144.
- (19) Løken, A.; Saeed, S. W.; Getz, M. N.; Liu, X.; Bjørheim, T. S. Alkali Metals as Efficient A-Site Acceptor Dopants in Proton Conducting BaZrO_3 . *J. Mater. Chem. A*. **2016**, *4* (23), 9229–9235. 10.1039/c6ta01446a.
- (20) Dawson, J. A.; Tanaka, I. Proton Trapping in y and Sn Co-Doped BaZrO_3 . *J. Mater. Chem. A*. **2015**, *3* (18), 10045–10051. 10.1039/c5ta01450f.
- (21) Zhou, Y.; Guan, X.; Zhou, H.; Ramadoss, K.; Adam, S.; Liu, H.; Lee, S.; Shi, J.; Tsuchiya, M.; Fong, D. D.; Ramanathan, S. Strongly Correlated Perovskite Fuel Cells. *Nature*, **2016**, *534* (7606), 231–234. 10.1038/nature17653.
- (22) Nico, C.; Monteiro, T.; Graça, M. P. F. Niobium Oxides and Niobates Physical Properties: Review and Prospects. *Prog. Mater. Sci.*, **2016**, *80*, 1–37. 10.1016/j.pmatsci.2016.02.001.
- (23) Zhao, L.; He, B.; Lin, B.; Ding, H.; Wang, S.; Ling, Y.; Peng, R.; Meng, G.; Liu, X. High Performance of Proton-Conducting Solid Oxide Fuel Cell with a Layered $\text{PrBaCo}_2\text{O}_{5+\delta}$ Cathode. *J. Power Sources*, **2009**, *194* (2), 835–837. 10.1016/j.jpowsour.2009.06.010.
- (24) Malavasi, L.; Fisher, C. A. J.; Islam, M. S. Oxide-Ion and Proton Conducting Electrolyte Materials for Clean Energy Applications: Structural and Mechanistic Features. *Chem. Soc. Rev.*, **2010**, *39* (11), 4370–4387. 10.1039/b915141a.

- (25) Jacobs, R.; Mayeshiba, T.; Booske, J.; Morgan, D. Material Discovery and Design Principles for Stable, High Activity Perovskite Cathodes for Solid Oxide Fuel Cells. *Adv. Energy Mater.*, **2018**, *8* (11). 10.1002/aenm.201702708.
- (26) Jacobs, R.; Liu, J.; Na, B. T.; Guan, B.; Yang, T.; Lee, S.; Hackett, G.; Kalapos, T.; Abernathy, H.; Morgan, D. Unconventional Highly Active and Stable Oxygen Reduction Catalysts Informed by Computational Design Strategies. *Adv. Energy Mater.*, **2022**, *12* (25). 10.1002/aenm.202201203.
- (27) Ma, T.; Jacobs, R.; Booske, J.; Morgan, D. Discovery and Engineering of Low Work Function Perovskite Materials. *J. Mater. Chem. C*, **2021**, *9*, 12778–12790. 10.1039/D1TC01286J.
- (28) Jacobs, R.; Luo, G.; Morgan, D. Materials Discovery of Stable and Nontoxic Halide Perovskite Materials for High-Efficiency Solar Cells. *Adv. Funct. Mater.*, **2019**, *29* (23). 10.1002/adfm.201804354.
- (29) Islam, M. S.; Wang, S.; Hall, A. T.; Mo, Y. First-Principles Computational Design and Discovery of Solid-Oxide Proton Conductors. *Chem. Mater.*, **2022**, *34* (13), 5938–5948. 10.1021/acs.chemmater.2c00867.
- (30) Kresse, G.; Furthmüller, J. Efficient Iterative Schemes for *Ab Initio* Total-Energy Calculations Using a Plane-Wave Basis Set *Phys. Rev. B*, **1996**, *54* (16), 11169–11186. 10.1103/PhysRevB.54.11169.
- (31) Perdew, J. P.; Yue, W. Accurate and Simple Density Functional for the Electronic Exchange Energy: Generalized Gradient Approximation. *Phys. Rev. B*, **1986**, *33* (12), 8800–8802. 10.1103/PhysRevB.33.8800.
- (32) Perdew, J. P.; Wang, Y. Accurate and Simple Analytic Representation of the Electron-Gas Correlation Energy. *Phys. Rev. B*, **1992**, *45* (23), 079904. 10.1103/PhysRevB.45.13244.
- (33) Kresse, G.; Joubert, D. From Ultrasoft Pseudopotentials to the Projector Augmented-Wave Method. *Phys. Rev. B*, **1999**, *59* (3), 1758–1775. 10.1103/PhysRevB.59.1758.
- (34) Blöchl, P. E. Projector Augmented-Wave Method. *Phys. Rev. B*, **1994**, *50* (24), 17953–17979. 10.1103/PhysRevB.50.17953.

- (35) Ong, S. P.; Richards, W. D.; Jain, A.; Hautier, G.; Kocher, M.; Cholia, S.; Gunter, D.; Chevrier, V. L.; Persson, K. A.; Ceder, G. Python Materials Genomics (Pymatgen): A Robust, Open-Source Python Library for Materials Analysis. *Comput. Mater. Sci.*, **2013**, *68*, 314–319. 10.1016/j.commatsci.2012.10.028.
- (36) Jain, A.; Ong, S. P.; Hautier, G.; Chen, W.; Richards, W. D.; Dacek, S.; Cholia, S.; Gunter, D.; Skinner, D.; Ceder, G.; Persson, K. A. Commentary: The Materials Project: A Materials Genome Approach to Accelerating Materials Innovation. *APL Mater.*, **2013**, *1* (1), 011002. 10.1063/1.4812323.
- (37) Dudarev, S. L.; Botton, G. A.; Savrasov, S. Y.; Humphreys, C. J.; Sutton, A. P. Electron-Energy-Loss Spectra and the Structural Stability of Nickel Oxide: An LSDAU Study. *Phys. Rev. B*, **1998**, *57* (3). 10.1103/PhysRevB.57.1505.
- (38) Wang, L.; Maxisch, T.; Ceder, G. Oxidation Energies of Transition Metal Oxides within the GGA+U Framework. *Phys. Rev. B*, **2006**, *73* (19). 10.1103/PhysRevB.73.195107.
- (39) Monkhorst, H. J.; Pack, J. D. Special Points for Brillouin-Zone Integrations. *Phys. Rev. B*, **1976**, *13* (12). 10.1103/PhysRevB.13.5188.
- (40) Wu, Y.; Lazic, P.; Hautier, G.; Persson, K.; Ceder, G. First Principles High Throughput Screening of Oxynitrides for Water-Splitting Photocatalysts. *Energy Environ. Sci.* **2013**, *6* (1), 157–168. 10.1039/c2ee23482c.
- (41) Saal, J. E.; Kirklin, S.; Aykol, M.; Meredig, B.; Wolverton, C. Materials Design and Discovery with High-Throughput Density Functional Theory: The Open Quantum Materials Database (OQMD). *JOM*. **2013**, *65* (11), 1501–1509. 10.1007/s11837-013-0755-4.
- (42) Ong, S. P.; Wang, L.; Kang, B.; Ceder, G. Li-Fe-P-O₂ Phase Diagram from First Principles Calculations. *Chem. Mater.*, **2008**, *20* (5), 1798–1807. 10.1021/cm702327g.
- (43) Jain, A.; Hautier, G.; Ong, S. P.; Moore, C. J.; Fischer, C. C.; Persson, K. A.; Ceder, G. Formation Enthalpies by Mixing GGA and GGA + U Calculations. *Phys. Rev. B*, **2011**, *84* (4). 10.1103/PhysRevB.84.045115.
- (44) Suthirakun, S.; Ammal, S. C.; Muñoz-García, A. B.; Xiao, G.; Chen, F.; zur Loye, H. C.; Carter, E. A.; Heyden, A. Theoretical Investigation of H₂ Oxidation on the

- Sr₂Fe_{1.5}Mo_{0.5}O₆ (001) Perovskite Surface under Anodic Solid Oxide Fuel Cell Conditions. *J. Am. Chem. Soc.*, **2014**, *136* (23), 8374–8386. 10.1021/ja502629j.
- (45) Bucher, E.; Sitte, W.; Klauser, F.; Bertel, E. Oxygen Exchange Kinetics of La_{0.58}Sr_{0.4}Co_{0.2}Fe_{0.8}O₃ at 600 °C in Dry and Humid Atmospheres. *Solid State Ion.*, **2011**, *191* (1), 61–67. 10.1016/j.ssi.2011.03.019.
- (46) Dunstan, M. T.; Jain, A.; Liu, W.; Ong, S. P.; Liu, T.; Lee, J.; Persson, K. A.; Scott, S. A.; Dennis, J. S.; Grey, C. P. Large Scale Computational Screening and Experimental Discovery of Novel Materials for High Temperature CO₂ Capture. *Energy Environ. Sci.*, **2016**, *9* (4), 1346–1360. 10.1039/c5ee03253a.
- (47) Kröger, F. A.; Vink, H. J. Relations between the Concentrations of Imperfections in Solids. *J. Phys. Chem. Solids*, **1958**, *5* (3), 208–223. 10.1016/0022-3697(58)90069-6.
- (48) Freysoldt, C.; Grabowski, B.; Hickel, T.; Neugebauer, J.; Kresse, G.; Janotti, A.; van de Walle, C. G. First-Principles Calculations for Point Defects in Solids. *Rev. Mod. Phys.*, **2014**, *86* (1), 253–305. 10.1103/RevModPhys.86.253.
- (49) Lindman, A.; Helgee, E. E.; Wahnström, G. Comparison of Space-Charge Formation at Grain Boundaries in Proton-Conducting BaZrO₃ and BaCeO₃. *Chem. Mater.*, **2017**, *29* (18), 7931–7941. 10.1021/acs.chemmater.7b02829.
- (50) Sun, W.; Dacek, S. T.; Ong, S. P.; Hautier, G.; Jain, A.; Richards, W. D.; Gamst, A. C.; Persson, K. A.; Ceder, G. The Thermodynamic Scale of Inorganic Crystalline Metastability. *Science*, **2016**, *2* (11), 1600225. 10.1126/sciadv.1600225.
- (51) Zhang, W.; Hu, Y. H. Progress in Proton-Conducting Oxides as Electrolytes for Low-Temperature Solid Oxide Fuel Cells: From Materials to Devices. *Energy Sci. Eng.* **2021**, *9*, 984–1011. 10.1002/ese3.886.
- (52) Ryu, K. H.; Haile, S. M. Chemical Stability and Proton Conductivity of Doped BaCeO₃–BaZrO₃ Solid Solutions. *Solid State Ion.* **1999**, *125* (1–4), 355–367. 10.1016/S0167-2738(99)00196-4.
- (53) Fabbri, E.; D’Epifanio, A.; Di Bartolomeo, E.; Licoccia, S.; Traversa, E. Tailoring the Chemical Stability of Ba_(Ce_{0.8-x}Zr_x)Y_{0.2}O_{3-δ} Protonic Conductors for

- Intermediate Temperature Solid Oxide Fuel Cells (IT-SOFCs). *Solid State Ion.* **2008**, 179 (15–16), 558–564. 10.1016/j.ssi.2008.04.002.
- (54) Yamazaki, Y.; Blanc, F.; Okuyama, Y.; Buannic, L.; Lucio-Vega, J. C.; Grey, C. P.; Haile, S. M. Proton Trapping in Yttrium-Doped Barium Zirconate. *Nat. Mater.*, **2013**, 12 (7), 647–651. 10.1038/nmat3638.
- (55) Kang, S. G.; Sholl, D. S. First-Principles Investigation of Chemical Stability and Proton Conductivity of M-Doped BaZrO₃ (M=K, Rb, and Cs). *J. Am. Ceram. Soc.* **2017**, 100 (7), 2997–3003. 10.1111/jace.14839.
- (56) Sun, W.; Liu, M.; Liu, W. Chemically Stable Yttrium and Tin Co-Doped Barium Zirconate Electrolyte for next Generation High Performance Proton-Conducting Solid Oxide Fuel Cells. *Adv. Energy Mater.* **2013**, 3 (8), 1041–1050. 10.1002/aenm.201201062.
- (57) Dawson, J. A.; Miller, J. A.; Tanaka, I. First-Principles Insight into the Hydration Ability and Proton Conduction of the Solid State Proton Conductor, Y and Sn Co-Doped BaZrO₃. *Chem. Mater.* **2015**, 27 (3), 901–908. 10.1021/cm504110y.
- (58) Jeong, Y. C.; Kim, D. H.; Kim, B. K.; Kim, Y. C. Migration and Interaction of Multi-Protons in Zinc-Doped Barium Zirconate. *Kor. J. Met Mater.* **2011**, 49 (12), 977–982. 10.3365/KJMM.2011.49.12.977.
- (59) Han, D.; Uda, T. The Best Composition of an Y-Doped BaZrO₃ Electrolyte: Selection Criteria from Transport Properties, Microstructure, and Phase Behavior. *J. Mater. Chem A.* **2018**, 6 (38), 18571–18582. 10.1039/c8ta06280c.
- (60) Ueno, K.; Hatada, N.; Han, D.; Uda, T. Thermodynamic Maximum of Y Doping Level in Barium Zirconate in Co-Sintering with NiO. *J. Mater. Chem. A.* **2019**, 7 (12), 7232–7241. 10.1039/c8ta12245h.

4.8 FIGURES AND TABLES

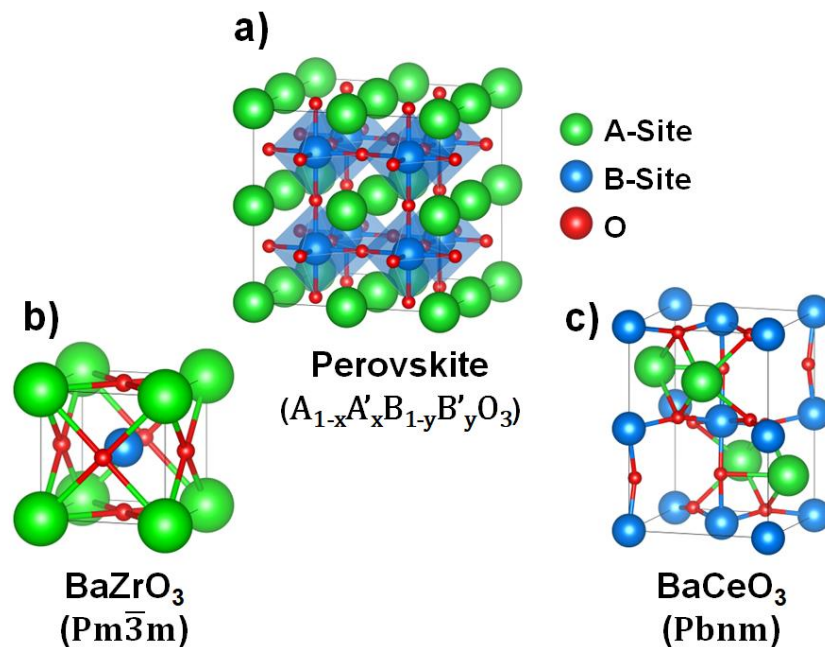


Figure 4.1: a) General structure of the perovskite oxide (ABO_3) used for all computed compositions in this study, b) cubic unit cell of $BaZrO_3$, and c) orthorhombic unit cell of $BaCeO_3$.

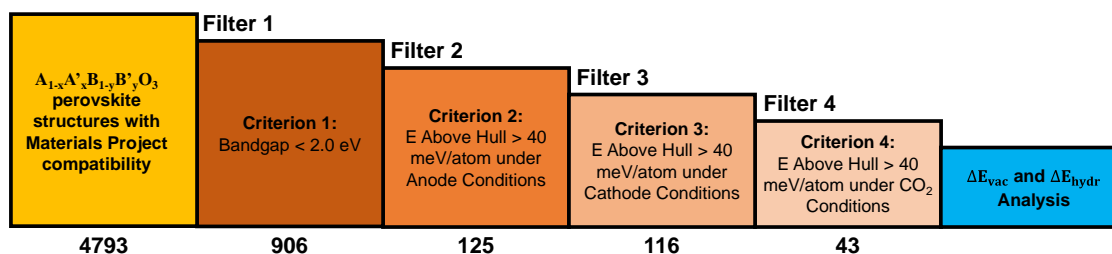


Figure 4.2: Computational workflow for the DFT-based high-throughput screening process used in this study. The number below each filter box refers to the number of materials that pass the corresponding filter criterion.

Table 4.1: List of materials that passed the four filters described in Figure 4.2. Included in this table are the elemental configuration, the computed bandgap (in eV), vacancy formation energy (ΔE_{vac} in eV), and hydration energy (ΔE_{hydr} in eV).

	A	A'	B	B'	B''	Bandgap (eV)	ΔE_{vac} (eV)	ΔE_{hydr} (eV)
Ba	1.000		Zr 1.000			3.329	6.757	-0.073
Sr	1.000		Zr 1.000			3.856	6.849	0.282
Y	1.000		Cr 1.000			3.847	5.737	0.461
Ba	1.000		Zr 0.875	Pt 0.125		2.043	2.924	1.530
Ba	1.000		Zr 0.875	Sn 0.125		3.468	4.658	2.309
Ba	1.000		Zr 0.875	Tc 0.125		2.285	5.381	-0.450
Ba	1.000		Zr 0.875	Ti 0.125		2.779	6.245	-0.909
Sr	1.000		Zr 0.875	Ge 0.125		3.861	4.901	0.793
Sr	1.000		Zr 0.875	Hf 0.125		3.818	6.643	0.025
Sr	1.000		Zr 0.875	Mn 0.125		3.169	3.186	-1.210
Sr	1.000		Zr 0.875	Sn 0.125		3.937	4.784	1.849
Sr	1.000		Zr 0.875	Ti 0.125		3.042	6.411	-0.852
Ba	1.000		Zr 0.750	Hf 0.125		3.366	6.771	0.012
Ba	1.000		Zr 0.750	Ir 0.125		2.149	4.024	-1.672
Ba	1.000		Zr 0.750	Hf 0.250		3.415	6.786	0.191
Ba	1.000		Zr 0.750	Ti 0.250		2.730	6.210	-1.233
Sr	1.000		Zr 0.750	Hf 0.250		3.805	6.646	0.163
Sr	1.000		Zr 0.750	Ti 0.250		3.120	6.392	-1.295
Ba	1.000		Zr 0.750	Sn 0.250		3.78	4.681	2.451
Sr	1.000		Zr 0.750	Sn 0.250		3.933	4.519	1.476
Ba	1.000		Zr 0.750	Nb 0.125	Fe 0.125	2.431	5.053	-2.039
Ba	1.000		Zr 0.750	Ta 0.125	Fe 0.125	2.808	5.327	-2.281
Ba	1.000		Zr 0.500	Hf 0.500		3.520	6.843	0.368
Sr	1.000		Zr 0.500	Hf 0.500		3.936	6.86	0.492
Ba	0.875	Ca 0.125	Zr 1.000			3.396	6.686	-0.313

Ba	0.875	Cd	0.125	Zr	1.000			2.967	4.572	-1.382
Ba	0.875	Rb	0.125	Zr	1.000			3.377	3.583	-3.859
Ba	0.875	Sr	0.125	Zr	1.000			3.350	6.721	-0.131
Sr	0.875	Ba	0.125	Zr	1.000			3.775	6.783	0.179
Sr	0.875	Ca	0.125	Zr	1.000			3.881	6.813	0.105
Sr	0.875	Zn	0.125	Zr	1.000			3.838	5.189	-0.395
Ba	0.875	Sr	0.125	Zr	0.875	Ti	0.125	2.930	6.253	-0.842
Sr	0.875	Ba	0.125	Zr	0.875	Sn	0.125	3.866	4.682	1.913
Sr	0.875	Ca	0.125	Zr	0.875	Ti	0.125	3.147	6.369	-0.927
Ba	0.875	Bi	0.125	Zr	0.875	Fe	0.125	3.505	4.342	-1.687
Ca	0.750	Ba	0.250	Zr	1.000			3.916	6.668	-0.041
Sr	0.750	Ba	0.250	Zr	1.000			3.445	6.272	-0.701
Ca	0.750	Sr	0.250	Zr	1.000			3.999	6.117	-1.042
Sr	0.750	Ca	0.250	Zr	1.000			3.899	6.788	-0.149
Ba	0.750	Sr	0.250	Zr	1.000			3.363	6.697	-0.223
Sr	0.750	Rb	0.250	Zr	0.750	Ta	0.250	3.296	6.282	-0.943
Ba	0.500	Sr	0.500	Zr	1.000			3.637	6.753	-0.040
Sr	0.500	Ca	0.500	Zr	1.000			4.034	6.792	0.341

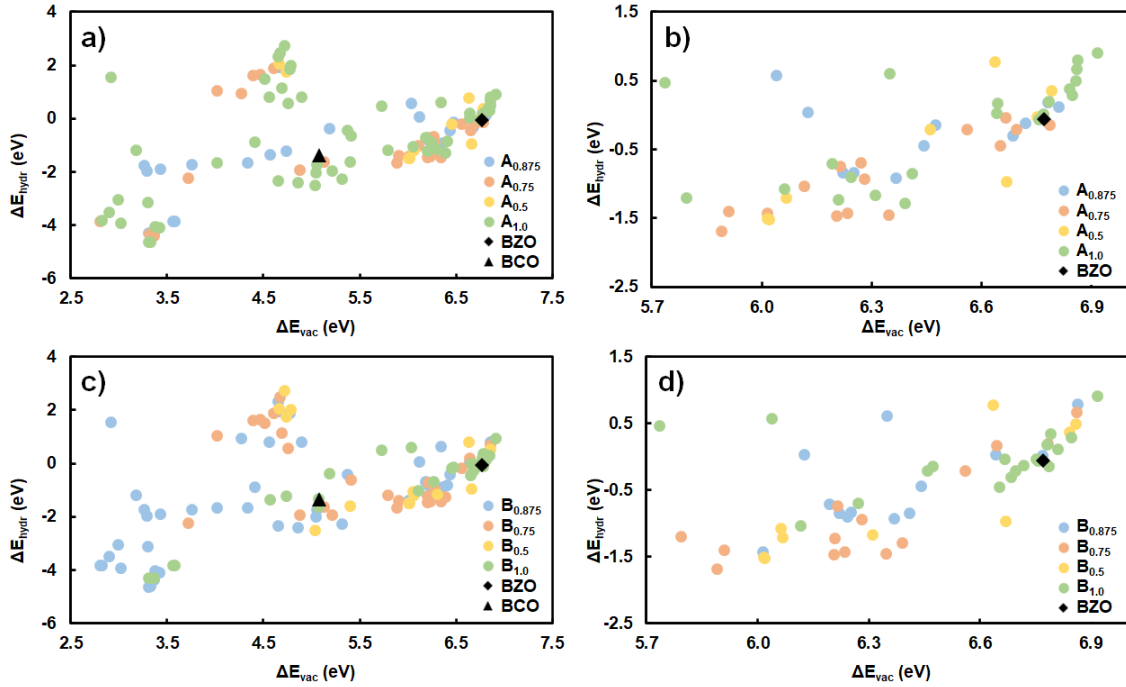


Figure 4.3: Scatter plots of vacancy formation energy (ΔE_{vac} in eV) versus hydration energy (ΔE_{hydr} in eV) for the 116 perovskite oxides that passed the first three filters. a) Materials organized with respect to A-site doping where $A_{1.0}$, $A_{0.875}$, $A_{0.75}$, and $A_{0.5}$ correspond to the materials with 0%, 12.5%, 25%, and 50% doping at the A-site, respectively, b) magnified scatter plot around BZO taken from a), c) materials organized with respect to B-site doping where $B_{1.0}$, $B_{0.875}$, $B_{0.75}$, and $B_{0.5}$ correspond to the materials with 0%, 12.5%, 25%, and 50% doping at the B-site, respectively, and d) magnified scatter plot around BZO taken from c).

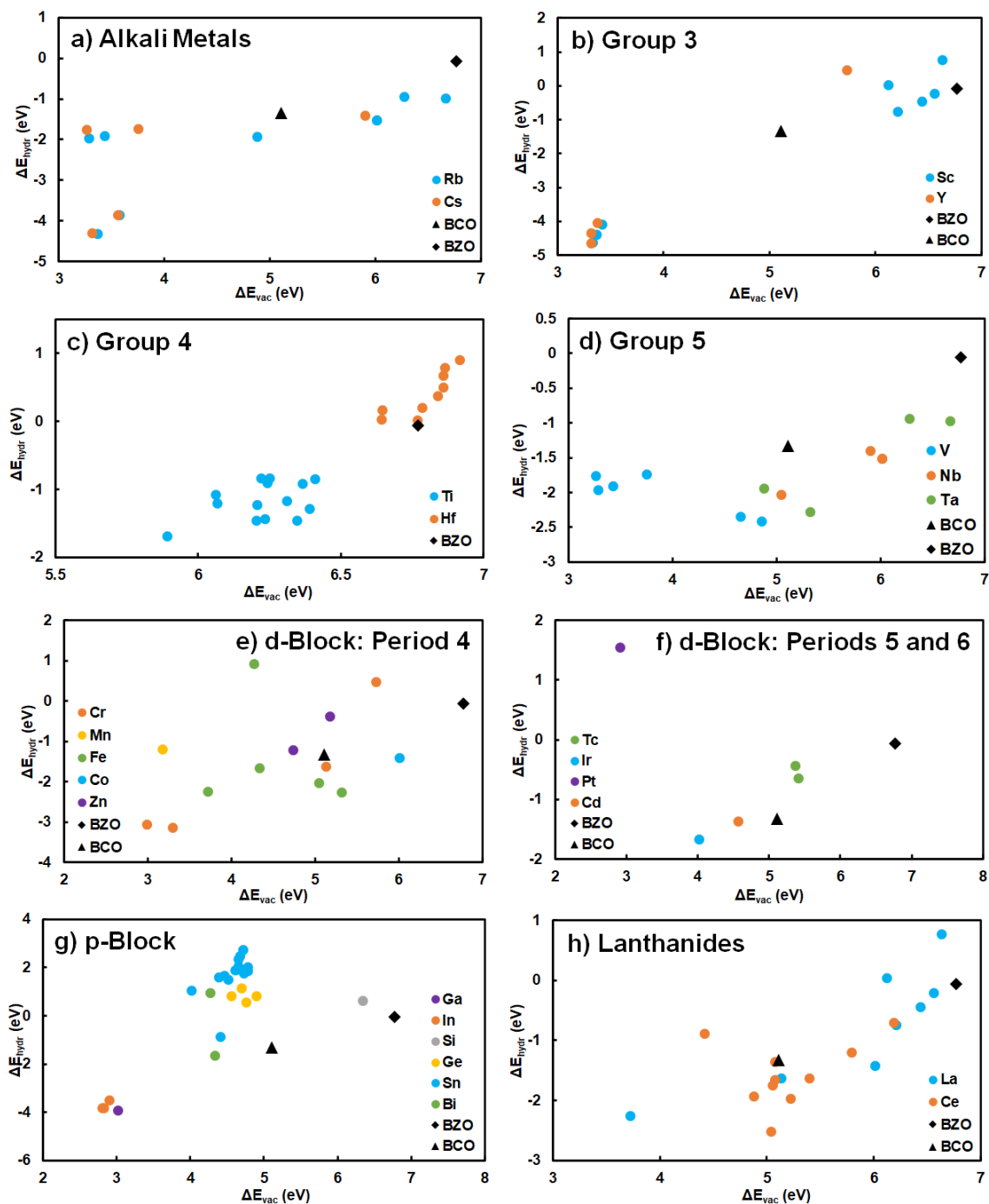


Figure 4.4: Scatter plots of vacancy formation energy (ΔE_{vac} in eV) versus hydration energy (ΔE_{hydr} in eV) for the 116 perovskite oxides that passed the first three filters categorized into the following groups, (a) alkali metals, (b) group 3 elements, (c) group 4 elements, (d) group 5 elements, (e) d-block: period 4 elements, (f) d-block: periods 5 and 6 elements, (g) p-block elements, and (h) lanthanides.

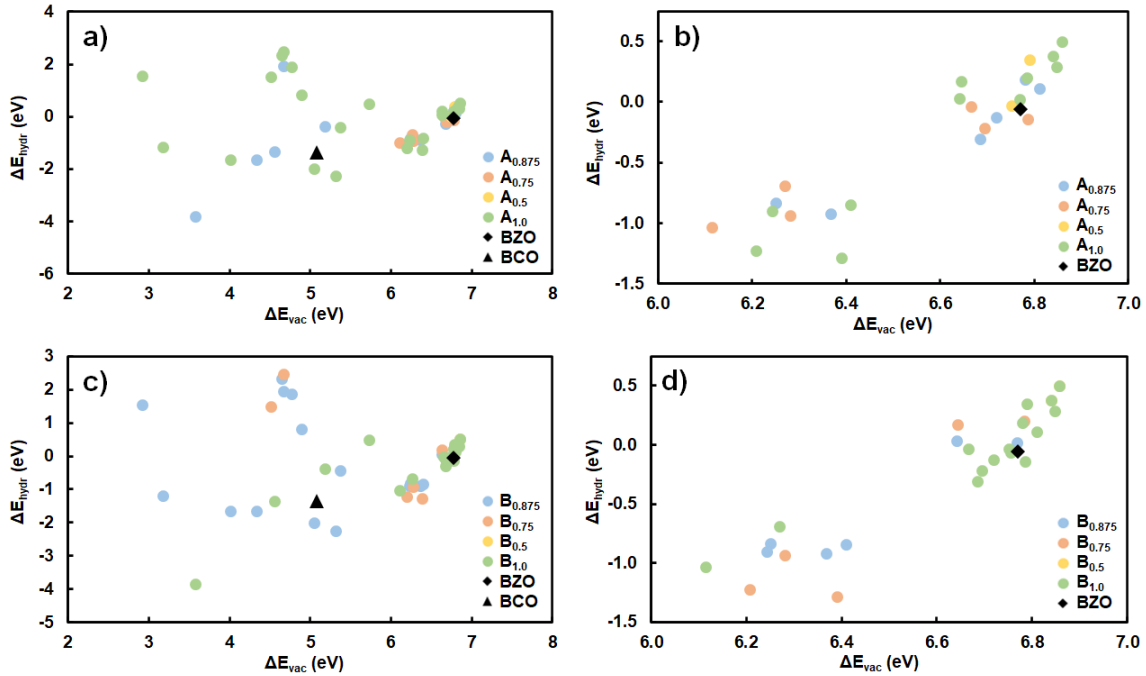


Figure 4.5: Scatter plots of vacancy formation energy (ΔE_{vac} in eV) versus hydration energy (ΔE_{hydr} in eV) for the 43 perovskite oxides that passed the first four filters. a) Materials organized with respect to A-site doping where $A_{1.0}$, $A_{0.875}$, $A_{0.75}$, and $A_{0.5}$ correspond to the materials with 0%, 12.5%, 25%, and 50% doping at the A-site, respectively, b) magnified scatter plot around BZO taken from a), c) materials organized with respect to B-site doping where $B_{1.0}$, $B_{0.875}$, $B_{0.75}$, and $B_{0.5}$ correspond to the materials with 0%, 12.5%, 25%, and 50% doping at the B-site, respectively, and d) magnified scatter plot around BZO taken from c). BCO did not pass the CO_2 stability test and is included in the figure only as a benchmark.

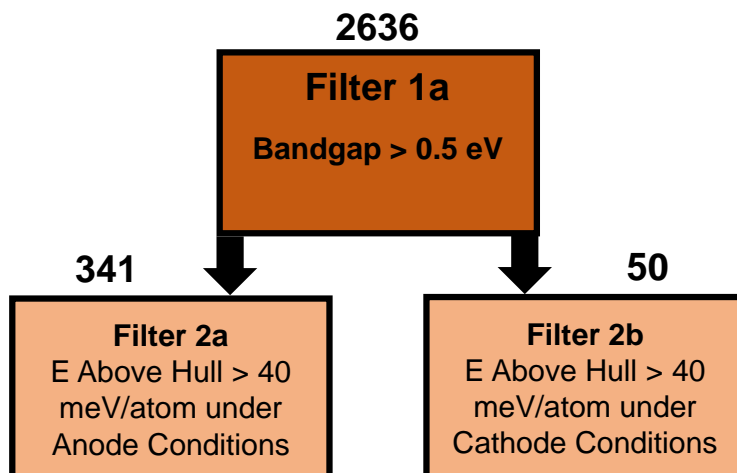


Figure 4.6: DFT-based high-throughput screening process used for identifying electrode materials. The number above each filter box refers to the number of materials that pass the corresponding filter criterion.

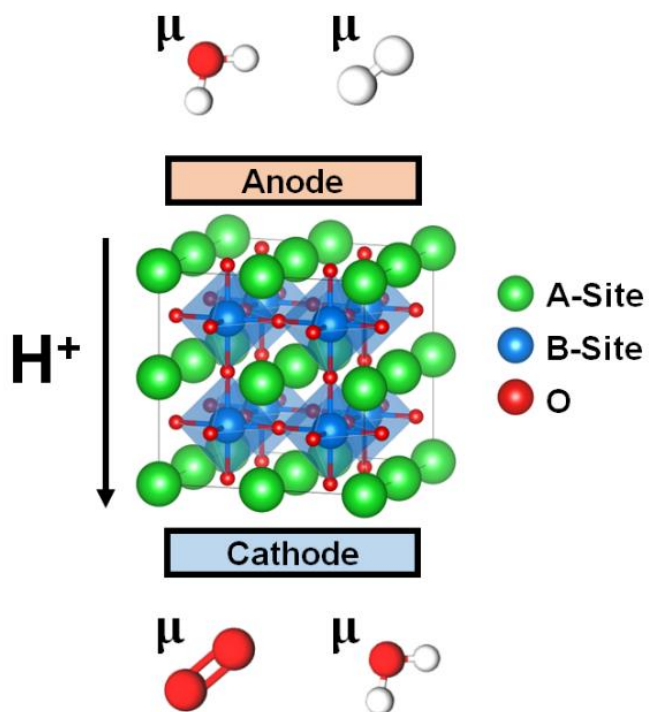


Figure 4.7: Graphical Abstract

CHAPTER 5

CONCLUSION

This dissertation outlines an expansion in the foundational knowledge regarding the doping analysis of complex oxides such as the Ruddlesden-Popper phase and the perovskite. Ruddlesden-Popper and perovskite oxides could serve as the primary electrode and electrolyte materials for the next-generation of solid oxide fuel cells (SOFCs) and solid oxide electrolyzer cells (SOECs). As a highly efficient energy conversion technology (e.g., SOFCs) and as a hydrogen production technology (e.g., SOECs), solid oxide-based electrochemical systems are an integral technology to addressing climate change, generating renewable energy, and building sustainable industrial processes. Despite this, state-of-the-art solid oxide devices are typically composed of lanthanum strontium manganite (LSM) cathodes, yttria-stabilized-zirconia (YSZ) electrolytes, and nickel on yttria-stabilized-zirconia (Ni/YSZ) anodes. These materials require high temperature to activate catalytic activity and oxygen mobility, and thus, cause premature material aging and long start-up procedures that lower the efficiency of solid oxide devices below theoretical efficiency. Therefore, understanding the role of elemental doping regarding Ruddlesden-Popper and perovskite oxide materials is key to yield active and stable materials for the next-generation of SOFCs and SOECs operating at lower temperatures.

For Chapter 2, a first principles analysis of $(\text{Sr}_{1-x}\text{Pr}_x)_2\text{FeO}_{4\pm\delta}$ (SPF) displays how

Pr^{3+} substitution at the A-site influences oxygen defect formation and transport. The structural and electronic properties of SPF are explained in terms of average Fe oxidation state. Electronic conductivity improves with a small introduction of Pr^{3+} . When the concentration of Pr^{3+} becomes 50%, the bandgap sharply increases, and the system becomes an insulator. The oxygen vacancy formation energy remains constant for all Pr^{3+} concentrations below 50%. A sharp increase is observed for 50% Pr^{3+} due to the overreduction of Fe. Interstitial defects exist in a peroxide state, and the interstitial formation energy is primarily a function of the identity of the neighboring A-site element. Lastly, ionic conductivity is primarily controlled by an oxygen vacancy-mediated process due to the high concentration of vacancy defects under both anodic and cathodic conditions. Based on the interstitial favorability under cathodic conditions for 50% Pr^{3+} , future work will investigate the role of interstitial-mediated diffusion for higher concentrations of Pr^{3+} . Overall, the limited introduction of Pr^{3+} (e.g., < 50%) at the A-site improves the electronic conductivity relative to Sr_2FeO_4 , maintains the high oxygen vacancy defect concentration of Sr_2FeO_4 , and matches or slightly improves the oxide migration barriers relative to Sr_2FeO_4 . This chapter is intended to help the design and optimization of Ruddlesden-Popper-based materials for direct use in SOFCs as either electrodes or electrolytes. Future work will investigate the role of B-site doping with the introduction of other transition metals to further tune electronic conductivity, defect formation, redox stability, and oxide migration. This procedure will closely follow the methodology outlined in Section 2.3.

For Chapter 3, the electrochemical oxidation of H_2 and CO fuels was investigated on the Ruddlesden-Popper, $\text{SrLaFeO}_{4-\delta}$ (SLF). Two distinct (001) FeO_2 -plane terminated

surface models (e.g., FeO₂-LaO and FeO₂-SrO) were used to model the electro-oxidation of H₂, CO, and syngas fuels for all operating voltage conditions. For syngas fuel, thermochemical water-gas shift was also modeled. Microkinetic modeling predicted an order of magnitude higher turnover frequency for the electro-oxidation of H₂ compared to CO for SLF at short circuit conditions. The FeO₂-SrO surface displayed three orders of magnitude greater activity for H₂ oxidation and 3x greater activity for CO oxidation activity relative to the FeO₂-LaO surface, respectively. At an operating voltage less than 0.7 V, surface H₂O/CO₂ formation was found to be the key rate-limiting step and the surface H₂O/CO₂ desorption was the key charge transfer step. For operating voltages above 0.9 V, bulk oxygen migration process was found to affect the overall rate at high cell voltage conditions. With the introduction of surface B-site substitutional dopants, an increase in TOF was observed for all dopants on LaO-based surface models at short circuit conditions. For SrO-based surface models, the calculated TOFs for the doped surfaces were found to be lower than the non-doped surface. Since doping significantly stabilizes the surface vacancy structure on the FeO₂-SrO surface, the oxidation reaction was found to be rate-controlled by bulk oxygen diffusion. Lastly, the dissociative adsorption of H₂S and the replacement of surface oxygen by sulfur reactions were used to analyze the sulfur poisoning mechanism of SLF surface models. The dissociative adsorption of H₂S reaction was found to be endergonic under SOFC operating conditions in the presence of 50 ppm of H₂S for all SLF surfaces while the Fe_{1-x}M_xO₂-LaO (x = 0.11; M = Co and Ni) and Fe_{1-x}Mn_xO₂-SrO (x = 0.11) surfaces were affected by the oxide replacement reaction especially at elevated H₂S concentrations. To conclude, SLF anodes display good oxidation activity for H₂ and syngas fuels, and exhibit sulfur resistance. The

introduction of Co improves and maintains the catalytic activity of SLF while maintaining sulfur tolerance. Future work will focus on the effect of B-site doping on the bulk oxygen diffusion barrier, electronic conductivity, and redox stability. This procedure will further expand the reaction network of electro-oxidation by incorporating effects of oxide vacancy diffusion across the electrolyte/electrode interface and cathode kinetics.

For the third aim of Chapter 4, a high throughput screening approach was used to filter 4793 perovskite oxides to discover promising electrolyte materials for proton-conducting SOFCs. The material set of 4793 perovskite oxides was composed of a wide variety of elements including alkali metals, alkaline earth metals, d-block transition metals, f-block lanthanides, and p-block metalloids. Furthermore, the material set includes both non-doped (e.g., binary) and doped (e.g., ternary, quaternary, and quinary) configurations to better clarify the role of doping ratios on stability and ionic conductivity. Four filters are applied in sequential order to isolate materials that are sufficiently insulating, redox stable, CO₂ (meta)stable, and ionically conductive materials. Promising materials from the high throughput screening include BaFe_{0.125}Ta_{0.125}Zr_{0.875}O₃, BaFe_{0.125}Nb_{0.125}Zr_{0.875}O₃, Bi_{0.125}Ba_{0.875}Fe_{0.125}Zr_{0.875}O₃, SrMn_{0.125}Zr_{0.875}O₃, BaRb_{0.125}Zr_{0.875}O₃, Rb_{0.125}Ba_{0.875}V_{0.125}Zr_{0.875}O₃, Rb_{0.125}Sr_{0.875}V_{0.125}Zr_{0.875}O₃, and Cs_{0.125}Ba_{0.875}ZrO₃. The acceptor-dopant configuration BaZr_{0.875}(Sc,Y)_{0.125}O₃ is also stable and active. Chapter 4 serves to aid the design of perovskite-based proton conducting electrolytes, such as outlining the role of elemental identity and doping ratios on thermodynamic stability and defect formation activity. Lastly, a secondary filtering scheme was utilized to outline electrically conductive and redox stable under anode and cathode operating conditions. These passing materials

could have use as electrode materials where future work will focus on outlining the catalytic activity of these materials. Furthermore, future work will focus on testing a greater number of quaternary and quinary configurations. A key focus will be calculating explicit proton migration pathways to elaborate activity relationships for the proton trapping effect.

REFERENCES

- (1) Sunarso, J.; Baumann, S.; Serra, J. M.; Meulenber, W. A.; Liu, S.; Lin, Y. S.; Diniz da Costa, J. C. Mixed Ionic-Electronic Conducting (MIEC) Ceramic-Based Membranes for Oxygen Separation. *J. Memb. Sci.*, **2008**, *320* (1–2), 13–41. 10.1016/j.memsci.2008.03.074.
- (2) Zhang, C.; Sunarso, J.; Liu, S. Designing CO₂-Resistant Oxygen-Selective Mixed Ionic–Electronic Conducting Membranes: Guidelines, Recent Advances, and Forward Directions. *Chem. Soc. Rev.*, **2017**, *46* (10), 2941–3005. 10.1039/c6cs00841k.
- (3) Riess, I. Mixed Ionic–Electronic Conductors—Material Properties and Applications. *Solid State Ion.*, **2003**, *157* (1–4), 1–17. 10.1016/S0167-2738(02)00182-0.
- (4) Adler, S. B. Factors Governing Oxygen Reduction in Solid Oxide Fuel Cell Cathodes. *Chem. Rev.*, **2004**, *104* (10), 4791–4843. 10.1021/cr020724o.
- (5) Yang, L.; Wang, S.; Blinn, K.; Liu, M.; Liu, Z.; Cheng, Z.; Liu, M. Enhanced Sulfur and Coking Tolerance of a Mixed Ion Conductor for SOFCs: BaZr_{0.1}Ce_{0.7}Y_{0.2-x}Yb_xO_{3-δ}. *Science*, **2009**, *326* (5949), 126–129. 10.1126/science.1174811.
- (6) Brett, D. J. L.; Atkinson, A.; Brandon, N. P.; Skinner, S. J. Intermediate Temperature Solid Oxide Fuel Cells. *Chem. Soc. Rev.*, **2008**, *37* (8), 1568–1578. 10.1039/b612060c.
- (7) Shao, Z.; Haile, S. M. A High-Performance Cathode for the next Generation of Solid-Oxide Fuel Cells. *Nature*, **2004**, *3* (1978), 170–173. 10.1038/nature02863.
- (8) Tietz, F.; Haanappel, V. A. C.; Mai, A.; Mertens, J.; Stöver, D. Performance of LSCF Cathodes in Cell Tests. *J. Power Sources*, **2006**, *156* (1), 20–22. 10.1016/j.jpowsour.2005.08.015.
- (9) Fu, C.; Sun, K.; Zhang, N.; Chen, X.; Zhou, D. Electrochemical Characteristics of LSCF–SDC Composite Cathode for Intermediate Temperature SOFC. *Electrochim. Acta*, **2007**, *52* (13), 4589–4594. 10.1016/j.electacta.2007.01.001.

- (10) Yang, C.; Yang, Z.; Jin, C.; Xiao, G.; Chen, F.; Han, M. Sulfur-Tolerant Redox-Reversible Anode Material for Direct Hydrocarbon Solid Oxide Fuel Cells. *Adv. Mater.*, **2012**, *24* (11), 1439–1443. 10.1002/adma.201104852.
- (11) Xiao, G.; Liu, Q.; Zhao, F.; Zhang, L.; Xia, C.; Chen, F. Sr₂Fe_{1.5}Mo_{0.5}O₆ as Cathodes for Intermediate-Temperature Solid Oxide Fuel Cells with La_{0.8}Sr_{0.2}Ga_{0.87}Mg_{0.13}O₃ Electrolyte. *J. Electrochem. Soc.*, **2011**, *158* (5). 10.1149/1.3556085.
- (12) Suthirakun, S.; Ammal, S. C.; Muñoz-García, A. B.; Xiao, G.; Chen, F.; Zur Loye, H. C.; Carter, E. A.; Heyden, A. Theoretical Investigation of H₂ Oxidation on the Sr₂Fe_{1.5}Mo_{0.5}O₆ (001) Perovskite Surface under Anodic Solid Oxide Fuel Cell Conditions. *J. Am. Chem. Soc.*, **2014**, *136* (23), 8374–8386. 10.1021/ja502629j.
- (13) Jiang, Y.; Wang, S.; Zhang, Y.; Yan, J.; Li, W. Kinetic Study of the Formation of Oxygen Vacancy on Lanthanum Manganite Electrodes. *J. Electrochem. Soc.*, **1998**, *145* (2), 373–378. 10.1149/1.1838271.
- (14) Jiang, S. P. Development of Lanthanum Strontium Cobalt Ferrite Perovskite Electrodes of Solid Oxide Fuel Cells – A Review. *Int. J. Hydrog. Energy*, **2019**, *44* (14), 7448–7493. 10.1016/j.ijhydene.2019.01.212.
- (15) Švarcová, S.; Wiik, K.; Tolchard, J.; Bouwmeester, H. J. M.; Grande, T. Structural Instability of Cubic Perovskite Ba_xSr_{1-x}Co_{1-y}Fe_yO_{3-δ}. *Solid State Ion.*, **2008**, *178* (35–36), 1787–1791. 10.1016/j.ssi.2007.11.031.
- (16) Hernández, A. M.; Mogni, L.; Caneiro, A. La₂NiO_{4+δ} as Cathode for SOFC: Reactivity Study with YSZ and CGO Electrolytes. *Int. J. Hydrog. Energy*, **2010**, *35* (11), 6031–6036. 10.1016/j.ijhydene.2009.12.077.
- (17) Guan, B.; Li, W.; Zhang, H.; Liu, X. Oxygen Reduction Reaction Kinetics in Sr-Doped La₂NiO_{4+δ} Ruddlesden-Popper Phase as Cathode for Solid Oxide Fuel Cells. *J. Electrochem. Soc.*, **2015**, *162* (7), F707–F712. 10.1149/2.0541507jes.
- (18) Yang, C.; Li, J.; Lin, Y.; Liu, J.; Chen, F.; Liu, M. In Situ Fabrication of CoFe Alloy Nanoparticles Structured (Pr_{0.4}Sr_{0.6})₃(Fe_{0.85}Nb_{0.15})₂O₇ Ceramic Anode for Direct Hydrocarbon Solid Oxide Fuel Cells. *Nano Energy*, **2015**, *11*, 704–710. 10.1016/j.nanoen.2014.12.001.
- (19) Kagomiya, I.; Jimbo, K.; Kakimoto, K. I.; Nakayama, M.; Masson, O. Oxygen Vacancy Formation and the Ion Migration Mechanism in Layered Perovskite (Sr,La)₃Fe₂O_{7-δ}. *Phys. Chem. Chem. Phys.*, **2014**, *16* (22), 10875–10882. 10.1039/c4cp00736k.
- (20) Ling, Y.; Guo, T.; Zhang, X.; Budiman, R. A.; Fujimaki, Y.; Nakamura, T.; Lin, B.; Kawada, T.; Amezawa, K. Evaluation of Electrical Conductivity and Oxygen

- Diffusivity of the Typical Ruddlesden-Popper Oxide $\text{Sr}_3\text{Fe}_2\text{O}_{7-\delta}$. *Ceram. Int.*, **2017**, 43 (18), 16264–16269. 10.1016/j.ceramint.2017.08.211.
- (21) Fossdal, A.; Einarsrud, M. A.; Grande, T. Phase Equilibria in the Pseudo-Binary System $\text{SrO}-\text{Fe}_2\text{O}_3$. *J. Solid State Chem.*, **2004**, 177 (8), 2933–2942. 10.1016/j.jssc.2004.05.007.
- (22) Yang, C.; Yang, Z.; Jin, C.; Liu, M.; Chen, F. High Performance Solid Oxide Electrolysis Cells Using $\text{Pr}_{0.8}\text{Sr}_{1.2}(\text{Co},\text{Fe})_{0.8}\text{Nb}_{0.2}\text{O}_{4+\delta}-\text{Co}-\text{Fe}$ Alloy Hydrogen Electrodes. *Int. J. Hydrog. Energy*, **2013**, 38 (26), 11202–11208. 10.1016/j.ijhydene.2013.06.086.
- (23) Tan, T.; Qin, M.; Li, K.; Zhou, M.; Liu, T.; Yang, C.; Liu, M. In-Situ Exsolved NiFe Alloy Nanoparticles on $\text{Pr}_{0.8}\text{Sr}_{1.2}(\text{Ni},\text{Fe})\text{O}_{4-\delta}$ for Direct Hydrocarbon Fuel Solid Oxide Fuel Cells. *Int. J. Hydrog. Energy*, **2020**, 45 (53), 29407–29416. 10.1016/j.ijhydene.2020.07.250.
- (24) Zhou, F.; Ozoliņš, V. Obtaining Correct Orbital Ground States in F-Electron Systems Using a Nonspherical Self-Interaction-Corrected LDA+U Method. *Phys. Rev. B*, **2009**, 80 (12), 1–6. 10.1103/PhysRevB.80.125127.
- (25) Tran, F.; Schweifer, J.; Blaha, P.; Schwarz, K.; Novák, P. PBE+U Calculations of the Jahn-Teller Effect in PrO_2 . *Phys. Rev. B*, **2008**, 77 (8), 1–9. 10.1103/PhysRevB.77.085123.
- (26) Blöchl, P. E.; Jepsen, O.; Andersen, O. K. Improved Tetrahedron Method for Brillouin-Zone Integrations. *Phys. Rev. B*, **1994**, 49 (23), 16223–16233. doi.org/10.1103/PhysRevB.49.16223.
- (27) Pack, J. D.; Monkhorst, H. J. Special Points for Brillouin-Zone Integrations. *Phys. Rev. B*, **1977**, 16 (4), 1748–1749. 10.1103/PhysRevB.16.1748.
- (28) Taylor, F. H.; Buckeridge, J.; Catlow, C. R. A. Defects and Oxide Ion Migration in the Solid Oxide Fuel Cell Cathode Material LaFeO_3 . *Chem. Mater.*, **2016**, 28 (22), 8210–8220. 10.1021/acs.chemmater.6b03048.
- (29) Suthirakun, S.; Xiao, G.; Ammal, S. C.; Chen, F.; Zur Loye, H. C.; Heyden, A. Rational Design of Mixed Ionic and Electronic Conducting Perovskite Oxides for Solid Oxide Fuel Cell Anode Materials: A Case Study for Doped SrTiO_3 . *J. Power Sources*, **2014**, 245, 875–885. 10.1016/j.jpowsour.2013.07.040.
- (30) Ammal, S. C.; Heyden, A. Modeling the Noble Metal/ TiO_2 (110) Interface with Hybrid DFT Functionals: A Periodic Electrostatic Embedded Cluster Model Study. *J. Chem. Phys.*, **2010**, 133 (16). 10.1063/1.3497037.
- (31) Atkins, P.; Paula, J. De; Keeler, J. *Atkins' Physical Chemistry*, 11th ed.; Oxford

University Press: Oxford, England, 2018.

- (32) Broberg, D.; Medasani, B.; Zimmermann, N. E. R.; Yu, G.; Canning, A.; Haranczyk, M.; Asta, M.; Hautier, G. PyCDT: A Python Toolkit for Modeling Point Defects in Semiconductors and Insulators. *Comput. Phys. Commun.*, **2018**, *226*, 165–179. 10.1016/j.cpc.2018.01.004.
- (33) Freysoldt, C.; Neugebauer, J.; Van De Walle, C. G. Fully Ab Initio Finite-Size Corrections for Charged-Defect Supercell Calculations. *Phys. Rev. Lett.*, **2009**, *102* (1), 1–4. 10.1103/PhysRevLett.102.016402.
- (34) Freysoldt, C.; Neugebauer, J.; Van de Walle, C. G. Electrostatic Interactions between Charged Defects in Supercells. *Phys. Status Solidi Basic Res.*, **2011**, *248* (5), 1067–1076. 10.1002/pssb.201046289.
- (35) Kumagai, Y.; Oba, F. Electrostatics-Based Finite-Size Corrections for First-Principles Point Defect Calculations. *Phys. Rev. B*, **2014**, *89* (19). 10.1103/PhysRevB.89.195205.
- (36) Buckeridge, J. Equilibrium Point Defect and Charge Carrier Concentrations in a Material Determined through Calculation of the Self-Consistent Fermi Energy. *Comput. Phys. Commun.*, **2019**, *244*, 329–342. 10.1016/j.cpc.2019.06.017.
- (37) Henkelman, G.; Arnaldsson, A.; Jónsson, H. A Fast and Robust Algorithm for Bader Decomposition of Charge Density. *Comput. Mater. Sci.*, **2006**, *36* (3), 354–360. 10.1016/j.commatsci.2005.04.010.
- (38) Tang, W.; Sanville, E.; Henkelman, G. A Grid-Based Bader Analysis Algorithm without Lattice Bias. *J. Phys. Condens. Matter*, **2009**, *21* (8). 10.1088/0953-8984/21/8/084204.
- (39) Qin, M.; Xiao, Y.; Yang, H.; Tan, T.; Wang, Z.; Fan, X.; Yang, C. Ru/Nb Co-Doped Perovskite Anode: Achieving Good Coking Resistance in Hydrocarbon Fuels via Core-Shell Nanocatalysts Exsolution. *Appl. Catal. B Environ.*, **2021**, *299*, 120613. 10.1016/j.apcatb.2021.120613.
- (40) Zhang, P.; Guan, G.; Khaerudini, D. S.; Hao, X.; Xue, C.; Han, M.; Kasai, Y.; Abudula, A. B-Site Mo-Doped Perovskite $\text{Pr}_{0.4}\text{Sr}_{0.6}(\text{Co}_{0.2}\text{Fe}_{0.8})_{1-x}\text{Mo}_x\text{O}_{3-\sigma}$ ($x = 0, 0.05, 0.1$ and 0.2) as Electrode for Symmetrical Solid Oxide Fuel Cell. *J. Power Sources*, **2015**, *276*, 347–356. 10.1016/j.jpowsour.2014.11.141.
- (41) Zhang, P.; Guan, G.; Khaerudini, D. S.; Hao, X.; Xue, C.; Han, M.; Kasai, Y.; Abudula, A. Mechanisms of Methane Decomposition and Carbon Species Oxidation on the $\text{Pr}_{0.4}\text{Sr}_{0.6}\text{Co}_{0.2}\text{Fe}_{0.7}\text{Nb}_{0.1}\text{O}_{3-\sigma}$ Electrode with High Catalytic Activity. *J. Mater. Chem. A*, **2015**, *3* (45), 22816–22823. 10.1039/c5ta07599h.
- (42) Chen, Y.; Jung, W.; Cai, Z.; Kim, J. J.; Tuller, H. L.; Yildiz, B. Impact of Sr

Segregation on the Electronic Structure and Oxygen Reduction Activity of SrTi_{1-x}Fe_xO₃ Surfaces. *Energy Environ. Sci.*, **2012**, 5 (7), 7979–7988. 10.1039/c2ee21463f.

- (43) Matsuno, J.; Okimoto, Y.; Kawasaki, M.; Tokura, Y. Variation of the Electronic Structure in Systematically Synthesized Sr₂MO₄ (M=Ti, V, Cr, Mn, and Co). *Phys. Rev. Lett.*, **2005**, 95 (17), 1–4. 10.1103/PhysRevLett.95.176404.
- (44) Shannon, R. D. Revised Effective Ionic Radii and Systematic Studies of Interatomic Distances in Halides and Chalcogenides. *Acta Crystallogr.*, **1976**, 32 (5), 751–767. 10.1107/S0567739476001551.
- (45) Ritzmann, A. M.; Muñoz-García, A. B.; Pavone, M.; Keith, J. A.; Carter, E. A. Ab Initio DFT+U Analysis of Oxygen Vacancy Formation and Migration in La_{1-x}Sr_xFeO_{3-δ} (x = 0, 0.25, 0.50). *Chem. Mater.*, **2013**, 25 (15), 3011–3019. 10.1021/cm401052w.
- (46) Adler, P.; Goncharov, A. F.; Syassen, K.; Schönherr, E. Optical Reflectivity and Raman Spectra of Sr₂FeO₄ under Pressure. *Phys. Rev. B*, **1994**, 50 (16), 11396–11402. 10.1103/PhysRevB.50.11396.
- (47) He, L.; Liu, F.; Hautier, G.; Oliveira, M. J. T.; Marques, M. A. L.; Vila, F. D.; Rehr, J. J.; Rignanese, G. M.; Zhou, A. Accuracy of Generalized Gradient Approximation Functionals for Density-Functional Perturbation Theory Calculations. *Phys. Rev. B*, **2014**, 89 (6), 1–15. 10.1103/PhysRevB.89.064305.
- (48) Miessler, G. L.; Tarr, D. A. *Inorganic Chemistry*, 2nd ed.; Pearson Education, Inc. Pearson Prentice Hall: Upper Saddle River, New Jersey, 1998.
- (49) Hu, X.; Li, M.; Xie, Y.; Yang, Y.; Wu, X.; Xia, C. Oxygen-Deficient Ruddlesden-Popper-Type Lanthanum Strontium Cuprate Doped with Bismuth as a Cathode for Solid Oxide Fuel Cells. *ACS Appl. Mater. Interfaces*, **2019**. 10.1021/acsami.9b05445.
- (50) Barcellos, D. R.; Coury, F. G.; Emery, A.; Sanders, M.; Tong, J.; McDaniel, A.; Wolverton, C.; Kaufman, M.; O’Hayre, R. Phase Identification of the Layered Perovskite Ce_xSr_{2-x}MnO₄ and Application for Solar Thermochemical Water Splitting. *Inorg. Chem.*, **2019**, 58 (12), 7705–7714. 10.1021/acs.inorgchem.8b03487.
- (51) Muñoz-García, A. B.; Ritzmann, A. M.; Pavone, M.; Keith, J. A.; Carter, E. A. Oxygen Transport in Perovskite-Type Solid Oxide Fuel Cell Materials: Insights from Quantum Mechanics. *Acc. Chem. Res.*, **2014**, 47 (11), 3340–3348. 10.1021/ar4003174.
- (52) Ritzmann, A. M.; Dieterich, J. M.; Carter, E. A. Density Functional Theory + U

Analysis of the Electronic Structure and Defect Chemistry of LSCF ($\text{La}_{0.5}\text{Sr}_{0.5}\text{Co}_{0.25}\text{Fe}_{0.75}\text{O}_{3-\delta}$). *Phys. Chem. Chem. Phys.*, **2016**, *18* (17), 12260–12269. 10.1039/c6cp01720g.

- (53) Xu, S.; Jacobs, R.; Morgan, D. Factors Controlling Oxygen Interstitial Diffusion in the Ruddlesden–Popper Oxide $\text{La}_{2-x}\text{Sr}_x\text{NiO}_{4+\delta}$. *Chem. Mater.*, **2018**, *30* (20), 7166–7177. 10.1021/acs.chemmater.8b03146.
- (54) Routbort, J. L.; Rothman, S. J.; Flandermeyer, B. K.; Nowicki, L. J.; Baker, J. E. Oxygen Diffusion in $\text{La}_{2-x}\text{Sr}_x\text{CuO}_{4-y}$. *J. Mater. Res.*, **1988**, *3* (1), 116–121. 10.1557/JMR.1988.0116.
- (55) Shri Prakash, B.; Senthil Kumar, S.; Aruna, S. T. Properties and Development of Ni/YSZ as an Anode Material in Solid Oxide Fuel Cell: A Review. *Renew. and Sustain. Energy Rev.*, **2014**, *36*, 149–179. 10.1016/j.rser.2014.04.043.
- (56) Tao, S.; Irvine, J. T. S. A Redox-Stable Efficient Anode for Solid-Oxide Fuel Cells. *Nat. Mater.*, **2003**, *2* (5), 320–323. 10.1038/nmat871.
- (57) Liu, Q.; Yang, C.; Dong, X.; Chen, F. Perovskite $\text{Sr}_2\text{Fe}_{1.5}\text{Mo}_{0.5}\text{O}_{6-\delta}$ as Electrode Materials for Symmetrical Solid Oxide Electrolysis Cells. *Int. J. Hydrog. Energy*, **2010**, *35* (19), 10039–10044. 10.1016/j.ijhydene.2010.08.016.
- (58) Liu, Q.; Dong, X.; Xiao, G.; Zhao, F.; Chen, F. A Novel Electrode Material for Symmetrical SOFCs. *Adv. Mater.*, **2010**, *22* (48), 5478–5482. 10.1002/adma.201001044.
- (59) Ruddlesden, S. N.; Popper, P. New Compounds of the K_2NiF_4 Type. *Acta Crystallogr.*, **1957**, *10*, 538–539. 10.1107/s0365110x57001929.
- (60) Takeguchi, T.; Yamanaka, T.; Takahashi, H.; Watanabe, H.; Kuroki, T.; Nakanishi, H.; Orikasa, Y.; Uchimoto, Y.; Takano, H.; Ohguri, N.; Matsuda, M.; Murota, T.; Uosaki, K.; Ueda, W. Layered Perovskite Oxide: A Reversible Air Electrode for Oxygen Evolution/Reduction in Rechargeable Metal-Air Batteries. *J. Am. Chem. Soc.*, **2013**, *135* (30), 11125–11130. 10.1021/ja403476v.
- (61) Zhao, H.; Mauvy, F.; Lalanne, C.; Bassat, J.; Fourcade, S.; Grenier, J. New Cathode Materials for ITSOFC: Phase Stability, Oxygen Exchange and Cathode Properties of $\text{La}_{2-x}\text{NiO}_{4+\delta}$. *Solid State Ion.*, **2008**, *179* (35–36), 2000–2005. 10.1016/j.ssi.2008.06.019.
- (62) Cao, Y.; Liang, J.; Li, X.; Yue, L.; Liu, Q.; Lu, S.; Asiri, A. M.; Hu, J.; Luo, Y.; Sun, X. Recent Advances in Perovskite Oxides as Electrode Materials for Supercapacitors. *Chem. Commun.*, **2021**, *57*, 2343–2355. 10.1039/d0cc07970g.

- (63) Li, X.; Zhao, H.; Liang, J.; Luo, Y.; Chen, G.; Shi, X.; Lu, S.; Gao, S.; Hu, J.; Liu, Q.; Sun, X. A-Site Perovskite Oxides: An Emerging Functional Material for Electrocatalysis and Photocatalysis. *J. Mater. Chem. A*, **2021**, *9*, 6650–6670. 10.1039/d0ta09756j.
- (64) Xu, L.; Yin, Y.-M.; Zhou, N.; Wang, Z.; Ma, Z.-F. Sulfur Tolerant Redox Stable Layered Perovskite SrLaFeO_{4-δ} as Anode for Solid Oxide Fuel Cells. *Electrochem. Commun.*, **2017**, *76*, 51–54. 10.1016/j.elecom.2017.01.017.
- (65) Wang, Z.; Yin, Y.-M.; Yu, Y.; Song, Y.; Ma, Z.-F.; Yin, J. Roles of Fe Ni Nanoparticles and SrLaFeO₄ Substrate in the Performance and Reliability of a Composite Anode Prepared through In-Situ Exsolution for Intermediate Temperature Solid Oxide Fuel Cells (I). *Int. J. Hydrog. Energy*, **2018**, *43* (22), 10440–10447. 10.1016/j.ijhydene.2018.04.090.
- (66) Wu, N.; Wang, W.; Zhong, Y.; Yang, G.; Qu, J.; Shao, Z. Nickel-Iron Alloy Nanoparticle-Decorated K₂NiF₄-Type Oxide as an Efficient and Sulfur-Tolerant Anode for Solid Oxide Fuel Cells. *ChemElectroChem*, **2017**, *4* (9), 2378–2384. 10.1002/celec.201700211.
- (67) Chang, H.; Chen, H.; Shao, Z.; Shi, J.; Bai, J.; Li, S.-D. In Situ Fabrication of (Sr,La)FeO₄ with CoFe Alloy Nanoparticles as an Independent Catalyst Layer for Direct Methane-Based Solid Oxide Fuel Cells with a Nickel Cermet Anode. *J. Mater. Chem. A*, **2016**, *4* (36), 13997–14007. 10.1039/C6TA04639H.
- (68) Park, S.; Han, H.; Choi, J.; Lee, S.; Park, M.; Kim, W. B. Ruddlesden–Popper Oxide (La_{0.6}Sr_{0.4})₂(Co,Fe)O₄ with Exsolved CoFe Nanoparticles for a Solid Oxide Fuel Cell Anode Catalyst. *Energy Technol.*, **2021**, *9* (7), 2100116. 10.1002/ente.202100116.
- (69) Li, H.; Song, Y.; Xu, M.; Wang, W.; Ran, R.; Zhou, W.; Shao, Z. Exsolved Alloy Nanoparticles Decorated Ruddlesden–Popper Perovskite as Sulfur-Tolerant Anodes for Solid Oxide Fuel Cells. *Energy Fuels*, **2020**, *34* (9), 11449–11457. 10.1021/acs.energyfuels.0c02228.
- (70) Chung, Y. S.; Kim, T.; Shin, T. H.; Yoon, H.; Park, S.; Sammes, N. M.; Kim, W. B.; Chung, J. S. In Situ Preparation of a La_{1.2}Sr_{0.8}Mn_{0.4}Fe_{0.6}O₄ Ruddlesden–Popper Phase with Exsolved Fe Nanoparticles as an Anode for SOFCs. *J. Mater. Chem. A*, **2017**, *5* (14), 6437–6446. 10.1039/c6ta09692a.
- (71) Tan, W.; Huan, D.; Yang, W.; Shi, N.; Wang, W.; Peng, R.; Wu, X.; Lu, Y. A First-Principles Study on Divergent Reactions of Using a Sr₃Fe₂O₇ Cathode in Both Oxygen Ion Conducting and Proton Conducting Solid Oxide Fuel Cells. *RSC Adv.* **2018**, *8* (47), 26448–26460. 10.1039/C8RA04059A.

- (72) Zhou, J.; Chen, G.; Wu, K.; Cheng, Y. Interaction of La_2NiO_4 (100) Surface with Oxygen Molecule: A First-Principles Study. *J. Phys. Chem. C*, **2013**, *117* (25), 12991–12999. 10.1021/jp403094x.
- (73) Akbay, T.; Staykov, A.; Druce, J.; Téllez, H.; Ishihara, T.; Kilner, J. A. The Interaction of Molecular Oxygen on LaO Terminated Surfaces of La_2NiO_4 . *J. Mater. Chem. A*, **2016**, *4* (34), 13113–13124. 10.1039/C6TA02715F.
- (74) Han, Z.; Dong, H.; Wu, Y.; Yang, Y. Locating the Rate-Limiting Step of Hydrogen Conversion on $\text{Sr}_2\text{Fe}_{1.5}\text{Mo}_{0.5}\text{O}_6$ (001) Surface: Implications for Efficient SOFC Anode Design. *Appl. Surf. Sci.*, **2022**, *595*, 153513. 10.1016/j.apsusc.2022.153513.
- (75) Ren, B.; Croiset, E.; Ricardez–Sandoval, L. A Theoretical Study on CO_2 Electrolysis through Synergistic Manipulation of Ni/Mn Doping and Oxygen Vacancies in $\text{La}(\text{Sr})\text{FeO}_3$. *J. Catal.*, **2020**, *383*, 273–282. 10.1016/j.jcat.2020.01.033.
- (76) Ammal, S. C.; Heyden, A. Reaction Kinetics of the Electrochemical Oxidation of CO and Syngas Fuels on a $\text{Sr}_2\text{Fe}_{1.5}\text{Mo}_{0.5}\text{O}_{6-\delta}$ Perovskite Anode. *J. Mater. Chem. A*, **2015**, *3* (43), 21618–21629. 10.1039/C5TA05056A.
- (77) Walker, E.; Ammal, S. C.; Suthirakun, S.; Chen, F.; Terejanu, G. A.; Heyden, A. Mechanism of Sulfur Poisoning of $\text{Sr}_2\text{Fe}_{1.5}\text{Mo}_{0.5}\text{O}_{6-\delta}$ Perovskite Anode under Solid Oxide Fuel Cell Conditions. *J. Phys. Chem. C*, **2014**, *118* (41), 23545–23552. 10.1021/jp507593k.
- (78) Perdew, J. P.; Wang, Y. Accurate and Simple Analytic Representation of the Electron-Gas Correlation Energy. *Phys. Rev. B*, **1992**, *45* (23), 13244–13249. 10.1103/PhysRevB.98.079904.
- (79) Ota, T.; Kizaki, H.; Morikawa, Y. Mechanistic Analysis of Oxygen Vacancy Formation and Ionic Transport in $\text{Sr}_3\text{Fe}_2\text{O}_{7-\delta}$. *J. Phys. Chem. C*, **2018**, *122* (8), 4172–4181. 10.1021/acs.jpcc.7b11904.
- (80) Szaro, N. A.; Ammal, S. C.; Chen, F.; Heyden, A. An Ab Initio Study of the Oxygen Defect Formation and Oxide Ion Migration in $(\text{Sr}_{1-x}\text{Pr}_x)_2\text{FeO}_{4+\delta}$. *J. Power Sources*, **2021**, *515*, 230602. 10.1016/j.jpowsour.2021.230602.
- (81) Monkhorst, H. J.; Pack, J. D. Special Points for Brillouin-Zone Integrations. *Phys. Rev. B*, **1976**, *13* (12), 5188–5192. 10.1103/PhysRevB.13.5188.
- (82) Makov, G.; Payne, M. C. Periodic Boundary Conditions in Ab Initio Calculations. *Phys. Rev. B*, **1995**, *51* (7), 4014–4022. 10.1103/PhysRevB.51.4014.

- (83) Henkelman, G.; Uberuaga, B. P.; Jónsson, H. A Climbing Image Nudged Elastic Band Method for Finding Saddle Points and Minimum Energy Paths. *J. Chem. Phys.*, **2000**, *113* (22), 9901–9904. 10.1063/1.1329672.
- (84) Heyden, A.; Bell, A. T.; Keil, F. J. Efficient Methods for Finding Transition States in Chemical Reactions: Comparison of Improved Dimer Method and Partitioned Rational Function Optimization Method. *J. Chem. Phys.*, **2005**, *123* (22), 224101. 10.1063/1.2104507.
- (85) Henkelman, G.; Jónsson, H. A Dimer Method for Finding Saddle Points on High Dimensional Potential Surfaces Using Only First Derivatives. *J. Chem. Phys.*, **1999**, *111* (15), 7010–7022. 10.1063/1.480097.
- (86) Olsen, R. A.; Kroes, G. J.; Henkelman, G.; Arnaldsson, A.; Jónsson, H. Comparison of Methods for Finding Saddle Points without Knowledge of the Final States. *J. Chem. Phys.*, **2004**, *121* (20), 9776–9792. 10.1063/1.1809574.
- (87) Ammal, S. C.; Heyden, A. Modeling the Noble Metal/TiO₂ (110) Interface with Hybrid DFT Functionals: A Periodic Electrostatic Embedded Cluster Model Study. *J. Chem. Phys.*, **2010**, *133* (16), 164703. 10.1063/1.3497037.
- (88) Nørskov, J. K.; Rossmeisl, J.; Logadottir, A.; Lindqvist, L.; Kitchin, J. R.; Bligaard, T.; Jónsson, H. Origin of the Overpotential for Oxygen Reduction at a Fuel-Cell Cathode. *J. Phys. Chem. B*, **2004**, *108* (46), 17886–17892. 10.1021/jp047349j.
- (89) Atkins, P. W.; Julio De Paula; Keeler, J. *Atkins' Physical Chemistry*; Oxford University Press: Oxford, 2018.
- (90) Peterson, A. A.; Abild-Pedersen, F.; Studt, F.; Rossmeisl, J.; Nørskov, J. K. How Copper Catalyzes the Electroreduction of Carbon Dioxide into Hydrocarbon Fuels. *Energy Environ. Sci.*, **2010**, *3* (9), 1311. 10.1039/c0ee00071j.
- (91) Yang, W.; Solomon, R. V.; Mamun, O.; Bond, J. Q.; Heyden, A. Investigation of the Reaction Mechanism of the Hydrodeoxygenation of Propionic Acid over a Rh(111) Surface: A First Principles Study. *J. Catal.*, **2020**, *391*, 98–110. 10.1016/j.jcat.2020.08.015.
- (92) Shampine, L. F.; Reichelt, M. W. The MATLAB Ode Suite. *SIAM J. Sci. Comput.*, **1997**, *18* (1), 1–22. 10.1137/S1064827594276424.
- (93) Stegelmann, C.; Andreasen, A.; Campbell, C. T. Degree of Rate Control: How Much the Energies of Intermediates and Transition States Control Rates. *J. Am. Chem. Soc.*, **2009**, *131* (23), 8077–8082. 10.1021/ja9000097.

- (94) Campbell, C. T. The Degree of Rate Control: A Powerful Tool for Catalysis Research. *ACS Catal.*, **2017**, 7 (4), 2770–2779. 10.1021/acscatal.7b00115.
- (95) Cheng, L.; Assary, R. S.; Qu, X.; Jain, A.; Ong, S. P.; Rajput, N. N.; Persson, K.; Curtiss, L. A. Accelerating Electrolyte Discovery for Energy Storage with High-Throughput Screening. *J. Phys. Chem. Lett.*, **2015**, 6 (2), 283–291. 10.1021/jz502319n.
- (96) Qu, X.; Jain, A.; Rajput, N. N.; Cheng, L.; Zhang, Y.; Ong, S. P.; Brafman, M.; Maginn, E.; Curtiss, L. A.; Persson, K. A. The Electrolyte Genome Project: A Big Data Approach in Battery Materials Discovery. *Comput. Mater. Sci.*, **2015**, 103, 56–67. 10.1016/j.commatsci.2015.02.050.
- (97) Jung, M. H.; Alsmadi, A. M.; Chang, S.; Fitzsimmons, M. R.; Zhao, Y.; Lacerda, A. H.; Kawanaka, H.; El-Khatib, S.; Nakotte, H. Magnetic Ordering in Single-Crystalline SrLaFeO₄ and Sr_{1.1}La_{0.9}FeO₄. *J. Appl. Phys.*, **2005**, 97 (10), 10A926 10.1063/1.1861416.
- (98) Sun, C.; Stimming, U. Recent Anode Advances in Solid Oxide Fuel Cells. *J. Power Sources*, **2007**, 171 (2), 247–260. 10.1016/j.jpowsour.2007.06.086.
- (99) Tealdi, C.; Ferrara, C.; Mustarelli, P.; Islam, M. S. Vacancy and Interstitial Oxide Ion Migration in Heavily Doped La_{2-x}Sr_xCoO_{4±δ}. *J. Mater. Chem.*, **2012**, 22 (18), 8969–8975. 10.1039/c2jm30769c.
- (100) Huan, D.; Wang, Z.; Wang, Z.; Peng, R.; Xia, C.; Lu, Y. High-Performanced Cathode with a Two-Layered R–P Structure for Intermediate Temperature Solid Oxide Fuel Cells. *ACS Appl. Mater. Interfaces*, **2016**, 8 (7), 4592–4599. 10.1021/acsami.5b10844.
- (101) Takamatsu, A.; Tamai, K.; Hosokawa, S.; Tanaka, T.; Ehara, M.; Fukuda, R. Oxidation and Storage Mechanisms for Nitrogen Oxides on Various Terminated (001) Surfaces of SrFeO_{3-δ} and Sr₃Fe₂O_{7-δ} Perovskites. *ACS Appl Mater Interfaces* **2021**, 13 (6), 7216–7226. 10.1021/acsami.0c20724.
- (102) Gu, X. K.; Nikolla, E. Design of Ruddlesden-Popper Oxides with Optimal Surface Oxygen Exchange Properties for Oxygen Reduction and Evolution. *ACS Catal.*, **2017**, 7 (9), 5912–5920. 10.1021/acscatal.7b01483.
- (103) Bockris, J. O.; Nagy, Z. Symmetry Factor and Transfer Coefficient. A Source of Confusion in Electrode Kinetics. *J. Chem. Educ.*, **1973**, 50 (12), 839. 10.1021/ed050p839.
- (104) Xie, W.; Lee, Y. L.; Shao-Horn, Y.; Morgan, D. Oxygen Point Defect Chemistry in Ruddlesden–Popper Oxides (La_{1-x}Sr_x)₂MO_{4±δ} (M = Co, Ni, Cu). *J. Phys. Chem. Lett.*, **2016**, 7 (10), 1939–1944. 10.1021/acs.jpcllett.6b00739.

- (105) McIntosh, S.; Gorte, R. J. Direct Hydrocarbon Solid Oxide Fuel Cells. *Chem. Rev.*, **2004**, *104* (10), 4845–4866. 10.1021/cr020725g.
- (106) Wachsman, E. D.; Lee, K. T. Lowering the Temperature of Solid Oxide Fuel Cells. *Science*, **2011**, *334* (6058), 935–939. 10.1126/science.1204090.
- (107) Ormerod, R. M. Solid Oxide Fuel Cells. *Chem. Soc. Rev.*, **2003**, *32* (1), 17–28. 10.1039/b105764m.
- (108) Steele, B. C. H.; Heinzl, A. Materials for Fuel-Cell Technologies. *Nature*, **2001**, *414* (6861), 345–352. 10.1038/35104620.
- (109) Fergus, J. W. Electrolytes for Solid Oxide Fuel Cells. *J. Power Sources*, **2006**, *162* (1), 30–40. 10.1016/j.jpowsour.2006.06.062.
- (110) Jaiswal, N.; Tanwar, K.; Suman, R.; Kumar, D.; Upadhyay, S.; Parkash, O. A Brief Review on Ceria Based Solid Electrolytes for Solid Oxide Fuel Cells. *J. Alloys Compd.*, **2019**, *781*, 984–1005. 10.1016/j.jallcom.2018.12.015.
- (111) Gao, Z.; Mogni, L. v.; Miller, E. C.; Railsback, J. G.; Barnett, S. A. A Perspective on Low-Temperature Solid Oxide Fuel Cells. *Energy Environ. Sci.*, **2016**, *9* (5), 1602–1644. 10.1039/C5EE03858H.
- (112) Hossain, S.; Abdalla, A. M.; Jamain, S. N. B.; Zaini, J. H.; Azad, A. K. A Review on Proton Conducting Electrolytes for Clean Energy and Intermediate Temperature-Solid Oxide Fuel Cells. *Renew. Sustain. Energy Rev.*, **2017**, *79*, 750–764. 10.1016/j.rser.2017.05.147.
- (113) Fabbri, E.; Pergolesi, D.; Traversa, E. Materials Challenges toward Proton-Conducting Oxide Fuel Cells: A Critical Review. *Chem. Soc. Rev.* **2010**, *39* (11), 4355. 10.1039/b902343g.
- (114) Fallah Vostakola, M.; Amini Horri, B. Progress in Material Development for Low-Temperature Solid Oxide Fuel Cells: A Review. *Energies*, **2021**, *14* (5), 1280. 10.3390/en14051280.
- (115) Singh, K.; Kannan, R.; Thangadurai, V. Perspective of Perovskite-Type Oxides for Proton Conducting Solid Oxide Fuel Cells. *Solid State Ion.*, **2019**, *339*, 114951. 10.1016/j.ssi.2019.04.014.

- (116) Tanner, C. W.; Virkar, A. v. Instability of BaCeO₃ in H₂O-Containing Atmospheres. *J. Electrochem. Soc.*, **1996**, *143* (4), 1386–1389. 10.1149/1.1836647.
- (117) Gregori, G.; Merkle, R.; Maier, J. Ion Conduction and Redistribution at Grain Boundaries in Oxide Systems. *Prog. Mater. Sci.*, **2017**, *89*, 252–305. 10.1016/j.pmatsci.2017.04.009.
- (118) Gopalan, S.; Virkar, A. v. Thermodynamic Stabilities of SrCeO₃ and BaCeO₃ Using a Molten Salt Method and Galvanic Cells. *J. Electrochem. Soc.*, **1993**, *140* (4), 1060–1065. 10.1149/1.2056197.
- (119) Zuo, C.; Zha, S.; Liu, M.; Hatano, M.; Uchiyama, M. Ba(Zr_{0.1}Ce_{0.7}Y_{0.2})O_{3-δ} as an Electrolyte for Low-Temperature Solid-Oxide Fuel Cells. *Adv. Mat.*, **2006**, *18* (24), 3318–3320. 10.1002/adma.200601366.
- (120) Sawant, P.; Varma, S.; Wani, B. N.; Bharadwaj, S. R. Synthesis, Stability and Conductivity of BaCe_{0.8-x}Zr_xY_{0.2}O_{3-δ} as Electrolyte for Proton Conducting SOFC. *Int. J. Hydrog. Energy*, **2012**, *37* (4), 3848–3856. 10.1016/j.ijhydene.2011.04.106.
- (121) Liu, Z.; Wang, X.; Liu, M.; Liu, J. Enhancing Sinterability and Electrochemical Properties of Ba(Zr_{0.1}Ce_{0.7}Y_{0.2})O_{3-δ} Proton Conducting Electrolyte for Solid Oxide Fuel Cells by Addition of NiO. *Int. J. Hydrog. Energy*, **2018**, *43* (29), 13501–13511. 10.1016/j.ijhydene.2018.05.089.
- (122) Lyagaeva, J.; Antonov, B.; Dunyushkina, L.; Kuimov, V.; Medvedev, D.; Demin, A.; Tsiakaras, P. Acceptor Doping Effects on Microstructure, Thermal and Electrical Properties of Proton-Conducting BaCe_{0.5}Zr_{0.3}Ln_{0.2}O_{3-δ} (Ln = Yb, Gd, Sm, Nd, La or Y) Ceramics for Solid Oxide Fuel Cell Applications. *Electrochim. Acta*, **2016**, *192*, 80–88. 10.1016/j.electacta.2016.01.144.
- (123) Zhou, Y.; Guan, X.; Zhou, H.; Ramadoss, K.; Adam, S.; Liu, H.; Lee, S.; Shi, J.; Tsuchiya, M.; Fong, D. D.; Ramanathan, S. Strongly Correlated Perovskite Fuel Cells. *Nature*, **2016**, *534* (7606), 231–234. 10.1038/nature17653.
- (124) Nico, C.; Monteiro, T.; Graça, M. P. F. Niobium Oxides and Niobates Physical Properties: Review and Prospects. *Prog. Mater. Sci.*, **2016**, *80*, 1–37. 10.1016/j.pmatsci.2016.02.001.

- (125) Zhao, L.; He, B.; Lin, B.; Ding, H.; Wang, S.; Ling, Y.; Peng, R.; Meng, G.; Liu, X. High Performance of Proton-Conducting Solid Oxide Fuel Cell with a Layered PrBaCo₂O_{5+δ} Cathode. *J. Power Sources*, **2009**, *194* (2), 835–837. 10.1016/j.jpowsour.2009.06.010.
- (126) Malavasi, L.; Fisher, C. A. J.; Islam, M. S. Oxide-Ion and Proton Conducting Electrolyte Materials for Clean Energy Applications: Structural and Mechanistic Features. *Chem. Soc. Rev.*, **2010**, *39* (11), 4370–4387. 10.1039/b915141a.
- (127) Momma, K.; Izumi, F. VESTA 3 for Three-Dimensional Visualization of Crystal, Volumetric and Morphology Data. *J. Appl. Crystallogr.*, **2011**, *44* (6), 1272–1276. 10.1107/S0021889811038970.
- (128) Jacobs, R.; Mayeshiba, T.; Booske, J.; Morgan, D. Material Discovery and Design Principles for Stable, High Activity Perovskite Cathodes for Solid Oxide Fuel Cells. *Adv. Energy Mater.*, **2018**, *8* (11). 10.1002/aenm.201702708.
- (129) Jacobs, R.; Liu, J.; Na, B. T.; Guan, B.; Yang, T.; Lee, S.; Hackett, G.; Kalapos, T.; Abernathy, H.; Morgan, D. Unconventional Highly Active and Stable Oxygen Reduction Catalysts Informed by Computational Design Strategies. *Adv. Energy Mater.*, **2022**, *12* (25). 10.1002/aenm.202201203.
- (130) Ma, T.; Jacobs, R.; Booske, J.; Morgan, D. Discovery and Engineering of Low Work Function Perovskite Materials. *J. Mater. Chem. C*, **2021**, *9*, 12778–12790. 10.1039/D1TC01286J.
- (131) Jacobs, R.; Luo, G.; Morgan, D. Materials Discovery of Stable and Nontoxic Halide Perovskite Materials for High-Efficiency Solar Cells. *Adv. Funct. Mater.*, **2019**, *29* (23). 10.1002/adfm.201804354.
- (132) Islam, M. S.; Wang, S.; Hall, A. T.; Mo, Y. First-Principles Computational Design and Discovery of Solid-Oxide Proton Conductors. *Chem. Mater.*, **2022**, *34* (13), 5938–5948. 10.1021/acs.chemmater.2c00867.
- (133) Kresse, G.; Furthmüller, J. Efficient Iterative Schemes for *Ab Initio* Total-Energy Calculations Using a Plane-Wave Basis Set *Phys. Rev. B*, **1996**, *54* (16), 11169–11186. 10.1103/PhysRevB.54.11169.

- (134) Perdew, J. P.; Yue, W. Accurate and Simple Density Functional for the Electronic Exchange Energy: Generalized Gradient Approximation. *Phys. Rev. B*, **1986**, *33* (12), 8800–8802. 10.1103/PhysRevB.33.8800.
- (135) Perdew, J. P.; Wang, Y. Accurate and Simple Analytic Representation of the Electron-Gas Correlation Energy. *Phys. Rev. B*, **1992**, *45* (23), 079904. 10.1103/PhysRevB.45.13244.
- (136) Kresse, G.; Joubert, D. From Ultrasoft Pseudopotentials to the Projector Augmented-Wave Method. *Phys. Rev. B*, **1999**, *59* (3), 1758–1775. 10.1103/PhysRevB.59.1758.
- (137) Blöchl, P. E. Projector Augmented-Wave Method. *Phys. Rev. B*, **1994**, *50* (24), 17953–17979. 10.1103/PhysRevB.50.17953.
- (138) Ong, S. P.; Richards, W. D.; Jain, A.; Hautier, G.; Kocher, M.; Cholia, S.; Gunter, D.; Chevrier, V. L.; Persson, K. A.; Ceder, G. Python Materials Genomics (Pymatgen): A Robust, Open-Source Python Library for Materials Analysis. *Comput. Mater. Sci.*, **2013**, *68*, 314–319. 10.1016/j.commatsci.2012.10.028.
- (139) Jain, A.; Ong, S. P.; Hautier, G.; Chen, W.; Richards, W. D.; Dacek, S.; Cholia, S.; Gunter, D.; Skinner, D.; Ceder, G.; Persson, K. A. Commentary: The Materials Project: A Materials Genome Approach to Accelerating Materials Innovation. *APL Mater.*, **2013**, *1* (1), 011002. 10.1063/1.4812323.
- (140) Dudarev, S. L.; Botton, G. A.; Savrasov, S. Y.; Humphreys, C. J.; Sutton, A. P. Electron-Energy-Loss Spectra and the Structural Stability of Nickel Oxide: An LSDAU Study. *Phys. Rev. B*, **1998**, *57* (3). 10.1103/PhysRevB.57.1505.
- (141) Wang, L.; Maxisch, T.; Ceder, G. Oxidation Energies of Transition Metal Oxides within the GGA+U Framework. *Phys. Rev. B*, **2006**, *73* (19). 10.1103/PhysRevB.73.195107.
- (142) Monkhorst, H. J.; Pack, J. D. Special Points for Brillouin-Zone Integrations. *Phys. Rev. B*, **1976**, *13* (12). 10.1103/PhysRevB.13.5188
- (143) Ong, S. P.; Wang, L.; Kang, B.; Ceder, G. Li-Fe-P-O₂ Phase Diagram from First Principles Calculations. *Chem. Mater.*, **2008**, *20* (5), 1798–1807. 10.1021/cm702327g.

- (144) Jain, A.; Hautier, G.; Ong, S. P.; Moore, C. J.; Fischer, C. C.; Persson, K. A.; Ceder, G. Formation Enthalpies by Mixing GGA and GGA + U Calculations. *Phys. Rev. B*, **2011**, *84* (4). 10.1103/PhysRevB.84.045115.
- (145) Bucher, E.; Sitte, W.; Klauser, F.; Bertel, E. Oxygen Exchange Kinetics of $\text{La}_{0.58}\text{Sr}_{0.4}\text{Co}_{0.2}\text{Fe}_{0.8}\text{O}_3$ at 600 °C in Dry and Humid Atmospheres. *Solid State Ion.*, **2011**, *191* (1), 61–67. 10.1016/j.ssi.2011.03.019.
- (146) Dunstan, M. T.; Jain, A.; Liu, W.; Ong, S. P.; Liu, T.; Lee, J.; Persson, K. A.; Scott, S. A.; Dennis, J. S.; Grey, C. P. Large Scale Computational Screening and Experimental Discovery of Novel Materials for High Temperature CO_2 Capture. *Energy Environ. Sci.*, **2016**, *9* (4), 1346–1360. 10.1039/c5ee03253a.
- (147) Kröger, F. A.; Vink, H. J. Relations between the Concentrations of Imperfections in Solids. *J. Phys. Chem. Solids*, **1958**, *5* (3), 208–223. 10.1016/0022-3697(58)90069-6.
- (148) Freysoldt, C.; Grabowski, B.; Hickel, T.; Neugebauer, J.; Kresse, G.; Janotti, A.; van de Walle, C. G. First-Principles Calculations for Point Defects in Solids. *Rev. Mod. Phys.*, **2014**, *86* (1), 253–305. 10.1103/RevModPhys.86.253.
- (149) Lindman, A.; Helgee, E. E.; Wahnström, G. Comparison of Space-Charge Formation at Grain Boundaries in Proton-Conducting BaZrO_3 and BaCeO_3 . *Chem. Mater.*, **2017**, *29* (18), 7931–7941. 10.1021/acs.chemmater.7b02829.
- (150) Wu, Y.; Lazic, P.; Hautier, G.; Persson, K.; Ceder, G. First Principles High Throughput Screening of Oxynitrides for Water-Splitting Photocatalysts. *Energy Environ. Sci.*, **2013**, *6* (1), 157–168. 10.1039/c2ee23482c.
- (151) Saal, J. E.; Kirklin, S.; Aykol, M.; Meredig, B.; Wolverton, C. Materials Design and Discovery with High-Throughput Density Functional Theory: The Open Quantum Materials Database (OQMD). *JOM*, **2013**, *65* (11), 1501–1509. 10.1007/s11837-013-0755-4.
- (152) Sun, W.; Dacek, S. T.; Ong, S. P.; Hautier, G.; Jain, A.; Richards, W. D.; Gamst, A. C.; Persson, K. A.; Ceder, G. The Thermodynamic Scale of Inorganic Crystalline Metastability. *Science*, **2016**, *2* (11), 1600225. 10.1126/sciadv.1600225.

- (153) Yamazaki, Y.; Blanc, F.; Okuyama, Y.; Buannic, L.; Lucio-Vega, J. C.; Grey, C. P.; Haile, S. M. Proton Trapping in Yttrium-Doped Barium Zirconate. *Nat. Mater.*, **2013**, *12* (7), 647–651. 10.1038/nmat3638.
- (154) Løken, A.; Saeed, S. W.; Getz, M. N.; Liu, X.; Bjørheim, T. S. Alkali Metals as Efficient A-Site Acceptor Dopants in Proton Conducting BaZrO₃. *J. Mater. Chem. A*. **2016**, *4* (23), 9229–9235. 10.1039/c6ta01446a.
- (155) Dawson, J. A.; Tanaka, I. Proton Trapping in y and Sn Co-Doped BaZrO₃. *J. Mater. Chem. A*. **2015**, *3* (18), 10045–10051. 10.1039/c5ta01450f.
- (156) Wu, Y.; Lazic, P.; Hautier, G.; Persson, K.; Ceder, G. First Principles High Throughput Screening of Oxynitrides for Water-Splitting Photocatalysts. *Energy Environ. Sci.* **2013**, *6* (1), 157–168. 10.1039/c2ee23482c.
- (157) Saal, J. E.; Kirklin, S.; Aykol, M.; Meredig, B.; Wolverton, C. Materials Design and Discovery with High-Throughput Density Functional Theory: The Open Quantum Materials Database (OQMD). *JOM*. **2013**, *65* (11), 1501–1509. 10.1007/s11837-013-0755-4.
- (158) Dawson, J. A.; Miller, J. A.; Tanaka, I. First-Principles Insight into the Hydration Ability and Proton Conduction of the Solid State Proton Conductor, Y and Sn Co-Doped BaZrO₃. *Chem. Mater.* **2015**, *27* (3), 901–908. 10.1021/cm504110y.
- (159) Jeong, Y. C.; Kim, D. H.; Kim, B. K.; Kim, Y. C. Migration and Interaction of Multi-Protons in Zinc-Doped Barium Zirconate. *Kor. J. Met Mater.* **2011**, *49* (12), 977–982. 10.3365/KJMM.2011.49.12.977.
- (160) Han, D.; Uda, T. The Best Composition of an Y-Doped BaZrO₃ Electrolyte: Selection Criteria from Transport Properties, Microstructure, and Phase Behavior. *J. Mater. Chem A*. **2018**, *6* (38), 18571–18582. 10.1039/c8ta06280c.
- (161) Ueno, K.; Hatada, N.; Han, D.; Uda, T. Thermodynamic Maximum of Y Doping Level in Barium Zirconate in Co-Sintering with NiO. *J. Mater. Chem. A*. **2019**, *7* (12), 7232–7241. 10.1039/c8ta12245h.
- (162) Szaro, N. A.; Ammal, S. C.; Chen, F.; Heyden, A. Theoretical Investigation of the Electrochemical Oxidation of H₂ and CO Fuels on a Ruddlesden-Popper SrLaFeO_{4±δ} Anode. *ACS Appl. Mater. Interfaces*, **2023**, *15* (25), 30139–30151, 10.1021/acsami.3c03256.

APPENDIX A

SUPPORTING INFORMATION FOR AN AB INITIO STUDY OF THE
OXYGEN DEFECT FORMATION AND OXIDE ION MIGRATION IN
 $(\text{Sr}_{1-x}\text{Pr}_x)_2\text{FeO}_{4\pm\delta}$

A.1 PHASE STABILITY OF $(\text{Sr}_{1-x}\text{Pr}_x)_2\text{FeO}_4$

The stability of the dopant-configurations were calculated with respect to all phases in the Sr-Pr-Fe-O space present in the Materials Project (MP) database via the Pymatgen toolkit¹⁻⁴. In order to ensure compatibility with the MP database, we verified that our pseudopotentials are the same as in the MP database and we adjusted the Hubbard Parameter for both Fe and Pr in accordance with the MP parameters of 5.3 and 0.0 eV, respectively. Test calculations showed that the change in Hubbard Parameters from those used in the rest of this paper did practically not have any influence on energy differences such as the defect formation free energy.

Mixed GGA/GGA+U calculations were utilized^{5,6}. For example, Fe was modeled with GGA while SrFeO_3 and Sr_2FeO_4 were modelled with GGA+U. Energy shifts due to mixed GGA/GGA+U calculations were subtracted from the calculated DFT energies. The GGA/GGA+U shift is 2.733 (eV/atom) for Fe⁷. Utilizing the Material Project database, the MP version of O_2 (mp-12957) was used in the convex hull calculation. Thus, we used the O_2 gas shift of 0.7023 eV/O subtracted from the calculated DFT energies⁷.

A.2 BIBLIOGRAPHY

- (1) Jain, A.; Ong, S. P.; Hautier, G.; Chen, W.; Richards, W. D.; Dacek, S.; Cholia, S.; Gunter, D.; Skinner, D.; Ceder, G.; Persson, K. A. Commentary: The Materials Project: A Materials Genome Approach to Accelerating Materials Innovation. *APL Mater.*, **2013**, 1 (1), 1–11. 10.1063/1.4812323.
- (2) Ong, S. P.; Richards, W. D.; Jain, A.; Hautier, G.; Kocher, M.; Cholia, S.; Gunter, D.; Chevrier, V. L.; Persson, K. A.; Ceder, G. Python Materials Genomics (Pymatgen): A Robust, Open-Source Python Library for Materials Analysis. *Comput. Mater. Sci.*, **2013**, 68, 314–319. 10.1016/j.commatsci.2012.10.028.
- (3) Ong, S. P.; Cholia, S.; Jain, A.; Brafman, M.; Gunter, D.; Ceder, G.; Persson, K. A. The Materials Application Programming Interface (API): A Simple, Flexible and Efficient API for Materials Data Based on REpresentational State Transfer

- (REST) Principles. *Comput. Mater. Sci.*, **2015**, 97, 209–215.
10.1016/j.commatsci.2014.10.037.
- (4) Ong, S. P.; Wang, L.; Kang, B.; Ceder, G. Li-Fe-P-O₂ Phase Diagram from First Principles Calculations. *Chem. Mater.*, **2008**, 20 (5), 1798–1807.
10.1021/cm702327g.
 - (5) Wang, L.; Maxisch, T.; Ceder, G. Oxidation Energies of Transition Metal Oxides within the GGA+U Framework. *Phys. Rev. B*, **2006**, 73 (19), 1–6.
10.1103/PhysRevB.73.195107.
 - (6) Jain, A.; Hautier, G.; Ong, S. P.; Moore, C. J.; Fischer, C. C.; Persson, K. A.; Ceder, G. Formation Enthalpies by Mixing GGA and GGA + U Calculations. *Phys. Rev. B*, **2011**, 84 (4), 1–10. 10.1103/PhysRevB.84.045115.
 - (7) Jacobs, R.; Mayeshiba, T.; Booske, J.; Morgan, D. Material Discovery and Design Principles for Stable, High Activity Perovskite Cathodes for Solid Oxide Fuel Cells. *Adv. Energy Mater.*, **2018**, 8 (11). 10.1002/aenm.201702708.
 - (8) Togo, A.; Tanaka, I. First Principles Phonon Calculations in Materials Science. *Scr. Mater.*, **2015**, 108, 1–5. 10.1016/j.scriptamat.2015.07.021.
 - (9) Grau-Crespo, R.; Hamad, S.; Catlow, C. R. A.; De Leeuw, N. H. Symmetry-Adapted Configurational Modelling of Fractional Site Occupancy in Solids. *J. Phys. Condens. Matter.*, **2007**, 19 (25). 10.1088/0953-8984/19/25/256201.
 - (10) Momma, K.; Izumi, F. VESTA 3 for Three-Dimensional Visualization of Crystal, Volumetric and Morphology Data. *J. Appl. Crystallogr.*, **2011**, 44 (6), 1272–1276.
10.1107/S0021889811038970.

A.3 FIGURES AND TABLES

Table A.1: Calculated harmonic phonon energy (E) and Helmholtz free energy (F) of vacancy formation energy due to vibrational contributions for Sr₂FeO₄ using calculations conducted with the DFPT and phonopy (version 2.1.3) code.

	T (K)	E (eV)	F (eV)
Pristine	0	2.635	2.635
	1100	15.673	-18.705
Vacancy	0	2.750	2.750
	1100	15.733	-18.699
Difference in Energy (eV)	0	0.114	0.114
	1100	0.060	0.0058

Table A.2: Relative energies of all possible conformers generated by the site-occupancy disorder (SOD) package for (Sr_{1-x}Pr_x)₂FeO₄ (x = 0.125) starting with the magnetic configuration A shown in Figure 2.1(b).

Configuration	Relative Energy (eV)
1	0.135
2	0.349
3	0.066
4	0.184
5	0.146
6	0.048
7	0.000

Table A.3: Relative energies of all possible conformers generated by the site-occupancy disorder (SOD) package for $(\text{Sr}_{1-x}\text{Pr}_x)_2\text{FeO}_4$ ($x = 0.25$) starting with the magnetic configuration A shown in Figure 2.1(b).

Configuration	Relative Energy (eV)
1	0.753
2	0.677
3	0.579
4	0.654
5	0.375
6	0.215
7	0.483
8	0.474
9	0.620
10	0.217
11	0.176
12	0.464
13	0.182
14	0.132
15	0.177
16	0.176
17	0.337
18	0.067
19	0.156
20	0.152
21	0.030
22	0.011
23	0.000
24	0.120
25	0.720
26	0.270
27	0.211
28	1.017
29	0.438
30	0.394
31	0.498
32	0.210
33	0.293
34	0.166
35	0.249
36	0.042
37	0.123
38	0.012
39	0.211

40	0.213
41	0.080
42	0.053

Table A.4: Relative energies of all possible conformers generated by the site-occupancy disorder (SOD) package for $(\text{Sr}_{1-x}\text{Pr}_x)_2\text{FeO}_4$ ($x = 0.375$) starting with the magnetic configuration A shown in Figure 2.1(b).

Configuration	Relative Energy (eV)						
1	0.706	31	0.372	62	0.261	93	0.076
2	1.389	32	0.633	63	0.206	94	0.334
3	0.597	33	0.247	64	0.106	95	0.115
4	0.436	34	0.274	65	0.104	96	0.151
5	0.518	35	0.300	66	0.371	97	0.135
6	0.800	36	0.247	67	0.164	98	0.107
7	0.357	37	0.098	68	0.191	99	0.072
8	0.390	38	0.155	69	0.149	100	0.082
9	0.349	39	0.406	70	0.356	101	0.263
10	0.072	40	0.304	71	0.278	102	0.315
11	0.311	41	0.658	72	0.612	103	0.252
12	1.265	42	0.255	73	0.329	104	0.244
13	1.168	43	0.271	74	0.380	105	0.030
14	0.517	44	0.266	75	0.353	106	0.033
15	0.451	45	0.088	76	0.299	107	0.582
16	0.698	46	0.395	77	0.287	108	0.696
17	0.642	47	0.537	78	0.285	109	0.823
18	0.350	48	0.227	79	0.643	110	0.643
19	0.701	49	0.254	80	0.133	111	0.668
20	0.385	50	0.477	81	0.101	112	0.619
21	0.336	51	0.553	82	0.135	113	0.541
22	0.311	52	0.076	83	0.095	114	0.623
23	0.151	53	0.311	84	0.272	115	0.489
24	0.459	54	0.379	85	0.333	116	0.519
25	1.153	55	0.063	86	0.086	117	0.954
26	0.663	56	0.000	87	0.091	118	0.752
27	0.615	57	0.162	88	0.222	119	0.774
28	0.471	58	0.164	89	0.280	120	0.723
29	0.425	59	0.422	90	0.046	121	0.702
30	0.301	60	0.237	91	0.047	122	0.595

Table A.5: Relative energies of all possible conformers generated by the site-occupancy disorder (SOD) package for $(\text{Sr}_{1-x}\text{Pr}_x)_2\text{FeO}_4$ ($x = 0.5$) starting with the magnetic configuration A shown in Figure 2.1(b).

Configuration	Relative Energy (eV)		
1	2.455	46	0.494
2	1.015	47	1.307
3	0.984	48	1.148
4	0.922	49	0.615
5	0.525	50	0.679
6	1.178	51	0.480
7	0.480	52	0.467
8	0.581	53	1.188
9	0.521	54	0.526
10	0.539	55	0.563
11	0.698	56	1.080
12	0.713	57	0.544
13	0.928	58	0.318
14	1.291	59	0.289
15	1.548	60	0.393
16	1.282	61	0.325
17	1.331	62	0.384
18	1.284	63	0.429
19	1.111	64	0.489
20	1.338	65	0.244
21	0.509	66	0.344
22	0.286	67	0.379
23	0.346	68	0.374
24	0.565	69	0.364
25	0.601	70	0.282
26	0.143	71	0.197
27	0.357	72	0.560
28	0.424	73	0.388
29	0.143	74	0.471
30	0.079	75	0.701
31	0.932	76	0.693
32	0.801	77	0.356
33	0.755	78	0.641
34	0.807	79	0.724
35	0.413	80	0.409
36	0.396	81	0.442
37	0.630	82	0.797
38	0.417	83	0.416
39	0.699	84	0.687
40	0.864	85	0.523

41	1.049	86	0.224
42	0.336	87	0.276
43	0.289	88	0.323
44	0.321	89	0.298
45	0.000	90	0.978
91	1.144	136	0.619
92	0.556	137	0.909
93	0.120	138	1.067
94	0.489	139	0.148
95	0.452	140	0.437
96	1.181	141	0.107
97	0.589	142	0.471
98	0.532	143	0.228
99	1.026	144	0.202
100	0.554	145	0.393
101	0.361	146	0.292
102	0.357	147	0.428
103	0.565	148	0.938
104	0.757	149	1.093
105	0.344	150	0.487
106	0.541	151	0.361
107	0.694	152	0.302
108	0.385	153	0.293
109	0.426	154	0.308
110	0.391	155	0.373
111	0.318	156	0.317
112	0.379	157	0.288
113	0.261	158	0.822
114	0.320	159	0.987
115	0.336	160	0.272
116	0.402	161	0.316
117	0.276	162	0.274
118	0.212	163	0.272
119	0.267	164	0.252
120	0.346	165	0.786
121	0.259	166	0.935
122	0.325	167	0.509
123	0.101	168	0.351
124	0.377	169	0.467
125	0.287	170	0.414
126	0.413	171	0.455
127	0.209	172	0.714
128	0.192	173	1.054
129	0.244	174	1.212
130	0.307	175	0.254
131	0.189	176	0.312
132	0.237	177	0.779
133	0.397	178	0.917

<i>134</i>	0.287	<i>179</i>	1.272
<i>135</i>	0.412	<i>180</i>	1.435
		<i>181</i>	1.598

Table A.6: Relative Energies (in eV) and average Fe Magnetic Moment (in μ_B) for the magnetic moment configurations presented in Figure 2.1(b) for $(\text{Sr}_{1-x}\text{Pr}_x)_2\text{FeO}_4$.

Config	x = 0		x = 0.125		x = 0.25		x = 0.375		x = 0.5	
	Relative Energy (eV)	μ_B								
FM	0.000	3.727	0.005	3.841	0.082	3.969	0.459	4.094	1.794	4.23
A	0.000	3.725	0.000	3.836	0.078	3.966	0.437	4.092	1.770	4.229
B	1.138	3.594	0.667	3.717	0.331	3.859	1.651	4.007	0.409	4.127
C	0.829	3.650	0.303	3.758	0.000	3.892	0.204	4.034	0.820	4.157
D	0.779	3.638	0.416	3.765	0.533	3.717	0.000	4.020	0.835	4.158
E	1.145	3.570	0.665	3.714	0.332	3.859	0.063	4.008	0.410	4.127
F	1.516	3.551	1.078	3.672	0.696	3.819	0.329	3.983	0.000	4.096

Table A.7: Relative Energies (in eV) for the magnetic moment configurations presented in Figure 2.1(b) for all minimum energy defect calculations.

Config	x = 0	x = 0.125	x = 0.25	x = 0.375	x = 0.5
	Relative Energy (eV)				
Vacancy					
FM	0.000	0.556	0.759	1.639	1.639
A	0.000	0.556	0.736	1.618	1.618
B	0.704	0.249	0.000	0.408	0.408
C	0.375	0.197	0.198	0.819	0.819
D	0.369	1.129	0.065	0.820	0.820
E	0.375	0.000	1.172	0.768	0.768
F	0.545	0.244	0.293	0.000	0.000
Interstitial					
FM	0.009	0.009	0.186	0.478	1.776
A	0.000	0.000	0.171	0.458	1.758
B	0.978	0.559	0.183	0.112	1.954
C	0.697	0.255	0.133	0.207	0.829
D	0.680	0.302	0.000	0.000	1.949
E	0.665	0.497	0.275	1.297	0.814
F	1.293	0.830	0.396	0.269	0.000

Table A.8: Oxygen Bader charges and the bond length between the interstitial defect and the next nearest oxygen (NNO) for each dopant-configuration.

Dopant-Configuration	q_o Defect (e)	q_o NNO (e)	$O_{\text{defect}}-O_{\text{NNO}}$ Bond Length (Å)
x = 0	-0.687	-0.666	1.445
x = 0.125	-0.749	-0.762	1.486
x = 0.25	-0.746	-0.754	1.485
x = 0.375	-0.736	-0.725	1.486
x = 0.5	-0.757	-0.752	1.488

Table A.9: Composite vacancy-mediated migration energy ($\Delta H_{f,vac} + \Delta H_{mig}$ in eV) for each dopant-configuration for all migration pathways.

Jump Route	Dopant-Configuration				
	x = 0	X = 0.125	x = 0.25	x = 0.375	x = 0.5
1. (O1 – O2)	4.117	5.214	5.464	5.283	9.574
2. (O1 – O3)	2.600	2.573	2.726	2.633	5.169
3. (O1 – O4)	2.899	2.625	2.754	2.627	8.495
4. (O1 – O5)	---	2.605	2.798	2.879	6.858
5. (O1 – O6)	---	2.543	2.751	2.676	---
6. (O1 – O7)	---	3.133	2.920	2.841	---
7. (O1 – O8)	---	2.989	2.656	3.234	---
8. (O1 – O9)	---	3.114	2.937	2.524	---
9. (O1 – O10)	---	3.213	3.202	3.178	---

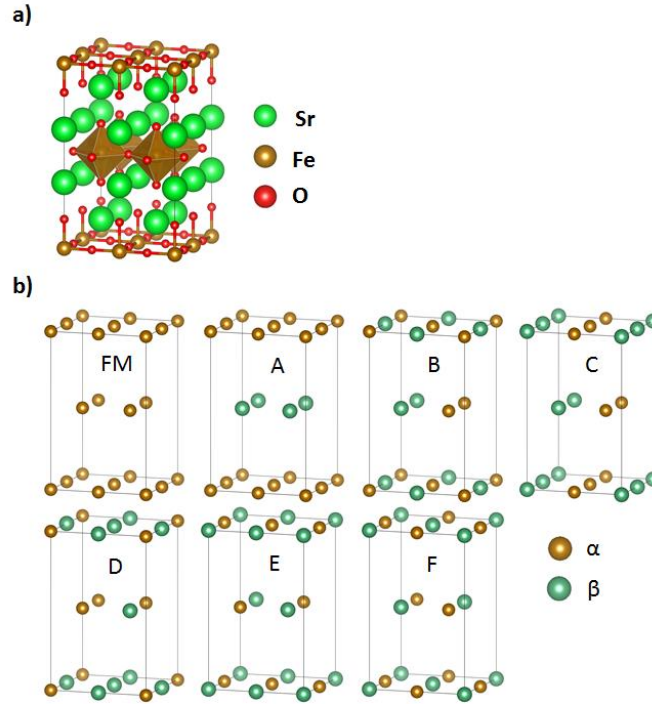


Figure A.1: a) The $2 \times 2 \times 1$ polyhedral representation of the $I4/mmm$ supercell model of Sr_2FeO_4 , and b) all unique Fe magnetic moment arrangements examined in this study. Structures visualized with VESTA ¹⁰.

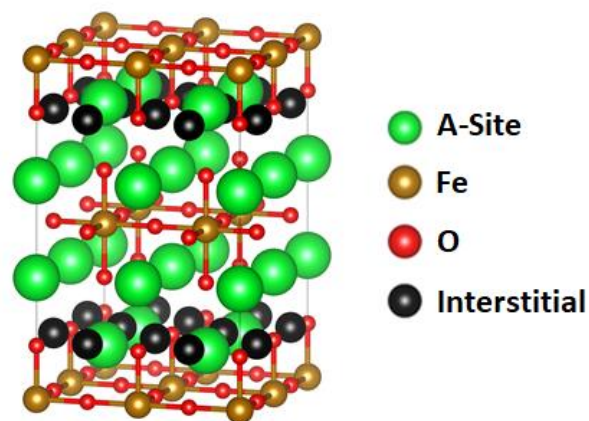


Figure A.2: Representative interstitial sites (black spheres) considered for $(\text{Sr}_{1-x}\text{Pr}_x)_2\text{FeO}_4$. The lattice parameters of all dopant configurations are fixed at the values of the pristine cell.

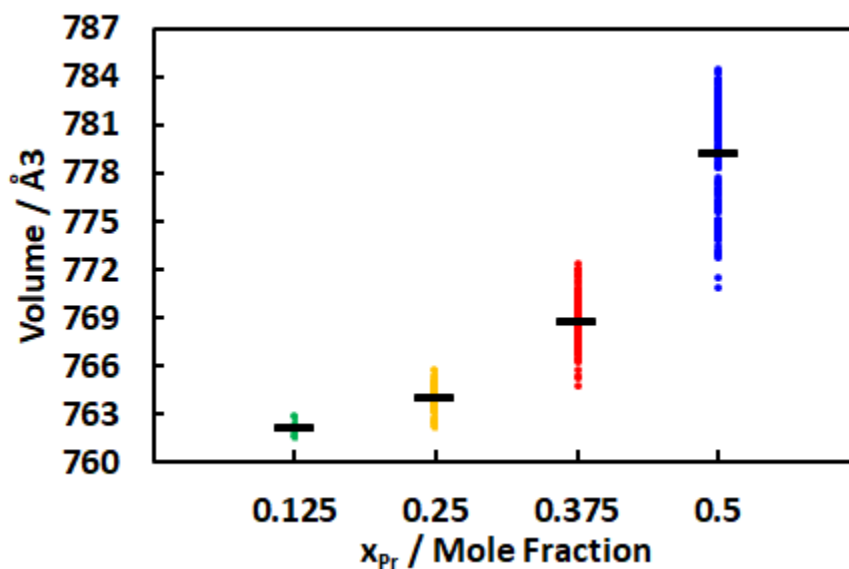


Figure A.3: Variation of supercell volume during structure optimization of $(\text{Sr}_{1-x}\text{Pr}_x)_2\text{FeO}_4$. All conformations generated by the SOD package⁹ are displayed for $x = 0.125$ (7 points, green), $x = 0.25$ (42 points, yellow), $x = 0.375$ (122 points, red) and $x = 0.5$ (181 points, blue). The black dashes represent the average volume for a given dopant-configuration.

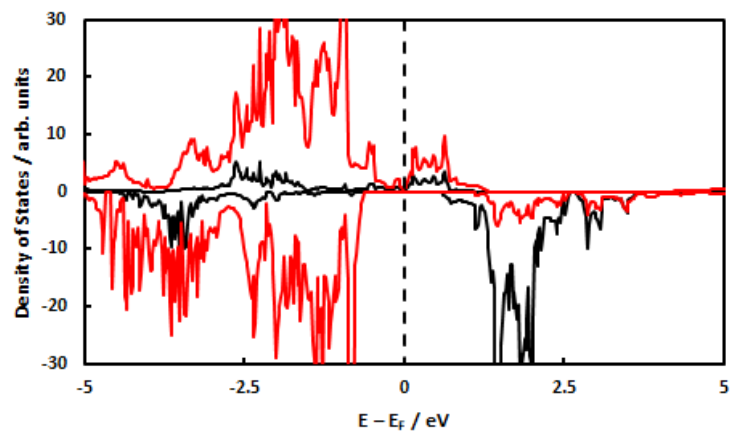


Figure A.4: PDOS for Fe 3d (black) and O 2p (red) states for the FM configuration of Sr_2FeO_4 . Energies are referred to the Fermi level (E_f). Positive PDOS values represent α -spin states and negative values represent β -spin states.

APPENDIX B

SUPPORTING INFORMATION FOR AN AB INITIO STUDY OF THE
OXYGEN DEFECT FORMATION AND OXIDE ION MIGRATION IN
 $(\text{Sr}_{1-x}\text{Pr}_x)_2\text{FeO}_{4\pm\delta}$

B.1 FREE ENERGIES FOR GASEOUS AND ADSORBATE SPECIES

For all gaseous species (e.g., H₂, O₂, CO, CO₂, H₂O, H₂S, CH₄), the chemical potential, $\mu_i(T, p^\circ)$ at a standard pressure p° of 1 atm is calculated using the following equations.

$$\mu_i(T, p^\circ) = E_{i,SCF} + E_{ZPE,i} - k_B T \ln(q_{trans,i} q_{rot,i} q_{vib,i} q_{elec,i}) \quad (\text{B.1})$$

$$E_{ZPE,i} = \sum_i \frac{1}{2} h \nu_i \quad (\text{B.2})$$

$$q_{vib,i} = \prod_i \frac{1}{1 - \exp\left(-\frac{h\nu_i}{k_B T}\right)} \quad (\text{B.3})$$

$E_{i,SCF}$ refers to the energy of the gas molecule calculated with the DFT functional, $E_{ZPE,i}$ is the zero-point energy obtained from calculated vibrational frequencies (ν_i), k_B refers to the Boltzmann constant, T is the temperature, and h refers to the Planck constant. q_{trans} , q_{rot} , and q_{elec} are the translational, rotational, and electronic partition functions, respectively and are calculated using the procedure outlined by McQuarrie 1. The vibrational partition function, q_{vib} is calculated using equation (B.3). The free energies of adsorbed species, $G_{slab+intermediate}$ are calculated with the following equation,

$$G_{slab+intermediate} = E_{slab+intermediate} + E_{ZPE} - k_B T \ln(q_{vib}) \quad (\text{B.4})$$

Figure B.1 displays the surface atoms that are perturbed in surface vibrational frequency calculations and displacements of 0.001 Å were used along the x, y, and z directions for all Hessian constructions.

B.2 ESTIMATION OF BULK VACANCY-MEDIATED MIGRATION ENERGIES

As outlined by Ritzmann et al. ², the vacancy-mediated self-hopping rate constant can be derived from the length normalized self-diffusion coefficient for vacancy-mediated diffusion (D_O):

$$k_f \cong \frac{D_O}{l_{hop}^2} = C_V \frac{D_V}{l_{hop}^2} \quad (\text{B. 5})$$

where C_V is the concentration of oxygen vacancies, l_{hop} is the vacancy jump or hop length, and D_V is the vacancy diffusion coefficient. C_V is calculated with the following equation:

$$C_V = \exp\left(\frac{-\Delta G_{vac}}{k_B T}\right) \quad (\text{B. 6})$$

The free energy of bulk vacancy formation (ΔG_{vac}) is defined as:

$$\Delta G_{vac}(T, P) = E_{vac} - E_{pristine} + \frac{1}{2} \mu_{O_2}(T, p) \quad (\text{B. 7})$$

E_{vac} and $E_{pristine}$ refer to the SCF energy of the supercell with an oxygen vacancy and the pristine supercell, respectively. Note that we ignored all vibrational contributions due to phonons for both the bulk pristine and vacancy structures; therefore, all entropic interactions are due to O_2 . D_V / l_{hop}^2 takes an Arrhenius form upon application of Transition State Theory.

$$\frac{D_V}{l_{hop}^2} = \frac{k_B T}{h} \exp\left(-\frac{\Delta G_{mig}}{k_B T}\right) \quad (\text{B. 8})$$

Multiplication of C_V and D_V / l_{hop}^2 yields the following equation:

$$k_f \cong \frac{k_B T}{h} \exp\left(\frac{-\Delta G_{vac}}{k_B T}\right) \exp\left(-\frac{\Delta G_{mig}}{k_B T}\right) \quad (\text{B. 9})$$

Upon application of the multiplying exponentials with the same base rule, the sum of ΔG_{vac} and ΔG_{mig} define the apparent free activation energy of the vacancy-mediated self-hopping rate constant or ΔG_{app} for SrLaFeO_{4- δ} (SLF). Based on our previous work on the Sr_{n+1}Fe_nO_{3n+1} RP oxides³, we examined primary vacancy migration along the bulk FeO₂-plane. The free energy of vacancy formation is calculated as 0.26 eV at 1073 K (P_{O₂} = 10⁻²⁰ atm) and the free energy of migration is calculated as 1.04 eV. Thus, a value of 1.30 eV is used for the bulk apparent free activation energy (ΔG_{app}) for the vacancy-mediated self-hopping rate constant of SLF. The vacancy-mediated self-hopping rate constant (i.e., the forward rate constant of R_{H25} and R_{CO5}) is computed with the following equation:

$$k_f = \frac{k_B T}{h} \exp\left(-\frac{\Delta G_{app}}{k_B T}\right) \quad (\text{B. 10})$$

The equilibrium constant of R_{H25} and R_{CO5} is computed with the following equation:

$$K_{eq} = \exp\left(-\frac{G_{IM1} - \frac{1}{2}G_{O_2}^\circ - G_{IM5}}{k_B T}\right) \quad (\text{B. 11})$$

G_{IM1} is the free energy of state IM1, G_{IM5} is the free energy of state IM5, and $G_{O_2}^\circ$ is the free energy of oxygen gas.

B.3 ESTIMATION OF SURFACE VACANCY CONCENTRATION

We performed a surface oxygen vacancy analysis at T = 1073 K and oxygen partial pressure P_{O₂} = 7 × 10⁻²⁰ atm. Entropic contributions are only considered for the gas phase O₂ molecule. The free energy for forming one surface vacancy ($\Delta G_{vac,1}$) is -0.83 and -2.56 eV for FeO₂-LaO (001) and FeO₂-SrO (001), respectively. The free energy for forming a second surface vacancy starting from the structure with one vacancy ($\Delta G_{vac,2}$) is 0.19 and -1.58 eV for FeO₂-LaO (001) and FeO₂-SrO (001), respectively. Formation of

a third surface oxygen vacancy is endergonic at reaction conditions for both surface structures. Since the second vacancy formation is endergonic already for the FeO₂-LaO (001) surface, we considered in this study a catalytic cycle between one and two surface oxygen vacancies for both surfaces.

B.4 MICROKINETIC MODEL AND ANODIC BIASING DETAILS

All computed forward and equilibrium rate constants are adapted into a chemical master equation of differential equations. We solved for the steady-state solution of probability densities for each discrete system state, θ_i . We present here the system of equations for the for H₂ oxidation at short-circuit conditions.

$$\frac{d\theta_{IM1}}{dt} = k_5 \left(\theta_{IM5} P_{O_2}^{\frac{1}{2}} - \frac{\theta_{IM1}}{K_{eq,5}} \right) - k_1 \left(\theta_{IM1} P_{H_2} - \frac{\theta_{IM2}}{K_{eq,1}} \right) \quad (B.12)$$

$$\frac{d\theta_{IM2}}{dt} = k_1 \left(\theta_{IM1} P_{H_2} - \frac{\theta_{IM2}}{K_{eq,1}} \right) - k_2 \left(\theta_{IM2} - \frac{\theta_{IM3}}{K_{eq,2}} \right) \quad (B.13)$$

$$\frac{d\theta_{IM3}}{dt} = k_2 \left(\theta_{IM2} - \frac{\theta_{IM3}}{K_{eq,2}} \right) - k_3 \left(\theta_{IM3} - \frac{\theta_{IM4} P_{H_2O}}{K_{eq,3}} \right) \quad (B.14)$$

$$\frac{d\theta_{IM4}}{dt} = k_3 \left(\theta_{IM3} - \frac{\theta_{IM4} P_{H_2O}}{K_{eq,3}} \right) - k_4 \left(\theta_{IM4} - \frac{\theta_{IM5}}{K_{eq,4}} \right) \quad (B.15)$$

$$\frac{d\theta_{IM5}}{dt} = k_4 \left(\theta_{IM4} - \frac{\theta_{IM5}}{K_{eq,4}} \right) - k_5 \left(\theta_{IM5} P_{O_2}^{\frac{1}{2}} - \frac{\theta_{IM1}}{K_{eq,5}} \right) \quad (B.16)$$

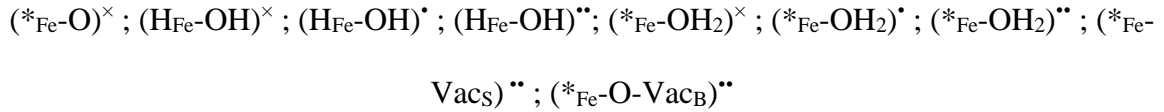
In the presence of anode bias potentials, the expanded microkinetic model utilizes modified forward rate and equilibrium constants for all elementary reactions that incorporate charge transfer. The equations for the corrected forward rate and equilibrium constant are presented as:

$$k_{f,j} = k_{f,j}^{\Delta V=0} \exp \left(-\frac{n_i \Delta V \beta F}{RT} \right) \quad (B.17)$$

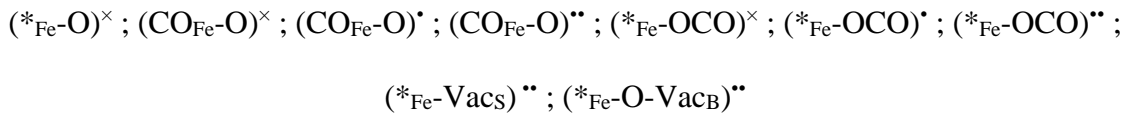
$$K_{eq,j} = K_{eq,j}^{\Delta V=0} \exp\left(-\frac{n_i \Delta V F}{RT}\right) \quad (\text{B. 18})$$

n_i refers to the number of electrons transferred in the elementary charge transfer step, F is the Faraday's constant, and ΔV refers to the applied cell voltage where $\Delta V = 0$ corresponds to the short circuit condition. The surface electro-oxidation process described for H_2 and CO oxidation involves three elementary steps ($R_{\text{H}_2}1$ to $R_{\text{H}_2}3$ and $R_{\text{CO}}1$ to $R_{\text{CO}}3$) that can incorporate charge transfer. Since it is currently unknown which of these elementary steps is involved in the charge transfer process, we allow for all states involved in these reactions to exchange in either a zero-, one-, or two-step electron charge transfer and all possible charge transfer reactions are incorporated into the microkinetic model. Overall, for non-short circuit conditions microkinetic modeling, the H_2 and CO oxidation reaction networks include nine additional elementary steps, as described in Tables B.1 and B.2. The following states exist in our non-short circuit condition microkinetic models:

H₂ Oxidation



CO Oxidation



B.5 BIBLIOGRAPHY

- (1) McQuarrie, D. A. *Statistical Mechanics*; Harper & Row, 1976.
- (2) Ritzmann, A. M.; Muñoz-García, A. B.; Pavone, M.; Keith, J. A.; Carter, E. A. Ab Initio DFT+U Analysis of Oxygen Vacancy Formation and Migration in La_1 .

$x\text{Sr}_x\text{FeO}_{3-\delta}$ ($x = 0, 0.25, 0.50$). *Chem. Mater.*, **2013**, 25 (15), 3011–3019.
10.1021/cm401052w.

- (3) Szaro, N. A.; Ammal, S. C.; Chen, F.; Heyden, A. An Ab Initio Study of the Oxygen Defect Formation and Oxide Ion Migration in $(\text{Sr}_{1-x}\text{Pr}_x)_2\text{FeO}_{4+\delta}$. *J Power Sources*, **2021**, 515, 230602. 10.1016/j.jpowsour.2021.230602.

B.6 FIGURES AND TABLES

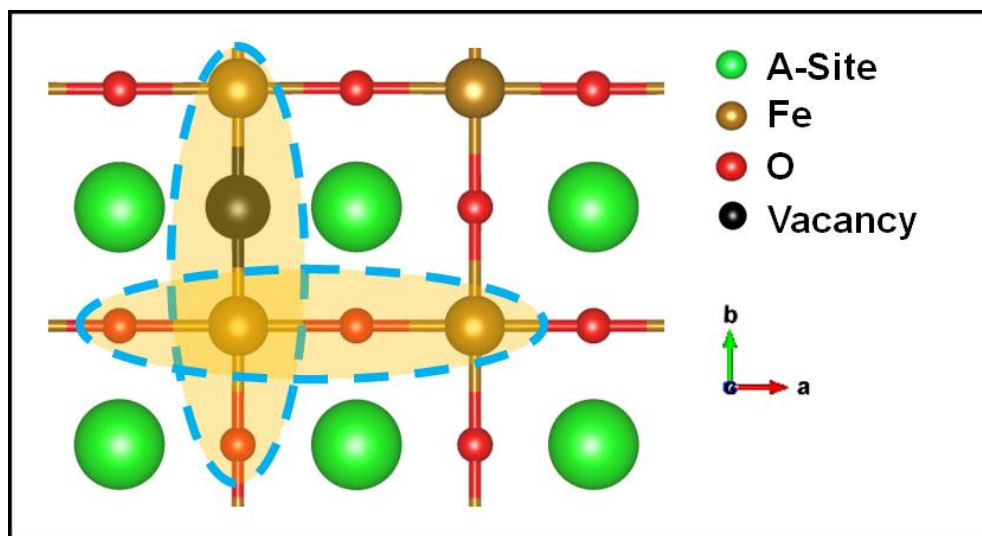


Figure B.1: Highlighted areas correspond to the atoms that are displaced for vibrational frequency calculations.

Table B.1: Reaction rates (in s^{-1}) calculated for the elementary steps of H_2 electro-oxidation on the FeO_2 -LaO and FeO_2 -SrO surface models at a representative temperature of 1073 K and a cell voltage of 0.7 V with different symmetry factor (β) values.

Microkinetic Reactions		Reaction Rate (s^{-1})			
		FeO ₂ -LaO		FeO ₂ -SrO	
		$\beta = 0.0$	$\beta = 0.5$	$\beta = 0.0$	$\beta = 0.5$
1	$(*_{Fe}-O)^{\times} + H_2(g) \rightarrow (H_{Fe}-OH)^{\times}$ (R1)	4.39×10^0	2.42×10^0	1.15×10^4	4.95×10^3
2	$(*_{Fe}-O)^{\times} + H_2(g) \rightarrow (H_{Fe}-OH)^{\cdot} + e'$	2.46×10^{-3}	1.54×10^{-3}	4.31×10^0	2.63×10^0
3	$(*_{Fe}-O)^{\times} + H_2(g) \rightarrow (H_{Fe}-OH)^{\bullet\bullet} + 2e'$	5.57×10^{-7}	7.78×10^{-7}	1.11×10^{-3}	1.33×10^{-3}
4	$(H_{Fe}-OH)^{\times} \rightarrow (*_{Fe}-OH_2)^{\times}$ (R2)	1.66×10^0	2.37×10^0	3.83×10^3	4.84×10^3
5	$(H_{Fe}-OH)^{\times} \rightarrow (*_{Fe}-OH_2)^{\cdot} + e'$	1.66×10^0	5.38×10^{-2}	3.83×10^3	1.10×10^2
6	$(H_{Fe}-OH)^{\times} \rightarrow (*_{Fe}-OH_2)^{\bullet\bullet} + 2e'$	1.08×10^0	1.22×10^{-3}	3.83×10^3	2.49×10^0
7	$(H_{Fe}-OH)^{\cdot} \rightarrow (*_{Fe}-OH_2)^{\cdot}$	1.38×10^{-3}	1.50×10^{-3}	2.15×10^0	2.57×10^0
8	$(H_{Fe}-OH)^{\cdot} \rightarrow (*_{Fe}-OH_2)^{\bullet\bullet} + e'$	1.08×10^{-3}	3.41×10^{-5}	2.15×10^0	5.83×10^{-2}
9	$(H_{Fe}-OH)^{\bullet\bullet} \rightarrow (*_{Fe}-OH_2)^{\bullet\bullet}$	5.57×10^{-7}	7.78×10^{-7}	1.11×10^{-3}	1.33×10^{-3}
10	$(*_{Fe}-OH_2)^{\times} \rightarrow (*_{Fe}-Vac_S)^{\bullet\bullet} + H_2O(g) + 2e'$ (R3)	1.66×10^0	2.37×10^0	3.83×10^3	4.84×10^3
11	$(*_{Fe}-OH_2)^{\cdot} \rightarrow (*_{Fe}-Vac_S)^{\bullet\bullet} + H_2O(g) + e'$	1.66×10^0	5.53×10^{-2}	3.83×10^3	1.12×10^2
12	$(*_{Fe}-OH_2)^{\bullet\bullet} \rightarrow (*_{Fe}-Vac_S)^{\bullet\bullet} + H_2O(g)$	1.08×10^0	1.26×10^{-3}	3.83×10^3	2.55×10^0
13	$(*_{Fe}-Vac_S)^{\bullet\bullet} \rightarrow (*_{Fe}-O-Vac_B)^{\bullet\bullet}$ (R4)	4.39×10^0	2.43×10^0	1.15×10^4	4.96×10^3
14	$(*_{Fe}-O-Vac_B)^{\bullet\bullet} + 1/2O_2(g) \rightarrow (*_{Fe}-O)^{\times}$ (R5)	4.39×10^0	2.43×10^0	1.15×10^4	4.96×10^3

Table B.2: Reaction rates (in s^{-1}) calculated for the elementary steps of CO electro-oxidation on the FeO_2 -LaO and FeO_2 -SrO surface models at a representative temperature of 1073 K and a cell voltage of 0.7 V with different symmetry factor (β) values.

Microkinetic Reactions		Reaction Rate (s^{-1})			
		FeO ₂ -LaO		FeO ₂ -SrO	
		$\beta = 0.0$	$\beta = 0.5$	$\beta = 0.0$	$\beta = 0.5$
1	$(*_{Fe}-O)^{\times} + CO(g) \rightarrow (CO_{Fe}-O)^{\times}$ (R1)	2.46×10^1	2.35×10^1	2.14×10^3	7.58×10^2
2	$(*_{Fe}-O)^{\times} + CO(g) \rightarrow (CO_{Fe}-O)^{\cdot} + e'$	6.29×10^{-3}	1.21×10^{-2}	7.34×10^{-1}	3.90×10^{-1}
3	$(*_{Fe}-O)^{\times} + CO(g) \rightarrow (CO_{Fe}-O)^{\bullet\bullet} + 2e'$	$< 10^{-10}$	6.08×10^{-6}	1.89×10^{-4}	1.97×10^{-4}
4	$(CO_{Fe}-O)^{\times} \rightarrow (*_{Fe}-OCO)^{\times}$ (R2)	1.24×10^1	2.29×10^1	7.13×10^2	7.41×10^2
5	$(CO_{Fe}-O)^{\times} \rightarrow (*_{Fe}-OCO)^{\cdot} + e'$	1.20×10^1	5.20×10^{-1}	7.13×10^2	1.68×10^1
6	$(CO_{Fe}-O)^{\times} \rightarrow (*_{Fe}-OCO)^{\bullet\bullet} + 2e'$	1.97×10^{-1}	1.18×10^{-2}	7.13×10^2	3.82×10^{-1}
7	$(CO_{Fe}-O)^{\cdot} \rightarrow (*_{Fe}-OCO)^{\cdot}$	6.19×10^{-3}	1.18×10^{-2}	3.67×10^{-1}	3.82×10^{-1}
8	$(CO_{Fe}-O)^{\cdot} \rightarrow (*_{Fe}-OCO)^{\bullet\bullet} + e'$	1.02×10^{-4}	2.68×10^{-4}	3.67×10^{-1}	8.66×10^{-3}
9	$(CO_{Fe}-O)^{\bullet\bullet} \rightarrow (*_{Fe}-OCO)^{\bullet\bullet}$	5.23×10^{-8}	6.08×10^{-6}	1.89×10^{-4}	1.97×10^{-4}
10	$(*_{Fe}-OCO)^{\times} \rightarrow (*_{Fe}-Vac_S)^{\bullet\bullet} + CO_2(g) + 2e'$ (R3)	1.24×10^1	2.29×10^1	7.13×10^2	7.41×10^2
11	$(*_{Fe}-OCO)^{\cdot} \rightarrow (*_{Fe}-Vac_S)^{\bullet\bullet} + CO_2(g) + e'$	1.20×10^1	5.32×10^{-1}	7.13×10^2	1.72×10^2
12	$(*_{Fe}-OCO)^{\bullet\bullet} \rightarrow (*_{Fe}-Vac_S)^{\bullet\bullet} + CO_2(g)$	1.97×10^{-1}	1.21×10^{-2}	7.13×10^2	3.91×10^{-1}
13	$(*_{Fe}-Vac_S)^{\bullet\bullet} \rightarrow (*_{Fe}-O-Vac_B)^{\bullet\bullet}$ (R4)	2.46×10^1	2.35×10^1	2.14×10^3	7.58×10^2
14	$(*_{Fe}-O-Vac_B)^{\bullet\bullet} + 1/2O_2(g) \rightarrow (*_{Fe}-O)^{\times}$ (R5)	2.46×10^1	2.35×10^1	2.14×10^3	7.58×10^2

Table B.3: Computed reaction rates (s^{-1}) for H_2 electro-oxidation, CO electro-oxidation, and WGS in the presence of syngas fuel with different $H_2:CO$ ratios at an operating voltage of 0.7 V and $\beta = 0.5$.

Reaction	FeO ₂ -LaO		
	75% H ₂ + 25% CO	50% H ₂ + 50% CO	25% H ₂ + 75% CO
H ₂ Oxidation (s^{-1})	-2.58×10^{-1}	-3.11×10^0	-5.96×10^0
CO Oxidation (s^{-1})	4.22×10^1	8.52×10^1	1.28×10^2
WGS (s^{-1})	4.24×10^1	8.83×10^1	1.34×10^2
Syngas Oxidation (s^{-1})	2.10×10^1	4.10×10^1	6.11×10^1
	FeO ₂ -SrO		
	75% H ₂ + 25% CO	50% H ₂ + 50% CO	25% H ₂ + 75% CO
H ₂ Oxidation (s^{-1})	3.98×10^3	2.68×10^3	1.35×10^3
CO Oxidation (s^{-1})	1.83×10^2	3.74×10^2	5.69×10^2
WGS (s^{-1})	-3.80×10^3	-2.31×10^3	-7.81×10^2
Syngas Oxidation (s^{-1})	2.06×10^3	1.51×10^3	9.39×10^2

Table B.4: Degree of rate control (DRC) and turnover frequencies calculated for H_2 and CO oxidation over FeO₂-LaO and FeO₂-SrO surfaces at an operating $V_{cell} = 0.7$ and $\beta = 0.5$ conditions ($T = 1073$ K, $P_{H_2,CO} = 1.00$ atm, $P_{H_2O,CO_2} = 0.03$ atm, and $P_{O_2} = 0.21$ atm).

	H ₂ Oxidation			CO Oxidation	
		FeO ₂ -LaO	FeO ₂ -SrO	FeO ₂ -LaO	FeO ₂ -SrO
Degree of Rate Control	R _{H2} 1	0.17	0.03	R _{CO} 1	0.00
	R _{H2} 2	0.73	0.86	R _{CO} 2	0.09
	R _{H2} 3	0.00	0.00	R _{CO} 3	0.00
	R _{H2} 4	0.00	0.03	R _{CO} 4	0.00
	R _{H2} 5	0.10	0.08	R _{CO} 5	0.91
Turnover Frequency (1/s)		2.43×10^0	4.96×10^3		2.35×10^1
					7.58×10^2

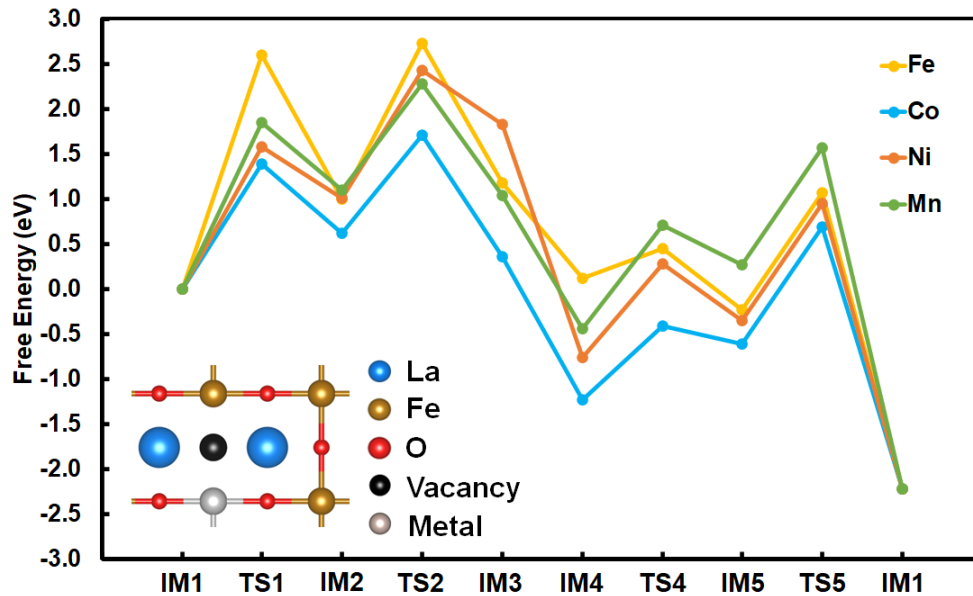


Figure B.2: Relative free energy profiles (eV) for the H_2 oxidation network on the $\text{Fe}_{1-x}\text{M}_x\text{O}_2\text{-LaO}$ ($x = 0.11$; $\text{M} = \text{Fe}, \text{Co}, \text{Mn},$ and Ni) surface models. All energies are with reference to the sum of the energies of the initial state (IM1) and the gas phase molecules ($T = 1073 \text{ K}$; $P_{\text{H}_2}(\text{gas}) = 1.0 \text{ atm}$; $P_{\text{H}_2\text{O}}(\text{gas}) = 0.03 \text{ atm}$; $P_{\text{O}_2}(\text{gas}) = 0.21 \text{ atm}$).

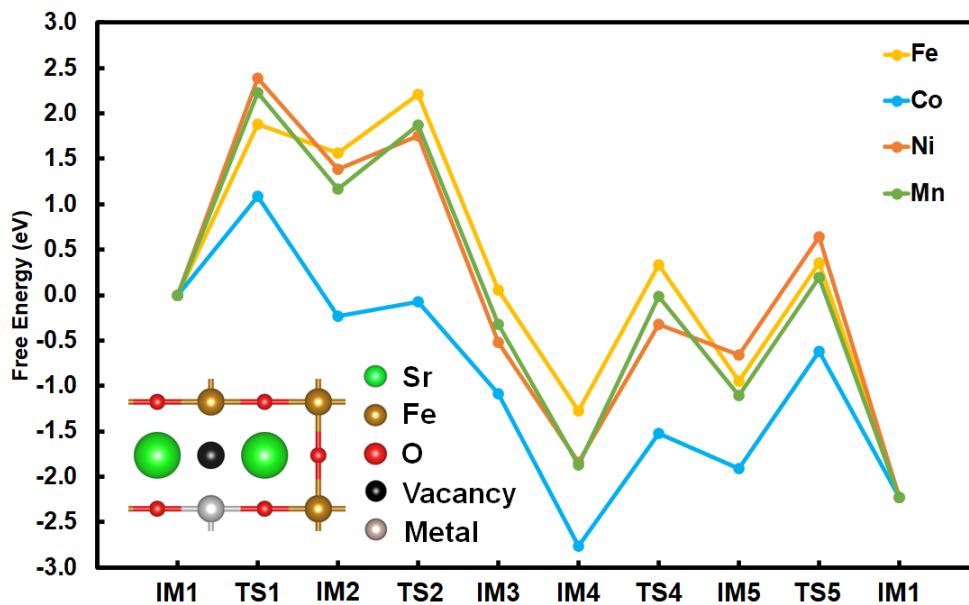


Figure B.3: Relative free energy profiles (eV) for the H_2 oxidation network on the $\text{Fe}_{1-x}\text{M}_x\text{O}_2\text{-SrO}$ ($x = 0.11$; $\text{M} = \text{Fe}, \text{Co}, \text{Mn},$ and Ni) surface models. All energies are with reference to the sum of the energies of the initial state for a given fuel (IM1) and the gas phase molecules ($T = 1073 \text{ K}$; $P_{\text{H}_2}(\text{gas}) = 1.0 \text{ atm}$; $P_{\text{H}_2\text{O}}(\text{gas}) = 0.03 \text{ atm}$; $P_{\text{O}_2}(\text{gas}) = 0.21 \text{ atm}$).

APPENDIX C

SUPPORTING INFORMATION FOR FIRST PRINCIPLES MATERIAL SCREENING AND DISCOVERY OF PEROVSKITE ELECTROLYTES FOR PROTON CONDUCTING SOLID OXIDE FUEL CELLS

C.1 MATERIAL CONFIGURATIONS IN THIS STUDY

C.1.1 PEROVSKITE COMPOSITION DEVELOPMENT

The entire list of materials computed in this study are provided in the Excel spreadsheet as Supplementary Information attached to this dissertation. The database of materials analyzed by Jacobs et al. ¹ and Ma et al. ² is expanded with the inclusion of Zr and Ce. After removing the materials that change phase during structural optimization, the resulting data set consists of 4793 compounds. The material configurations have a general stoichiometry of $A_{1-x}A'_x B_{1-y}B'_y O_3$ (written as $A_{1-x}A'(x)B_{1-y}B'(y)O_3$) where A, A', and x correspond to the main element, dopant, and doping concentration at the A-site, respectively, and B, B', and y correspond to the main element, dopant, and doping concentration at the B-site, respectively. The $(2 \times 2 \times 2)$ supercell used in our calculations has 40 atoms with a stoichiometry of $A_8B_8O_{24}$. Thus, the number of each element can range from 1 to 8 in value at either the A- or B-site, where 1 corresponds to a doping ratio of 12.5% and 8 corresponds to a non-doped site (100%). Lastly, based on the Jacobs et al. ¹ and Ma et al. ² material databases, 12 structures dope the A-site with a 37.5% doping ratio and are included in this study as $Sr_{0.375}La_{0.625}MnO_3$, $Zn_{0.375}La_{0.625}CoO_3$, $Zn_{0.375}La_{0.625}FeO_3$, $Zn_{0.375}La_{0.625}NiO_3$, $Zn_{0.375}La_{0.625}MnO_3$, $La_{0.125}Bi_{0.25}La_{0.625}FeO_3$, $La_{0.125}Cd_{0.25}La_{0.625}FeO_3$, $La_{0.125}Sn_{0.25}La_{0.625}FeO_3$, $Ca_{0.375}La_{0.625}Fe_{0.75}Co_{0.25}O_3$, $Sr_{0.375}La_{0.625}Co_{0.75}Fe_{0.25}O_3$, $Sr_{0.375}La_{0.625}Fe_{0.75}Co_{0.25}O_3$, and $Sr_{0.375}La_{0.625}Fe_{0.75}Cu_{0.25}O_3$.

C.1.2 SCHEMATIC STRUCTURES

Note: These orientations are equivalent to those used in Ma et al. ².

C.2 PHASE STABILITY ANALYSIS

C.2.1 GAS PHASE CHEMICAL POTENTIALS ANODE AND CAHTHODE

OPERATING CONDITIONS

The chemical potential values of H₂, O₂, H₂O, CO, and CO₂ used in the phase stability analysis tools in Pymatgen were calculated from standard gas phase thermodynamic equations. We calculated the chemical potentials using standard statistical mechanics (e.g., see McQuarrie³) and computed DFT energies.

$$\mu_i(T, p^\circ) = E_{i,SCF} + E_{ZPE,i} - k_B T \ln(q_{trans,i} q_{roto,i} q_{vib,i} q_{elec,i}) \quad (C.1)$$

$$E_{ZPE,i} = \sum_i \frac{1}{2} h \nu_i \quad (C.2)$$

$$q_{vib,i} = \prod_i \frac{1}{1 - \exp\left(-\frac{h\nu_i}{k_B T}\right)} \quad (C.3)$$

$E_{i,SCF}$ refers to the energy of the DFT calculated state, $E_{ZPE,i}$ refers to the zero-point energy of the DFT calculated state, k_B refers to the Boltzmann constant, T refers to the temperature, h refers to the Planck constant, and ν_i refers to the i th vibrational frequency (s^{-1}). Displacements of 0.001 Å were used along the x, y, and z directions for all Hessian constructions. Note, we use the $E_{i,SCF}$ from Materials Project database⁴ – mp-12957 (O₂), mp-697111 (H₂O), mp-995183 (CO), and mp-20066 (CO₂).

For anode operating conditions (e.g., $T = 1073$ K, $p(\text{O}_2) = 1.087 \times 10^{-18}$ atm, $p(\text{H}_2) = 1.00$ atm), we obtain an O chemical potential of -8.006 eV/O and a H chemical potential of -4.024 eV/H. $P(\text{O}_2)$ is derived from the equilibrium gas phase pressure of the reaction $\text{H}_2 + 1/2 \text{O}_2 \rightarrow \text{H}_2\text{O}$, where $P(\text{H}_2\text{O}) = 0.03$ atm.

For cathode operating conditions (e.g., $T = 1073 \text{ K}$, $p(\text{O}_2) = 0.210 \text{ atm}$, $p(\text{H}_2) = 7.222 \times 10^{-10} \text{ atm}$), we obtain an O chemical potential of -6.166 eV/O and a H chemical potential of -4.997 eV/H . $P(\text{H}_2)$ is derived from the equilibrium gas phase pressure of the reaction $\text{H}_2 + 1/2 \text{ O}_2 \rightarrow \text{H}_2\text{O}$, where $P(\text{H}_2\text{O}) = 9.525 \times 10^{-3} \text{ atm}$ – a pressure equivalent to a relative humidity of 30% at 298 K ⁵.

For CO_2 environmental conditions (e.g., $T = 1073 \text{ K}$, $p(\text{CO}_2) = 1.000 \text{ atm}$, $P(\text{O}_2) = 7.401 \times 10^{-3} \text{ atm}$), we obtain a CO_2 chemical potential of -24.388 eV/CO_2 and an O chemical potential of -6.320 eV/O . $P(\text{O}_2)$ is derived from the equilibrium gas phase pressure of the reaction $\text{CO} + 1/2 \text{ O}_2 \rightarrow \text{CO}_2$ where $P(\text{CO}) = 1.00 \times 10^{-9} \text{ atm}$. Shifting CO to 1 ppt does not affect our conclusions. We adapt the stability testing methodology of Dunstan et al. ⁶ for CO_2 stability.

C.2.2 PEROVSKITE MATERIAL ENERGY CORRECTIONS

We utilized the *MaterialsProject2020Compatibility* class for energy corrections to be consistent with the Materials Project database. This class employs two energy shifts that are applied to all calculated materials: 1) oxide correction and 2) GGA/GGA+U mixing. The oxide correction is required because of the use of GGA-based DFT which is notorious for overbinding the O_2 molecule. Therefore, the *MaterialsProject2020Compatibility* uses a -0.687 eV/O shift to all calculated solid phase energies. For the $2 \times 2 \times 2$ perovskite supercell, there are 24 oxygen atoms; therefore, we apply a $-16.488 \text{ eV/material}$ to our computed configurations. The GGA/GGA+U mixing energy shift is used for materials with certain transition metals where the phase stability analysis involves elements/oxides from the Materials Project database calculated with and without GGA+U correction. For example, in a phase stability analysis of Fe and O,

elemental Fe is computed with GGA while Fe₂O₃ is computed with GGA+U. In this study, we incorporated mixed GGA/GGA+U phase spaces for transition metals Co, Cr, Fe, Mn, Ni, and V. For the computed perovskite materials that incorporate a U-J metal, *MaterialsProject2020Compatibility* shifts the computed energy by the number of U-J metals that require a correction multiplied by energy shift per atom. We outline the U-J values for these elements and the energy shift per atom in Table C.1.

C.2.3 PYMATGEN GRAND POTENTIAL PHASE STABILITY ANALYSIS

Pymatgen or the Python Materials Genomics toolkit is an open-source Python library for materials analysis and design. For our work here, we use Pymatgen version v2022.10.22 for all stability calculations⁷. Our primary module for this work is the *pymatgen.analysis.phase_diagram* module. We use the *GrandPotPDEntry* class for each computed material. *GrandPotPDEntry* requires use of the *Composition* class from the *pymatgen.core.composition* module. The *Composition* class includes information such as the elemental composition and the number of atoms for a computed entry. We use the *GrandPotentialPhaseDiagram* class with an array of *GrandPotPDEntry* inputs necessary to compute the stability of a given computed perovskite. The array input utilizes the Materials Project database to fill out the entire elemental phase space defined by the elemental composition of a given computed perovskite. Each *GrandPotPDEntry* requires an energy input – this value is either 1) the perovskite computed DFT energy as corrected according to Section C.2.2, or 2) the corrected energy extracted from Materials Project. After the inputs are inserted into the *GrandPotentialPhaseDiagram* class and the phase space is calculated, we extract the energy above the convex hull using a *get_decomp_and_e_above_hull* function call of the *GrandPotentialPhaseDiagram* class.

The O₂, H₂, and CO₂ molecules in Materials Project do not incorporate chemical potential corrections consistent with the applied environmental conditions. We update the MP energies of O₂, H₂, and CO₂ with the corrected chemical potentials from Section C.1.1 for each of these molecules for a given environmental condition. For C-containing species extracted from Materials Project, we sort these compounds into two pools: 1) those that contain at least one C and at least two Os, and 2) those that contain C with either one or zero Os. For the pool that contains at least one C and at least two Os, we convert repeating units of CO₂ into arbitrary element X where the chemical potential of CO₂ is applied to element X. As an example of this conversion, “C3O5” becomes “X₂CO”.

C.3 VACANCY AND HYDRATION FORMATION ANALYSIS

C.3.1 DEFECT FORMATION ENERGY

For this first-pass screening study, we focus on charge neutral defect formation. We examine two defects: V_O^\times (oxygen vacancy) and OH^\times (protonic).

The hydration energy is derived from the following three reactions:

Formal Reaction Expressions



Defect Formation Reaction Equations

$$\Delta E_{f,V_O^\times} = E_{V_O^\times} - E_{pristine} + \mu_O \quad (C.7)$$

$$\Delta E_{f,OH^\times} = E_{OH^\times} - E_{pristine} - \mu_H \quad (C.8)$$

$$\Delta E_{hydr} = 2E_{OH^\times} - E_{pristine} - E_{V_O^\times} - \mu_{H_2O} \quad (C.9)$$

For the chemical potential contributions, the chemical potential of O is given as $\mu_O = \frac{\mu_{O_2}}{2}$ and $\mu_H = \frac{\mu_{H_2O} - \mu_O}{2}$ ^{8,9}. The chemical potential of O₂ and H₂O are computed at 0 K and without pressure correction, and therefore, equal to E_{O_2} and E_{H_2O} , respectively. Solving for E_{OH^\times} and $E_{V_O^\times}$ with the correct chemical potential expressions:

$$E_{V_O^\times} = \Delta E_{f,V_O^\times} + E_{pristine} - \frac{E_{O_2}}{2} \quad (C.10)$$

$$E_{OH^\times} = \Delta E_{f,OH^\times} + E_{pristine} + \frac{E_{H_2O} - \frac{E_{O_2}}{2}}{2} \quad (C.11)$$

Substituting equation (C.10) and equation (C.11) into equation (C.9) yields equation (4.4) in Chapter 4.

For E_{H_2O} , this value is equal to the ZPE-corrected SCF energy of water. For E_{O_2} , this value is corrected as GGA methods tend to overestimate the binding energy of O₂. E_{O_2} is calculated from the ZPE-corrected $E_{O_2,corr}$ as calculated using the correction scheme based on the water splitting reaction¹⁰⁻¹².

$$E_{O_2,corr} = 2[(E_{DFT,H_2O} + E_{ZPE,Exp. H_2O}) - (E_{DFT,H_2} + E_{ZPE,Exp. H_2}) - E_{Exp. HOF}] - E_{ZPE,Exp. O_2} \quad (C.12)$$

C.3.2 BZO BCO THERMODYNAMIC STABILITY and DEFECT ANALYSIS

For BaZrO₃ (BZO), we use the established Pm $\bar{3}$ m space group model¹³. For BaCeO₃ (BCO), Pm $\bar{3}$ m and Pbnm are both conformers found in SOFC applications¹⁴. We follow the approach of Lindman et al.⁸ and use the orthorhombic model of BCO - Pbnm. We

use a $(2 \times 2 \times 2)$ supercell of the Pbnm unit cell with 32 Ba atoms, 32 Ce atoms, and 96 O atoms. BZO and BCO unit cells are visualized in Figure 4.1 in Chapter 4.

BZO and BCO both pass Filter 3, i.e., they are stable under anodic and cathodic conditions with high bandgaps. BCO is commonly reported in the literature to decompose under water-containing environments and our results are consistent with experimental reports by Tanner and Virkar¹⁵. They present a plot (e.g., Figure 1 of Tanner and Virkar) of the equilibrium partial pressure of water for the coexistence of BCO, CeO₂, and Ba(OH)₂. Their abscissa is $1000/T$ (K); therefore, at 1073 K, at an abscissa value of ~ 0.93 , their reported coexistence partial pressure of water is approximately 10^{-1} to 10^{-2} bar. Furthermore, they report that BCO decomposes at ~ 430 torr H₂O at temperatures below 1173 K. For our cathodic conditions, BCO is stable experimentally. For our anodic conditions, BCO is in the partial pressure range subject to uncertainty in experiment – we hold that BCO is either metastable or in thermodynamic equilibrium with CeO₂ and Ba(OH)₂. Higher humidity anodes and lower temperatures will decompose BCO.

Sundell et al.¹⁶ report a $\Delta E_{f,V_O^\times}$ value of 6.57 eV and Björketun et al.¹³ report a $\Delta E_{f,OH^\times}$ of 3.42 eV for BZO. Our values for BZO ($\Delta E_{f,V_O^\times} = 6.76$ eV and $\Delta E_{f,OH^\times} = 3.34$ eV) closely agree with these values (within ~ 0.2 eV for $\Delta E_{f,V_O^\times}$ and 0.1 eV for $\Delta E_{f,OH^\times}$) indicating that our computational approach is consistent with the literature. Lindman et al.⁸ report a ΔE_{hydr} of -1.42 eV for BCO – a value that is approximately within 0.1 eV from our computed value ($\Delta E_{hydr} = -1.36$ eV). From a molecular dynamics study of BCO, Glöckner et al.¹⁴ report a ΔE_{hydr} equal to -0.51 eV. They used the following expression:

$$\Delta E_{f,hydr} = 2E_{OH^\times} - E_{V_O^\times} + E_{PT} \quad (C.13)$$

where E_{PT} is reported as the energy of the gas phase reaction: $O^{2-} + H_2O = 2OH^-$. Our hydration energy is approximately 0.7 eV more negative than this value since we used a different computational approach as explained in section C.3.1 for calculating hydration energies.

C.3.3 COMMENTARY ON THERODYNAMIC FOCUS ON PROTON CONDUCTION

Islam et al.⁹ computed the kinetic barrier of proton migration for promising proton conducting materials. We do not include proton migration as we argue that thermodynamic protonic formation energies display a wider range than protonic migration energies for perovskite materials. We examine the promising perovskites reported by Islam et al. and found a standard deviation of 0.638 eV for protonic defect formation energies versus 0.263 eV for proton migration energies. The difference between the highest and lowest protonic defect formation energy is 2.040 eV. For proton migration, the difference between the highest and lowest values is 0.84 eV. Furthermore, BZO displays a proton migration barrier of 0.27 eV^{17,18} versus 0.54 eV for BCO¹⁹ – the difference of hydration energies for the benchmark compounds is 1.27 eV, a value that is approximately 4.7x the difference of the proton migration barrier. Therefore, we conclude that the thermodynamic barrier of protonic defect formation is both more variable and larger in span than proton migration (e.g., thermodynamics will display a larger effect on proton conductivity relative to proton migration). For the sake of a first-pass screening and with the aforementioned argument, we do not conduct proton migration analysis in this study.

C.3.5 TIN-CONTAINING REGION ANALYSIS OF DEFECT FORMATION

ENERGIES

We use $\text{Ba}_{0.125}\text{Sr}_{0.875}\text{Sn}_{0.125}\text{Zr}_{0.875}\text{O}_3$ as a representative Sn compound for our Bader charge analysis^{17,18}. All charges (e.g., q) are in units of e^- . Below are the Bader charge results for $\text{Ba}_{0.125}\text{Sr}_{0.875}\text{Sn}_{0.125}\text{Zr}_{0.875}\text{O}_3$ vs. BCO as displayed in Table C.3. Ce partially reduces upon vacancy formation but reduces back to native 4^+ state with hydration. Sn reduces upon vacancy formation and partially oxidizes with hydration.

C.5 BIBLIOGRAPHY

- (1) Jacobs, R.; Mayeshiba, T.; Booske, J.; Morgan, D. Material Discovery and Design Principles for Stable, High Activity Perovskite Cathodes for Solid Oxide Fuel Cells. *Adv. Energy Mater.*, **2018**, 8 (11). 1702708. 10.1002/aenm.201702708.
- (2) Ma, T.; Jacobs, R.; Booske, J.; Morgan, D. Discovery and Engineering of Low Work Function Perovskite Materials. *J. Mater. Chem. C*, **2021**, 9, 12778–12790. 10.1039/D1TC01286J.
- (3) McQuarrie, D. A. *Statistical Mechanics*; Harper & Row.
- (4) Jain, A.; Ong, S. P.; Hautier, G.; Chen, W.; Richards, W. D.; Dacek, S.; Cholia, S.; Gunter, D.; Skinner, D.; Ceder, G.; Persson, K. A. Commentary: The Materials Project: A Materials Genome Approach to Accelerating Materials Innovation. *APL Mater.*, **2013**, 1 (1), 011002. 10.1063/1.4812323.
- (5) Bucher, E.; Sitte, W.; Klauser, F.; Bertel, E. Oxygen Exchange Kinetics of $\text{La}_{0.58}\text{Sr}_{0.42}\text{Co}_{0.2}\text{Fe}_{0.8}\text{O}_3$ at 600 °C in Dry and Humid Atmospheres. *Solid State Ion.*, **2011**, 191 (1), 61–67. 10.1016/j.ssi.2011.03.019.
- (6) Dunstan, M. T.; Jain, A.; Liu, W.; Ong, S. P.; Liu, T.; Lee, J.; Persson, K. A.; Scott, S. A.; Dennis, J. S.; Grey, C. P. Large Scale Computational Screening and Experimental Discovery of Novel Materials for High Temperature CO_2 Capture. *Energy Environ. Sci.*, **2016**, 9 (4), 1346–1360. 10.1039/c5ee03253a.

- (7) Ong, S. P.; Richards, W. D.; Jain, A.; Hautier, G.; Kocher, M.; Cholia, S.; Gunter, D.; Chevrier, V. L.; Persson, K. A.; Ceder, G. Python Materials Genomics (Pymatgen): A Robust, Open-Source Python Library for Materials Analysis. *Comput. Mater. Sci.*, **2013**, *68*, 314–319. 10.1016/j.commatsci.2012.10.028.
- (8) Lindman, A.; Helgee, E. E.; Wahnström, G. Comparison of Space-Charge Formation at Grain Boundaries in Proton-Conducting BaZrO₃ and BaCeO₃. *Chem. Mater.*, **2017**, *29* (18), 7931–7941. 10.1021/acs.chemmater.7b02829.
- (9) Islam, M. S.; Wang, S.; Hall, A. T.; Mo, Y. First-Principles Computational Design and Discovery of Solid-Oxide Proton Conductors. *Chem. Mater.*, **2022**, *34* (13), 5938–5948. 10.1021/acs.chemmater.2c00867.
- (10) Ammal, S. C.; Heyden, A. Modeling the Noble Metal/TiO₂ (110) Interface with Hybrid DFT Functionals: A Periodic Electrostatic Embedded Cluster Model Study. *J. Chem. Phys.*, **2010**, *133* (16), 164703. 10.1063/1.3497037.
- (11) Nørskov, J. K.; Rossmeisl, J.; Logadottir, A.; Lindqvist, L.; Kitchin, J. R.; Bligaard, T.; Jónsson, H. Origin of the Overpotential for Oxygen Reduction at a Fuel-Cell Cathode. *J. Phys. Chem. B*, **2004**, *108* (46), 17886–17892. 10.1021/jp047349j.
- (12) Atkins, P. W.; Julio De Paula; Keeler, J. *Atkins' Physical Chemistry*; Oxford University Press: Oxford, 2018. pp 886
- (13) Björketun, M. E.; Sundell, P. G.; Wahnström, G. Structure and Thermodynamic Stability of Hydrogen Interstitials in BaZrO₃ Perovskite Oxide from Density Functional Calculations. *Faraday Discuss.*, **2007**, *134*, 247–265. 10.1039/b602081j.
- (14) Glöckner, R. Protons and Other Defects in BaCeO₃: A Computational Study. *Solid State Ion.*, **1999**, *122* (1–4), 145–156. 10.1016/S0167-2738(99)00070-3.
- (15) Tanner, C. W.; Virkar, A. v. Instability of BaCeO₃ in H₂O-Containing Atmospheres. *J. Electrochem. Soc.*, **1996**, *143* (4), 1386–1389. 10.1149/1.1836647.

- (16) Sundell, P. G.; Björketun, M. E.; Wahnström, G. Thermodynamics of Doping and Vacancy Formation in BaZrO₃ Perovskite Oxide from Density Functional Calculations. *Phys. Rev. B*, **2006**, *73* (10), 104112. 10.1103/PhysRevB.73.104112.
- (17) Bork, N.; Bonanos, N.; Rossmeisl, J.; Vegge, T. Simple Descriptors for Proton-Conducting Perovskites from Density Functional Theory. *Phys. Rev. B*, **2010**, *82* (1), 014103. 10.1103/PhysRevB.82.014103.
- (18) Kalinina, M. v.; Arsent'ev, M. Y.; Kotlyarov, N. S.; Fedorenko, N. Y.; Tikhonov, P. A.; Shilova, O. A. Synthesis and Research Using Computer Simulation of Proton-Conducting Solid Electrolytes Based on Hafnate and Barium Zirconate. *Glass Phys. Chem.*, **2021**, *47* (4), 366–371. 10.1134/S1087659621040106.
- (19) Hermet, J.; Torrent, M.; Bottin, F.; Dezanneau, G.; Geneste, G. Hydrogen Diffusion in the Protonic Conductor BaCe_{1-x}Gd_xO_{3-x/2} from Density Functional Theory. *Phys. Rev. B*, **2013**, *87* (10), 104303. 10.1103/PhysRevB.87.104303.
- (20) Henkelman, G.; Arnaldsson, A.; Jónsson, H. A Fast and Robust Algorithm for Bader Decomposition of Charge Density. *Comput. Mater. Sci.*, **2006**, *36* (3), 354–360. 10.1016/j.commatsci.2005.04.010.
- (21) Tang, W.; Sanville, E.; Henkelman, G. A Grid-Based Bader Analysis Algorithm without Lattice Bias. *J. Phys. Condens. Matter*, **2009**, *21* (8), 084204. 10.1088/0953-8984/21/8/084204

C.6 FIGURES AND TABLES

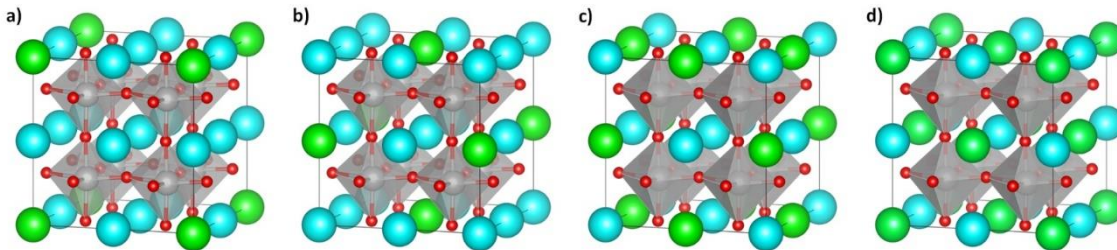


Figure C.1: Schematic structures of $A_xA'_{1-x}BO_3$: a) $A_{0.875}A'_{0.125}BO_3$, b), $A_{0.75}A'_{0.25}BO_3$, c) $A_{0.625}A'_{0.375}BO_3$, and d) $A_{0.5}A'_{0.5}BO_3$.

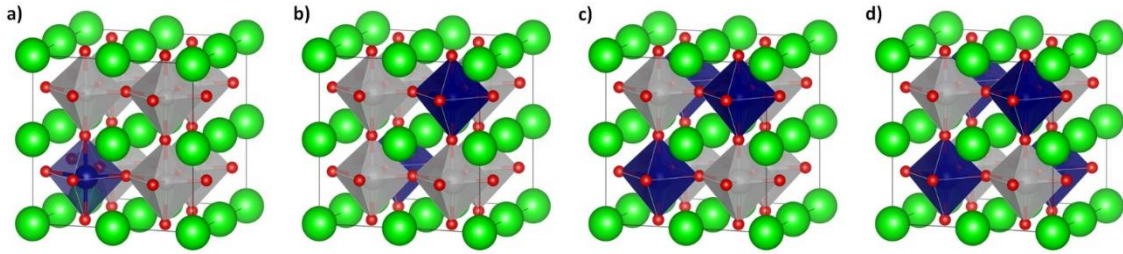


Figure C.2: Schematic structures of $AB_y A'_{1-y} O_3$: a) $AB_{0.875} B'_{0.125} BO_3$, b) $AB_{0.75} B'_{0.25} O_3$, c) $AB_{0.625} B'_{0.375} O_3$, and d) $AB_{0.5} B'_{0.5} O_3$.

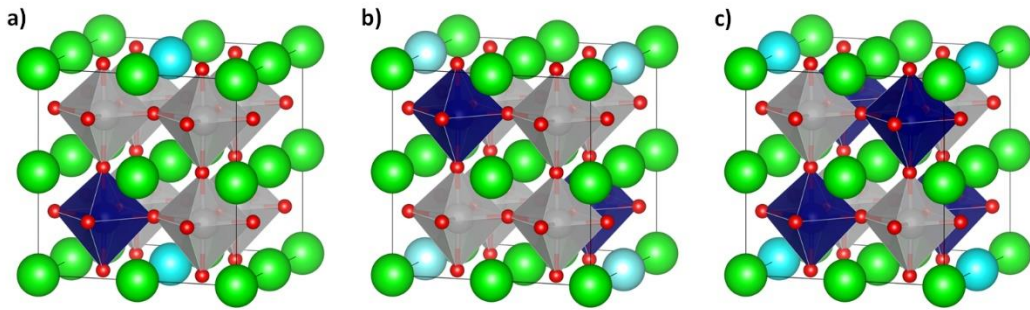


Figure C.3: Schematic structures of $A_{0.875} A'_{0.125} B_y A'_{1-y} O_3$: a) $A_{0.875} A'_{0.125} B_{0.875} B'_{0.125} BO_3$, b) $A_{0.875} A'_{0.125} B_{0.75} B'_{0.25} O_3$, and c) $A_{0.875} A'_{0.125} B_{0.5} B'_{0.5} O_3$.

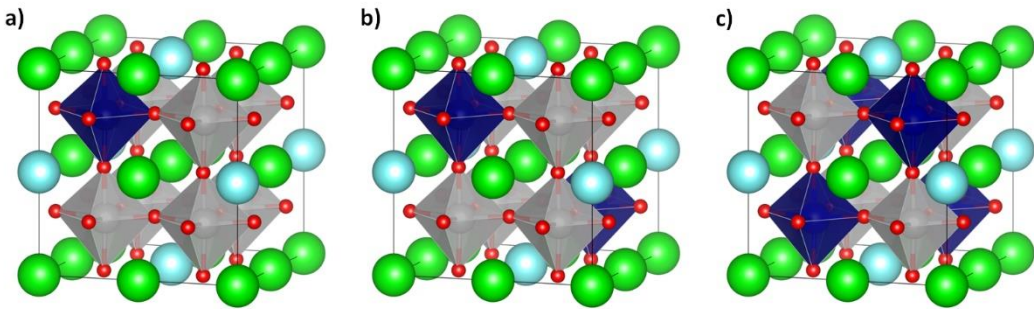


Figure C.4: Schematic structures of $A_{0.75} A'_{0.25} B_y A'_{1-y} O_3$: a) $A_{0.75} A'_{0.25} B_{0.875} B'_{0.125} BO_3$, b) $A_{0.75} A'_{0.25} B_{0.75} B'_{0.25} O_3$, and c) $A_{0.75} A'_{0.25} B_{0.5} B'_{0.5} O_3$.

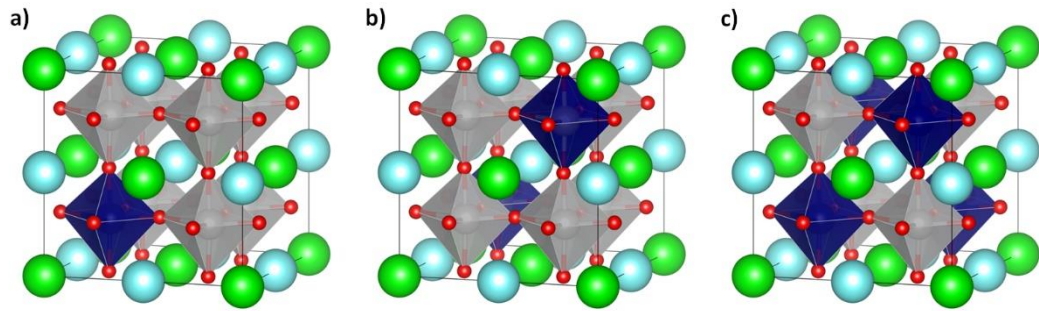


Figure C.5: Schematic structures of $A_{0.5}A'_{0.5}B_yA'_{1-y}O_3$: a) $A_{0.5}A'_{0.5}B_{0.875}B'_{0.125}BO_3$, b), $A_{0.5}A'_{0.5}B_{0.75}B'_{0.25}O_3$, and c) $A_{0.5}A'_{0.5}B_{0.5}B'_{0.5}O_3$.

Table C.1: Transition metals that have U-J values and require energy shifts for mixed GGA/GGA+U energetics in this study.

Element	U-J (eV)	GGA/GGA+U shift (eV/atom)
Co	3.32	-1.638
Cr	3.70	-1.999
Fe	5.30	-2.256
Mn	3.90	-1.668
Ni	6.20	-2.541
V	3.25	-1.700

Table C.2: Table of configurations that pass Filter 3 (e.g., insulating, stable under anodic and cathodic operating conditions) with computed vacancy and protonic defect formation, and hydration energies.

Material Configuration	E_{f,V_O^\times} (eV)	E_{OH^\times} (eV)	$\Delta E_{f,hydr}$ (eV)
Ba0.875Bi0.125Zr0.875Fe0.125O3	4.342	1.327	-1.687
Ba0.875Ca0.125Zr1O3	6.686	3.187	-0.313
Ba0.875Cd0.125Zr1O3	4.572	1.595	-1.382
Ba0.875Cs0.125Zr1O3	3.566	-0.148	-3.862
Ba0.875Mg0.125Zr1O3	6.475	3.160	-0.155
Ba0.875Rb0.125Zr1O3	3.583	-0.138	-3.859
Ba0.875Sr0.125Ce1O3	5.084	1.707	-1.670
Ba0.875Sr0.125Zr1O3	6.721	3.295	-0.131
Ba0.875Zn0.125Zr1O3	4.745	1.752	-1.241
Sr0.875Ba0.125Zr1O3	6.783	3.481	0.179
Sr0.875Ca0.125Zr1O3	6.813	3.459	0.105
Sr0.875Cs0.125Zr1O3	3.318	-0.495	-4.308
Sr0.875Mg0.125Zr1O3	6.040	3.303	0.565
Sr0.875Rb0.125Zr1O3	3.369	-0.478	-4.326
Sr0.875Zn0.125Zr1O3	5.189	2.397	-0.395
Ba0.875Ca0.125Zr0.875Ti0.125O3	6.223	2.687	-0.849
Ba0.875Cs0.125Zr0.875V0.125O3	3.760	1.009	-1.742
Ba0.875La0.125Zr0.875Sc0.125O3	6.443	2.998	-0.448
Ba0.875Rb0.125Zr0.875V0.125O3	3.437	0.762	-1.914
Ba0.875Sr0.125Zr0.875Ti0.125O3	6.253	2.705	-0.842
Sr0.875Ba0.125Zr0.875Sn0.125O3	4.682	3.298	1.913
Sr0.875Ca0.125Zr0.875Ti0.125O3	6.369	2.721	-0.927
Sr0.875Cs0.125Zr0.875V0.125O3	3.269	0.749	-1.772
Sr0.875La0.125Zr0.875Sc0.125O3	6.128	3.078	0.028
Sr0.875Rb0.125Zr0.875V0.125O3	3.294	0.659	-1.976
Ba0.25Ca0.75Zr1O3	6.668	3.313	-0.041

Ba _{0.25} Sr _{0.75} Zr ₁ O ₃	6.272	2.786	-0.701
Sr _{0.25} Ca _{0.75} Zr ₁ O ₃	6.117	2.538	-1.042
Ba _{0.75} Bi _{0.25} Zr _{0.875} Fe _{0.125} O ₃	4.280	2.595	0.911
Ca _{0.25} Ba _{0.75} Zr ₁ O ₃	6.654	3.099	-0.456
Ca _{0.25} Sr _{0.75} Zr ₁ O ₃	6.788	3.320	-0.149
Sr _{0.25} Ba _{0.75} Zr ₁ O ₃	6.697	3.237	-0.223
La _{0.25} Ba _{0.75} Co _{0.125} Zr _{0.875} O ₃	6.017	2.291	-1.434
Sr _{0.25} Ba _{0.75} In _{0.125} Zr _{0.875} O ₃	2.811	-0.525	-3.862
Sr _{0.25} Ba _{0.75} Sc _{0.125} Zr _{0.875} O ₃	3.372	-0.513	-4.399
Sr _{0.25} Ba _{0.75} Y _{0.125} Zr _{0.875} O ₃	3.325	-0.513	-4.351
Ba _{0.25} Sr _{0.75} Zr _{0.75} Sn _{0.25} O ₃	4.026	2.520	1.013
Ba _{0.25} Sr _{0.75} Zr _{0.75} Ti _{0.25} O ₃	5.892	2.099	-1.694
Ca _{0.25} Ba _{0.75} Zr _{0.75} Sn _{0.25} O ₃	4.395	2.989	1.583
Ca _{0.25} Ba _{0.75} Zr _{0.75} Ti _{0.25} O ₃	6.207	2.368	-1.470
Ca _{0.25} Sr _{0.75} Zr _{0.75} Sn _{0.25} O ₃	4.472	3.051	1.631
Ca _{0.25} Sr _{0.75} Zr _{0.75} Ti _{0.25} O ₃	6.347	2.441	-1.466
Cs _{0.25} Sr _{0.75} Zr _{0.75} Nb _{0.25} O ₃	5.910	2.253	-1.404
La _{0.25} Ba _{0.75} Zr _{0.75} Sc _{0.25} O ₃	6.562	3.172	-0.218
La _{0.25} Sr _{0.75} Zr _{0.75} Cr _{0.25} O ₃	5.138	1.748	-1.642
La _{0.25} Sr _{0.75} Zr _{0.75} Fe _{0.25} O ₃	3.729	0.732	-2.264
La _{0.25} Sr _{0.75} Zr _{0.75} Sc _{0.25} O ₃	6.216	2.733	-0.749
Rb _{0.25} Ba _{0.75} Ce _{0.75} Ta _{0.25} O ₃	4.885	1.470	-1.945
Rb _{0.25} Sr _{0.75} Zr _{0.75} Ta _{0.25} O ₃	6.282	2.669	-0.943
Sr _{0.25} Ba _{0.75} Zr _{0.75} Sn _{0.25} O ₃	4.617	3.242	1.868
Sr _{0.25} Ba _{0.75} Zr _{0.75} Ti _{0.25} O ₃	6.236	2.399	-1.438
Ba _{0.5} Ca _{0.5} Zr ₁ O ₃	6.460	3.123	-0.213
Ba _{0.5} Sr _{0.5} Zr ₁ O ₃	6.753	3.357	-0.040
Sr _{0.5} Ca _{0.5} Zr ₁ O ₃	6.792	3.566	0.341
Ba _{0.5} Sr _{0.5} Ti _{0.5} Zr _{0.5} O ₃	6.068	2.427	-1.214

Ba _{0.5} Sr _{0.5} Zr _{0.5} Sn _{0.5} O ₃	4.665	3.354	2.044
Rb _{0.5} Ba _{0.5} Nb _{0.5} Zr _{0.5} O ₃	6.022	2.250	-1.522
Rb _{0.5} Sr _{0.5} Nb _{0.5} Zr _{0.5} O ₃	6.018	2.249	-1.519
Rb _{0.5} Sr _{0.5} Ta _{0.5} Zr _{0.5} O ₃	6.670	2.848	-0.975
Sr _{0.5} Ca _{0.5} Zr _{0.5} Sn _{0.5} O ₃	4.740	3.238	1.737
Sr _{0.5} La _{0.5} Sc _{0.5} Zr _{0.5} O ₃	6.638	3.701	0.763
Ba ₁ Hf ₁ O ₃	6.919	3.909	0.899
Ba ₁ Zr ₁ O ₃	6.757	3.342	-0.073
Sr ₁ Zr ₁ O ₃	6.849	3.566	0.282
Y ₁ Cr ₁ O ₃	5.737	3.099	0.461
Ba ₁ Ce ₁ O ₃	5.082	1.860	-1.362
Ba ₁ Zr _{0.75} Nb _{0.125} Fe _{0.125} O ₃	5.053	1.507	-2.039
Ba ₁ Zr _{0.75} Ta _{0.125} Fe _{0.125} O ₃	5.327	1.523	-2.281
Ba ₁ Ce _{0.875} Sn _{0.125} O ₃	4.420	1.759	-0.902
Ba ₁ Ce _{0.875} Zr _{0.125} O ₃	5.062	1.651	-1.759
Ba ₁ Hf _{0.875} Zr _{0.125} O ₃	6.865	3.826	0.786
Ba ₁ Zr _{0.875} Ce _{0.125} O ₃	6.195	2.739	-0.717
Ba ₁ Zr _{0.875} Cr _{0.125} O ₃	2.995	-0.036	-3.067
Ba ₁ Zr _{0.875} Ga _{0.125} O ₃	3.025	-0.458	-3.940
Ba ₁ Zr _{0.875} Ge _{0.125} O ₃	4.563	2.678	0.793
Ba ₁ Zr _{0.875} Hf _{0.125} O ₃	6.771	3.392	0.012
Ba ₁ Zr _{0.875} In _{0.125} O ₃	2.907	-0.309	-3.526
Ba ₁ Zr _{0.875} Ir _{0.125} O ₃	4.024	1.176	-1.672
Ba ₁ Zr _{0.875} Pt _{0.125} O ₃	2.924	2.227	1.530
Ba ₁ Zr _{0.875} Sc _{0.125} O ₃	3.428	-0.343	-4.115
Ba ₁ Zr _{0.875} Sn _{0.125} O ₃	4.658	3.483	2.309
Ba ₁ Zr _{0.875} Tc _{0.125} O ₃	5.381	2.466	-0.450
Ba ₁ Zr _{0.875} Ti _{0.125} O ₃	6.245	2.668	-0.909
Ba ₁ Zr _{0.875} V _{0.125} O ₃	4.656	1.152	-2.353

Ba1Zr0.875Y0.125O3	3.379	-0.344	-4.067
Sr1Zr0.875Cr0.125O3	3.303	0.074	-3.155
Sr1Zr0.875Ge0.125O3	4.901	2.847	0.793
Sr1Zr0.875Hf0.125O3	6.643	3.334	0.025
Sr1Zr0.875In0.125O3	2.834	-0.506	-3.846
Sr1Zr0.875Mn0.125O3	3.186	0.988	-1.210
Sr1Zr0.875Sc0.125O3	3.335	-0.654	-4.644
Sr1Zr0.875Si0.125O3	6.351	3.476	0.601
Sr1Zr0.875Sn0.125O3	4.784	3.317	1.849
Sr1Zr0.875Ti0.125O3	6.411	2.779	-0.852
Sr1Zr0.875V0.125O3	4.866	1.225	-2.416
Sr1Zr0.875Y0.125O3	3.320	-0.667	-4.653
Ba1Hf0.25Zr0.75O3	6.786	3.489	0.191
Ba1Ti0.25Zr0.75O3	6.210	2.488	-1.233
Ba1Zr0.25Ce0.75O3	5.224	1.624	-1.975
Sr1Hf0.25Zr0.75O3	6.646	3.405	0.163
Sr1Ti0.25Zr0.75O3	6.392	2.548	-1.295
Ba1Ce0.25Zr0.75O3	5.796	2.295	-1.207
Ba1Ge0.25Zr0.75O3	4.701	2.906	1.111
Ba1Sn0.25Zr0.75O3	4.681	3.566	2.451
Ba1Tc0.25Zr0.75O3	5.416	2.381	-0.653
Ba1Zr0.25Hf0.75O3	6.862	3.762	0.662
Sr1Ge0.25Zr0.75O3	4.765	2.652	0.539
Sr1Sn0.25Zr0.75O3	4.519	2.998	1.476
Ba1Hf0.5Zr0.5O3	6.843	3.605	0.368
Ba1Ti0.5Zr0.5O3	6.064	2.492	-1.080
Ba1Zr0.5Ce0.5O3	5.402	1.884	-1.634
Ba1Zr0.5Sn0.5O3	4.725	3.721	2.717
Sr1Hf0.5Zr0.5O3	6.860	3.676	0.492

Sr1Ti0.5Zr0.5O3	6.312	2.568	-1.177
Sr1Zr0.5Ce0.5O3	5.042	1.257	-2.528
Sr1Zr0.5Sn0.5O3	4.788	3.385	1.982

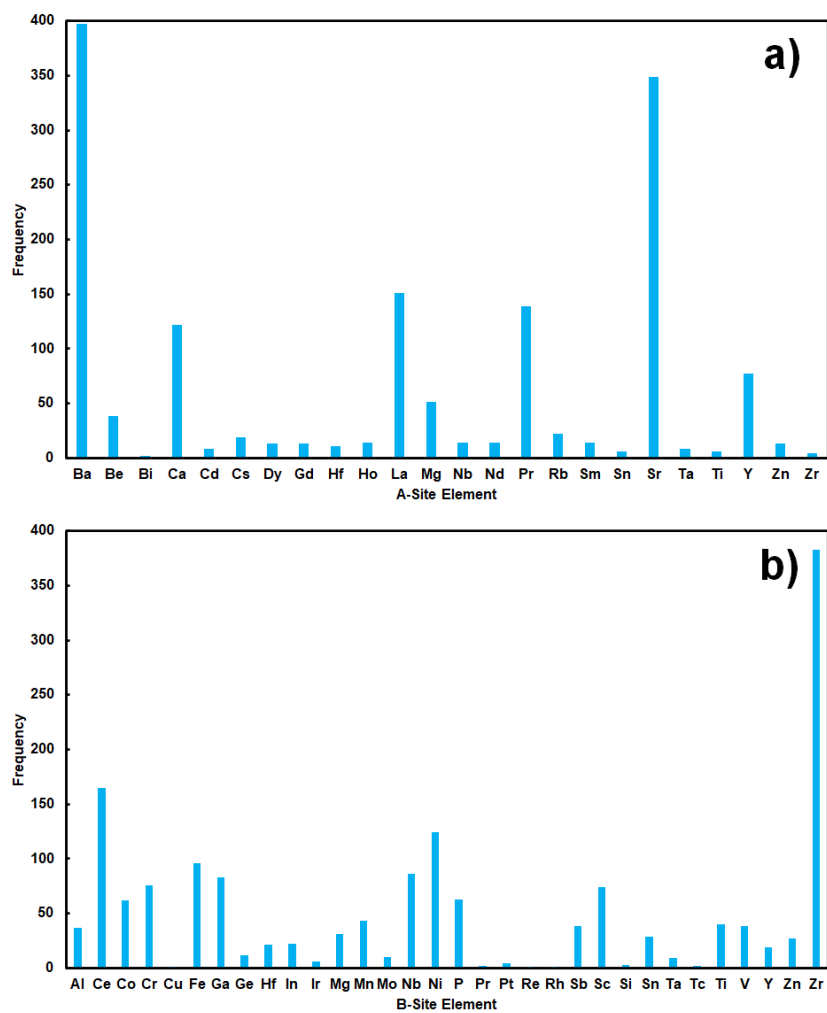


Figure C.6: a) Bar graph of the A-site elemental frequency of Filter 1 passing configurations (e.g., > 2.0 eV bandgap) and b) a bar graph of the B-site elemental frequency of Filter 1 passing configurations.

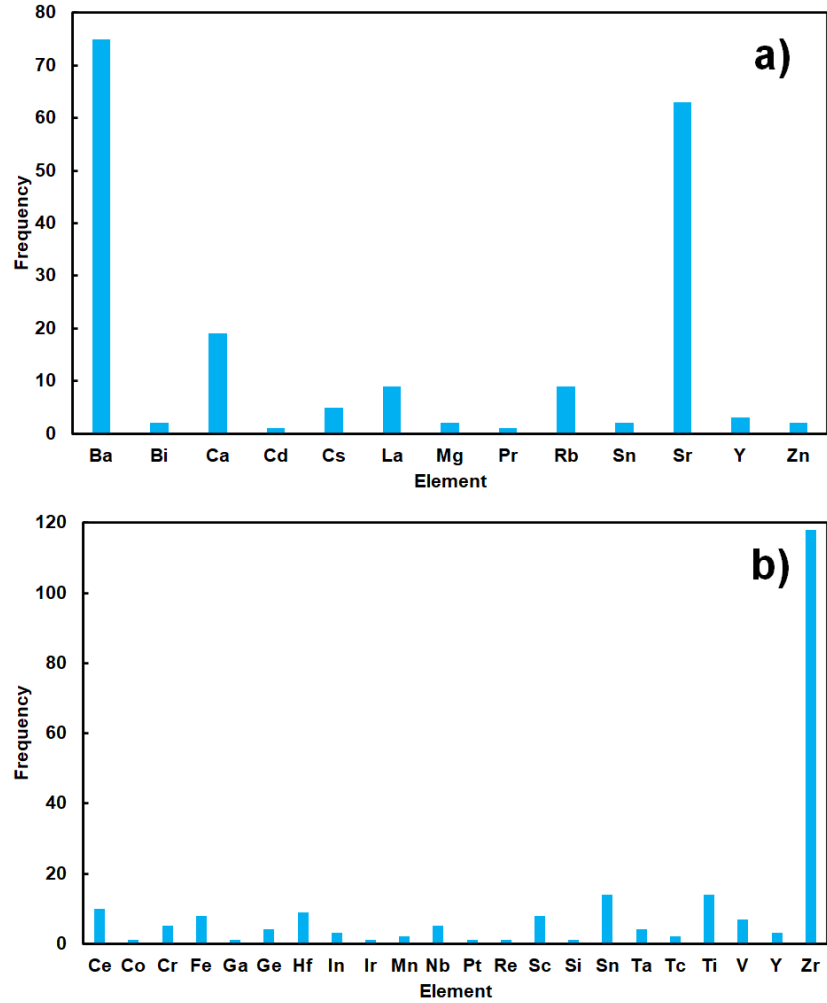


Figure C.7: a) Bar graph of the A-site elemental frequency of Filter 2 passing configurations and b) a bar graph of the B-site elemental frequency of Filter 2 passing configurations (e.g., > 2.0 eV bandgap, $E_{\text{hull}} < 0.041$ eV/atom under anode conditions).

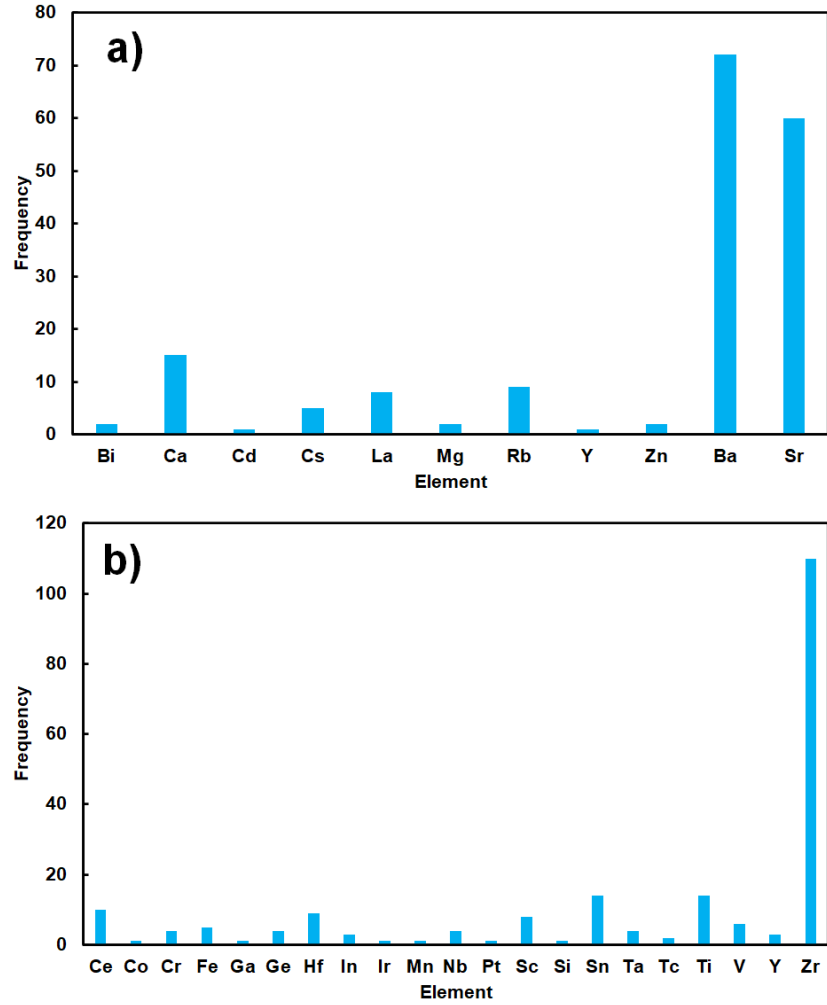


Figure C.8: a) Bar graph of the A-site elemental frequency of Filter 3 passing configurations and b) a bar graph of the B-site elemental frequency of Filter 3 passing configurations (e.g., > 2.0 eV bandgap, $E_{\text{hull}} < 0.041$ eV/atom under both anode and cathode conditions).

Table C.3: List of materials that are stable under anodic and cathodic conditions but yield a bandgap between 1.0 and 2.0 eV.

Configuration	Bandgap (eV)	$E_{\text{hull,CO}_2}$ (eV/atom)
Ba _{0.875} Ca _{0.125} Zr _{0.875} Mn _{0.125} O ₃	1.16	0.085
Ba _{0.875} Sr _{0.125} Zr _{0.875} Mn _{0.125} O ₃	1.175	0.053
Sr _{0.875} Ba _{0.125} Zr _{0.875} Cr _{0.125} O ₃	1.106	0.066
Sr _{0.875} Ba _{0.125} Zr _{0.875} V _{0.125} O ₃	1.873	0.077
Sr _{0.875} Ca _{0.125} Zr _{0.875} Mn _{0.125} O ₃	1.558	0.044
Ba _{0.25} Sr _{0.75} Mn _{0.125} Zr _{0.875} O ₃	1.408	0.057
Ca _{0.25} Sr _{0.75} Mn _{0.125} Zr _{0.875} O ₃	1.576	0.052
Rb _{0.5} Ba _{0.5} Ce _{0.5} Nb _{0.5} O ₃	1.926	0.221
Rb _{0.5} Ba _{0.5} Ta _{0.5} Ce _{0.5} O ₃	1.862	0.176
Ba ₁ Zr _{0.875} Mn _{0.125} O ₃	1.123	0.043
Ba ₁ Zr _{0.875} Os _{0.125} O ₃	1.418	0.095
Ba ₁ Zr _{0.875} Rh _{0.125} O ₃	1.71	0.033
Ba ₁ Zr _{0.875} Ru _{0.125} O ₃	1.551	0.026
Sr ₁ Zr _{0.875} Os _{0.125} O ₃	1.567	0.097
Sr ₁ Zr _{0.875} Ru _{0.125} O ₃	1.727	0.041

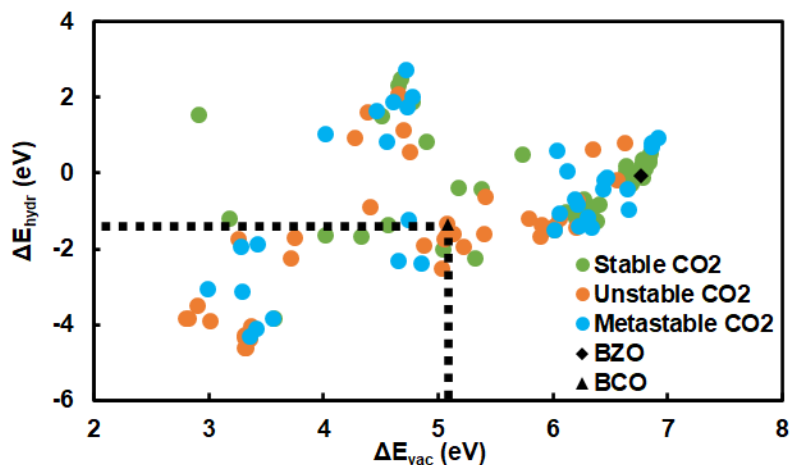


Figure C.9: a) Scatter plot of vacancy formation energy (ΔE_{vac} in eV) versus hydration energy (ΔE_{hydr} in eV) for the 116 materials that passed the first three filters organized with respect to their stability under CO_2 environment. The legends stable, metastable, and unstable refer to the materials exhibiting $E_{\text{hull}} < 0.041$ eV/atom, $E_{\text{hull}} = 0.041$ - 0.081 eV/atom, and $E_{\text{hull}} > 0.081$ eV/atom, respectively under CO_2 environment. Dashed lines outline the regime with favorable defect formation activity (low ΔE_{vac} and ΔE_{hydr} values). BZO and BCO are included as benchmarking materials as a black diamond and triangle, respectively.

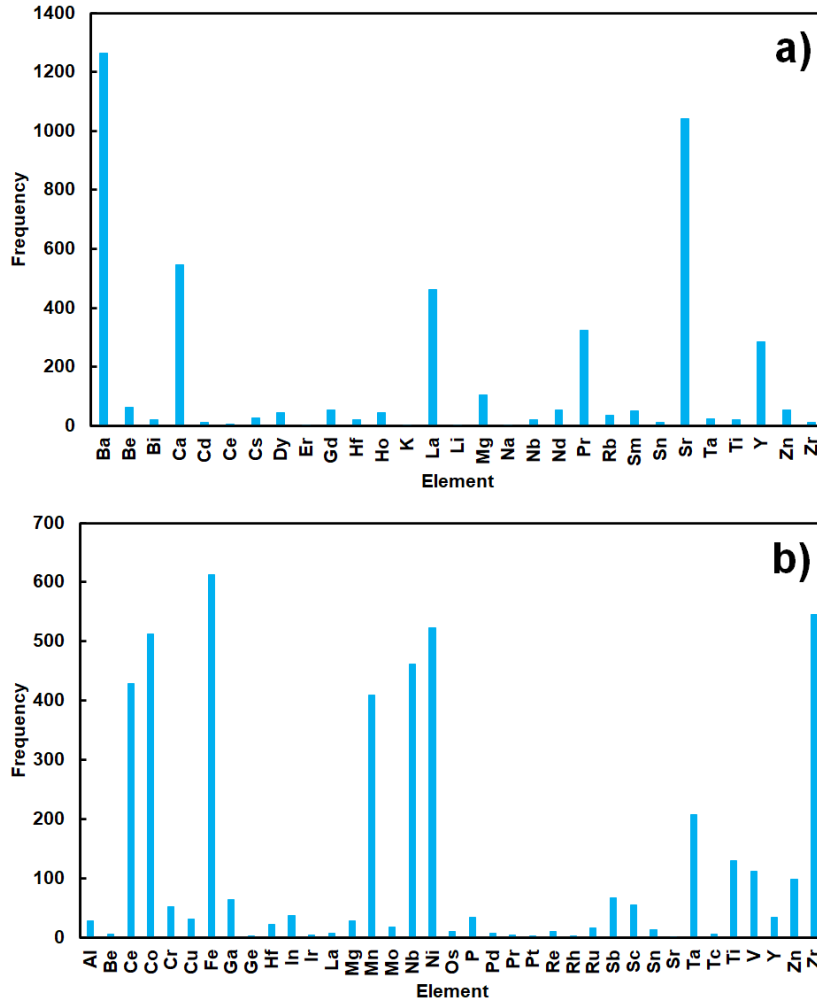


Figure C.10: a) Bar graph of the A-site elemental frequency of Filter 1a passing configurations and b) a bar graph of the B-site elemental frequency of Filter 1a passing configurations (e.g., < 0.5 eV bandgap).

Table C.4: Calculated Bader charges for $\text{Ba}_{0.125}\text{Sr}_{0.875}\text{Sn}_{0.125}\text{Zr}_{0.875}\text{O}_3$ and BCO based on the lowest energy vacancy site.

BCO			
S/N	q_M (Nearest Ce)	q_O	q_H
Defect Free	2.189	-1.249	N/A
Oxygen Vacancy	1.980	N/A	N/A
Hydrogen Interstitial	2.171	-1.736	1.000
$\text{Ba}_{0.125}\text{Sr}_{0.875}\text{Sn}_{0.125}\text{Zr}_{0.875}\text{O}_3$			
S/N	q_M (Nearest Sn)	q_O	q_H
Defect Free	2.410	-1.345	N/A
Oxygen Vacancy	1.254	N/A	N/A
Hydrogen Interstitial	1.890	-1.761	1.000

Table C.5: List of materials that passed Filter 3 (e.g., greater than > 2.0 eV bandgap; stable in anodic and cathodic) and display CO_2 metastability with E_{hull} values between 0.041 and 0.081 eV/atom.

Configuration	E_{f,V_O^\times} (eV)	E_{f,O_H^\times} (eV)	ΔE_{hydr} (eV)	$E_{\text{hull},\text{CO}_2}$ (eV/atom)
Ba0.875Cs0.125Zr1O3	3.57	-0.15	-3.86	0.055
Ba0.875Mg0.125Zr1O3	6.48	3.16	-0.16	0.072
Ba0.875Zn0.125Zr1O3	4.75	1.75	-1.24	0.079
Sr0.875Mg0.125Zr1O3	6.04	3.30	0.57	0.067
Sr0.875Rb0.125Zr1O3	3.37	-0.48	-4.33	0.058
Ba0.875Ca0.125Zr0.875Ti0.125O3	6.22	2.69	-0.85	0.050
Ba0.875La0.125Zr0.875Sc0.125O3	6.44	3.00	-0.45	0.047
Ba0.875Rb0.125Zr0.875V0.125O3	3.44	0.76	-1.91	0.060
Sr0.875La0.125Zr0.875Sc0.125O3	6.13	3.08	0.03	0.049
Sr0.875Rb0.125Zr0.875V0.125O3	3.29	0.66	-1.98	0.073
Ca0.25Ba0.75Zr1O3	6.65	3.10	-0.46	0.046
Ba0.25Sr0.75Zr0.75Sn0.25O3	4.03	2.52	1.01	0.076
Ca0.25Sr0.75Zr0.75Sn0.25O3	4.47	3.05	1.63	0.042
Ca0.25Sr0.75Zr0.75Ti0.25O3	6.35	2.44	-1.47	0.061
Sr0.25Ba0.75Zr0.75Sn0.25O3	4.62	3.24	1.87	0.045
Sr0.25Ba0.75Zr0.75Ti0.25O3	6.24	2.40	-1.44	0.063
Ba0.5Ca0.5Zr1O3	6.46	3.12	-0.21	0.073

Rb0.5Ba0.5Nb0.5Zr0.5O3	6.02	2.25	-1.52	0.042
Rb0.5Sr0.5Ta0.5Zr0.5O3	6.67	2.85	-0.97	0.048
Sr0.5Ca0.5Zr0.5Sn0.5O3	4.74	3.24	1.74	0.079
Ba1Hf1O3	6.92	3.91	0.90	0.071
Ba1Hf0.875Zr0.125O3	6.87	3.83	0.79	0.059
Ba1Zr0.875Ce0.125O3	6.19	2.74	-0.72	0.061
Ba1Zr0.875Cr0.125O3	3.00	-0.04	-3.07	0.064
Ba1Zr0.875Ge0.125O3	4.56	2.68	0.79	0.044
Ba1Zr0.875Sc0.125O3	3.43	-0.34	-4.11	0.072
Ba1Zr0.875V0.125O3	4.66	1.15	-2.35	0.075
Sr1Zr0.875Cr0.125O3	3.30	0.07	-3.15	0.050
Sr1Zr0.875V0.125O3	4.87	1.22	-2.42	0.059
Ba1Zr0.25Hf0.75O3	6.86	3.76	0.66	0.047
Ba1Ti0.5Zr0.5O3	6.06	2.49	-1.08	0.065
Ba1Zr0.5Sn0.5O3	4.73	3.72	2.72	0.065
Sr1Ti0.5Zr0.5O3	6.31	2.57	-1.18	0.050
Sr1Zr0.5Sn0.5O3	4.79	3.39	1.98	0.060

APPENDIX D

COPYRIGHTS AND PERMISSIONS



An ab initio study of the oxygen defect formation and oxide ion migration in $(\text{Sr}_{1-x}\text{Pr}_x)\text{2FeO}_{4\pm\delta}$

Author: Nicholas A. Szaro, Salai Cheettu Ammal, Fanglin Chen, Andreas Heyden

Publication: Journal of Power Sources

Publisher: Elsevier

Date: 15 December 2021

© 2021 Elsevier B.V. All rights reserved.

Journal Author Rights

Please note that, as the author of this Elsevier article, you retain the right to include it in a thesis or dissertation, provided it is not published commercially. Permission is not required, but please ensure that you reference the journal as the original source. For more information on this and on your other retained rights, please visit: <https://www.elsevier.com/about/our-business/policies/copyright#Author-rights>

BACK

CLOSE WINDOW



Theoretical Investigation of the Electrochemical Oxidation of H₂ and CO Fuels on a Ruddlesden-Popper SrLaFeO_{4-δ} Anode

Author: Nicholas A. Szaro, Salai Cheettu Ammal, Fanglin Chen, et al

Publication: Applied Materials

Publisher: American Chemical Society

Date: Jun 1, 2023

Copyright © 2023, American Chemical Society

PERMISSION/LICENSE IS GRANTED FOR YOUR ORDER AT NO CHARGE

This type of permission/license, instead of the standard Terms and Conditions, is sent to you because no fee is being charged for your order. Please note the following:

- Permission is granted for your request in both print and electronic formats, and translations.
- If figures and/or tables were requested, they may be adapted or used in part.
- Please print this page for your records and send a copy of it to your publisher/graduate school.
- Appropriate credit for the requested material should be given as follows: "Reprinted (adapted) with permission from (COMPLETE REFERENCE CITATION), Copyright (YEAR) American Chemical Society." Insert appropriate information in place of the capitalized words.
- One-time permission is granted only for the use specified in your RightsLink request. No additional uses are granted (such as derivative works or other editions). For any uses, please submit a new request.

If credit is given to another source for the material you requested from RightsLink, permission must be obtained from that source.

BACK

CLOSE WINDOW